NASA TECHNICAL MEMORANDUM

NASA TM X-62,334

NASA TM X-62,334

A FLIGHT INVESTIGATION OF THE STOL CHARACTERISTICS OF AN AUGMENTED JET FLAP STOL RESEARCH AIRCRAFT

Hervey C. Quigley and Robert C. Innis

Ames Research Center
Moffett Field, Calif. 94035

and

Seth Grossmith

Ministry of Transport, Canada

May 1974

SYMBOLS

A_X	acceleration along longitudinal axis
A_Z	acceleration along vertical axis
BLC	boundary layer control
$\bar{c}$	mean aerodynamic chord, 12.1 ft (3.68 m)
C_D	drag coefficient, $\frac{\text{drag}}{q(\text{wing area})}$
C_{D_A}	drag coefficient excluding hot thrust contribution
C_{D_G}	drag coefficient in ground effect
C_J	jet momentum coefficient, isentropic, $\frac{\text{cold thrust}}{q(\text{wing area})}$
C_ℓ	rolling moment coefficient, $\frac{\text{rolling moment}}{q(\text{wing area})(\text{wing span})}$
C_{ℓ_β}	$\frac{\partial C_\ell}{\partial \beta}$
C_L	lift coefficient, $\frac{\text{lift}}{\bar{q}\,(\text{wing area})}$
C_{L_A}	lift coefficient excluding hot thrust contribution
C_{L_G}	lift coefficient in ground effect
C_{L_T}	total lift coefficient, $\frac{Wn_z}{\bar{q}\,(\text{wing area})}$
C_M	pitching moment coefficient, $\frac{\text{pitching moment}}{\bar{q}\,\bar{c}\,(\text{wing area})}$
C_{M_G}	pitching moment coefficient in ground effect
C_T	thrust (hot) coefficient, $\frac{\text{thrust}}{\bar{q}\,(\text{wing area})}$
F_{COL}	column (stick) force, lb
F_W	wheel force, lb
K	degrees Kelvin
M_E	mass flow of air in engine
M_B	mass flow of bypass air

N_H	high pressure engine rotor speed, rpm
n_z	vertical load factor
$\bar{q}$	free-stream dynamic pressure, $1/2\ \rho V^2$, lb/ft^2
P	period of oscillation, sec
P_1	engine inlet pressure, psi
P_T	engine bypass air total pressure, psi
r	yawing rate, rad/sec
rpm	revolution per minute
SAS	Stability Augmentation System
t	time, sec
$T_{1/2}$	time to 1/2 amplitude, sec
T_2	time to double amplitude, sec
T_1	engine inlet temperature, °K
V	velocity, ft/sec or knots
V_E	equivalent air speed (EAS), knots
V_S	sink rate, ft/sec
VFR	visual flight rules
VSS	Variable Stability System
W	weight, lb
α_F	angle of attack of fuselage, positive nose up, deg
β	angle of sideslip, positive nose left, deg
γ	flight path angle, positive up, deg
δ_{AIL}	aileron deflection, positive T.E. down, deg
δ_{CH}	choke deflection, positive T.E. up, deg

δ_{COL} control column deflection in pitch, positive aft, deg

δ_e elevator deflection, positive T.E. down, deg

δ_f flap deflection, positive T.E. down, deg

δ_p rudder pedal deflection, positive left forward, in.

δ_{sp} spoiler deflection, positive T.E. up, deg

δ_w control wheel deflection, positive clockwise, deg

θ pitch angle, positive nose up, deg

μ braking coefficient

ν nozzle deflection, positive down from full aft, relative to fuselage datum line, deg

ξ damping ratio

ρ ambient air density, slugs/ft^3

τ_A apparent roll mode time constant

ϕ roll angle, positive right wing down, deg

ϕ_1 roll angle after 1 sec, deg

ψ yaw angle, positive nose right, deg

ω_n natural frequency, rad/sec

A FLIGHT INVESTIGATION OF THE STOL CHARACTERISTICS OF AN AUGMENTED JET FLAP STOL RESEARCH AIRCRAFT

Hervey C. Quigley and Robert C. Innis
Ames Research Center

and

Seth Grossmith
Ministry of Transport, Canada

INTRODUCTION

Several powered lift concepts are being studied by NASA for possible future use on fan jet STOL transport airplanes. The augmented jet flap or augmentor wing concept has been recognized by both government (ref. 1) and industry (refs. 2-4) as one of the promising concepts for further research and development.

A cooperative NASA/Canadian Government research program on the augmented jet flap concept began in 1965. The program included analysis and small-scale static and wind-tunnel tests (ref. 5); large-scale tests in the Ames 40- by 80-Ft Wind Tunnel (refs. 6-8) conducted by NASA in cooperation with the Canadian Defense Research Board using a de Havilland built model; and NASA design feasibility and simulator studies. Research progress by early 1970 warranted development of a proof-of-concept aircraft to test the jet STOL principle in flight. The U.S. and Canadian governments entered into an international agreement whereby the NASA and the Canadian Department of Industry Trade and Commerce (DITC) would modify a de Havilland C-8A Buffalo to an augmented jet flap STOL research aircraft. The DITC contracted with the de Havilland Aircraft of Canada, Ltd., and their subcontractor Rolls Royce of Canada, Ltd., to provide and modify the jet engines and modify the nacelles. The NASA contracted with The Boeing Company to modify the aircraft, provide the augmented jet flap system, install the propulsion system, and perform the initial flight tests. Reference 9 summarizes the contractor development program and describes the augmented jet flap STOL research aircraft.

The C-8A Buffalo aircraft was chosen on the basis of a design feasibility study, which showed that with required aircraft modifications, the primary research objective could be achieved at a reasonable cost and within an acceptable time span. In addition, considerable design data were available from extensive testing in the Ames 40- by 80-Ft Wind Tunnel of a large-scale model having a wing planform similar to the C-8A (refs. 6-8). (Simulation inputs to the development of the aircraft are discussed in refs. 10-12.)

The first flight of the aircraft was made on May 1, 1972, at Seattle, Washington. The initial airworthiness flight test program was conducted by The Boeing Company (ref. 13). During these tests the aircraft was flown within a flight envelope of from 50 to 180 knots and at load factors sufficient to demonstrate that the aircraft flight loads were within design and the airplane flutter free. The aircraft was delivered to NASA on July 31, 1972.

The flight test program objectives are (1) to determine the in-flight aerodynamic, performance, and handling qualities of a jet STOL aircraft incorporating the augmented jet flap concept; (2) to compare the results obtained in flight with characteristics predicted from wind tunnel and simulator test results; (3) to contribute to the development of criteria for design and operation of jet STOL transport aircraft; and (4) to provide a jet STOL transport aircraft for STOL systems research and development.

This report presents results obtained during the first 8 months of proof-of-concept flight testing of the aircraft in STOL configurations. Included are a brief description of the aircraft, fan-jet engines, and systems; a discussion of the aerodynamic, stability and control, and STOL performance; and pilot opinion of the handling qualities and operational characteristics. The tests did not include flight near maximum lift coefficient because of the limitations of the longitudinal control system. Flight tests at high angles of attack at or near $C_{L_{max}}$ will be conducted following modifications to the aircraft to incorporate a powered longitudinal control system.

The flight tests were conducted by a project team consisting of the following personnel; all are at NASA-Ames Research Center unless otherwise specified:

Project Management
- David D. Few
- Hervey C. Quigley

Project Pilots
- Robert C. Innis
- Seth Grossmith, Ministry of Transport, Canada

Project Engineers
- Jerry P. Barrack
- Alfred G. Boissevain
- Bruce Lilley, The de Havilland Aircraft of Canada, Ltd.
- Jack W. Ratcliff
- Brian Swan, Department of National Defence, Canada
- Richard F. Vomaske
- John W. Weyers

THE RESEARCH AIRCRAFT

The research aircraft is a highly modified de Havilland C-8A Buffalo military turboprop transport. Its high wing and high "T" tail made it especially suitable for application of a powered lift system. The landing and takeoff configurations of the aircraft are shown in figure 1. Table 1 lists the geometric and mass characteristics of the aircraft. Figure 2 is a three-view drawing of the aircraft. Special features of the aircraft are described briefly below; a more complete description is presented in reference 9.

Engine

Two Rolls Royce Spey MK 801-SF split flow engines, one mounted in each of two nacelles (fig. 2), provide the thrust for the aircraft as well as the air for the augmentation system. The engine is mounted to the same nacelle structure as used for the T-64 installation in the original C-8A. The MK 801-SF engine (fig. 3) is a hybrid engine of 0.6 bypass ratio, which was assembled from several engines by Rolls Royce. It consists of a Spey MK 511-8 core, a Spey MK 512 low pressure compressor, a Spey MK 555-15 high pressure compressor external gearbox, Avon MK 101 low pressure dump valves, a new bypass air duct, a Pegasus MK 5 trouser piece, and new vectorable conical nozzles. Existing engine hardware was used to the extent possible to reduce development time, risk, and costs. The resulting engine represents a very useful research tool, but is not necessarily an optimum configuration for future augmentor wing aircraft. A more detailed description of the engine and a discussion of its development is provided in reference 14.

The low pressure compressor for the engine has five stages, the first and fifth being made of titanium with mid-span snubbers to make the compressor more tolerant of inlet flow distortions and deviations from the nominal compressor working line. Its maximum pressure ratio is 2.5.

The engine bypass air is collected and discharged through two 13-in.-diameter (0.3 m) ducts located at the top of the engine (fig. 4); it is distributed to the augmentor fuselage and aileron nozzles by the air distribution system discussed below.

The flow from the hot section of the engine is discharged into a slightly strengthened Pegasus trouser piece and out through two conical nozzles. The trouser piece was originally designed for a much larger engine, and a "colander plate" (fig. 3) between the turbine and the trouser piece allows proper matching of the compressors and turbines without the fear of possible disturbances in the trouser piece or nozzle affecting engine operation. The colander plate is a 1-in. steel plate with 400 one-inch-diameter (2.54 cm) holes, 36 of which are plugged to accommodate the engine discharge flow area requirement. The conical nozzles can be vectored by means of a Hawker Siddeley nozzle control system from 0° to 98° down relative to the engine centerline (6° to 104° relative to the fuselage waterline) to provide flight path control and increase experimental versatility. The nozzle vector angle control handles, one for each engine, are located in the cockpit overhead console adjacent to the throttles within easy reach of the pilot.

The Spey MK 801-SF engine operating parameters are shown in figure 5. The bypass (cold) thrust shown is isentropic cold thrust at the engine offtake.

Air Distribution System

The air distribution system directs the engine bypass air to the upper and lower augmentor nozzles, to the fuselage boundary layer blowing nozzles, and to the aileron blowing nozzles (figs. 6 and 7). A crossover ducting system is used so that approximately 64 percent of the bypass mass flow of each engine is ducted to the augmentor and aileron nozzles on the opposite wing and to half of the fuselage boundary-layer blowing nozzles, while the remaining 36 percent of the bypass mass flow is ducted aft to the augmentor nozzles on the same side of the aircraft as the engine. The air distribution systems for each engine are completely separate, but identical. This unique arrangement provides for engine-out operation without large rolling or yawing moments.

The mass flow from the inboard offtake port (36 percent of the total mass flow) of each engine is ducted aft in the nacelle to a tee in the lower (inner) augmentor nozzle assembly. This duct from the engine aft to the lower augmentor nozzle duct contains a calibrated flow measuring station.

The mass flow from the outboard offtake duct (64 percent of the total mass flow) of each engine is directed through a 14-in.-diameter (0.35 m) duct along the front spar of the wing and across the interior of the fuselage to the upper (outer) augmentor nozzle duct at the rear spar of the opposite wing. A calibrated mass flow measuring station is located in the straight section of the duct along the wing front spar. A 6-in.-diameter (0.15 m) duct is tapped into the fuselage crossover duct to provide air for the fuselage boundary-layer blowing nozzles. Of the 64 percent of the engine mass flow carried by the crossover ducting system, approximately 7.1 percent is used for fuselage blowing, 44 percent by the upper augmentor nozzles, and the remaining 12.9 percent by the aileron boundary-layer control nozzles (fig. 7).

The design duct Mach number of the air distribution system was 0.3 to prevent excessive flow losses. The resulting bypass air flow losses are summarized in figure 8. For the purposes of this report, all bypass thrust levels are defined as the isentropic thrust that would be obtained for fully expanded flow based on the pressure, temperature, and mass flow measurements just downstream of the engine offtakes.

At takeoff, the mass flow through the air distribution system is 79 lb/sec per engine at 270° F and a pressure ratio of 2.5. The installation thrust losses due to pressure drops in the supply ducts to the flaps are about 4 percent of the fan thrust. An additional thrust loss of about 7 percent occurs through the high aspect ratio nozzles and the flap ducts. Additional information on duct losses are provided in reference 9.

Augmented Jet Flap

Figure 9 is a sketch of the general arrangement of the augmented jet flap and its major components. The flap geometry is basically the same as that of the large-scale model tested in the Ames 40- by 80-Ft Wind Tunnel (ref. 7). The flaps have constant chord and are made in four equal spanwise segments, two on each side of the aircraft. To reduce the overall cost of the modification program, the flap assembly was not designed to retract into the streamlined airfoil contour as would be required for high speed flight.

The entire augmentor flap assembly, including the augmentor nozzle duct, is supported on beams external to the wing that attach to the front and rear spars. This arrangement permits accurate alignment of the flap and nozzle assembly and minimizes the effects of wing deflection.

The flaps are deflected by hydraulic linear actuators mounted external to the wing. The minimum (flaps up) angle is 5.6° and the maximum flap angle is 72°.

The ducts that supply the air to the flaps are mounted just aft of the rear spars and provide air independently from each engine. The inner duct air is supplied from the engine on the same side of the aircraft as the engine, while the outer duct is supplied from the engine on the opposite side.

The flap itself is made up of two surfaces, each of which has slots for added air flow and boundary-layer control. As the flap deflects, the intake door on the top surface also deflects (fig. 10) to allow a smoother outside air entry into the flap system and to retard flow separation from the upper surface of the shroud. Note also that the flap system pivots about a point within the Coanda leading edge portion of the lower surface so that the ejected air from the nozzles is tangent to the surface of the Coanda as the flap deflects. Static tests of a 0.7-scale model (ref. 15) showed that the location of this tangency point relative to the eflux centerline was of critical importance for obtaining the maximum augmentation ratio. Also, the optimum Coanda surface position for each flap deflection is at a different location. The location chosen for the aircraft represents a compromise that favors a flap deflection of 45°. The sensitivity of performance to physical positioning of the flap components resulted in a design of relatively rigid structure to minimize deformation.

Fixed leading edge slats were installed to help maintain airflow over the wing at the high values of circulation obtained during powered-lift operation.

Flight Control System

Several modifications were made to the basic C-8A Buffalo flight control system. In the cockpit (fig. 11), the control wheel was replaced with a wheel instrumented to read out lateral and longitudinal control forces. The only other change in the cockpit flight controls was the addition of an electrical lateral and pitch trim switch, which the pilot could control with his left thumb and the co-pilot with his right thumb; the manual trim was retained.

The longitudinal control system is the basic C-8A Buffalo manual spring tab system modified to reduce the stick forces for "one hand" pilot operation. The static stick force variation with control column position is shown in figure 12. The dynamic force characteristic of a spring tab system requires an initial force to deflect the tab that is momentarily higher than the static force characteristics. As discussed later, these force characteristics along with mass balance forces at low speeds were found to be undesirable.

The directional control system consists of a two-panel rudder, the aft panel being hinged to the trailing edge of the forward panel and geared to it with a 2:1 deflection ratio. The rudder is fully powered through an irreversible dual hydraulic actuator controlled by cables from the pedals. The only modification to the basic Buffalo directional control system was the addition of a Stability

Augmentation System (*SAS*) actuator mechanically summed in series with pilot inputs. The rudder pedal force and gearing are shown in figure 13.

The lateral control system is completely new. Three separate surfaces are used to produce the required rolling moments: ailerons with boundary-layer control, spoilers in front of the ailerons, and an augmentor choke. Figure 14 shows the position and function of each element. The ailerons are mechanically programmed to droop as a function of the flap deflection as shown in figure 15(a). Full droop is 35° and is reached at flap deflection of about 70°. The differential aileron deflection from the droop position is ±17°. Blowing boundary-layer control is used on the aileron to increase the effectiveness of both the aileron and spoiler. The augmentor chokes are designed to control the lift of the augmented jet flap system by changing the exit of the augmentor. Full lateral control reduces the exit area as a function of flap deflection to a maximum of 55 percent on the downgoing wing (fig. 15(b)). The chokes function much the same as spoilers on a conventional airplane. Although there are augmentor chokes in each of the four sections of the flap, only the chokes in the outboard section of each wing are used for lateral control. All four chokes are activated on the ground after landing for lift dump.

The three lateral control surfaces are programmed to give nearly linear effectiveness with control wheel deflection (fig. 16(a)). The aileron and spoiler operate from 0° wheel deflection, and the augmentor choke is phased in at 17° control wheel deflection. The spoilers are fully deflected at 48° wheel deflection.

Lateral control wheel forces are low (fig 16(b)) and are produced by a simple spring system. The lateral control surfaces are activated by a central dual hydraulic power actuator, located on the rear spar, which drives the ailerons through a cable system. The central lateral power actuator also drives spoilers and augmentor choke control valves through a second cable. The spoiler and choke actuators are on different hydraulic systems.

Stability Augmentation System

Two independent stability augmentation systems, one for the lateral and one for the directional aircraft axis are provided. Each system offers the pilot two modes of *SAS* operation: normal mode having fixed gains for near optimum characteristics and a variable stability mode with gain adjustment. The normal mode is used for basic STOL operations, and the variable stability mode is used for changes in gain setting in handling-qualities testing.

The *SAS* actuators are positioned by closed-loop servos and summed in series with the pilot's control system. The *SAS* electronics is single channel, and relies on limited rate and displacement authority for safety. The wheel lateral rate limit is 50°/sec while the displacement authority is limited to ±20° (27 percent) equivalent wheel displacement. The maximum directional rate is 25°/sec of rudder travel, and displacement is limited to ±5° (20 percent) of forerudder deflection.

The lateral *SAS* in the normal mode performs the following functions:

1. Spiral stability augmentation, using yaw feedback to the lateral controls.

2. Roll damping augmentation, using roll rate feedback to the lateral controls.

3. Lateral control quickening, using wheel position feed forward (±3° maximum) to the lateral controls.

The directional *SAS* in the normal mode perform the following functions:

1. Turn coordination, using roll rate and roll attitude feedback to the rudder.

2. Dutch roll damping, using yaw rate and roll attitude feedback to the rudder.

Normal mode gains (fig. 17) are programmed with flap position and are automatically switched off above 100 knots. Figure 17(c) is the schematic for the lateral control aileron quickener, which doubles the lateral control gearing for the first three degrees of control wheel travel to improve the control characteristics near zero deflection.

Data Acquisition System

An onboard data acquisition system gathers data on about 95 parameters measured during all ground and flight testing. A pulse code modulated (PCM) digital system records the data on magnetic tape. Recorded flight test data include stability and control, *SAS* signals, engine performance, augmentor performance, and guidance information. Each channel is sampled 100 times per second. The PCM word length is 10 bits. The system's 14-track tape recorder has a capacity of about 50 min recording time per reel of tape. To allow data gathering during flights that exceed 50 min duration, the pilot may start and stop the recorder at will.

The PCM data is processed on a Sigma-7 digital computer programmed with the desired calculations for determining such parameters as engine thrust, lift and drag coefficients, flight path angle, and corrected airspeed.

The onboard data acquisition system also includes a recording oscillograph, which is used for additional recording requirements when the available number of PCM channels are exceeded. The oscillograph also has a much higher (to 5000 Hz) frequency response used for recording such parameters as loads and vibration.

FLIGHT TEST PROCEDURE

The flight tests were initiated from Moffett Field and flown in test areas in the vicinity of Moffett Field and at the Crows Landing Naval Auxiliary Landing Facility. The flights were made by project pilots from NASA, the Canadian Ministry of Transport, The de Havilland Aircraft of Canada, and The Boeing Company.

The flight tests included the following general categories: calibration, aerodynamics, stability and control, performance, and operational and handling qualities.

Calibration Tests

The airspeed and static pressure position errors were determined by a "pacer" helicopter towing a calibrated "trailing airspeed bomb." Flap angles for these calibration flights were 5.6°, 30°, 50°, and 65°. In general, the engine power was that required for level flight with nozzles at minimum deflection (~ 6°). For some of the 30° flap tests, the power was held fixed at 96 percent *rpm* and nozzle vectored between 50° and 80° to maintain level flight over the test speed range. Tests were also conducted with 65° flaps, 94 percent *rpm*, and varied nozzle deflection over the speed range of 60 to 75 knots. The test altitude was between 3000 and 5000 ft (900 and 1500 m), and gross weight varied between 37,000 and 44,000 lb (16,800 and 20,000 kg).

The angle-of-attack position error calibrations were made in conjunction with the aerodynamics tests described later. In general, the angle of attack was determined by the difference between airplane attitude and flight path. The airplane attitude was determined from the pitch attitude gyro and the longitudinal accelerometer. Flight path was determined from rate of change of altitude and airplane airspeed.

The position error data derived in these tests for airspeed, altitude, and angle of attack is presented in the appendix.

Aerodynamic Tests

The airplane aerodynamics tests were conducted by flying in unaccelerated flight for about 10 sec, holding angle of attack steady at the various test conditions. Extensive tests were performed in wings-level flight, while efforts at turning flight ("wind-up turns") testing were sharply limited by pilot difficulty in establishing steady conditions. Recorded test data were used in determining lift, drag, thrust, and control characteristics. Aerodynamics tests included the following configurations and conditions: gross weights, 37,000 to 45,000 lb (16,800 to 20,400 kg); flaps, 5.6°, 30°, 40°, 50°, 65°, 72°; altitude, sea level to 10,000 ft (3000 m); engine power, 80 to 100 percent *rpm* including single engine; engine [illegible]° to 104°; and angle of attack, −4° to 18°.

Stability and Control Tests

Stability and control testing may be separated into two categories, lateral-directional and longitudinal. Some stability and control test data were gathered during aerodynamics and calibration testing. Test configurations were generally cruise (5.6° flaps) at 150 knots, landing approach (65° flaps) at about 65 knots, and takeoff (30° flaps) at about 80 knots. Power for level flight was used for the cruise and landing approach testing, while maximum continuous power was used for the takeoff tests. Engine-out testing was conducted using takeoff power on one engine and idle on the other.

Stability and control tests were performed to determine the following: control systems characteristics, control power; static stability; dynamic stability; acceleration characteristics; and trim changes.

Longitudinal test maneuvers included the following: trim change with speed (two and one engine); trim change with power and with nozzle deflection; elevator steps, reversals, and doublets; rapid pitch attitude changes; wind-up turns; engine power lever steps; engine nozzle lever steps; trim change with flap deflection; phugoid; and trim change in ground effect.

Lateral-directional test maneuvers included the following, with *VSS* and *SAS* both on and off: lateral control steps and reversals; directional control steps and reversals; Dutch-roll; spiral stability; rapid bank angle changes; and trim change with speed, one engine operating.

Tests were also conducted to determine the effects of partial hydraulic failure on lateral control and on *SAS* operation. The lateral control augmentor chokes and the spoilers were deactivated separately to test their effect on control power. The directional and lateral control channels of the *SAS* were deactivated separately, again to determine their effect on stability and control.

Performance

The STOL take-off climb, transition, approach, landing, waveoff, and simulated single-engine performance characteristics were measured and evaluated by the project pilots. A Pulse Coded Optical Landing Aid (PCOLA) was used by the pilots for guidance on the approaches. A Fairchild Analyzer Camera was used for redundant measurements of takeoff and landing performance.

Operational and Handling Qualities

Operational and handling-qualities testing was conducted in conjunction with the other tests. In addition, STOL landing, transition, takeoff, and waveoff operation, and ground effect testing were conducted as part of the evaluation of operational and handling-qualities characteristics. Single-engine landing approaches and takeoffs were also conducted.

FLIGHT TEST RESULTS AND DISCUSSION

The results of the flight investigation of the STOL characteristics of the augmented jet flap STOL research aircraft are discussed under five general categories: (1) aerodynamics, (2) stability and control, (3) handling qualities, (4) performance and operational characteristics, and (5) engine-out control and performance.

Aircraft Aerodynamics

The aerodynamics characteristics for the augmented jet flap aircraft, like those of conventional aircraft, are functions of flap deflection and of angle of attack. Unique to the augmented jet flap aircraft, however, are the additional parameters of cold (fan or bypass) engine thrust, of the augmented jet flap nozzles, hot (primary) engine thrust, and hot thrust vector angle. These effects are discussed here, together with the landing and takeoff operational envelopes that result from the

aerodynamic characteristics of the augmented jet flap aircraft, and the effect of the ground proximity on the aircraft aerodynamics.

The aerodynamic parameters – lift, drag, jet momentum, thrust coefficients, and angle of attack – can be computed from flight-measured quantities. It is difficult to derive generalized lift and drag curves from individual data points, however, because the jet momentum and thrust coefficients (C_J and C_T) vary with each flight point as airspeed and atmospheric conditions change. Consequently, the lift and drag curves presented are for varying values of C_J and C_T.

Effects of airplane configuration on aerodynamic characteristics– The effect of flap deflection on aerodynamic characteristics is shown in figure 18 for flap angles of 5.6° (flaps up), 30° (takeoff), and 65° (landing). The engine nozzle angle for these data was about 15°, the engine *rpm* was 94 percent ($\delta_f = 5.6°$ and 30°) and 95 percent ($\delta_f = 65°$), and the altitude varied between 2400 and 9400 ft (730 and 2900 m). The data are shown as a function of aerodynamic lift coefficient C_{L_A}, which is defined as the total trimmed lift coefficient minus the hot thrust (C_T) contribution. Similarly, the drag coefficient includes the thrust of the augmented jet flap but not the hot thrust. The flight data were obtained during trimmed steady-state flight at selected airspeeds resulting in the C_T and C_J variation being nearly identical for each flap setting shown. The C_J values in figure 18 are lower than those used in STOL landings. Because of the method for obtaining these data, the C_J increases with decreasing airspeed (increasing angle of attack), which results in a larger C_{L_A} than would be produced by a change in angle of attack alone – that is, with constant C_J.

The effect of engine *rpm* on the aircraft aerodynamics is shown in figure 19 for a flap deflection of 67°. At a given angle of attack, an increase in engine *rpm* results in an increase in C_J resulting in a large increase in C_{L_A} and some increase in C_D. Also, the lift curve slope increases with increasing engine *rpm*.

The effect of engine nozzle deflection on the total C_{L_T} and aerodynamic C_{L_A} of the airplane for a 67° flap angle is shown in figure 20. Although the C_J and C_T variations are not the same for the nozzle angles shown, a large change in total C_{L_T} occurs when the nozzles are deflected. Because the C_J was not matched for all nozzle deflections, the effect of nozzle deflection on C_{L_A} cannot be readily determined from this figure. However, preliminary flight test data suggest that the larger nozzle deflections may cause some reduction in aerodynamic lift or increase in drag, or both.

Landing and takeoff aerodynamic characteristics– Flight-derived aerodynamic characteristics, engine thrust, geometrical characteristics, and the downwash (ref. 16) were used in the trim algorithm of reference 17 to compute the typical takeoff and landing aerodynamic characteristics shown in figure 21 for a sea-level standard day at constant engine *rpm*. The curves shown in this figure represent the change in aerodynamic parameters produced by varying airspeed in 1-g flight only. These curves were derived from flight test data shown in figures 18-20. For the landing configuration ($\delta_f = 65°$), 92 and 95 percent engine speed (N_H) characteristics are shown since the engine power usually varied between these two values on a −7.5° approach path (γ). The characteristics shown for the takeoff configuration ($\delta_f = 30°$) represent conditions for near minimum takeoff distance using takeoff power (99 percent N_H).

Landing operational envelope– Landing operational envelopes computed for various configurations for a sea-level standard day are shown in figures 22 through 27. These computations followed the same mathematical model as those for the lift and drag curves discussed above. Figure 22 shows the effect of engine *rpm* on the landing operational envelope ($\delta_f = 65°$) at a gross weight of 40,000 lb (18,000 kg), and for the nozzles deflected 90° relative to the fuselage waterline. At a nominal STOL approach condition of 60 knots and $\gamma = -7.5°$, $\alpha \sim 3°$ and $N_H \sim 94$ percent. At these conditions, the flight path angle is changed by about 0.3° per percent change in N_H. Therefore, large changes in N_H are required for large changes in γ. Flight path control methods are discussed further in the section on performance and operational characteristics.

The effect of nozzle angle on the landing operational envelope is shown in figure 23 for $\delta_f = 65°$, gross weight of 40,000 lb (18,000 kg), and $N_H = 94$ percent. For the nominal approach condition of $\gamma = -7.5°$ and a speed of 60 knots, the angle of attack and nozzle angle are about 3° and 85°, respectively. The nozzle is a very effective means of controlling flight path angle.

The computed variations in aircraft flight path angle with airspeed shown in figures 22 and 23 are based on a mathematical model of the airplane. For verification purposes, these data were compared with specific flight test points. Flight test data on flight path angle are compared in figure 24 with the computed performance of the airplane at the same gross weight, flap angle, altitude, airspeed, engine *rpm*, and ambient temperature. The solid symbols in the figure are flight test points, and the open symbols at the same airspeed are the computed values. With the nozzles at 12°, the flight test and computed values of γ show very good agreement. With the nozzles deflected to about 90°, the measured flight test value for γ is perhaps a little below the computed value, indicating that there may be a nozzle interference effect. This effect will be investigated further in future flight tests. (For the most part, however, the data shown good agreement.)

Takeoff and climb operational envelopes– The takeoff operational envelope for the airplane was computed using the mathematical model of the airplane discussed earlier. The effect of engine *rpm* on the airplane flight path angle for a wing flap angle of 30°, engine nozzles at 6° (fully up), and sea-level standard day is shown in figure 25 for gross weights of 40,000 and 45,000 lb (18,200 and 20,500 kg). At full takeoff power, the airplane has the capability of climbing at angles of about 12° at 45,000 lb (20,500 kg) and 16° at 40,000 lb (18,200 kg). The airplane retains significant climb performance even at reduced power setting.

The effect of engine *rpm* on the climb operational envelope at a wing flap angle of 5.6° (fully retracted) for a sea-level standard day at 40,000 and 45,000 lb (18,200 and 20,500 kg) gross weight is shown in figure 26. With the 5.6° flap angle, the airplane has about 2° to 3° greater climb angle capability at the engine power settings shown than with the flaps at 30°, even at a greater airspeed.

Figure 27 shows flight path angles computed from a mathematical model of the aircraft for specific flight test data points compared with measured flight test flight path angle at flap angles of 30° and 5.6° The measured values for flight path angle were about 1° greater than the computed values for 30° flap angle. But at 5.6° flap angle, the measured values of flight path angle were about 1° less than the computed values.

Ground effect– The ground effect with the airplane in the landing configuration ($\delta_f = 65°$) shows a marked decrease in drag, a nosedown pitching moment, and a slight increase in lift as the

airplane descends to ground level. Figure 28 shows the effect of ground proximity on the lift, drag, and pitching moment coefficients obtained from several landings in which the airplane descended slowly to touchdown. The discrete data points shown were derived from test data (assumed quasi-steady-state) collected with flaps 65°, $C_{L_A} = 2.3$ and 3.0, and engine nozzles deflected between 50° and 80°. Separate flight conditions were used for determining lift, drag, and pitching moments ground effects. The engine power varied between 93 and 96 percent N_H, depending on flight conditions and gross weight. Figure 28 also presents fairings ($C_{L_A} = 2.65$) based on a least-squares fit to the entire data for four runs using a regression parameter identification technique. The data show good agreement between the two data methods. With the airplane flying at ground level ($C_{L_A} = 2.65$), the drag is about 60 percent and lift 105 percent of the basic values. The nosedown pitching moment at ground level for the same conditions is equivalent to about 8° of elevator deflection ($\Delta C_M = -0.3$). The values of C_{L_T} shown are based on a nominal flight condition of 65 knots, 65° nozzle deflection, and 94.5 percent engine *rpm*. There is evidence that the ground effect varies as a function of C_{L_A}. The parameter identification processing of the test data indicated the following changes of ground effect with C_{L_A} at ground level:

$$\frac{\Delta(C_{L_G}/C_{L_A})}{\Delta C_{L_A}} = -0.12$$

$$\frac{\Delta(C_{D_G}/C_{D_A})}{\Delta C_{L_A}} = -0.05$$

$$\frac{\Delta C_{M_G}}{\Delta C_{L_A}} = -0.30$$

The exponential decay of the ground effect with increasing altitude (h) is expressed by e^{-kh}. The theoretical value for the scale height (k) is approximately 0.06 based on the aspect ratio (ref. 18). Parameter identification processing yielded a scale height value near the theoretical value for C_{L_G}, and approximately 0.07 for C_{D_G} and for ΔC_{M_G}.

Aircraft Stability and Control

Longitudinal control– The longitudinal control system used for these tests was the basic Buffalo spring tab system modified to reduce the control forces. During the initial flight tests, the pilots found that the longitudinal control dynamic feel chracteristics were unsatisfactory, and the maximum control that could be obtained at STOL airspeeds with reasonable forces was only about +10° to −17° elevator deflection (δ_e), although the full travel of the elevator is +15° to −25°. (This problem is discussed in more detail in ref. 10. For subsequent testing, the elevator control system was modified to a fully powered system. Data discussed here, however, pertain to the original spring tab system.) The static force variation with deflection is shown in figure 12.

Elevator control power was assessed in longitudinal control reversal maneuvers. A typical control reversal at 65 knots is shown in figure 29. The variation of pitch angular acceleration with elevator angle at various speeds for 65°, 30°, and 5.6° flaps is given in figure 30, and maximum pitch rates achieved in the reversal maneuvers are shown in figure 31.

Initial pitch sensitivity (pitch acceleration per unit deflection, $\ddot{\theta}/\delta_C$, shown in fig. 30) is about 0.097 rad/sec^2/in. at 65 to 69 knots, 0.088 at 60 to 64 knots, and 0.076 at 57 to 59 knots. In pilot opinion, the sensitivity was satisfactory.

The maximum control power could not be assessed, of course, because of the limitation on achieving maximum control. The pilots found that normal STOL takeoffs and landings could be achieved with the available elevator control. The data indicate that a maximum control power of about 0.5 rad/sec^2 was available at takeoff rotation and landing approach speeds of 60 to 65 knots. Elevator deflections as high as −18° (about 15° above trim) were used in some takeoffs and flares, but the pilots did not report a large increase in force or other limitations due to the control system in any of these maneuvers. It is not known whether knowledge of restricted elevator deflection influenced pilot use of the control. The airplane was restricted from conducting stalls because of the dynamic feel characteristics and low control power at very low airspeed resulting from the reduced elevator deflection with low forces.

Longitudinal static stability – The stick-fixed static longitudinal characteristics of the aircraft were obtained by flying steady 1 g trim conditions and measuring elevator deflection. Tests were conducted at flap settings of 70°, 65°, 50°, 30°, and 5.6° with various power settings over a range of nozzle positions. The center of gravity (*CG*) varied between 28.9 and 30.7 percent of the mean aerodynamic chord, and test weights ranged from 35,800 to 46,600 lb (16,300 to 21,200 kg). Variation of *CG* position with weight is shown in figure 32.

Figures 33, 34, and 35 illustrate typical variations of elevator deflection with flap deflection, nozzle position, and power setting respectively. These data correspond to the aerodynamic data given in figures 18, 19, and 20. Figure 33 presents measured elevator-to-trim values. For these flight conditions, 1 g trim is achieved with elevator deflections of less than 4° for the range of airspeeds tested. Larger up elevator deflections were required with lower flap angles. Maximum trim elevator used was about −7° with flaps up. No attempt was made to determine elevator for minimum airspeed because of the hazard of approaching stall conditions.

Static longitudinal stability levels were found to be low, as expected. Elevator required to trim at a given airspeed is given in figures 33 to 35; variations in stick force, elevator deflection, and angle of attack with airspeed are given in figures 36 and 37 for the flap angles of 67°, 32°, and 5.6°. With flaps up, both stick-fixed and stick-free stability are positive. At 30° and 65° flap deflection stick-fixed stability is positive except at speeds below about 65 knots where stability tends to become neutral. Stick-free stability (stick force required to change airspeed) at constant power is nonexistent at both 30° and 65° flap deflections. At 30° flaps and speeds below about 80 knots and at 65° flaps below 60 knots, stability even becomes slightly negative although the force variation is within the friction band. At 70° flap deflection, stick-free stability deteriorated further, becoming negative throughout the landing approach speed range. The low longitudinal stability and "spongy" elevator response at low speeds, combined with poor stick-centering capability (large friction band), made it difficult for pilots to maintain both pitch attitude and airspeed during landing approaches.

Longitudinal dynamic stability– The dynamic longitudinal short period stability characteristics were approximated by analyzing the response of the aircraft to control pulses and step inputs. Figure 38 is a typical time history of an elevator step at 62 knots. The data illustrate the low short-period stability of the aircraft at this speed. Pitch rate is almost constant for the approximately 3.0 sec while the controls are held fixed, and the pitch rate response of the airplane to the control input appears to be almost first order with a time constant of about 0.5 sec. Figure 39 is a time history of a phugoid oscillation from a trimmed condition of 65 knots with the nozzle deflected 77°. Aircraft short-period and phugoid characteristics are summarized in table 2 for several configurations.

The pilots were not satisfied with the short-period dynamic characteristics of the aircraft because of the high pilot workload to control pitch attitude and flight path angle at airspeeds below 65 to 70 knots. Approaches under visual flight rules (*VFR*) were performed without difficulty in winds as high as 30 knots with gusts to 45 knots because the low stability results in only small low-frequency disturbance; under such conditions, however, the pilot workload increased.

Longitudinal maneuvering characteristics– This section covers the vertical and longitudinal acceleration responses of the aircraft to control inputs used for flight path and airspeed control. Three controls are available to the pilot in this propulsive lift aircraft to achieve these responses: (1) changes of angle of attack with elevator control, (2) changes in engine thrust with the throttles, and (3) changes in hot thrust vector angles with nozzle control levers. All three of these controls affect the lift, drag, and pitching moment of the aircraft.

The aircraft exhibited stable maneuvering characteristics at constant speed, thrust, and nozzle angle. Figure 40 compares predicted values from reference 19 with maneuvering data, which are given in terms of angle of attack, elevator position, and stick force per g variation with airspeed obtained from wind-up turns and pitch attitude steps. Specific data points are presented in figures 41 and 42 for the landing and takeoff configurations, respectively. Elevator-per-g is close to the predicted value based on the wind-up turn data with high values of between 25° and 30° per g at airspeeds between 60 and 65 knots. Figure 41 shows that at 67° flap deflection stick force per g is close to predicted values up to 1.1 g, above which it falls below the predicted value. At 30° flaps, the stick force per g is well below the predicted level. These data were obtained with the spring-tab elevator control system. In the fully powered elevator control system installed subsequently, the forces are a function of airspeed and elevator deflection from trim.

Load factor per unit angle of attack becomes quite low as airspeed is reduced (fig. 40). The measured value of 1.6 g/rad at 63 knots, which is representative of a landing approach condition, is close to the predicted value; a measured point at 100 knots is about 4 g/rad.

The variation of vertical acceleration with changes in angle of attack obtained during pitch attitude changes are presented in figure 43. The data shows that for an airspeed of 63 knots, the slope of the variation of $\Delta\alpha_F$ with g is about the same as that obtained in wind-up turns for negative and low positive values of $\Delta\alpha_F$. At values of $\Delta\alpha_F$ above 6°, however, very little if any increase in load factor is achieved with increased angle of attack. A maximum load factor of only 0.14 is available at 63 knots with the pitch attitude changes used in these tests. At 68 knots, the maximum value of load factor is 0.23 and the curve again flattens at about $\Delta\alpha_F = 6°$. At 98 knots, the variation of Δg with $\Delta\alpha_F$ is quite linear to a Δn_z value of 0.4 g.

Figure 44 shows time histories of 5° and 10° pitch attitude changes at a trim speed of 63 knots. Note that as attitude is increased the airspeed decreases such that the peak value of vertical acceleration does not occur at the peak value of angle of attack for the 10° case, which accounts for the flattening of the variation of Δn_z with $\Delta\alpha_F$ in figure 43. With attitude changes of 5°, acceleration follows angle of attack more closely and airspeed changes are much smaller and do not affect the peak load factor. Figure 45 presents similar time history data for negative attitude changes. The response of the airplane with pitch attitude changes is typical of operation on the back side of the thrust required curve.

Figure 46 shows aircraft response to nozzle rotation downward from the aft position, with the pilot controlling elevator to hold angle of attack nearly constant. The effect is somewhat similar to a decrease of power in a conventional aircraft because the main effect of vectoring thrust on the flight characteristics is in the drag direction. When the nozzle is moved from full aft to normal to the flight path on the approach, the lift change is only about 20 percent of the weight of the airplane. Airspeed decreases quickly as the thrust vector is rotated from aft to vertical position, then increases as the aircraft pitches down and rate of sink increases, exciting the phugoid. The new trim speed is lower than initial trim. If attitude were held constant, angle of attack would increase and speed would further decrease. An initial increase in positive vertical acceleration would accompany a more rapid down nozzle deflection. The effect of rotating nozzles from the forward to aft position is shown in figure 47. The aircraft sinks momentarily, about −0.1 g, as the lifting force due to thrust is removed, then pitches up, increases speed, and climbs. With exception of the initial increased sink rate due to the lift changes, the response is similar to a power increase in a conventional aircraft. Figure 48 illustrates similar effects for smaller changes in nozzle position.

Forward rotation of nozzles proved effective as a means of decreasing speed and flight path for glideslope interception. Once on the approach, modulation of the nozzles in the range 70° to 90° provided a very effective airspeed control, taking the place of conventional throttles. The initial tendency for the aircraft to sink on aft vectoring of the nozzles, however, restricted their use as a means of controlling flare in proximity to the ground, and the pilots preferred to revert to throttle and elevator control for touchdown. Caution was also required in vectoring nozzles aft on low altitude waveoffs to avoid sinking, although it was subsequently found that increasing pitch attitude as nozzles moved aft effectively countered the problem.

Aircraft response to changes in throttle setting is conventional in cruise configuration with nozzles aft, but is unconventional, as expected, in landing configuration with flaps and nozzles down. Figures 49 and 50 illustrate response to a step increase and a step decrease in power, respectively, in the landing configuration. The pilot is controlling elevator to maintain constant pitch attitude. Increasing thrust produces a lifting force instead of an axial force causing the aircraft to heave upward. Figure 49 shows a peak of 0.11 g for a step from about 92.5 to 98.5 percent *rpm*. The data show no increase in longitudinal acceleration A_X. Flight path shallows initially, but the subsequent decrease in speed tends to wash out the change in flight path angle. Similarly, the short-term effect of reducing power (fig. 50) with attitude held constant is a decrease in load factor and a steepened flight path angle, but as speed increases the flight path tends to shallow. With thrust as primary flight path control this adverse speed-path coupling made it necessary for pilots to continually monitor both attitude and thrust to achieve desired corrections in flight path and speed. Where required flight path corrections were large, pilots had to revert to nozzle modulation, or to a combination of nozzle and thrust control to achieve the desired response.

Lateral and directional control– Lateral control power was measured by conducting lateral control reversals. The wheel was applied in one direction and then rapidly reversed and held in the opposite direction with rudder pedal neutral. Maximum acceleration was measured as roll rate passed through zero. A typical reversal at 65° flaps with *SAS* off is presented in figure 51 and with *SAS* on in figure 52. Results are compared with predictions (ref. 19) in figure 53.

In the approach configuration (flaps 65°), at approximately 40,000 lb (18,200 kg) gross weight, maximum roll acceleration available is about 0.67 rad/sec^2 at 69 knots, slightly above the predicted value and representing a rolling moment coefficient of about 0.16. Extrapolating the data, and assuming control power varies with dynamic pressure, we find that control power at 60 knots is about 0.51, well in excess of the design criterion of 0.4 rad/sec^2.

The contributions of aileron, spoiler, and choke to the rolling moment are illustrated in figure 54. Data are shown for *SAS* on and off conditions. *SAS* had some effect on maximum control power because of the control deflections due to *SAS*. For the maximum control condition shown in figure 54, ailerons alone produce about 35 percent of the moment, the spoilers produce 27 percent, and the choke about 38 percent. Lateral control sensitivity (roll acceleration per unit wheel displacement) is about 0.11 rad/sec^2/in., compared to predictions of about 0.095. The sensitivity was considered satisfactory by the pilots.

Figure 55 presents roll acceleration data measured at a gross weight of 45,000 lb, flaps 65°. Maximum acceleration available is about 0.53 rad/sec^2 at 69 knots at this higher weight because of the increased inertia with fuel in the wings.

In figures 51 and 52, it can be seen that with *SAS* on or off at STOL airspeeds, yaw acceleration due to lateral control deflection is very small.

Figure 56 presents roll acceleration data for the 30° and 5.6° flap deflection configurations at gross weights of 44,000 to 45,000 lb (20,000 to 20,500 kg). With 30° flaps, maximum rolling acceleration at 78 knots is about 0.53 rad/sec^2, representing a rolling moment coefficient (C_ℓ) of about 0.14, which allowing for the higher weight is above the predicted value. With flaps up, the measured maximum rolling acceleration of 1.27 rad/sec^2 at 166 knots ($C_\ell = 0.075$) is much higher than predicted, due in part to the flap deflection at nominal flaps up being 5.6° instead of 0°, and because the predictions did not consider the lower surface of the chokes acting as ailerons.

Maximum roll rates achieved in the wheel reversal maneuvers, flaps 65°, are given in figure 57 for *SAS* on and off conditions at about 40,000 lb gross weight. Maximum rate available, *SAS* on, is above 23°/sec at 70 knots. Minimum criterion at 60 knots is 20°/sec.

Maximum control surface rates achieved in reversal maneuvers were:

$$\dot{\delta}_w \geq 200°/\text{sec}$$
$$\dot{\delta}_{AIL} \geq 50°/\text{sec}$$
$$\dot{\delta}_{sp} \geq 120°/\text{sec}$$
$$\dot{\delta}_{CH} \geq 95 \text{ percent/sec}$$

Full lateral control from neutral position can be achieved in less than 0.5 sec.

Directional control power was evaluated by conducting rudder reversals with wheel at neutral. Maximum yaw acceleration was measured as yaw rate passed through zero. Results for 65° and 30° flap conditions with *SAS* on and off are presented in figure 58. A typical directional reversal with *SAS* off is shown in figure 59 and with *SAS* on in figure 60. At 65° flaps and an airspeed of 70 knots, a yaw acceleration of 0.3 rad/sec^2 was measured at 70 percent rudder deflection equivalent to 0.22 rad/sec^2 when extrapolated to 60 knots. This is higher than the predicted value of about 0.26 rad/sec^2 at 70 knots with maximum 25° rudder deflection and is well above the criterion of 0.15 rad/sec specified for adequate maneuvering at 60 knots. At 33° flaps and 80 knots, a yawing acceleration of 0.33 rad/sec^2 was achieved at 70 percent rudder. It is expected that at rudder deflections above 70 percent, the acceleration curve bends over fairly quickly as shown by the dotted lines in figure 58. During the reversal maneuver, yaw acceleration tends to reach maximum before the rudder has had sufficient time to come to its commanded position because the rate is building up rapidly. At 70 knots, maximum rate of rudder movement appears to be about 38°/sec with full pedal input. Roll acceleration due to directional control, *SAS* on, is small (fig. 60).

Maximum yaw rates achieved during reversal maneuvers are shown in figure 61. At 65° flaps and 69 knots, a maximum rate of 12.5°/sec was measured with *SAS* off, and about 13°/sec with *SAS* on. In both cases, controls were removed before maximum rates were achieved.

Lateral directional static stability— These stability characteristics were assessed by performing steady sideslip maneuvers. Test results are presented for takeoff, approach, and cruise configurations in figures 62 through 66. The aircraft exhibits positive stability about both lateral and directional axis for all configurations tested.

Figures 62 and 63 present data for the 65° flap condition. Figure 62 shows variation of rudder deflection, wheel deflection, bank angle, and elevator position with sideslip; figure 63 shows the same data as a function of rudder angle and indicates a positive dihedral effect. The data fall within the range of C_{ℓ_β} as predicted by wind tunnel tests, correlating better with $C_{\ell_\beta} = -0.004$ than with $C_{\ell_\beta} = 0$.

Rudder and wheel deflections are reasonably linear with sideslip angles out to ±15°. At 65 flaps and 65 knots, sideslip produced by 10° rudder is about 22 percent less than the predicted value, indicating a higher directional stability than predicted for large sideslip angles. At speeds below 90 knots, the aircraft exhibited a low amplitude directional snaking characteristic ($\beta = \pm 1 - 2°$) indicating that near $\beta = 0°$ directional stiffness may be very low. Attempts to document any nonlinearities were not successful. About half available rudder and less than half available wheel throw are required to achieve 15° β at 65 to 70 knots. (Note that above 100 knots sideslip is limited due to tail loads.) In STOL configurations, 15° of sideslip is achieved with bank angles of about 5°, indicating low net sideforces. Ratios of bank angle to sideslip angle in steady-state sideslips, ϕ/β, were approximately as follows:

δ_f	ν	V_e	N_H	ϕ/β
65	6	65	93	0.25
30	6	75	90	0.30
5.6	6	120	PFLF	0.65
5.6	6	150	PFLF	0.85

The low ϕ/β at landing approach speeds below 65 knots results in very little lateral acceleration A_y with sideslip. The absence of the lateral acceleration cue requires the pilot to use the sideslip indicator in the cockpit much more as speed is reduced to maintain low sideslip angles. The low directional stability aggravates this problem.

Longitudinal trim change with sideslip is small for all configurations, requiring less than 1° elevator deflection with flaps at 65° and less than 6° elevator deflection with flaps up and at 30°.

Lateral directional dynamic stability – Lateral directional characteristics were evaluated at flap settings of 65°, 30°, and 5.6° with *SAS* both on and off (*SAS* is automatically off above 100 knots), and with combinations of roll and yaw *SAS* on separately in the landing configuration. Dutch-roll characteristics are summarized in figure 67 and table 3; roll damping characteristics are shown in figures 68 and 69.

At the landing approach flap deflection of 65°, the Dutch-roll damping with *SAS* off is quite low with a damping ratio between 0.1 and 0.2. The Dutch-roll period is about 6 sec/cycle and is close to the predicted value at 70 knots. Measured period is slightly less than predicted at 75 to 90 knots indicating a trend toward greater directional stiffness than predicted at the higher speeds. A typical Dutch-roll, *SAS* off, is shown in figure 70. The oscillation is primarily a yawing motion with $|\phi|/|\beta|$ amplitude ratio about 1.0. With *SAS* on, Dutch-roll damping ratio increases to about 0.3. A typical *SAS* on time history is shown in figure 71. The *SAS* on period is about 7 sec and is less than predicted. With roll axis *SAS* off and yaw axis *SAS* on it was difficult to obtain Dutch-roll data because the aircraft exhibited a marked tendency to "roll off" with controls fixed; therefore, table 3 does not show Dutch-roll data for this case. The roll axis *SAS* off has little effect on the Dutch roll; with roll axis *SAS* on and yaw axis *SAS* off, Dutch-roll characteristics were similar to the all *SAS* off case.

As noted in the discussion of static stability, a residual directional snaking characteristic was common at speeds below 90 knots even with basic *SAS* on. Pilots found this characteristic objectionable. By using the *VSS*, $\dot{\beta}$-damping was doubled, increasing the Dutch-roll damping ratio to about 0.45 (fig. 67). The higher damping markedly improved the pilots' opinion of the directional characteristics at landing approach speeds.

Time histories showing the aircraft spiral mode with flaps at 67° deflection and nozzles at 15° *SAS* off and on, are shown in figure 72. Spiral stability with *SAS* off at 65° flaps, nozzles up, is unstable as expected with time to double amplitude of about 6 sec at 60 to 75 knots. With nozzle angle increased to 90°, time to double amplitude appears to increase slightly. Precise spiral behavior with *SAS* off was not always discernible due to small lateral offsets and atmospheric perturbations. With only yaw *SAS* on, spiral mode was similar to the *SAS* off condition with a tendency to diverge more rapidly, T_2 being 4 to 6 sec. With only the roll *SAS* on, spiral stability is positive. Times to half amplitude of 7 to 10 sec were noted at 69 knots. With all *SAS* on, spiral stability at 65° flaps is neutral to slightly positive. Increasing nozzle angle to 90° appears again to give a small increase in stability. Measurement of precise times to converge with *SAS* on was difficult due to nonlinearities introduced by *SAS* inputs and/or atmospheric turbulence.

The roll damping at 65° flaps with *SAS* off is low with an apparent roll mode time constant (τ_A) of about 1.0 sec as determined from roll reversal maneuvers (fig. 68). *SAS* on time constant is approximately 0.45 sec. The pilots considered the roll damping with *SAS* on satisfactory.

With takeoff flaps at 30°, Dutch-roll damping, *SAS* off, is low at 100 knots, but with *SAS* on, damping increases to a satisfactory level of about 0.31 at 79 knots. *SAS* off period at 100 knots is about 4.5 sec and *SAS* on period at 79 knots is about 6.4 sec. The spiral mode is unstable with *SAS* off ($T_2 \cong 8$ sec at 78 knots), and shows neutral to positive stability with *SAS* on. The apparent roll mode time constant is about 1.0 sec (fig. 69) and is apparently about the same *SAS* on or off.

In cruise configuration, Dutch-roll characteristics are satisfactory with damping and period close to predicted levels. Spiral mode is neutral to positive, and apparent roll mode time constant is about 0.8 sec at 134 knots and 0.7 sec at 166 knots, both near predicted values.

Turn entry coordination– Turn entries were conducted at 65°, 30°, and 5.6° flaps to evaluate aircraft lateral control and turn entry characteristics. Tests were carried out with *SAS* both on and off, and with *VSS* system in operation with several roll-rate-to-rudder gains. Turn coordination characteristics, $\Delta\beta/\Delta\phi$ versus airspeed, are summarized in figure 73. With *SAS* on, the aircraft exhibits satisfactory turn coordination characteristics. With *SAS* off, response in turn entries degrades markedly as airspeed is reduced below 80 knots due to adverse sideslip, giving $\Delta\beta/\Delta\phi$ ratios above the maximum level of 0.3 generally considered acceptable, reference 20.

With 65° flap deflection at 65-75 knots, *SAS* off, $\Delta\beta/\Delta\phi$ ratios are between 0.4 and 0.6. The time history of a turn entry at 68 knots (fig. 74) shows the large adverse sideslip generated on initiation of the turn entry. Yaw rate lags roll rate by about 2 sec. The large sideslip with bank angle and the lag between bank angle and turn rate greatly increase the pilot's workload when maneuvering laterally during low speed approaches without *SAS*. With *SAS* on, turn coordination is much improved as shown in figure 74. Yaw rate now follows roll rate with a small lag, and adverse sideslip is reduced. The *SAS* reduces $\Delta\beta/\Delta\phi$ ratios to a value of about 0.3, which the pilots considered satisfactory. The stability augmentation improves the turn coordination by deflecting the rudder proportional to roll rate. Adverse yaw due to lateral control is negligible in both examples.

At 30° flaps with *SAS* off, some difficulty was encountered in setting up initial steady-state conditions, with β varying ±1° about a steady bias of approximately −2°. The $\Delta\beta/\Delta\phi$ ratio data in figure 73, therefore, showed scatter with an average value of about 0.37 at 77 knots. No adverse yaw due to lateral control deflection was evident, but yaw rate lagged roll rate by 1 to 2 sec due to adverse sideslip, giving unsatisfactory turn coordination overall. With *SAS* on, adverse sideslip and yaw rate lag were reduced and turn coordination was considered satisfactory.

In the flaps up configuration (with *SAS* automatically off above 100 knots), $\Delta\beta/\Delta\phi$ has a value of about 0.1 at 165 knots and 0.13 at 135 knots. In flaps up turn entries, no adverse sideslip was evident and yaw rate followed roll rate without lag, indicating satisfactory turn coordination.

Aircraft Handling Qualities

The aircraft handling qualities evaluated in the flight test program are discussed in both qualitative and quantitative terms. The quantitative values are compared to established criteria.

Longitudinal stability and control– The longitudinal stability and control characteristics of the aircraft during STOL operations were considered marginal by the pilots. Once the proper

procedures had been determined, the pilots had no problems accomplishing *VFR* STOL takeoffs, transitions, approaches, or landings, but they considered the workload high.

The primary approach path control is accomplished by use of either engine thrust or thrust vector changes combined with the elevator. Large glide path corrections or low frequency response that give essentially direct drag or thrust control are best accomplished by means of engine nozzle vectoring, while small (high frequency) corrections are most easily made by thrust variation (essentially direct lift control). The elevator response in flight path control for STOL approach ($\gamma = -7.5°$) condition (65° flaps, 65 knots) is summarized in table 4 along with criteria from various references. The pilots found that in addition to the sluggish load factor response, the pitch control sensitivity (θ/δ_c) is marginal (0.08). The nosedown pitching moment in ground effect effectively reduces the pitch control sensitivity below a satisfactory level.

The elevator control system characteristics are considered marginal at airspeeds under about 65 knots. The decreased elevator damping, dynamic force characteristics, and excessive column forces for elevator deflections greater than about 14° from trim that reduced the usable control autnority were all objectionable at the lower airspeeds. The effect of elevator overbalance on stability at speeds less than 60 knots that resulted in reduced control forces was also objectionable. At zero stick force, the elevator mass balance produces full trailing edge up elevator at speeds up to about 30 knots. These undesirable characteristics (ref. 13) are associated with the spring tab control system and mass balance; the spring tab control system subsequently was replaced with a fully powered hydraulic control system. The elevator system characteristics at the 65 knot approach speed and referenced criteria are summarized in table 5.

The engine speed control is unsatisfactory when used for flight path control because the thrust level to control handle gearing in the approach is too sensitive and has hysteresis. One inch of handle movement gives a change of 475 *rpm* ($\Delta T/W = 0.10$ where $W = 38{,}000$ lb) at the approach power setting. Hysteresis of ±1/3 in. in the engine speed control system was also quite objectionable, especially with the high sensitivity. Engine acceleration and deceleration times in the normal operating range are considered acceptable for control on a STOL approach, but the spooldown time after the throttle is retarded on touchdown is too long. The engine nozzle control sensitivity and effectiveness was satisfactory. Use of the nozzles during flare was avoided because of the initial lift loss and the probability of hot gas reingestion on the ground at large nozzle deflections. If the nozzles are used to control flight path at constant speed, a concurrent change in pitch attitude must accompany any sizable nozzle angle change. Control of flight path by means of engine thrust requires little or no accompanying attitude change.

The longitudinal stability is satisfactory over the normal operating envelope except in the STOL approach speed region below about 65 knots. The static longitudinal stability becomes neutral and unstable as speed is reduced. The neutral to unstable slope of flight path with decreasing velocity is objectionable and increases the pilots workload on the approach. Characteristics of the longitudinal stability and criteria are summarized in table 6 for the 65 knot approach case.

Lateral-directional stability and control– The lateral-directional stability and control characteristics are satisfactory over the operational speed range with *SAS* in the normal mode except for an objectionable low amplitude directional snaking at landing approach speeds and unsatisfactory lateral control forces. With *SAS* off in the landing approach (65 knots, 65° flaps), turn

coordination, Dutch-roll damping, roll damping, and spiral damping are unsatisfactory, as discussed in the previous section. With the variable *SAS* (*VSS*) programmed to increase the "Beta-dot" damping, the objectional snaking was reduced to a satisfactory level. The lateral control breakout force was about 5 lb (2.3 kg) [with friction forces of about ±1.5 lb (±0.7 kg)], and because of the low force gradient [10 lb (4.5 kg) at maximum wheel deflection], the breakout felt like a strong detente and was objectionable. A modification to correct this condition will be evaluated during the next test period.

Characteristics of the lateral and directional control systems and criteria are presented in table 7. The lateral control power and sensitivity are satisfactory. Although large wheel deflections are required for maximum roll control power, 90 percent of the effectiveness is achieved at about 60° wheel deflection at STOL speeds (fig. 54). The configuration of the lateral control system may be varied by selectively shutting off power to the spoilers and chokes. Tests were conducted with the spoilers and chokes inoperative only in the landing approach configuration. In the landing approach, the lateral control power is satisfactory with all control surfaces operating; with either the spoiler or choke surfaces inoperative, however, it is unsatisfactory because of the low sensitivity with spoiler off and nonlinearity with the choke off. The low control power and sensitivity with both spoiler and choke off make the aircraft unacceptable for STOL operation. The control power and sensitivity for the various lateral control configurations are given below for the landing approach [65 knots, gross weight 38,000 to 40,000 lb (17,800 to 18,200 kg)]. The lateral control "quickener" (fig. 17), which is operational when *SAS* is on, was not specifically evaluated in flight; however, pilots did not comment on any noticeable reduction of control sensitivity or dead band when flying with the *SAS* turned off.

	$\ddot{\phi}$ max rad/sec^2	ϕ/δ_w, ($\delta_w < 40°$) rad/sec^2/deg
All surfaces operating	0.67	0.0129
Spoilers inoperative	.47	.0075
Chokes inoperative	.40	.0129 ($\delta_w < 17°$) .0088 ($\delta_w > 17°$)
Spoilers and chokes inoperative	.22	.0037

The directional control power is considered satisfactory for all flight conditions including crosswind landings when the crosswind component is as great as 20 knots.

The lateral and directional control power characteristics with referenced criteria are summarized in table 8 for the landing approach and takeoff conditions. The maximum sideslip (β max) given in the table is based on a tail stall tendency at large sideslip angles. The de Havilland Company has some evidence of vertical stabilizer and rudder stall between 20° and 25° sideslip.

The lateral-directional dynamic stability is satisfactory with normal *SAS* for all flight conditions except for the low amplitude snaking motion, which is experienced with the *SAS* operating in the landing approach and is somewhat random with no identifiable period or damping. The amplitude is low with changes in yaw angle of only 2° or 3°. Increasing the Dutch-roll damping ratio from 0.30 to 0.45 did not eliminate the tendency but reduced it to a level that the pilot considered

satisfactory. With *SAS* off, the Dutch-roll damping, roll damping, spiral damping, and turn coordination unsatisfactory in the landing approach and takeoff. The lateral-directional dynamic characteristics for the landing approach and takeoff with normal *SAS* are summarized in table 9 with criteria from various references.

Aircraft Performance and Operational Characteristics

This section discusses the performance and operational characteristics of the research aircraft in the STOL takeoff and landing phase of operation. Cruise and conventional takeoff and landing data are given in reference 13. The preliminary STOL takeoff and landing performance data are summarized in table 10.

Takeoff– The nominal takeoff configuration is with a flap deflection of 30°, ailerons drooped 17° and the nozzles full aft. Takeoff procedure is to advance the throttles to a speed of 93 to 96 percent with the brakes locked, release the brakes, and add power to the takeoff engine speed of 99 percent. Takeoffs were conventional for an aircraft with a thrust/weight ratio of 0.4 to 0.5 except that events occurred more rapidly during the takeoff maneuver. The elevator has sufficient control power to start rotation at about 60 knots. Back stick is held until liftoff, at about 75 knots, and 8° angle of attack, when the control is eased forward to maintain a constant angle of attack until climb rate and velocity are both established. Both directional and lateral control are acceptable.

A time history from brake release of a typical takeoff is shown in figure 75 for a low gross weight of 39,220 lb (17,800 kg). The distance traveled, S, is calculated from the measured velocity. (The wind conditions were calm.) Full thrust is achieved about 1 sec after brake release. Rotation was initiated at 65 knots, 7 sec after start. Liftoff occurred 8 sec after start at a velocity of 73 knots and 510 ft (155 m) after start; 820 ft (249 m) and 10.4 sec after start, the aircraft cleared 35 ft (10 m). An angle of attack of 8° was reached just at liftoff and held until full climb rate was established. Figure 76 is a Fairchild Analyzer Camera sequential photograph of another takeoff. In this no-wind takeoff, the flight path angle gradually increased up to 20° at about a 300-ft (90-m) altitude. The previous figure showed a steady climb rate of about 19° by the time a 60-ft (18-m) altitude was reached.

Figure 76 gives some indication of the nose-high attitude of the aircraft during the climbout. An angle of attack of 2° and a climb angle of 19° places the aircraft pitch attitude at 21° above the horizon.

A compilation of several takeoffs in figure 77 shows the effect of takeoff weight on the distance required to clear 35 ft (10 m). These data were corrected for wind conditions but not temperature. Large variations in performance are present, as expected, but an upper boundary is fairly well defined. The data show that the performance is about as predicted (ref. 10). During these tests no attempt was made to determine the optimum flap deflection for minimum takeoff performance; 30° flap deflection was chosen as nominal takeoff flap deflection for engine considerations.

Except for the rapid rotation necessary for these takeoffs and the poor visibility over the nose of the aircraft during the initial climb, the pilots considered the takeoffs comfortable, with little change in control techniques required for STOL operation.

Climb and transition to cruise– Although the angle of attack during climb with takeoff flap is low, from 1° to 5°, the flight path angle of up to about 20° contributes significantly to a very steep nose-up attitude during climb. Visibility over the nose was greatly restricted. Directional and lateral controls remained acceptable, and no problems were experienced during turbulent and gusty conditions. Figure 78 shows the measured values of takeoff climb gradient for several flights that had stabilized conditions. The climb values computed from aerodynamics data shown previously in figure 25 are included for comparison, but it should be noted that the flight data shown were taken under nonstandard conditions, between 40° and 50° F, and have not been corrected for this temperature difference. In general, the agreement is good, with the measured climb angle being slightly higher.

Transition to cruise or flaps up climb configuration is straightforward as the flaps are retracted from the takeoff and initial climb deflection of 30° to full up. Some flights were made with the automatic trim-flap interconnect removed with no significant change in handling qualities or pilot workload. Part of this is due to the low static margin and the very light control forces of the elevator in its present configuration.

Transition and landing approach– Pilot evaluation of approaches and landings with 55°, 65°, and 72° flap deflections indicated that a flap deflection of 65° is near optimum for the aircraft on −7.5° approaches. An increase in flap deflection to 72° results in very little lift increase.

Transition to the approach configuration of 65° flap deflection and nozzle angle of 80° was docile, and can be accomplished in either level flight or by decelerating on the approach. Speed is reduced from cruise (150 to 160 knots) to flap extend speeds (table 1) by either reduction of power or downward rotation of the nozzles. Both methods are satisfactory, as is a combination of the two. Although attitude transients occur during the configuration changes, no excessive control inputs are required, trim is adequate, and pilot workload is not excessive.

An experimental glidepath indication called a Pulse Coded Optical Landing Aid (PCOLA) was used that identified for the pilot the scheduled glideslope and indicated angular distance from the optimum slope. The PCOLA is an optical device located next to the runway and provides a variable pulse width, indicative of deviation from established glide slope. The pilots considered it useful and simple to interpret.

The technique that evolved was to slow to 90 knots while on a high base leg, with flaps at 30° and nozzles full aft. Flaps were then lowered to 65° just prior to or while intercepting the −7.5° glideslope. A speed of about 90 knots was maintained at an angle of attack of about +2° by adjusting power. Speed was reduced at an altitude of about 800 ft (240 m) speed by moving the nozzles down as required while increasing power to about 93 percent and maintaining the established glideslope with nozzle deflection at angle of attack of 2°. Deceleration to 60 to 65 knots was usually completed at about 500 ft (150 m) and the remainder of the approach was flown at constant airspeed. The use of nozzle angle modulation (vectored thrust) at constant thrust has proven satisfactory for small or large glidepath corrections. With nozzles, glidepath angle changes can be made with little change in angle of attack or airspeed (fig. 23). With nozzle fixed at 80°, the use of thrust for glidepath control is also a satisfactory technique provided large glidepath corrections are not necessary. This technique permits small glidepath changes with nearly constant airspeed and attitude, but angle of attack changes (fig. 22). An increase in power on approach at constant angle of attack decreases both the rate of descent and speed. The use of thrus alone to correct for

large glidepath angle changes is not adequate because of the airspeed changes, and it usually is necessary to revert to nozzle angle modulation. The pilots' consensus was that the transition and approach had to be tightly controlled to keep the workload acceptable. Correction for large excursions from nominal values of airspeed and/or glidepath raised the pilot workload to an unacceptable level because of the difficulty in controlling both airspeed and glidepath angle.

Most of the approaches to a landing were made at a nominal −7.5° flight path angle using the PCOLA for guidance. Figure 79 shows a time history of such a landing approach starting at an altitude of about 200 ft (60 m). Although the trace shows a gradual increase in angle of attack starting between 5 and 6 sec before touchdown, flare initiation as used in the following discussion is taken as the time at which a sharp change appears in the elevator position, in this case almost 3 sec before touchdown. An an altitude of a little over 100 ft (30 m) there appears to be a gradual decrease in glideslope and a small decrease in velocity.

The variation of approach speeds with gross weight is shown in figure 80 and is representative of observed speeds between about 200-ft (60-m) altitude and the flare height for a series of approaches on a nominal −7.5° glidepath. Changes in the minimum observed approach speed with gross weight were such that lift coefficient remains approximately constant. The pilots considered the ability to make a precise flare the limiting factor in choosing the minimum approach speed. The angle-of-attack margin or the airspeed margin from the stall were not limiting factors. The angle-of-attack margin on the approach was over 15° and was 10° to 12° in the flare. Since the load factor response to angle-of-attack changes (n_z/α) is an important factor for control in the flare appropriate values of n_z/α are shown in the figure. The band depicts the minimum approach speed for acceptable flight path control in the landing flare. When landing flares from flight paths of −7.5° were executed below this speed, the change in flight path that could be produced in a reasonable time by the change in attitude was insufficient to arrest the sink rate to values less than about 5 ft/sec (1.5 m/sec).

Landing– Landings are best accomplished by leaving the nozzles at about 80° and flying the last 100 ft (30 m) with elevator and throttle control. The sink rate is arrested by attitude change, and power is usually reduced for the actual touchdown. The point at which flare is initiated must be picked precisely for a good landing. There is a strong feeling that the nose wheel is going to hit first if flare is delayed, and there is a tendency to float if flare is accomplished too soon. The typical flare angle-of-attack change from a −7.5° approach path was 10° with vertical acceleration levels 1.2 g or less. The load factor response time is also important. The longer it takes to attain the load factor the slower the flare. Based on the vertical response shown in figures 43 and 44 an acceleration response time constant (n_z), of approximately 1.5 sec is estimated to be typical of this airplane when allowing for control transport and response lages. Reference 21 indicates a τn_z of 1.5 sec is about the maximum acceptable.

Figure 81 shows the change in sink rate during the flare maneuver from pitch up to touchdown for a number of landings and the predicted changes in sink rate for given average values of normal load factor n_z, although the actual variation in n_z with time is more nearly triangular than rectangular. The sink rate at touchdown is shown in figure 82. Only a few landings were made at sink rates greater than 4 ft/sec, and these were considered to be exceptionally "firm" by the pilots.

Crosswind landings presented no difficulties. The rudder was very powerful and allowed precise decrabbing just before touchdown. Pitch control was considered sluggish at low speeds and contributes to the lack of precise attitude control during the flare and landing phases of the

approach. Experience built some confidence, but the elevator control lacks the crisp, precise characteristics of the lateral control system.

Minimum ground roll landing tests were not conducted because of the poor brake feel system. Initial attempts to conduct rapid decelerations on the ground resulted in flat spots on the tires due to brake grab and a danger of blowing out a tire. Installation of an improved braking system with anti-skid control is planned. Figure 83 shows the estimated landing distance over 35 ft (10 m), which is felt to be representative of the performance that can be obtained with the present braking system; the landing distance also shows a curve for a braking coefficient of 0.38, which is an estimate of the performance possible with the anti-skid system.

Waveoff– Waveoffs were accomplished easily, but the unique ground rules of this aircraft required nonstandard actions. The procedure developed is to increase engine speed to 99 percent, rotate the nozzles aft, concurrently increasing the pitch attitude, and then gradually decrease the flap deflection as speed increases. The thrust must be increased first because the transient effects of changing nozzle position are opposite to the steady-state effects. Deflection of the nozzles aft to achieve more longitudinal acceleration decreases the lift. A concurrent increase in engine speed or angle of attack is therefore necessary to compensate for the momentary loss in lift as well as to arrest the sink rate for the waveoff.

Engine-Out Control and Performance

Single engine failures were simulated in the test program on approaches and takeoffs by abruptly retarding one engine to flight idle. The relatively long deceleration time (18 to 25 sec) peculiar to the engines caused a very moderate onset of any out of trim conditions.

Engine failure on takeoff – Figure 84 is a time history of a simulated engine failure on takeoff at an aircraft weight of 41,000 lb (18,600 kg) with flaps at 33° and the nozzles vectored aft. The right-hand engine was cut at rotation speed, and the left engine remained at 99.9 percent *rpm*. Recovery requires less than 20° wheel deflection and less than 10° rudder deflection. Similar control inputs were used in recovery from another simulated failure conducted just after liftoff at a weight of 44,400 lb (20,200 kg) and a speed of 88 knots. In general, pilots described aircraft behavior during the simulated failures as "very docile with little corrective control required," and considered recovery from the simulated failures to be no more demanding than for some conventional twin-engine aircraft.

At 30° flaps and approximately takeoff thrust, single-engine climb gradients were low as predicted. Measured climb gradients for several takeoff weights and flap settings are shown in figure 85, along with a predicted value for 45,000 lb (20,500 kg) gross weight. At 44,400 lb (20,200 kg) and flaps at 32°, the best single-engine rate of climb achieved was about 200 ft/min (60 m/sec) at 88 knots. The operating engine was at 99.5 percent *rpm* and the other at flight idle. For an emergency condition, the engine can be increased to about 103 percent *rpm*, which would increase the climb angle about one-half a degree.

Engine failure on approach – Single engine failures were simulated on nominal −7.5° landing approaches at altitudes between 550 and 800 ft (167 and 243 m). Flaps were at 70°, nozzles were vectored vertically, and airspeed at engine cut was about 70 knots. All simulated failures were

followed by a waveoff with power restored at 100- to 200-ft (30- to 60-m) altitude. No actual single engine landings were made. The time histories in figure 86 show a "failure" from 95 percent N_H approach power setting. Recovery was accomplished by first increasing power on the good engine, then rotating nozzles aft (recovery technique A). Figure 87 shows a simulated failure from 95 percent N_H in which nozzles are first vectored aft, then power increased on the good engine (recovery technique B).

In the illustration of technique A (fig. 86), cutting the left engine increases rate of sink from 950 ft/min to 1450 ft/min (290 m/min to 440 m/min) as total vertical force is decreased and airspeed tends to increase. Elevator is applied, pitching the aircraft nose up, and power is increased on the good engine to arrest sink rate. As nozzles are vectored aft, with airspeed at 65 knots, sink rate further increases to 1800 ft/min (550 m/min) until the aft vectored thrust causes speed to increase, producing positive g and a decrease in sink rate. About 20 sec are required to bring the rate of descent to zero. Nozzles are then modulated to reestablish speed and regain the flight path. Laterally, cutting the left engine rolls the aircraft about 4° to the left due to the asymmetric hot thrust moment (partially offset by an opposite moment from asymmetric distribution of cold thrust). An increase in right-hand engine power contributes further to the left moment, which is corrected by application of 10° to 20° right wheel input. As nozzles are now vectored aft, the roll moment becomes a yawing moment requiring 8° of right rudder to counteract sideslip, and the wheel deflection is reduced to level the wings. Although control inputs are small and easily accomplished, considerable coordination of control is required throughout the recovery procedure. In a genuine emergency with rapid asymmetric thrust loss, pilot workload would be high.

In the illustration of technique B (fig. 87), sink rate increases rapidly from about 850 ft/min to 1400 ft/min and airspeed increases as the right-hand engine is cut and nozzles are vectored aft. Pitch attitude is increased and thrust on the opposite engine is advanced to takeoff power to arrest sink rate. As speed increases, the flight path shallows. Laterally and directionally the recovery procedure involves primarily rudder input. As the engine is cut and nozzles are vectored aft, the momentary roll moment becomes a yaw moment, which is corrected with about 5° of left rudder. As power of the good engine is increased, a further 5° of rudder is applied in the same direction. Technique B is simpler than A in that reversal of wheel position is avoided, but in a genuine emergency this procedure may tend to give a larger initial increase in sink rate due to an initial decrease in lift as nozzles are vectored aft prior to an increase in power. Single-engine climbs with flaps at 65° or above were not possible with any technique except at the very low gross weights.

Waveoff from single-engine approaches required only vectoring the thrust aft, increasing airspeed, and retracting the flaps. The control and performance were then similar to the engine-out takeoff case. These recovery examples are not necessarily optimum for minimizing altitude loss or for reestablishing the approach flight path, but they do illustrate the primary control inputs used to recover from an engine loss.

REFERENCES

1. Bradford H. Wick and Richard A. Kuhn, "Turbofan STOL Research at NASA." Astronautics and Aeronautics, vol. 9, no. 5, May 1971.

2. D. C. Whittley, "The Augmentor Wing: A New Means of Engine Airframe Integration for STOL Aircraft." AIAA paper no. 64-574 presented at Fourth ICAS Conference, Paris, 1964.

3. J. E. Middlebrook, H. C. Tinney, and D. C. Whittley, "The Evolutionary Development and Current Status of the Augmentor Wing Concept." Paper 700812 presented at SAE National Aeronautics and Space Engineering and Manufacturing Meeting, Los Angeles, October 1970.

4. G. S. Kelley and R. P. Gerend, "Propulsion Systems for Commercial STOL Aircraft." AIAA paper no. 71-746, AIAA/SAE 7th Propulsion Joint Specialist Conference, Salt Lake City, June 1971.

5. D. C. Whittley, "The Augmentor Wing Research Program: Past, Present, and Future." AIAA paper no. 67-741, Tenth Anglo-American Aeronautical Conference, Los Angeles, October 1967.

6. D. G. Koenig, V. R. Corsiglia, and J. P. Morelli, "Aerodynamic Characteristics of a Large Scale Model with an Unswept Wing and Augmented Jet Flap." NASA TN D-4610, 1968.

7. A. M. Cook and T. N. Aiken, "Low Speed Aerodynamic Characteristics of a Large Scale STOL Transport Model with an Augmented Jet Flap." NASA TM X-62,017, 1971.

8. M. D. Falarski and D. G. Koenig, "Aerodynamic Characteristics of a Large-Scale Model with a Swept Wing and Augmented Jet Flap." NASA TM X-62,029, 1971.

9. R H. Ashleman and H. Skavdahl, "The Development of an Augmentor Wing Jet STOL Research Aircraft (Modified C-8A), vol. I. Summary, NASA CR-114503, 1972.

10. H. C. Quigley, S. R. M. Sinclair, T. C. Nark, and J. V. O'Keefe, "A Progress Report on the Development of an Augmentor Wing Jet STOL Research Aircraft." SAE Paper 710757, National Aeronautic and Space Engineering and Manufacturing Meeting, Los Angeles, September 1971.

11. R. E. Spitzer, P. C. Rumsey, and H. C. Quigley, "Use of the Flight Simulator in the Design of a STOL Research Aircraft." AIAA Paper 72-762, August 1972.

12. R. C. Innis and S. B. Anderson, "Comparison of Simulator and Flight Results on Augmentor Wing Jet STOL Research Aircraft." NASA SP-320, Paper 21, 1972.

13. H. Skavdahl and D. H. Patterson, "The Development of an Augmentor Wing Jet STOL Research Aircraft (Modified C-8A), vol. II. Analysis of Contractor's Flight Test, August 1972.

14. John A. Conway, "The Development of an Integral Propulsion System for Jet STOL Flight Research." Paper presented at AGARD Propulsion and Energetics Panel Meeting on V/STOL Propulsion, September 1973.

15. D. L. Harkonen, C. F. Wintermeyer, and F. L. Wright, "Static Tests of a 0.7 Scale Augmentor Wing Flap for the Modified C-8A Airplane – Test Results and Analysis." NASA CR-114315, 1971.

16. William B. Cleveland, Richard F. Vomaske, and S. R. M. Sinclair, "Augmentor Wing Jet STOL Research Aircraft Digital Simulation Model." NASA TM X-62,149, 1972.

17. Susan E. Post, "Computer Programs for Estimation of STOL Takeoff, Handling, and Static Performance." NASA TM X-62,217, 1972.

18. H. E. Hoerner, "Fluid-Dynamic Drag." Published by the author, 1965.

19. R. E. Spitzer, "Predicted Flight Characteristics of the Augmentor Wing Jet STOL Research Aircraft." NASA CR-114463, 1972.

20. R. G. Innis, C. A. Holzhauser, and H. C. Quigley, "Airworthiness Considerations for STOL Aircraft." NASA TN D-5594, 1970.

21. Anon.: "V/STOL Handling-Qualities Criteria," AGARD Report no. 577, December 1970.

22. R. L. Allison, "Design Evaluation Criteria for Commercial STOL Transports." NASA CR-114454, 1972.

23. Anon.: "Military Specification – Flying Qualities of Piloted Airplanes." MIL-F-8785B (ASG), August 1969.

24. Anon.: "Tentative Airworthiness Standards for Powered Lift Transport Category Aircraft." Part XX, Federal Aviation Administration, August 1970.

25. Anon.: "Military Specification – Flying Qualities of Piloted V/STOL Aircraft." MIL-F-83300, December 1970.

26. P. M. Condit, L. G. Kinbrel, and R. G. Root, "Inflight and Ground-Based Simulation of Handling Qualities of Very Large Airplanes in Landing Approach." NASA CR-635, 1966.

APPENDIX

FLIGHT TEST AIRSPEED, ALTITUDE, AND ANGLE OF ATTACK CORRECTION

The nose boom airspeed and altitude position error corrections are presented in figure 88 for 5.6°, 30°, and 65° flaps. The parameter ($\Delta P/q_i$) is the ratio of the measured static pressure error (ΔP) to the uncorrected impact pressure (q_i). The parameter C_{L_i} is the trim lift coefficient of the aircraft based on indicated airspeed.

The angle of attack calibration is presented in figure 89, also for flap deflections of 5.6°, 30°, and 65°. In this figure, α_i is the measured or vane deflection (indicated angle of attack) referenced to the nose boom measuring station, and α_F is the corrected angle of attack referenced to the fuselage centerline.

TABLE 1.– RESEARCH AIRCRAFT CHARACTERISTICS

Weights, lb (kg)			
Maximum gross	48,000 (21,800)		
Maximum gross (STOL takeoff)	45,000 (20,500)		
Maximum landing (STOL landing)	43,000 (19,500)		
Operational empty	32,600 (14,800)		
Maximum fuel	14,000 (6,350)		
Areas, ft^2 (m^2)			
Wing area, total including ailerons flaps and 111 ft^2 (10) of fuselage		865	(80)
Wing flap area, projected, including ailerons aft of wing line		187.10	(17)
Total aileron area aft of hinge line, including trim tab		46.30	(4)
Horizontal tail area, total		233	(21)
Elevator aft of hinge line		81.5	(7)
Vertical tail area, total		152	(14)
Rudder aft of hinge line			
Fore		30	(3)
Trailing		30	(3)
Dimensions and General Data			
Wing, ft (m)			
Span		78.75	(24)
Root chord		12.58	(3.8)
Tip chord		7.74	(2.3)
Mean aerodynamic chord		12.1	(3.7)
Aerofoil section			
Root	NACA	$64_3A417.5$ (MOD)	
Tip	NACA	63_2A615 (MOD)	
Sweepback at 40 percent chord, deg		0.0	
Dihedral, outer wing only, deg		5.0	
(Note: Wing taper and dihedral each start 17.6 ft from plane of symmetry.)			
Aspect ratio		7.2	
Ailerons, ft (m)			
Span		11.50	(3.5)
Chord aft of hinge line		2.01	(0.6)
Distance from plane of symmetry to centroid of aileron		33.70	(10.2)
Aerodynamic balance, percent		20.0	
Spoilers, ft (m)			
Span		11.30	(3.4)
Chord		1.18	(0.3)
Position of hinge line, percent wing chord (average)		62.4	
Flaps, ft (m)			
Span (each side)		23.0	(7.0)
Chord aft of hinge line		3.2	(1.0)

TABLE 1.- RESEARCH AIRCRAFT CHARACTERISTICS – Continued

Horizontal tail, ft (m)		
Span		32.0 (9.7)
Root chord		8.33 (2.5)
Mean aerodynamic chord		6.25 (1.9)
Aerofoil section		
Root	NACA	63_A214 (MOD) (inverted)
Tip	NACA	63-212 (MOD) (inverted)
Sweep of leading edge, deg		4.8
Dihedral, deg		0.0
Aspect ratio		4.4
Vertical tail, ft (m)		
Span		13.60 (4.1)
Root chord		14.00 (4.2)
Tip chord		8.33 (2.5)
Mean aerodynamic chord		11.41 (3.5)
Airfoil section	NACA	$63_{(215)}014$ (MOD)
Sweep of leading edge, deg		22.6
Aspect ratio		1.2
Overall height, ft (m)		28.7 (8.8)
Overall length (with nose boom of 16 ft), ft (m)		93.32 (28.3)
Distance, wing MAC, 1/4C, to horizontal tail MAC, 1/4C, ft (m)		46.3 (14.1)
Distance, wing MAC, 1/4C, to vertical tail MAC, 1/4C, ft (m)		43.4 (13.2)
Wing incidence angle, deg		+2.5
Horizontal tail incidence angle (ground adjustable), deg		+1.0

Control Surface Deflections and Rates

Flaps	5.6° down to 72° down 4°/sec extension and retraction
Conical nozzles	6° to 104° (down from aft of aircraft) 90°/sec
Ailerons	±17° about +35° max droop angle 30°/sec
Spoilers	−50° 100°/sec
Augmentor choke	55% choke gap area closure at 75° flap deflection 30°/sec
Rudder	±25° forward segment ±25° trailing segment −50°/sec
Elevator (usable from trim)	−15° +10°

TABLE 1.– RESEARCH AIRCRAFT CHARACTERISTICS – Concluded

Maximum Design Speeds, knots

Dive speed (V_D)	180
Cruise speed (V_C)	160
30° Flaps down speed (V_{f30}	120
>50° Flaps down speed ($V_{f>50°}$)	90

TABLE 2.- AIRCRAFT SHORT PERIOD AND PHUGOID CHARACTERISTICS

						Short period			Phugoid		
δ_f, deg	ν, deg	V_E, knots	Weight, lb	Weight, kg	C_J	ω_n, rad/sec	ζ	P, sec	ω_n, rad/sec	ζ	P, sec
67	9	62	41,340	18,800	...	1.00	0.72	9.1	0.17	0.09	37.8
66	40	64	38,800	17,600	0.38	.87	.90	16.5	.19	.09	33.1
67	77	65	37,600	17,100	.49	1.03	.90	14.1	.19	.10	33.6
33	14	78	40,000	18,200	.22	1.20	.86	10.1	.18	0	31.9

TABLE 3. – LATERAL DIRECTIONAL DYNAMIC CHARACTERISTICS

						Dutch Roll			Spiral Mode		Roll Mode
SAS	ξ_f	ν	V_E	$\frac{W}{X10^3}$	C_J	P	ζ	ω_n	$T_{1/2}$	T_2	τ_A(sec)
OFF	67°	~10°	~70	37-40	.11-.35	6	~.15	1.06	---	5-7	1.0
Roll on/Yaw off				38	.34	7	.13	.91	8	---	---
Roll off/Yaw on				38	.34	---	---	---	---	5	---
ON				39	.35	6.8	.33	.98	Neut → Pos.	---	0.45
OFF	33	~10°	102	40	.15	4.9	.16	1.3	---	---	~1.0
			105	40	.21	4.3	.12	1.45	---	---	---
			78	44.5	.27	6.8	.10	.94	---	8	---
ON			79	43.9	.29	6.4	.31	1.03	Neut → Pos.	---	~1.0
N/A	6°	~10°	168	45	.06	4.2	.16	1.51	Neut → Pos.	---	0.70
N/A	6°	~10°	135	40 & 44	.075	5.0	.15	1.27	Neut → Pos.	---	0.80

TABLE 4.– ELEVATOR RESPONSE AND FLIGHT PATH CONTROL FOR THE STOL APPROACH CONDITION.

	AWJSRA	Criterion (ref.)
Elevator control power (F_{col} = 40 lbs), rad/sec^2	0.33, −0.34	> 0.05 to 0.20 (21)
Pitch control sensitivity (θ/δ_c), rad/sec^2/inch	0.08	> 0.08 to 0.12 (21)
Stick force per g, lb/g	30	< 20 to 40, >3 (21)
Effective vertical speed crossover time (t_h^*), sec	0.9	$\overline{<}$ 0.8 (22)
Load factor response time constant (τ_{n_z}), sec	~1.5	< 1.5 (21)
Load factor per unit control deflection (n_z/δ_{col}), g/inch	0.15	~ 0.1 (22)
Load factor per unit angle of attack (n_z/α), g/rad	1.5	> 2.3 (23)
Flare control load factor, g	> 1.1-1.15	$\overline{>}$ 1.20 (22)
Pitch angle after 1 sec, deg ($F_{col} \approx$ 40#)	2.2°	> 2 to 4 (21)

TABLE 5.– ELEVATOR SYSTEM CHARACTERISTICS AT STOL APPROACH SPEED.

	AWJSRA	Criterion (ref.)
Elevator deflection from trim @ 40# F_{col}, deg	−13, +14	–
Control column deflection, in.	+7.5, −5	> ±4, < ±6.5 (21)
Elevator to column gearing, deg/in.	3.0	–
Force gradient ($\Delta\delta_e$<10°) lb/in.	4.8	> 2, < 5 (21)
Column force at TEU maximum usable δ_e, lb	40	< 75 (24)

TABLE 6.—LONGITUDINAL STABILITY CHARACTERISTICS AT STOL APPROACH SPEED.

	AWJSRA	Criterion (ref.)
Stick-fixed stability ($\Delta\delta_e/\Delta V$), deg/knot	0.1	>0 (24)
Stick-free stability ($\Delta F_c/\Delta V$), lb/knot	0	>0 (24)
Change of flight path with velocity ($\Delta\gamma/\Delta V$), deg/knot	0	≤ 0.06 (23)
Short-period natural frequency (ω_n), rad/sec	0.9	>0.47 (25)
Short-period damping ratio (ζ)	1.2	>1.06 (25)
Phugoid natural frequency (ω_p), rad/sec	0.2	–
Phugoid damping ratio (ζ)	0.1	>0 (25)
Change of θ with velocity ($\Delta\theta/\Delta V$), deg/knot	−0.8	<0 (22)

TABLE 7.– LATERAL AND DIRECTIONAL CONTROL CHARACTERISTICS.

	AWJSRA	Criterion (ref.)
Lateral		
Control wheel travel at max ϕ, deg	± 77	± 60 (20)
Control travel, in. (m)	± 11.2 (± 0.3)	–
Breakout force, lb (kg)	± 5 (± 2.3)	1/2 to 4 (25)
Force gradient ($\delta_w \lesssim 20°$), lb/in. (kg/m)	0.8	1 to 3 (21)
Maximum force at max. $\ddot{\phi}$, lb (kg)	10 (4.5)	< 20 (20)
Control response (full control), sec	0.3	< 0.3 sec. for 63%$\ddot{\phi}_{max}$ (21)
Directional		
Rudder pedal travel, in. (n)	± 3.9 (± 0.1)	2.5 to 4.5 (21)
Force gradient (± 25 percent Rudder pedal), lb/in. (kg/m)	45 (800)	10 to 35 (21)
Maximum force, lb (kg)	98 (44.5)	< 130 (24)
Control response (full control), sec	0.7	< 0.3 for 63% $\ddot{\psi}_{max}$ (21)

TABLE 8.– LATERAL AND DIRECTIONAL CONTROL POWER CHARACTERISTICS FOR LANDING APPROACH AND TAKEOFF CONDITIONS.

	AWJSRA			Criterion (ref.)
	Landing		Takeoff	
	SAS On	SAS Off	SAS On	
Lateral				
φ max, rad/sec^2	0.67	0.70	0.60	>0.4 (20)
ϕ_1/δ_w deg/in.*	1.0	1.46	1.25	>0.8 (26)
Time to 30°ϕ, sec*	2.4	1.75	1.9	≤ 2.4 (20)
ϕ/δ_w, rad/sec^2/in., ($\delta_w < 40°$)	0.106	0.110	0.095	>0.07 (26)
Directional				
ψ_{max}, rad/sec^2	0.37	0.37	0.40	>0.15 (21)
β_{max}, deg	20	20	20	≥ 25 (22)
Decrab ($\Delta\psi_{2.0}$), deg	21	23	---	10 to 15 (22)
Decrab time ($\Delta\psi = 15°$), sec	1.6	1.5	---	<2.0 (21)
Sensitivity ($\delta_p < 1$ in), rad/sec^2/in.	0.12	0.12	0.13	>0.05 (21)

*Based on a ramp wheel input (ramp time = 0.5 sec.)

TABLE 9.– LATERAL–DIRECTIONAL DYNAMIC CHARACTERISTICS FOR LANDING APPROACH AND TAKEOFF CONDITIONS.

	AWJSRA			Criterion (ref.)
	Landing		Takeoff	
	SAS On	SAS Off	SAS On	
Dutch roll damping ($\zeta\omega_d$), 1/sec	0.30*	0.16	0.36	> 0.087 (20)
Dutch-roll frequency (ω_d), 1/sec	0.98	1.06	1.06	> 0.523 (20)
Roll time constant (τ_R), sec	0.45	1.1	1.0	< 1.4 (23)
Spiral time constant (τ_s), sec	~0	−0.11	~0	> −0.035 (20)
Turn coordination ($\Delta\beta/\Delta\phi$)	0.25	0.65	0.15	< 0.3 (20)
Dihedral effect ($d\delta_w/d\beta$)	1.2	1.2	1.4	> 0 (21)
Dihedral effect ($Fw_{\beta max}$), lb	8	8	8	< 10 (21)

*The Dutch-roll damping parameter ($\zeta\omega_d$) is increased to 0.45 with the VSS engaged in the landing approach configuration.

TABLE 10.– STOL TAKEOFF AND LANDING PERFORMANCE.

Takeoff		Landing	
Gross weight (max), lb	45,000 (20,500 kg)	Gross weight (max), lb	43,000 (19,500 kg)
Engine thrust, percent	99	Engine thrust, percent	93
Flap deflection, deg	30	Flap deflection, deg	65
Aileron droop, deg	17	Aileron droop, deg	30
Nozzle position, deg	6	Nozzle position, deg	80
Rotation speed, knots	65	Approach speed, knots	65
Lift-off speed, knots	75	Touchdown speed, knots	60
Climb speed, knots	86	Ground roll distance (est.), ft	840 (256 m)
Climb angle, deg	16	Total distance from 35 ft (est.), ft	1200 (365 m)
Ground roll distance, ft	700 (213 m)		
Total distance to 35 ft, ft	1100 (334 m)		

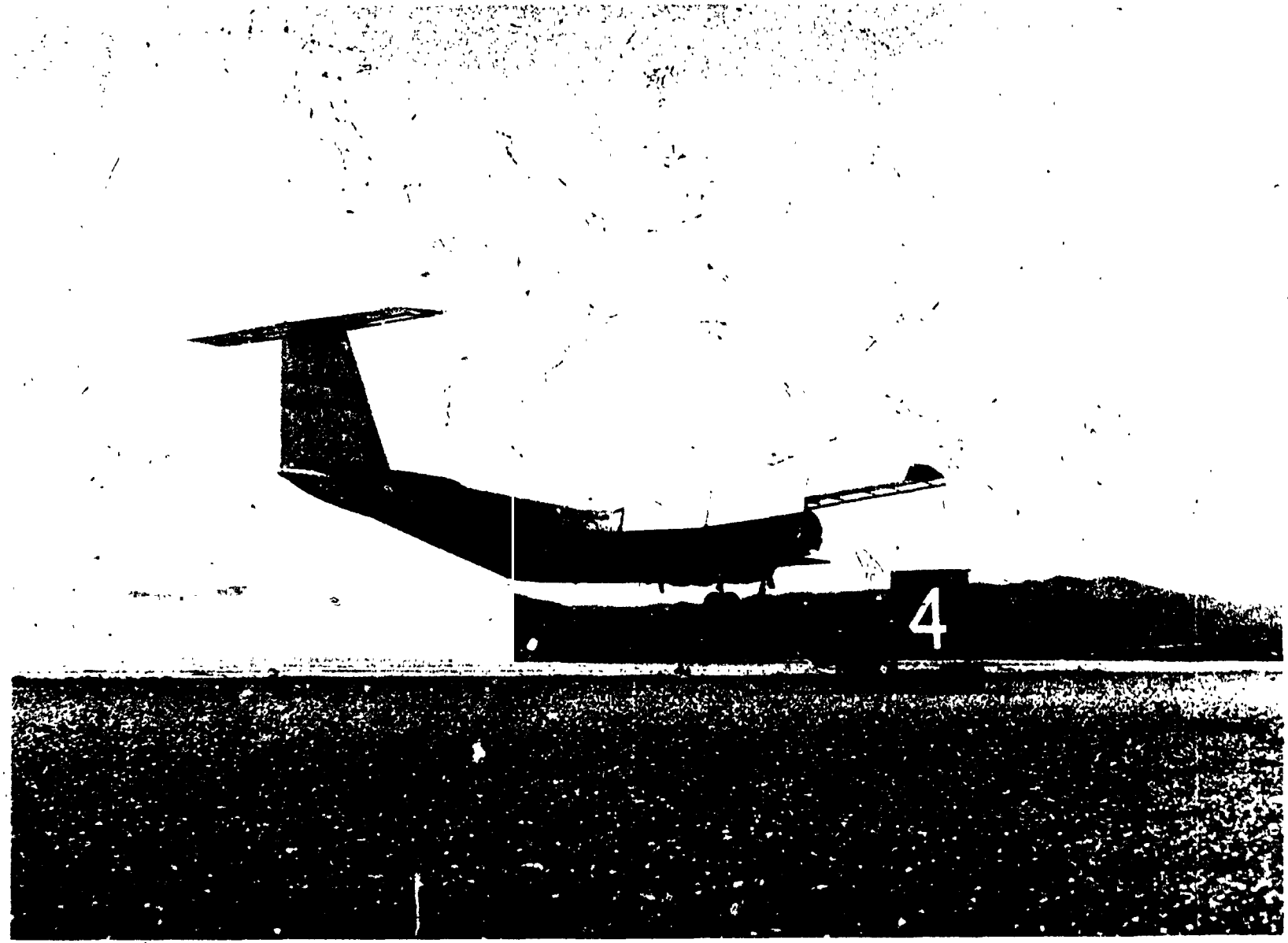

(a) Landing configuration

Figure 1.– Augmented wing jet STOL research aircraft.

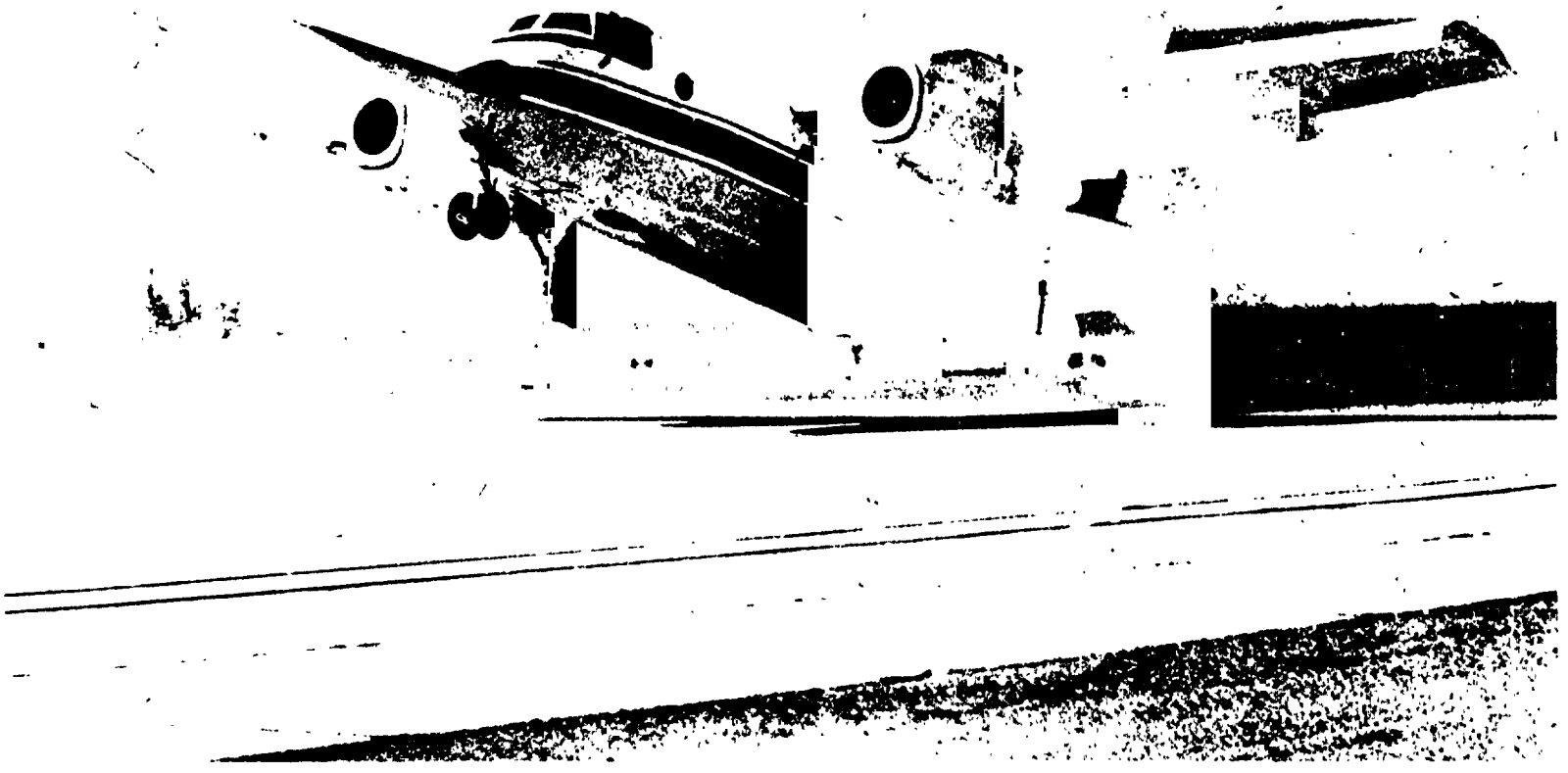

(b) Takeoff configuration

Figure 1. - Concluded.

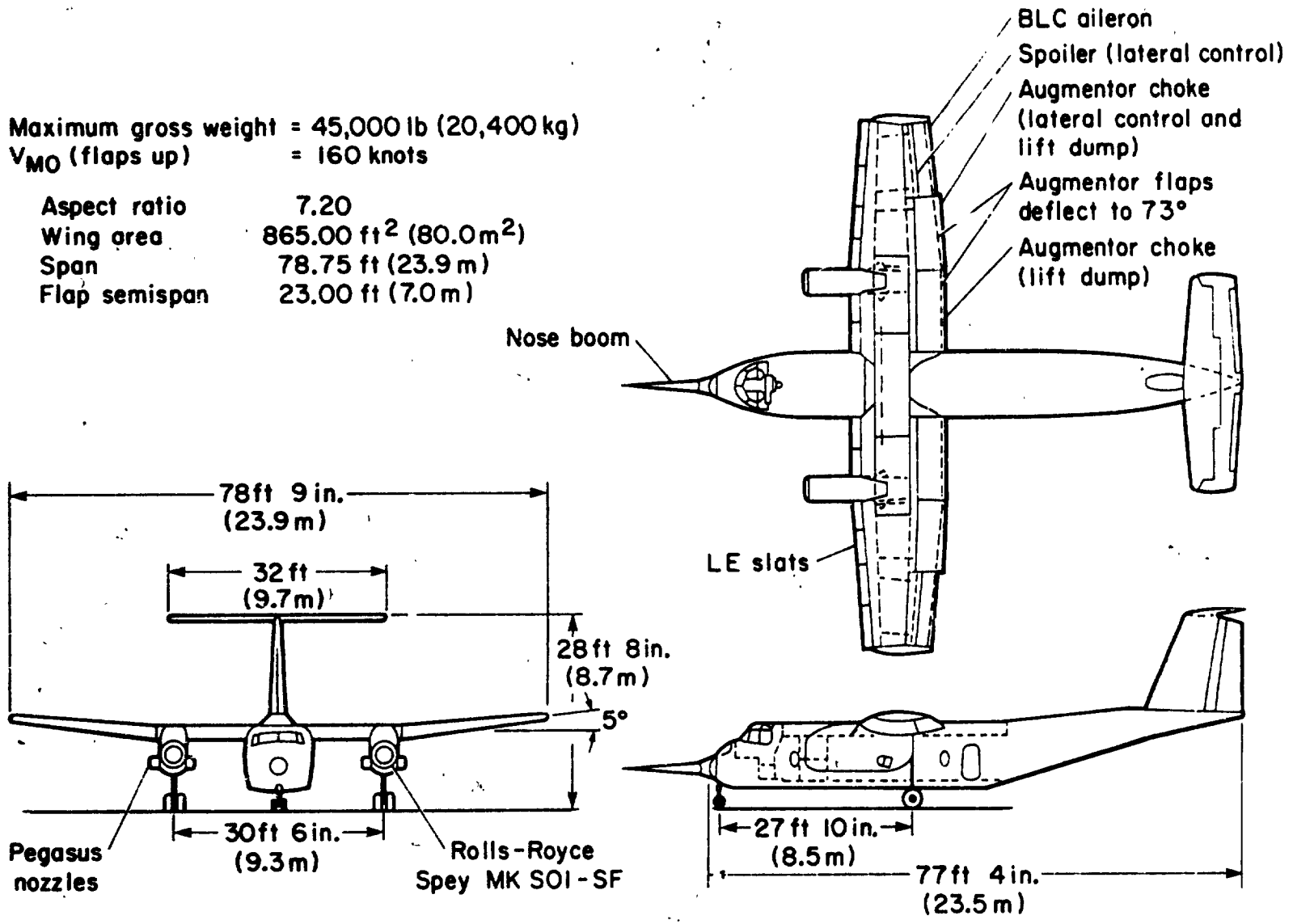

Figure 2.– Three-view drawing of modified C-8A.

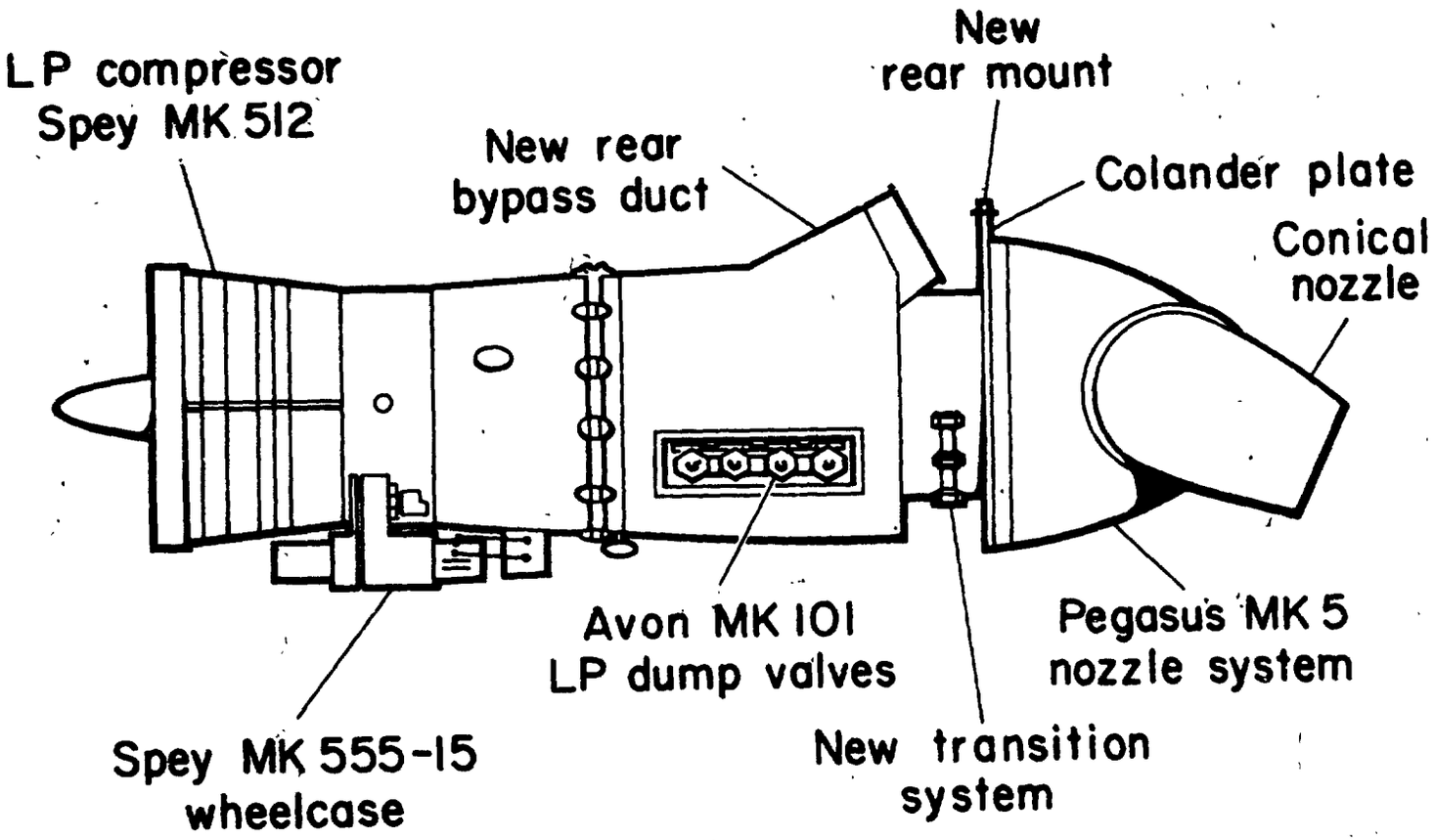

Figure 3.– Derivation of MK 801-SF components.

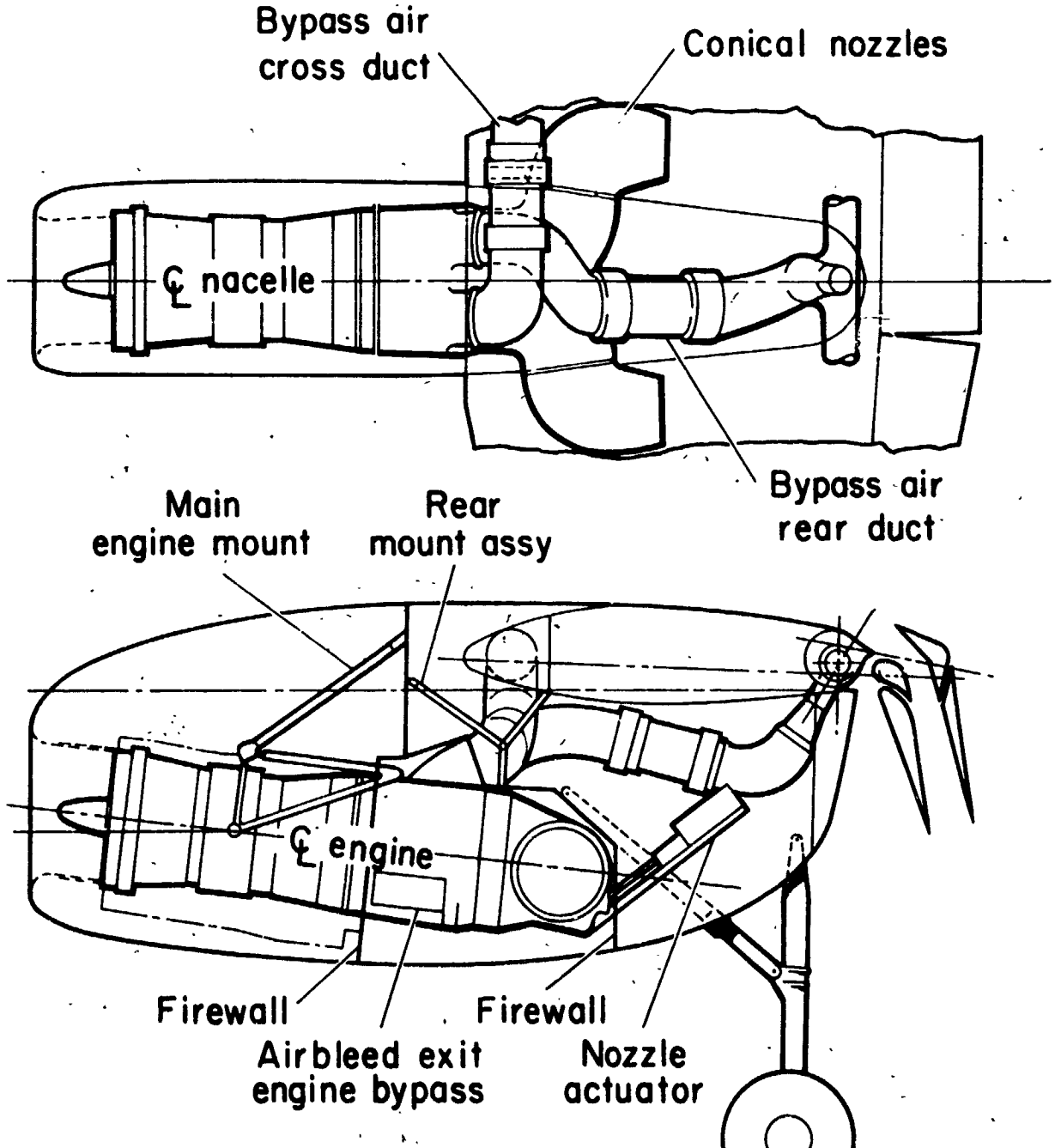

Figure 4. - Nacelle installation.

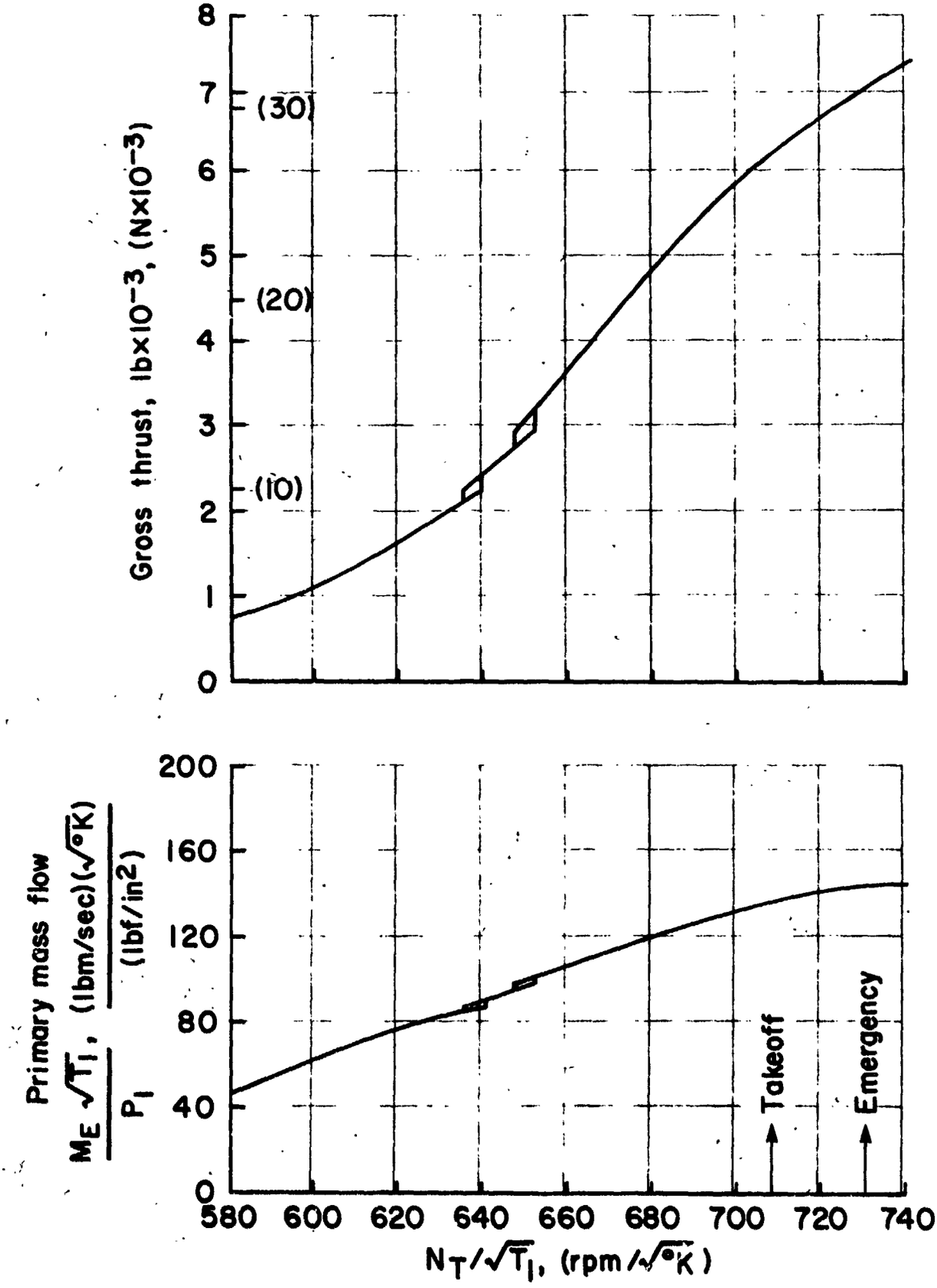

(a) Primary mass flow and gross (hot) thrust.

Figure 5.– Nominal SPEY 801-SF engine operating parameters.

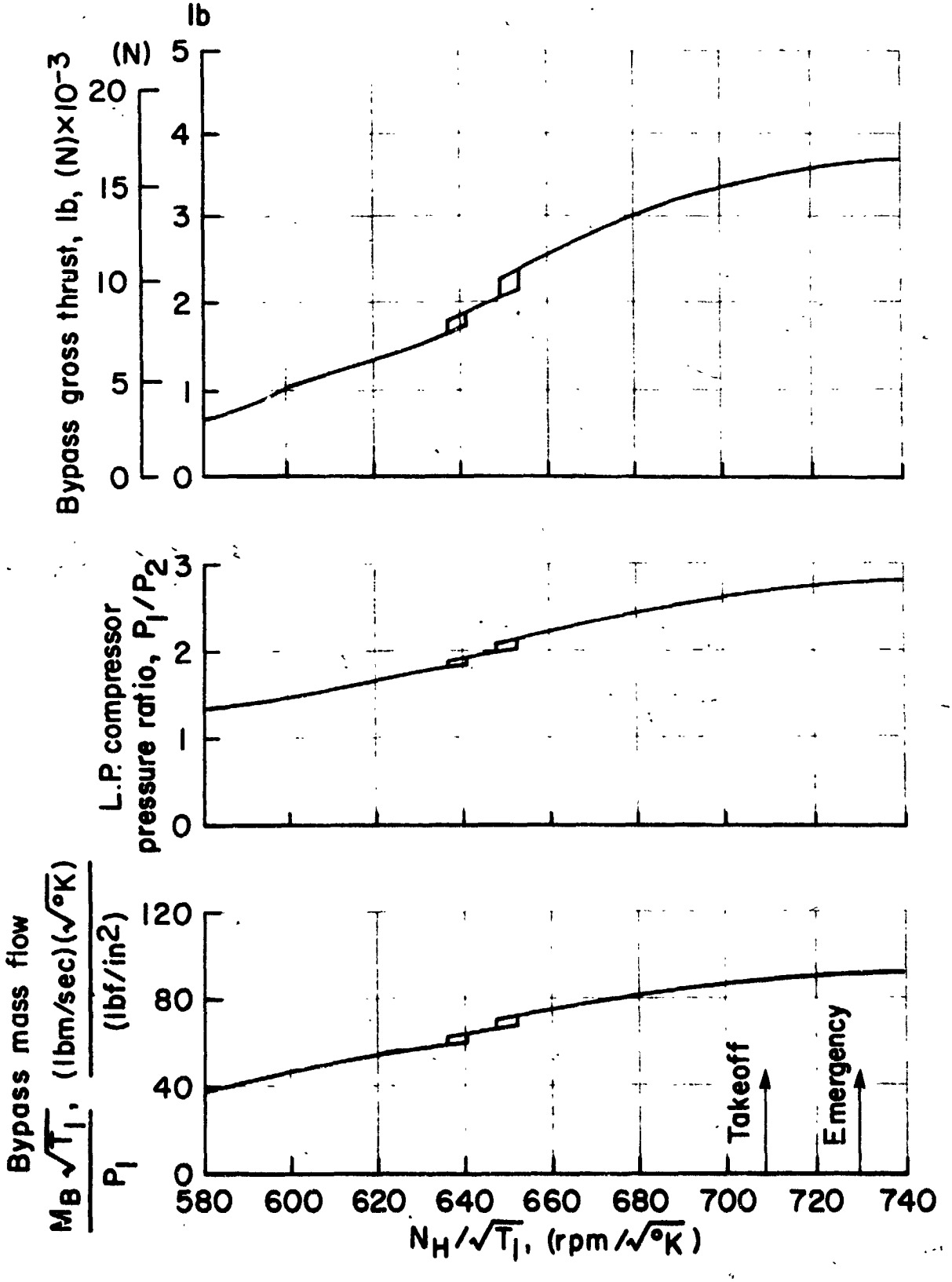

(b) Bypass (cold) thrust, L.P. compressor pressure ratio, and bypass mass flow.

Figure 5.– Concluded.

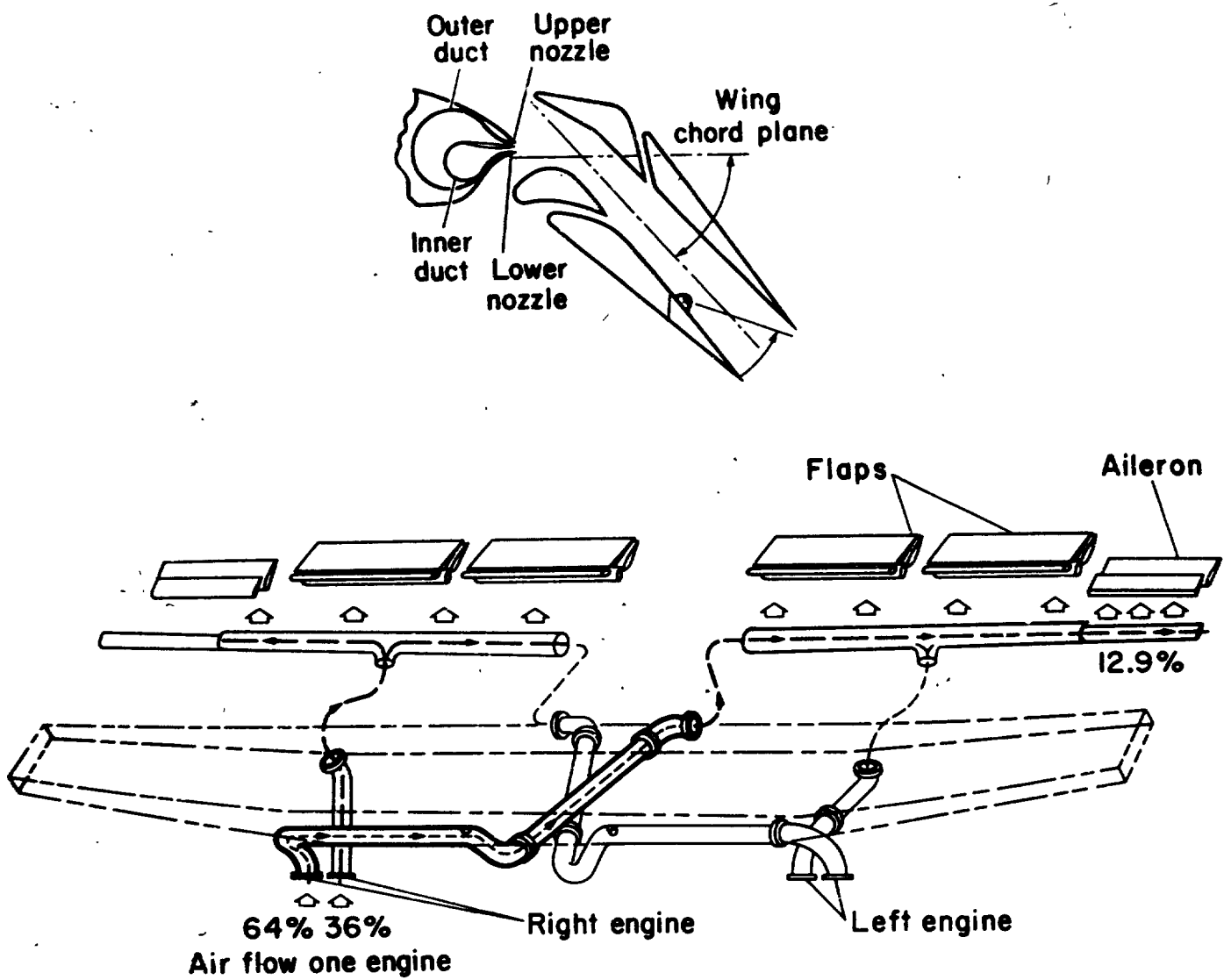

Figure 6.– Air distribution system.

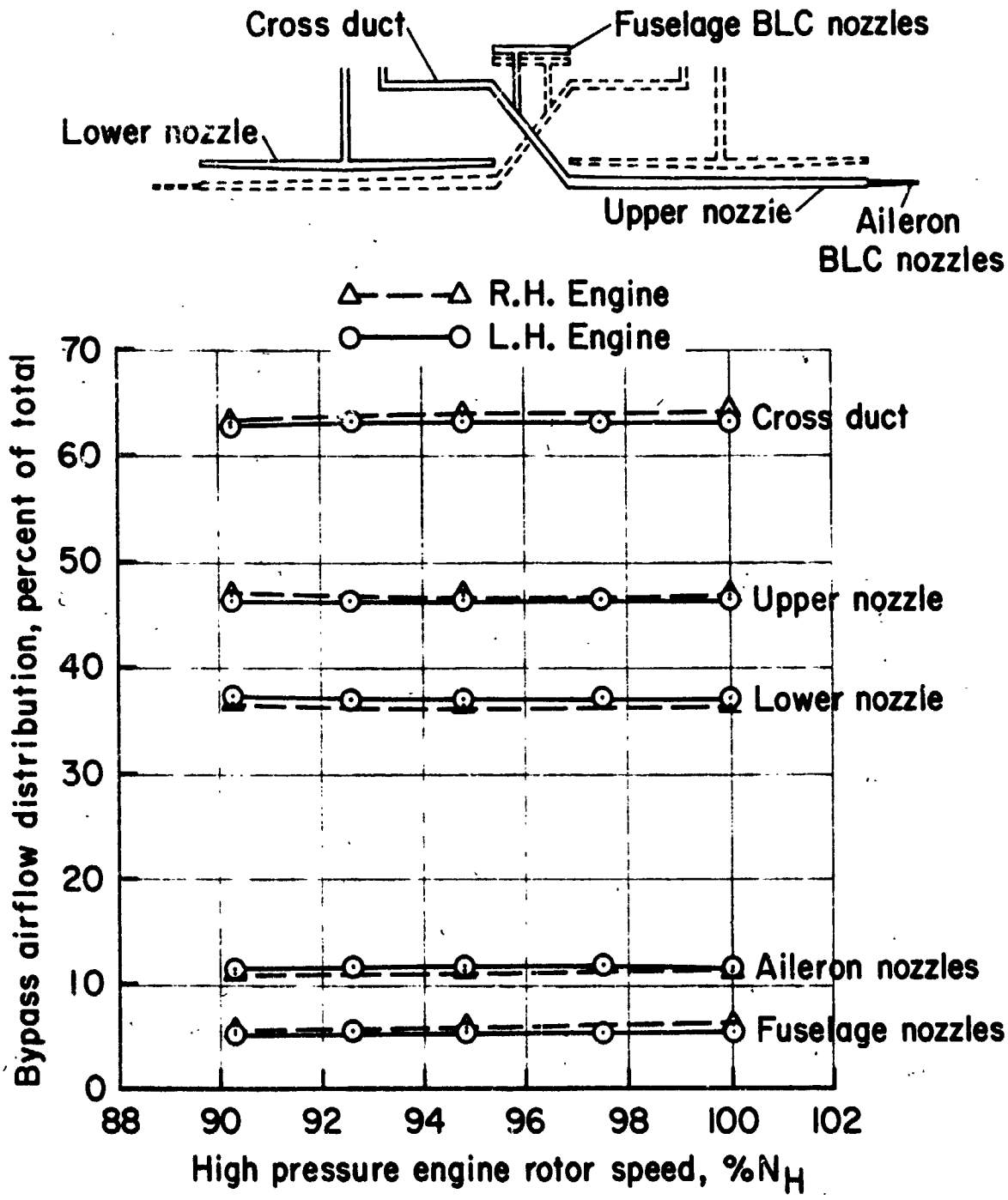

Figure 7.– Bypass flow distribution.

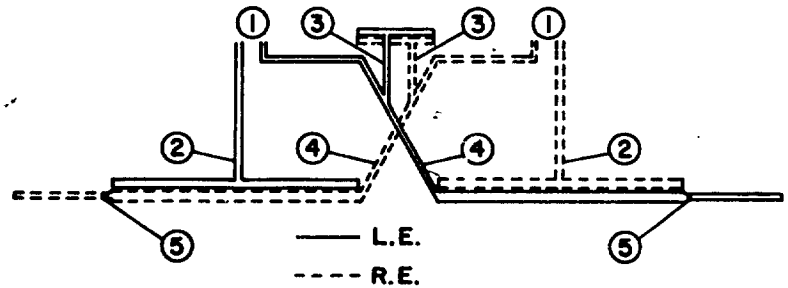

65° Flap 6° Nozzle	
Airflow, lb/sec	$N_T/\sqrt{T}$
L.E. = 79.32	L.E. 706
R.E. = 78.44	R.E. 705
P_T ~ in HgA	
L.E. = 79.6	(At engine)
R.E. = 79.2	(At engine)

Thrust loss, %		
Item	Left	Right
Engine ①	1.50	1.60
Ducts ② & ④	3.68	3.62
Nozzles	7.12	7.21
Total	12.30	12.43

Location	Item	Pressure loss ~ in. Hg	
		Left engine	Right engine
1	Port loss (aft)	2.40	2.40
	Port loss (cross)	2.80	2.80
1 – 2	To aft ref sta	3.94	3.69
1 – 3	To body duct calib sta	9.43	9.27
1 – 4	To cross duct ref sta	6.90	7.50
1 – 5	To aileron calib sta	10.12	10.20

Figure 8.– Air distribution system losses.

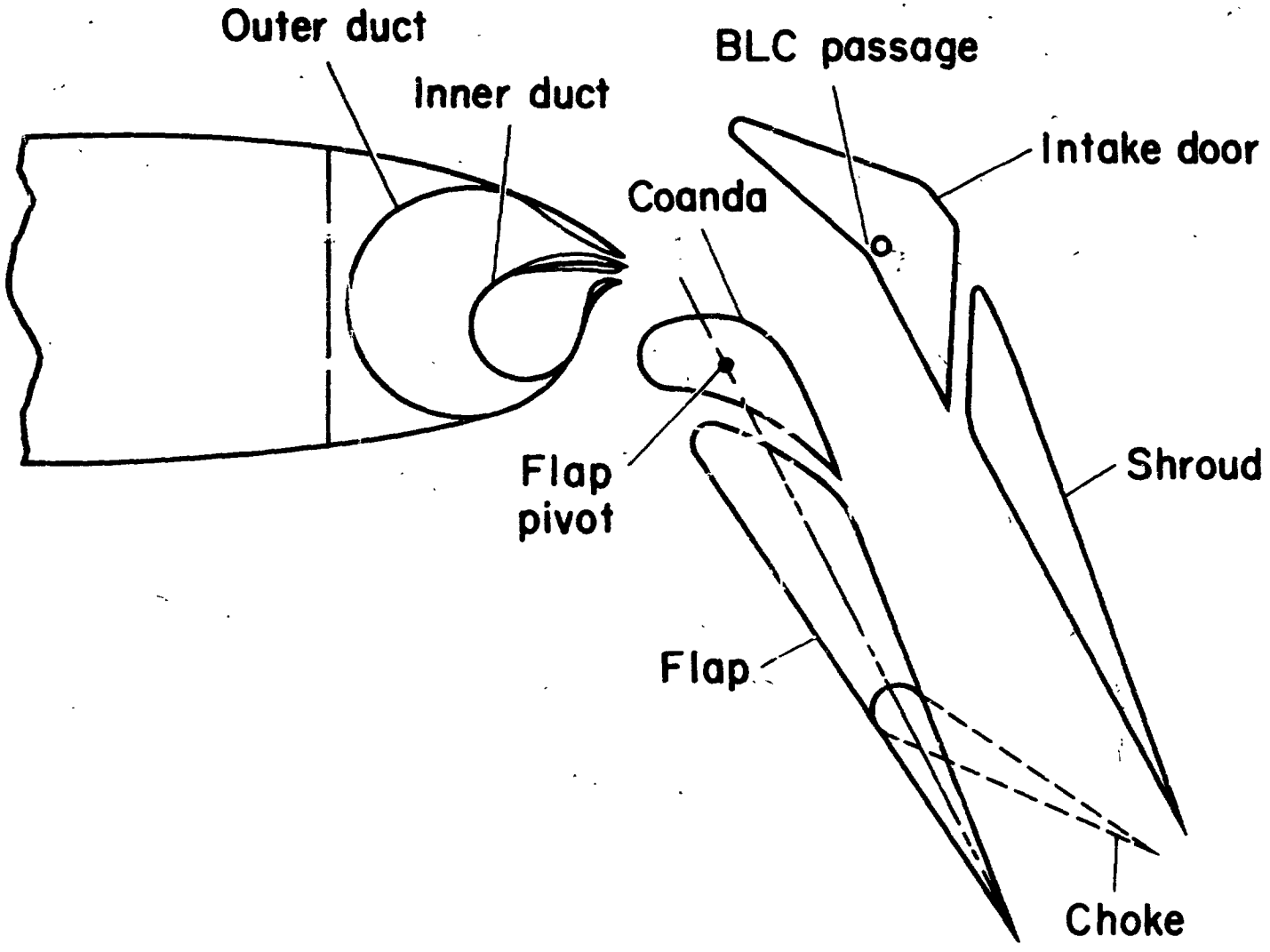

Figure 9.— Augmented jet flap details.

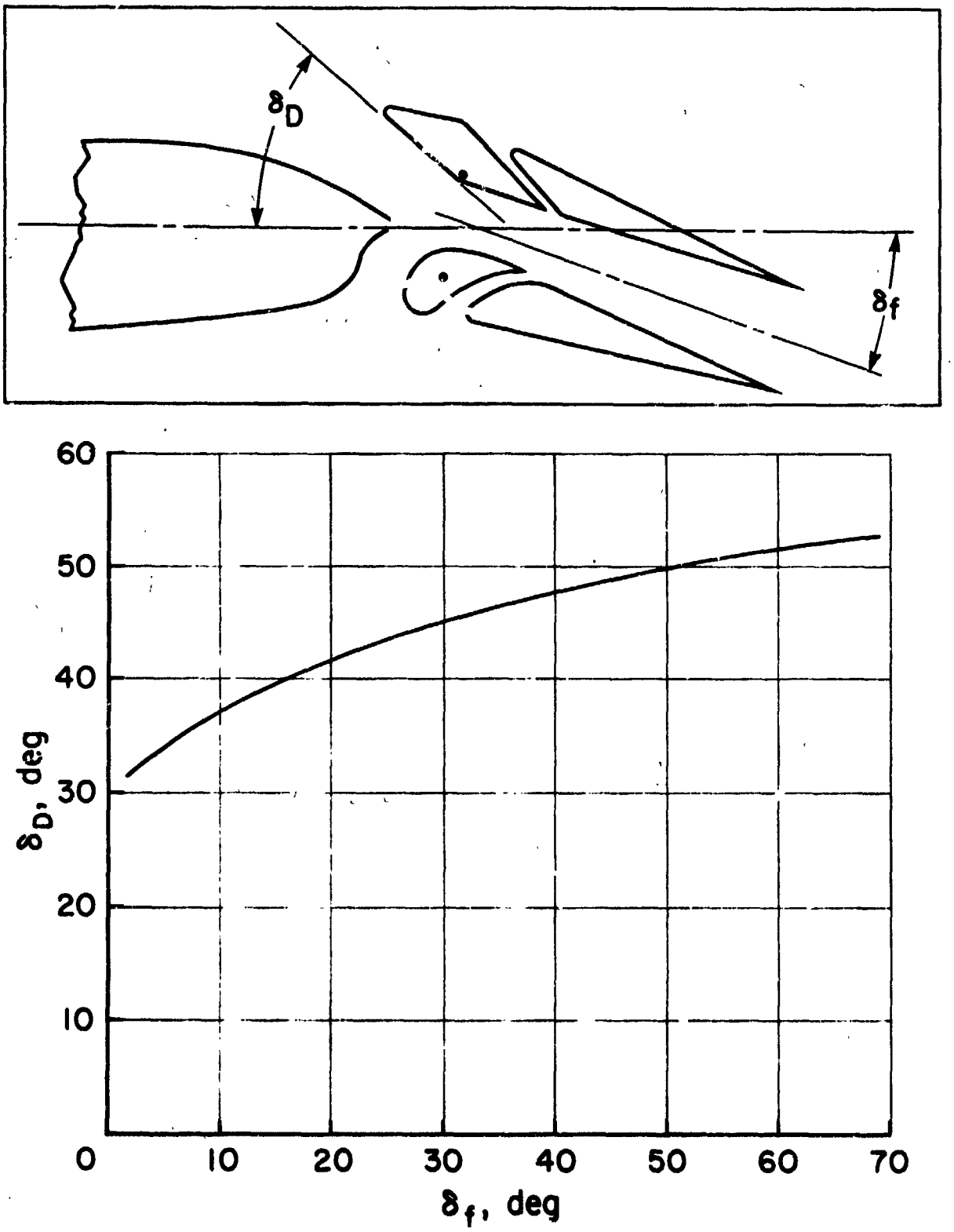

Figure 10.-- Flap intake door schedule.

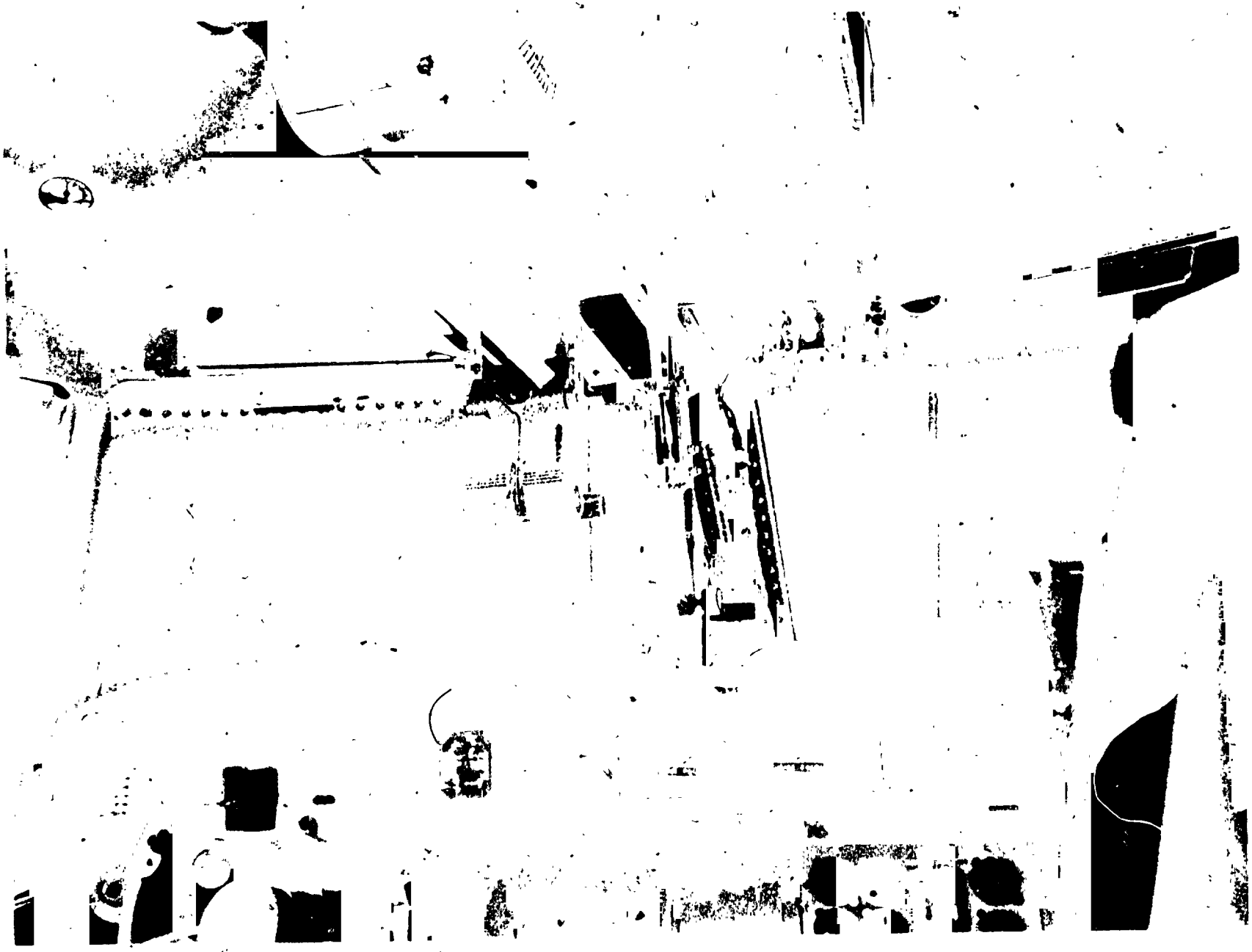

(a) Overhead console

Figure 11.– Cockpit interior.

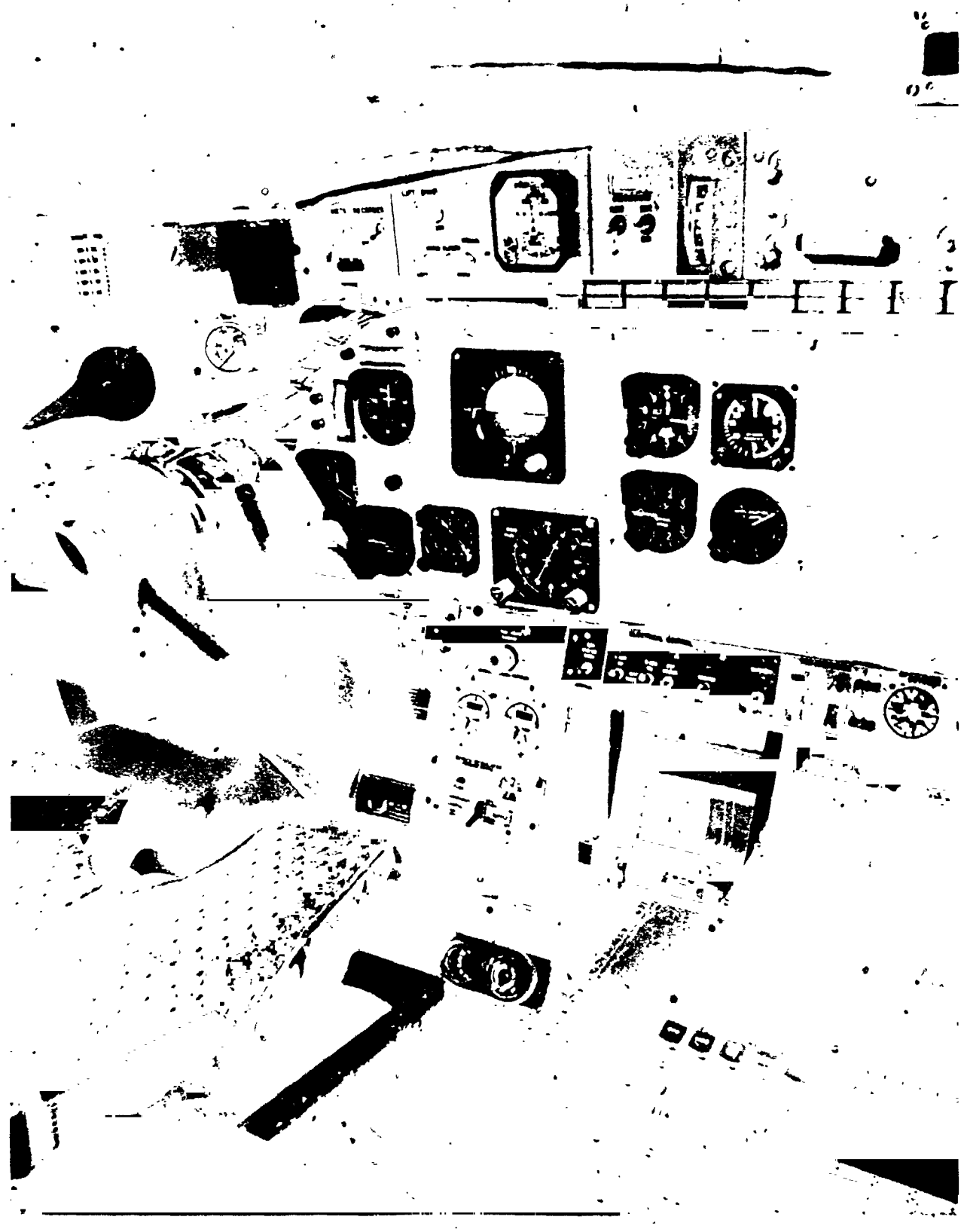

(b) Main panel

Figure 11. Concluded.

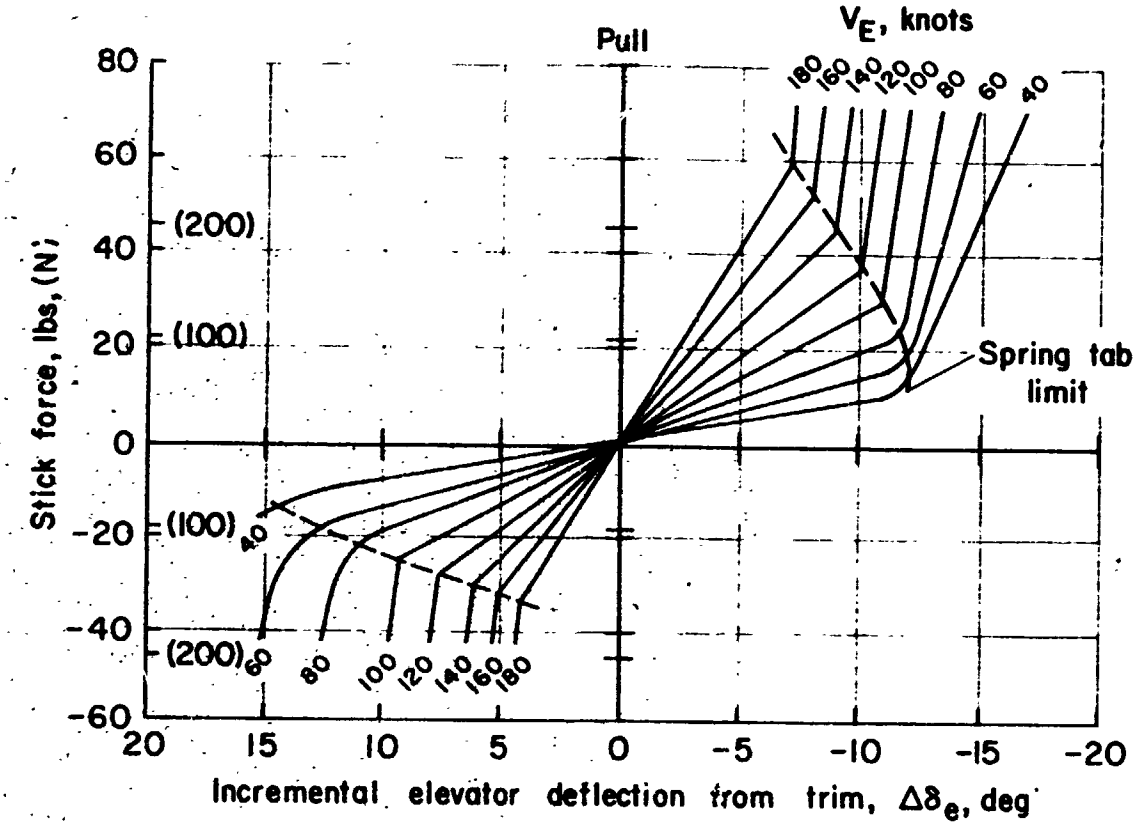

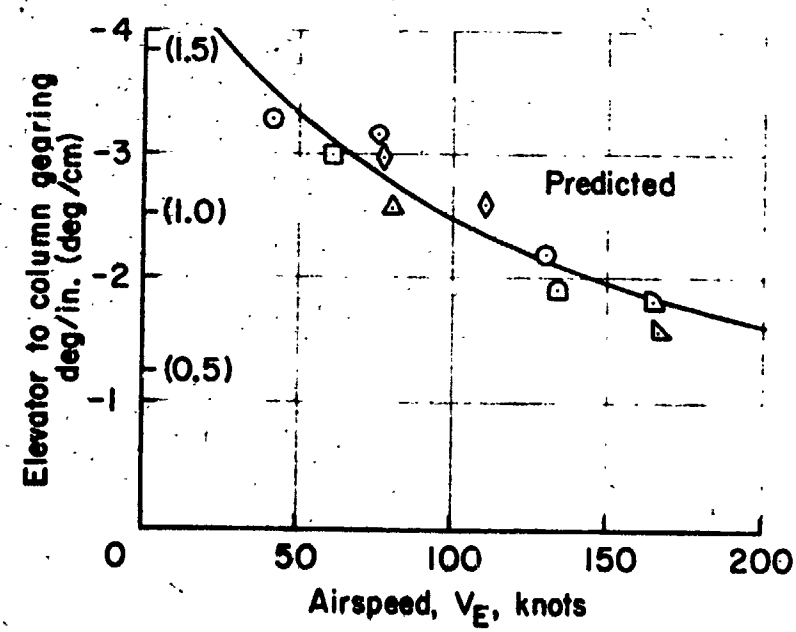

Figure 12.– Elevator characteristics.

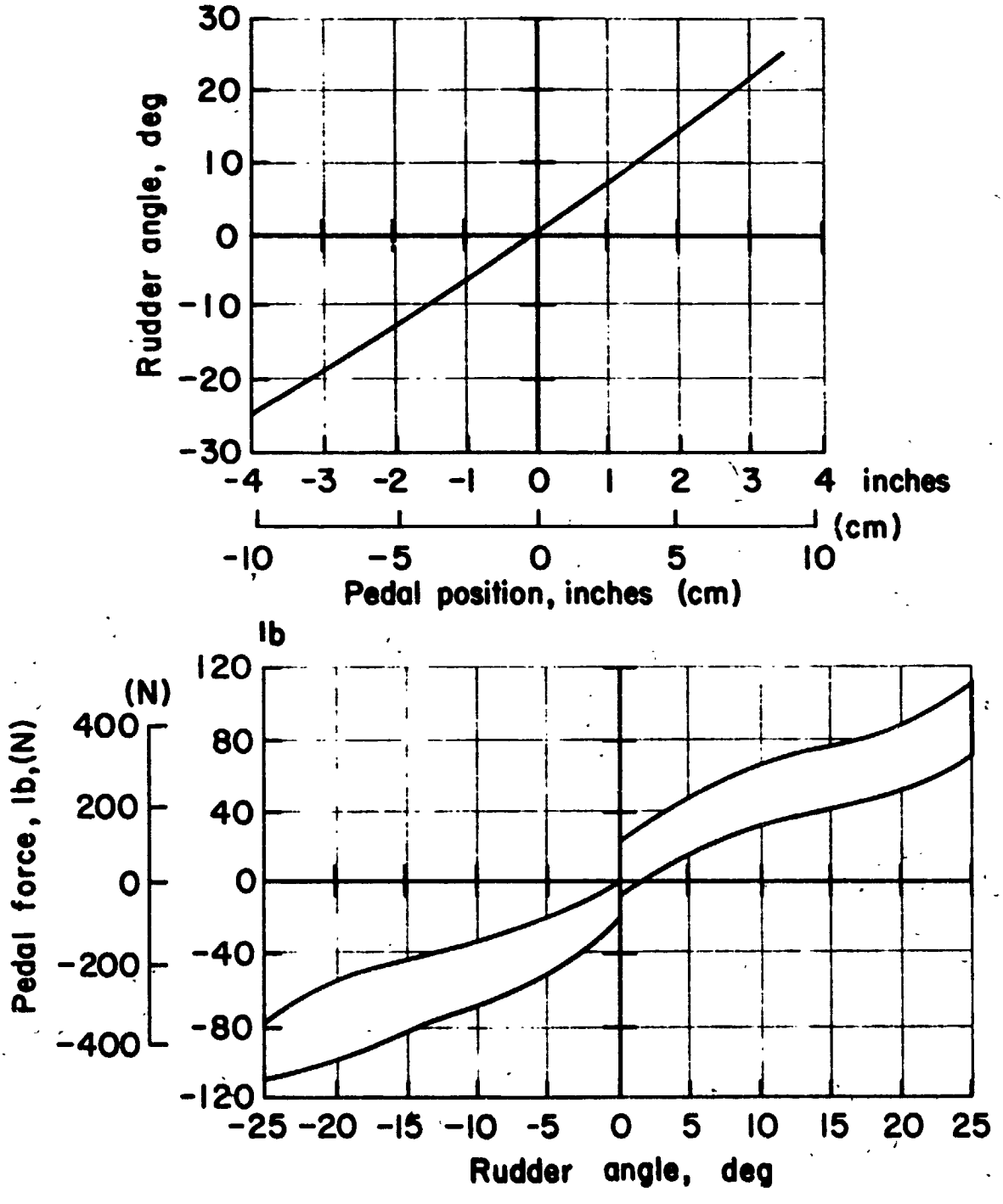

Figure 13.– Directional control characteristics, pedal force and gearing.

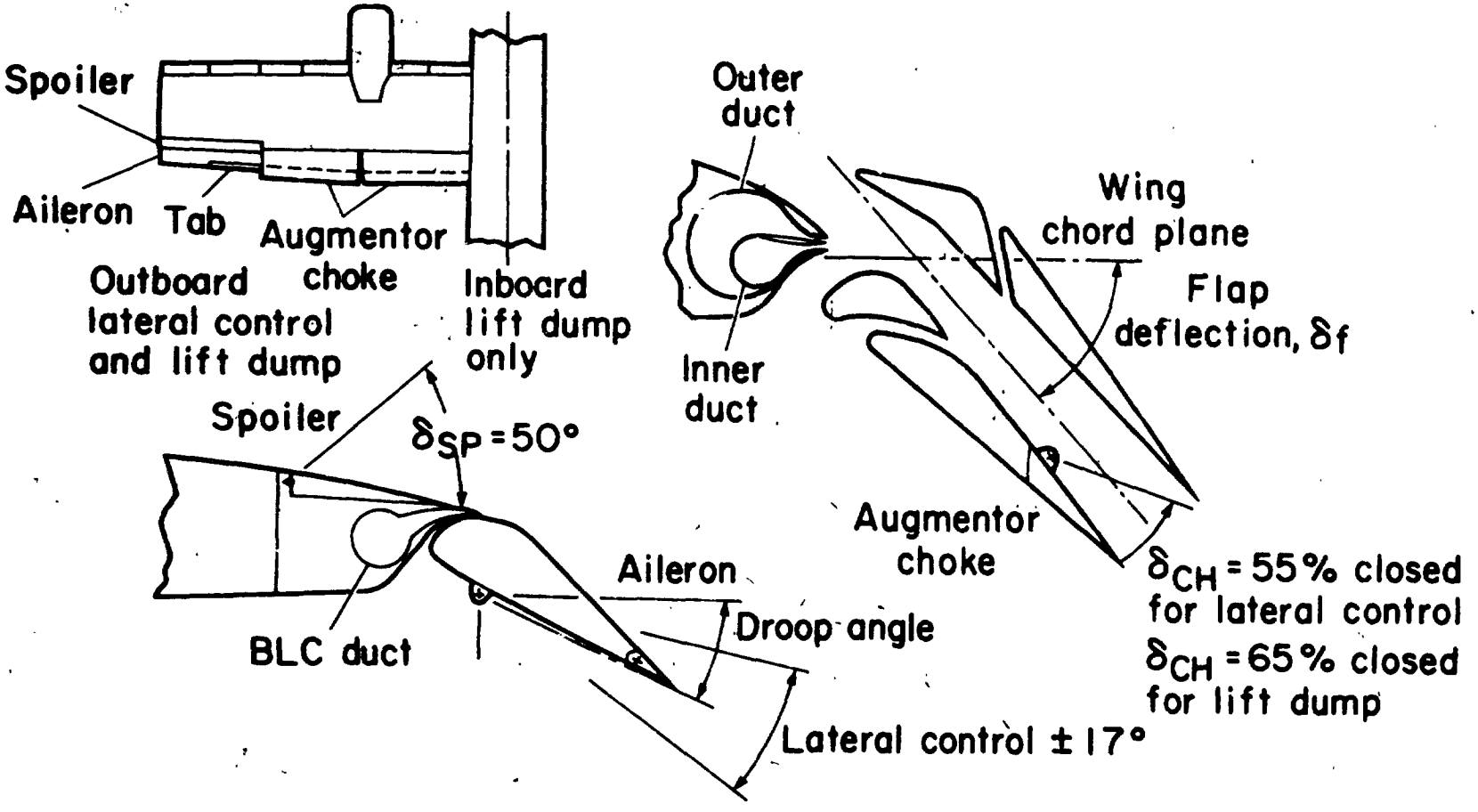

Figure 14.– Augmentor flap and lateral control geometry.

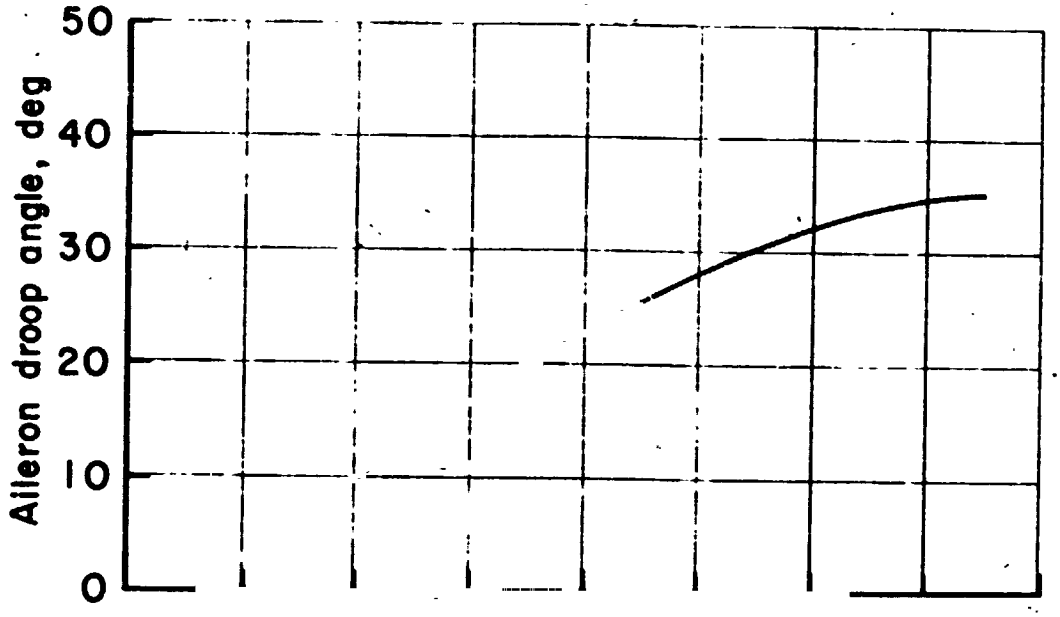

(a) Aileron droop program

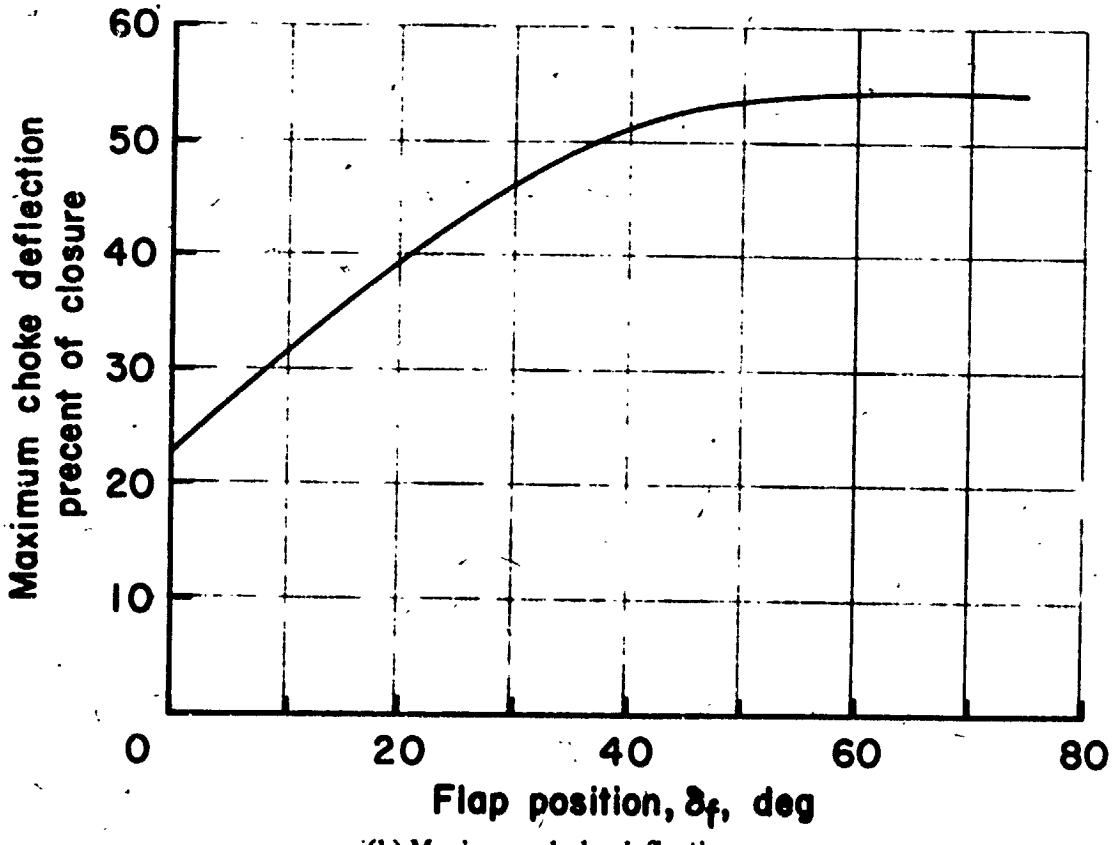

(b) Maximum choke deflection program

Figure 15.– Lateral control deflection.

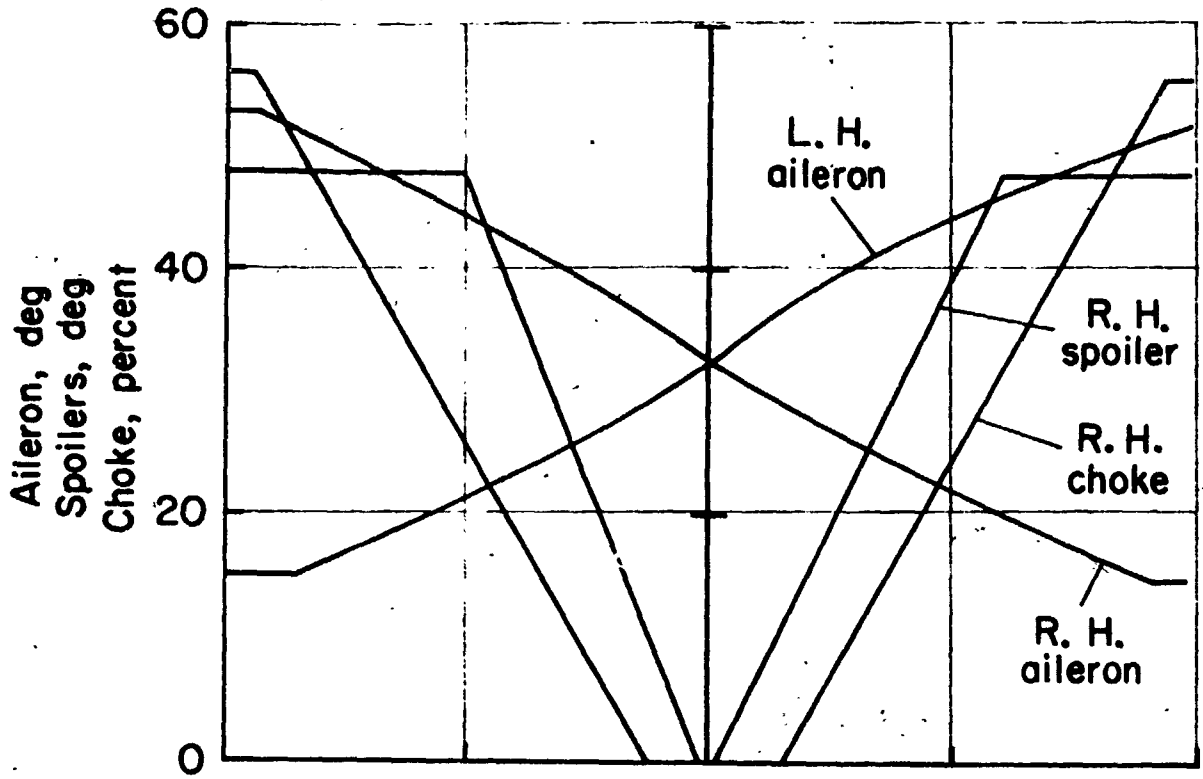

(a) Lateral control gearing, with flaps deflected 65°.

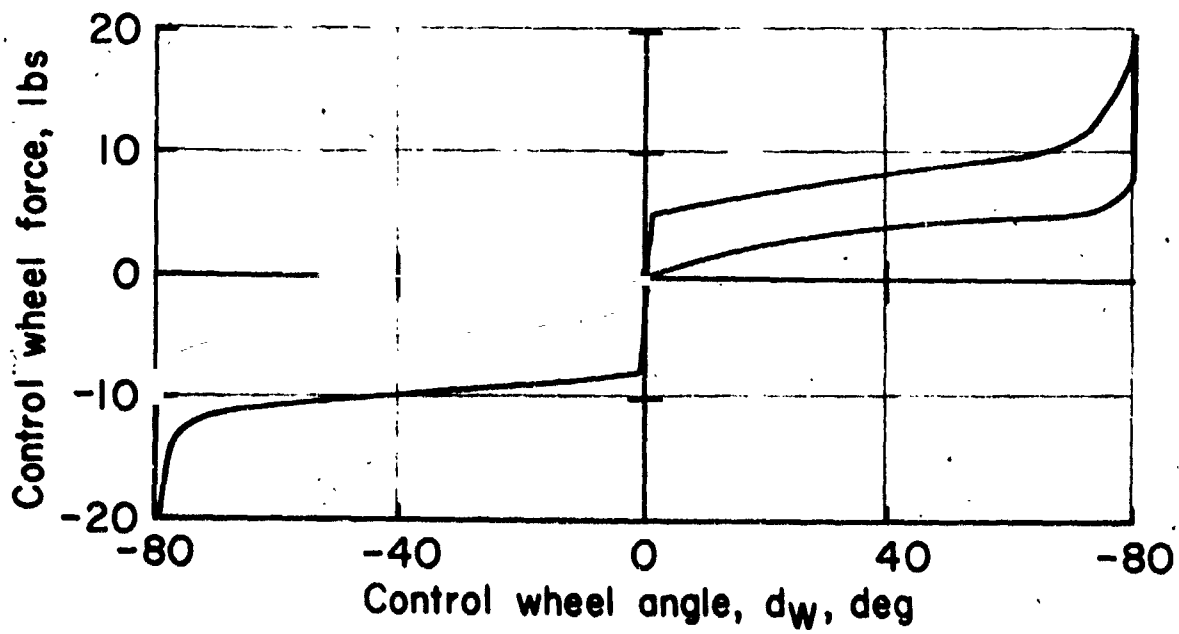

(b) Lateral control force

Figure 16.– Lateral control characteristics.

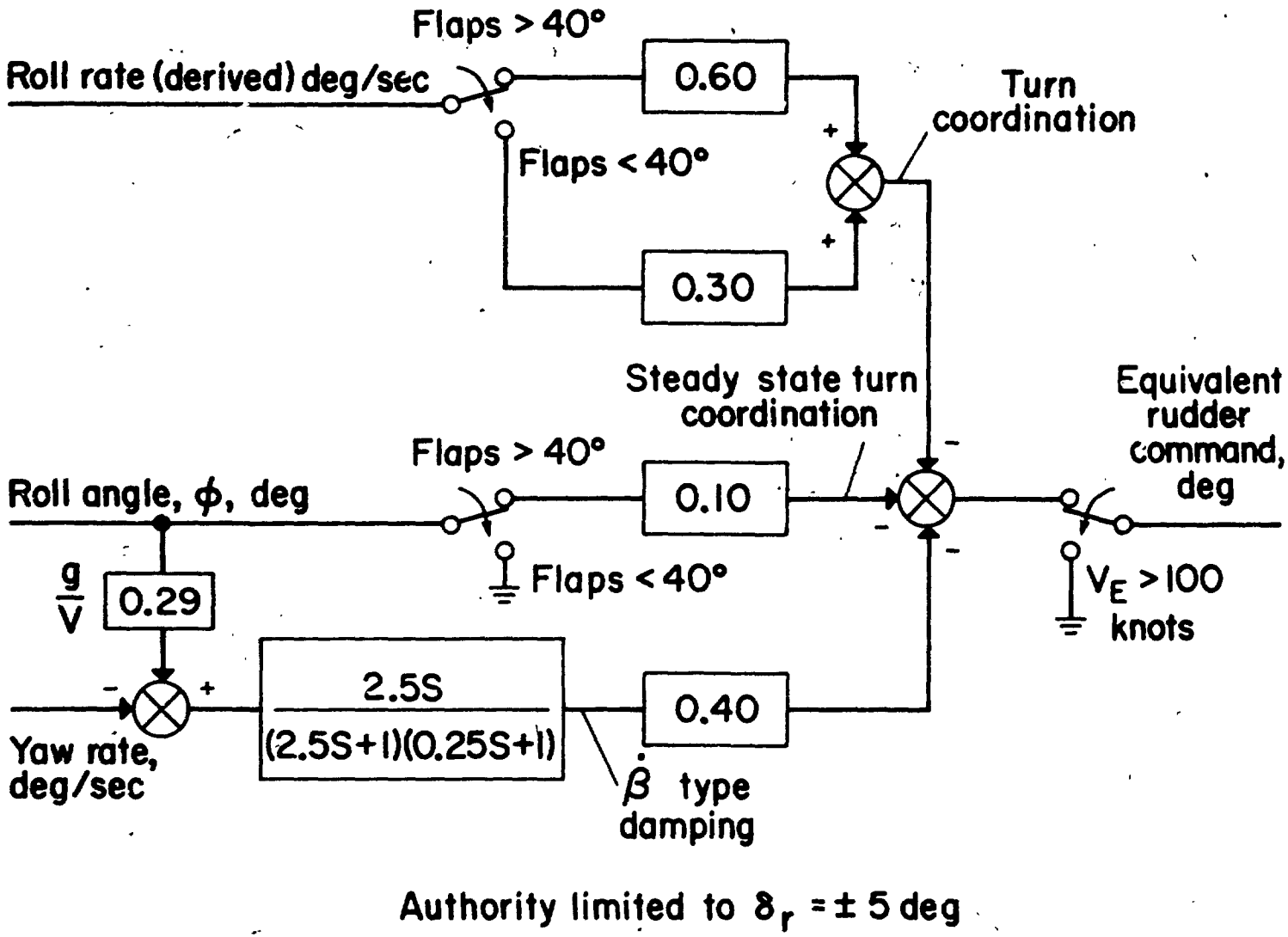

(a) Directional axis

Figure 17.— Stability augmentation (normal mode).

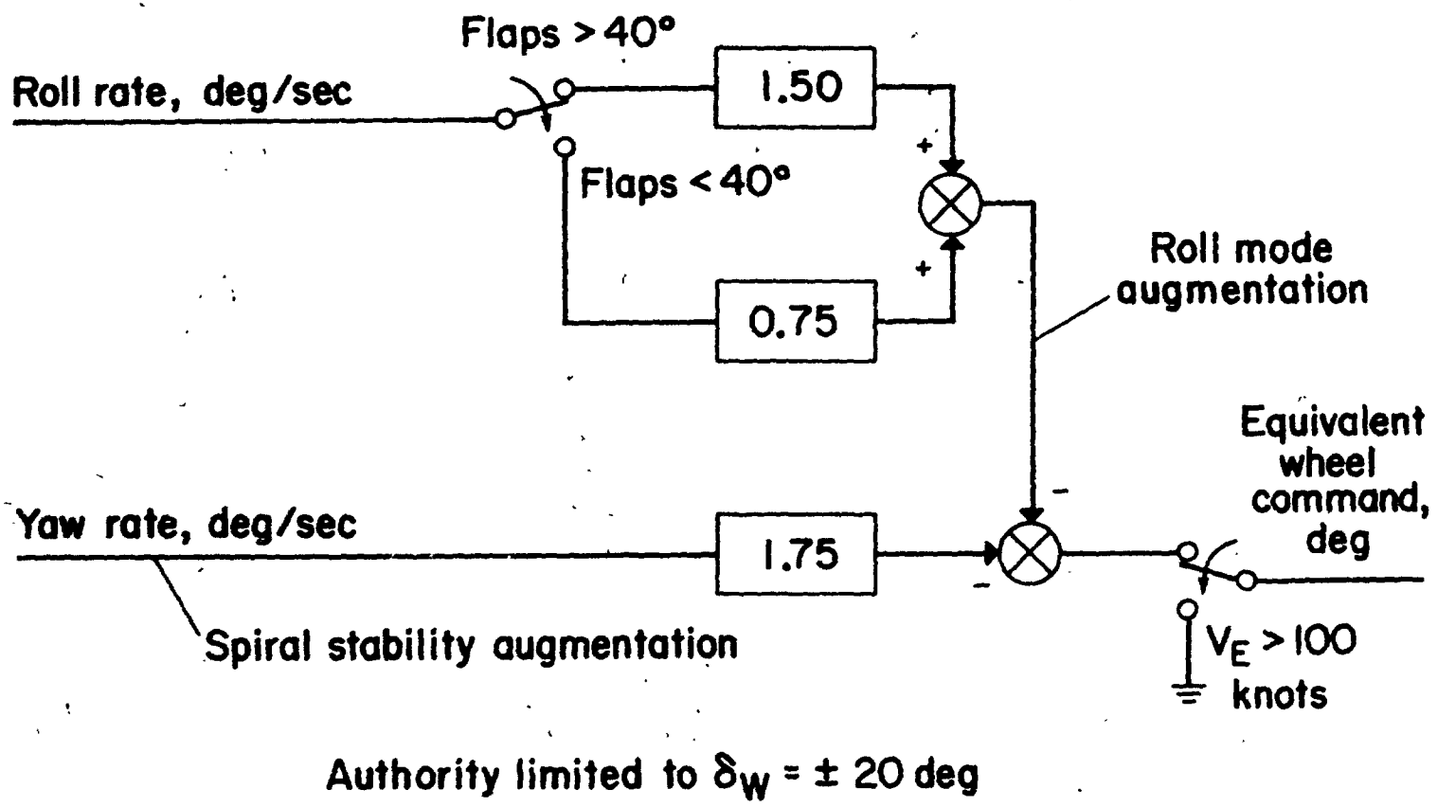

(b) Lateral axis

Figure 17.– Continued.

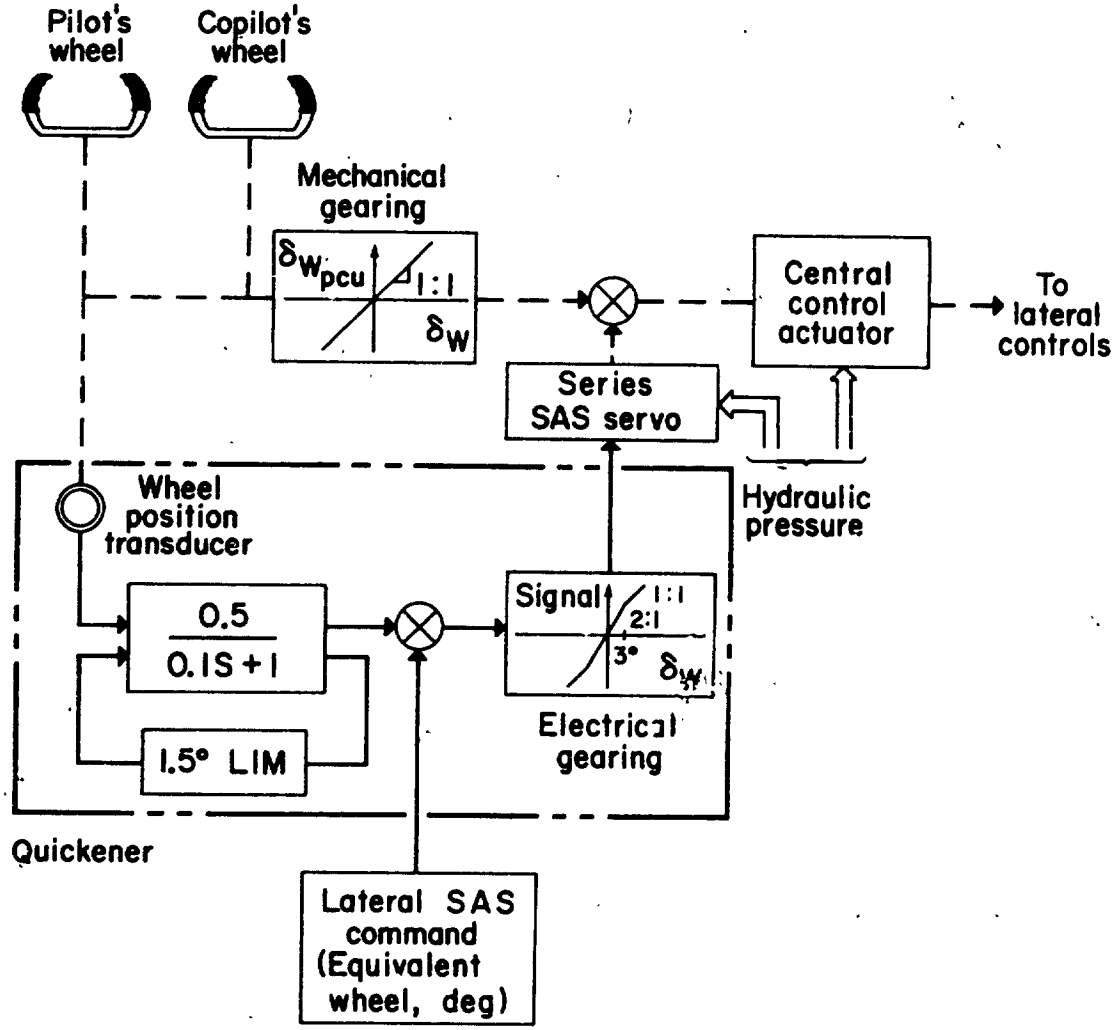

(c) Lateral control, aileron quickener

Figure 17.– Concluded.

Sym	δ_f, deg	N_H, %	Altitude, ft	Weight, lbs
○	67	95	2400 to 3500	43000 to 45000
□	33	94	4400 to 7200	42500 to 43500
◇	5.6	94	2400 to 9400	44000 to 45000

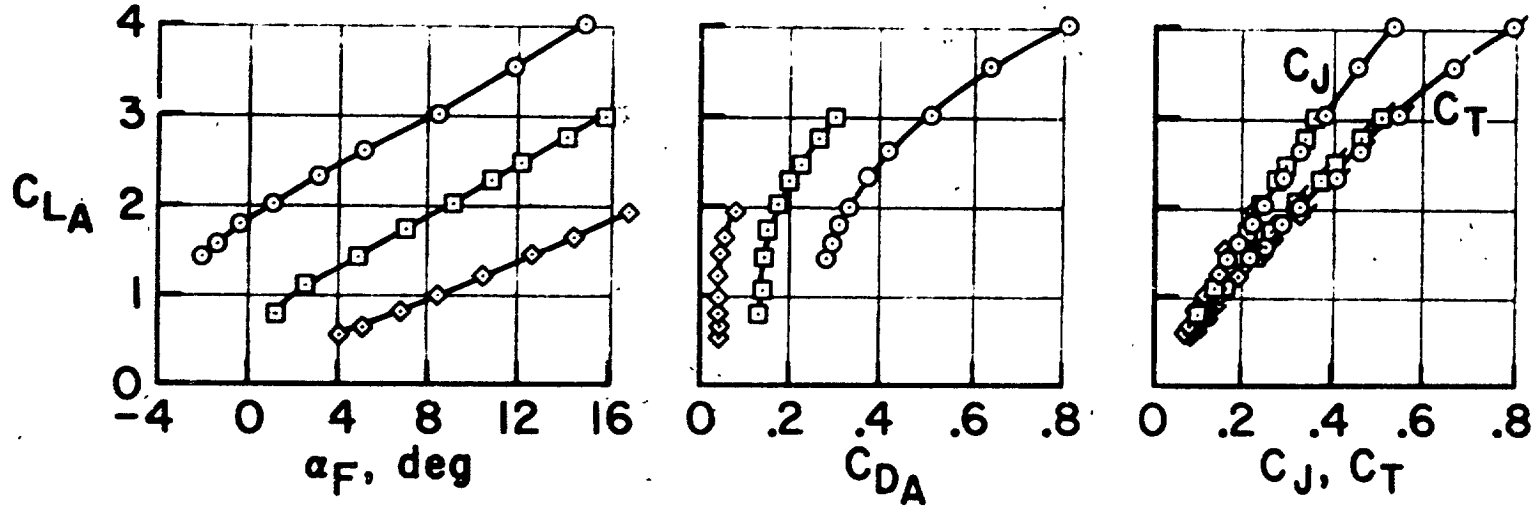

Figure 18.– Effect of flap deflection on aerodynamic characteristics. Nozzle deflection 15 degrees.

Sym	N_H, %	ν, deg	Altitude, ft	Weight, lbs
△	95	15	2400 to 3500	43000 to 45000
◇	93	10	3300 to 5200	44000 to 45000
□	90	15	2000 to 4200	41000 to 43000
○	80	7	4600 6700	43500 to 44000

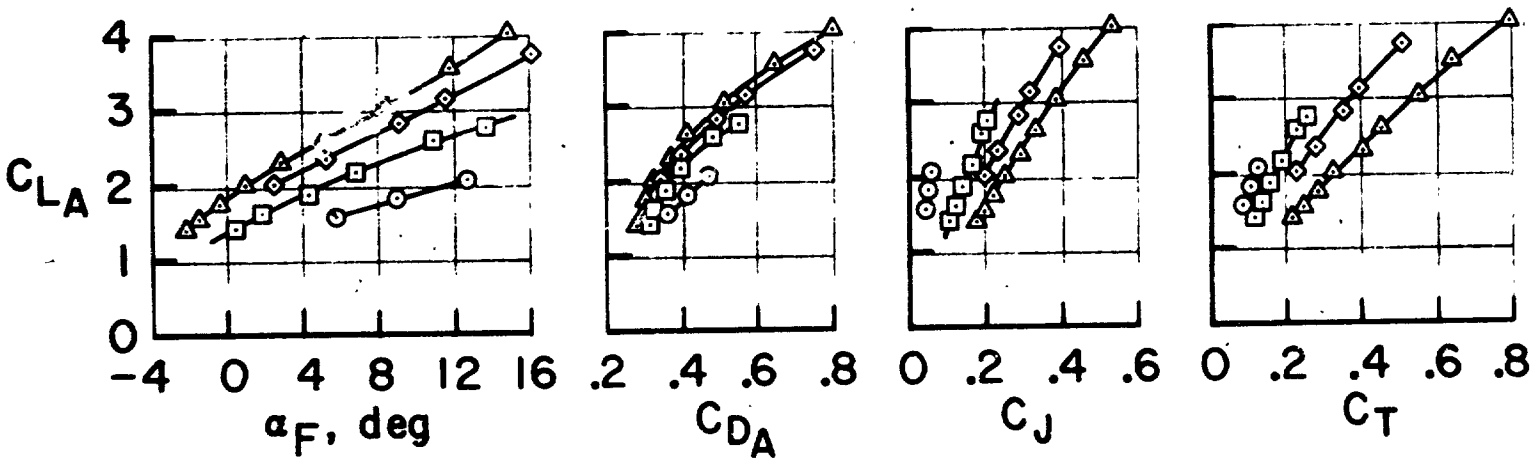

Figure 19.– Effect of engine power on aerodynamic characteristics. Flap deflection 67 degrees, nozzle deflection 15 degrees.

Sym	ν, deg	Altitude, ft	Weight, lbs
○	15	2400 to 3500	43000 to 45000
□	35	2600 to 3700	42000 to 43000
△	88	2100 to 3600	44000 to 45000

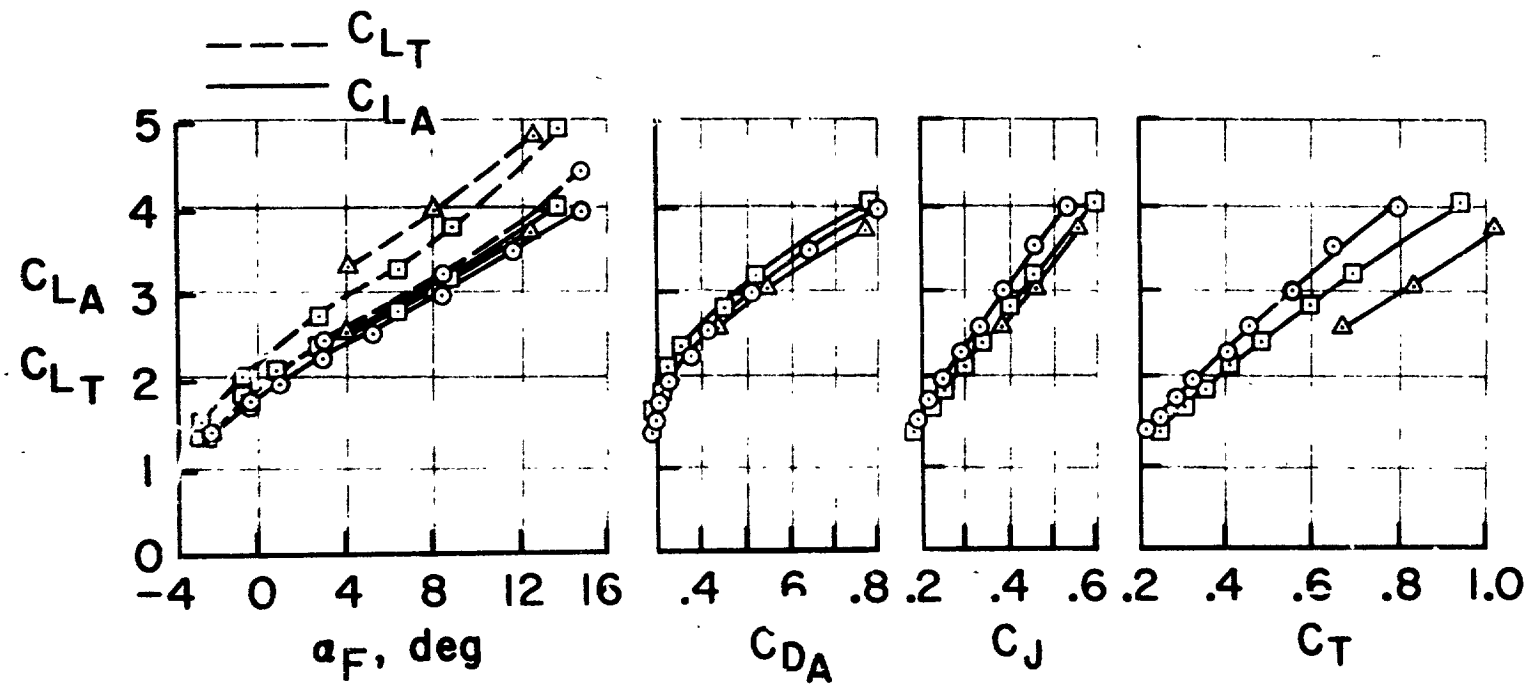

Figure 20.– Effect of engine nozzle deflection on aerodynamic characteristics. Flaps 67 degrees, engine *rpm* 95% N_H.

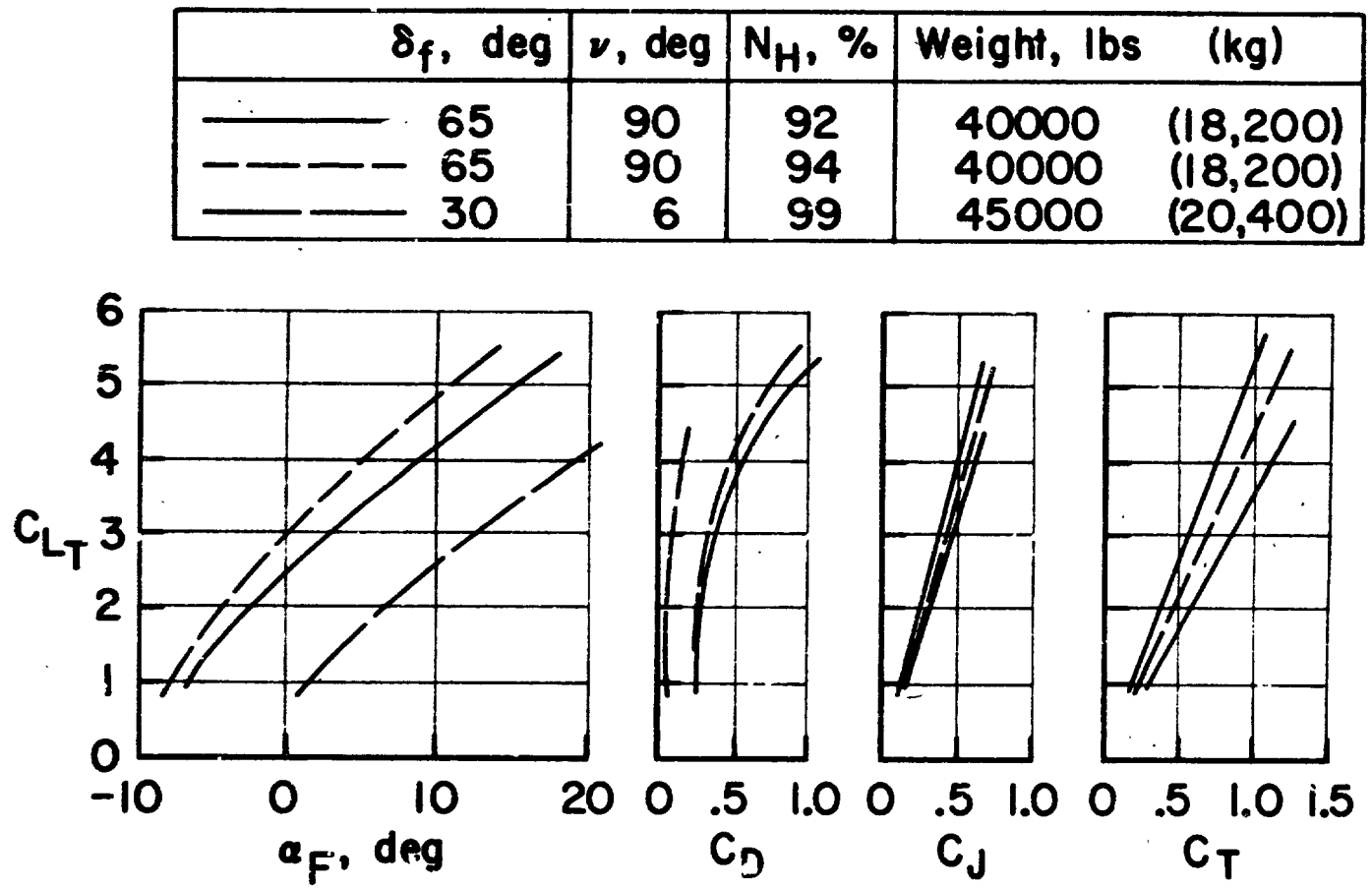

Figure 21.– Landing and takeoff aerodynamic characteristics, constant engine *rpm*, sea level standard conditions.

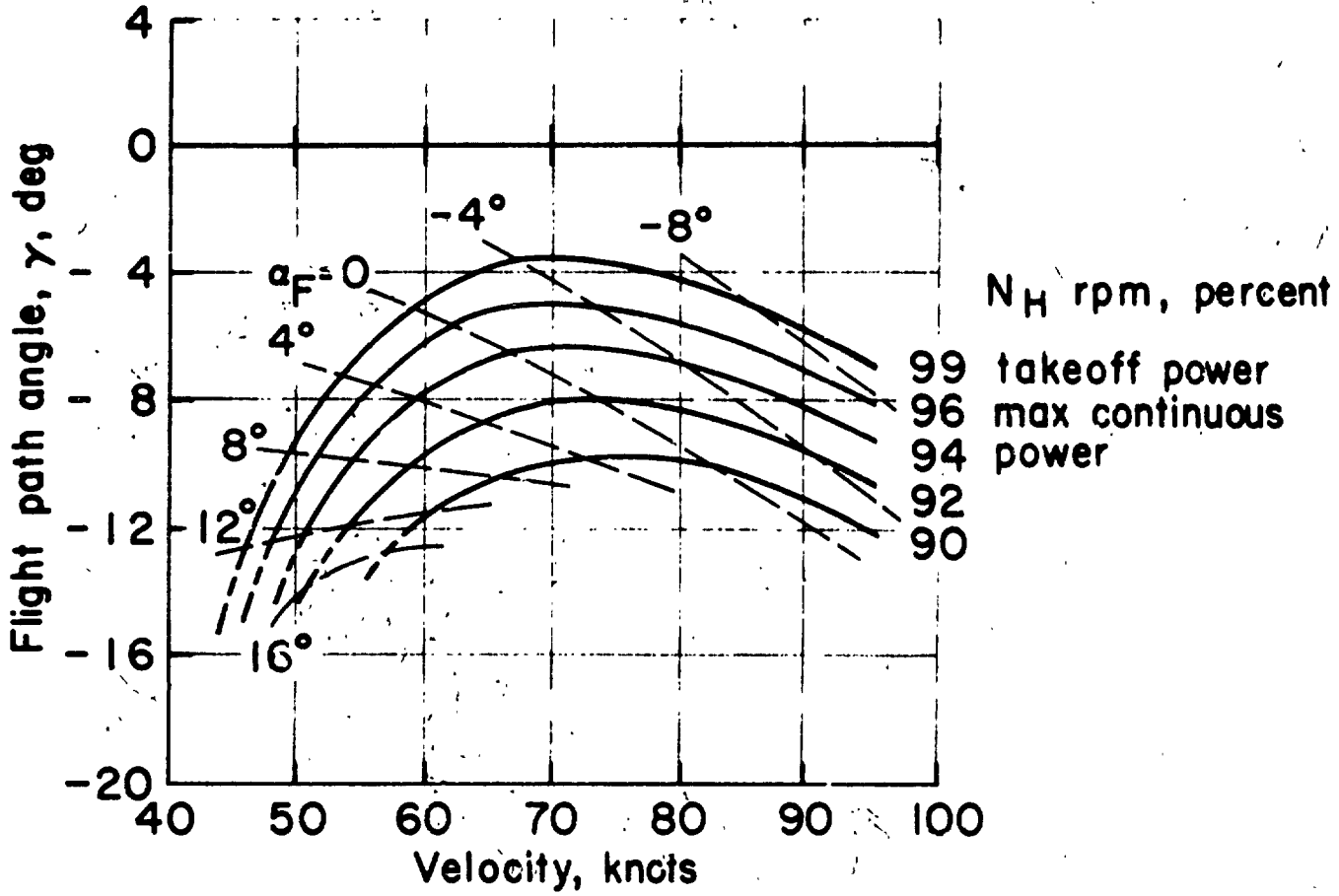

Figure 22.– Effect of engine *rpm* on landing operational envelope. $\delta_f = 65°$. $\nu = 90°$. Weight = 40,000 lb (18,200 kg). Sea level standard day.

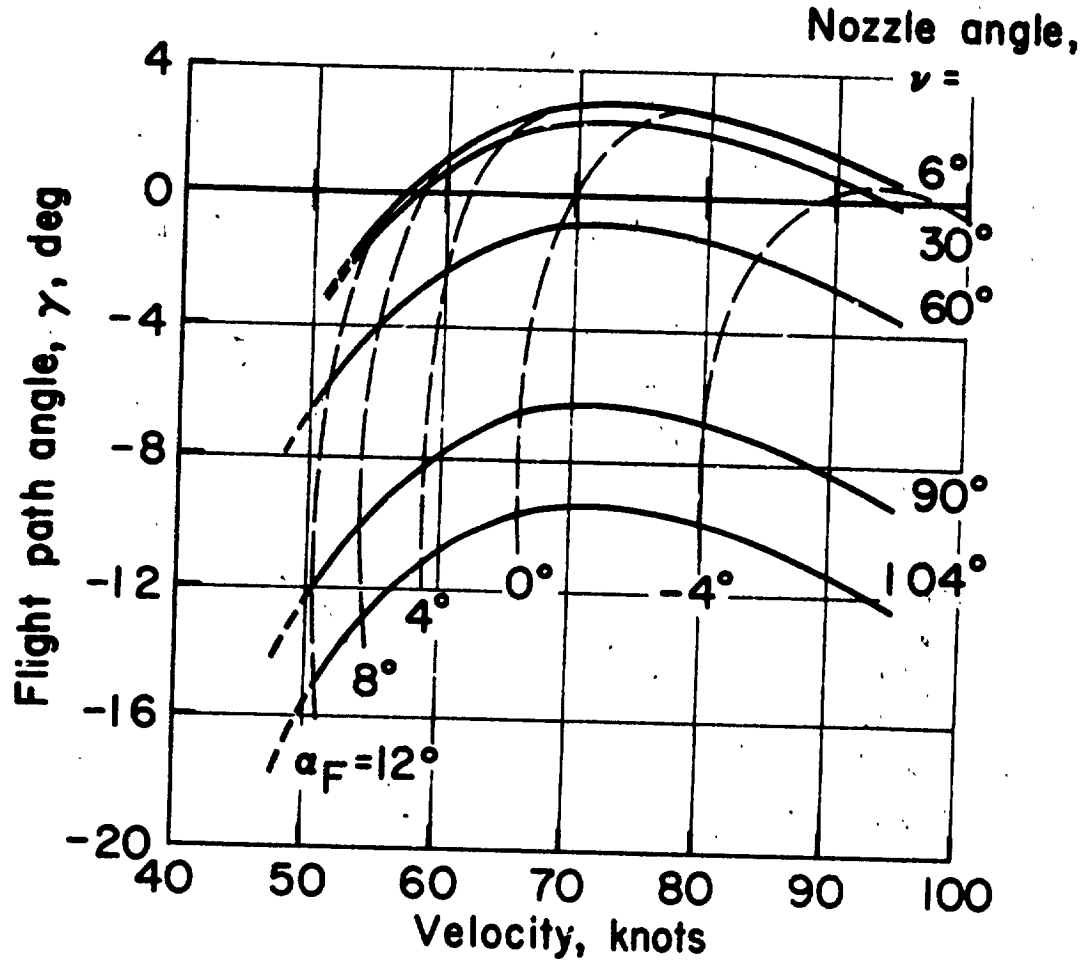

Figure 23.– Effect of nozzle angle on landing operational envelope. $\delta_f = 65°$. $N_H = 94\%$. Weight = 40,000 lb (18,200 kg). Sea level standard day.

Sym	Altitude, ft	(meters)	Weight, lbs	(kilograms)
○ ●	3000 – 4000	(900 – 1200)	39,300 – 40,700	(17,900 – 18,500)
△ ▲	3000 – 5300	(900 – 1600)	41,000 – 42,900	(18,600 – 19,500)
□ ■	1600 – 3100	(500 – 900)	37,900 – 38,500	(17,300 – 17,500)
◿ ◢	2400 – 3300	(700 – 1000)	43,900 – 44,600	(20,000 – 20,300)
◇ ◆	500 – 7900	(200 – 2400)	39,100 – 42,600	(17,800 – 19,400)

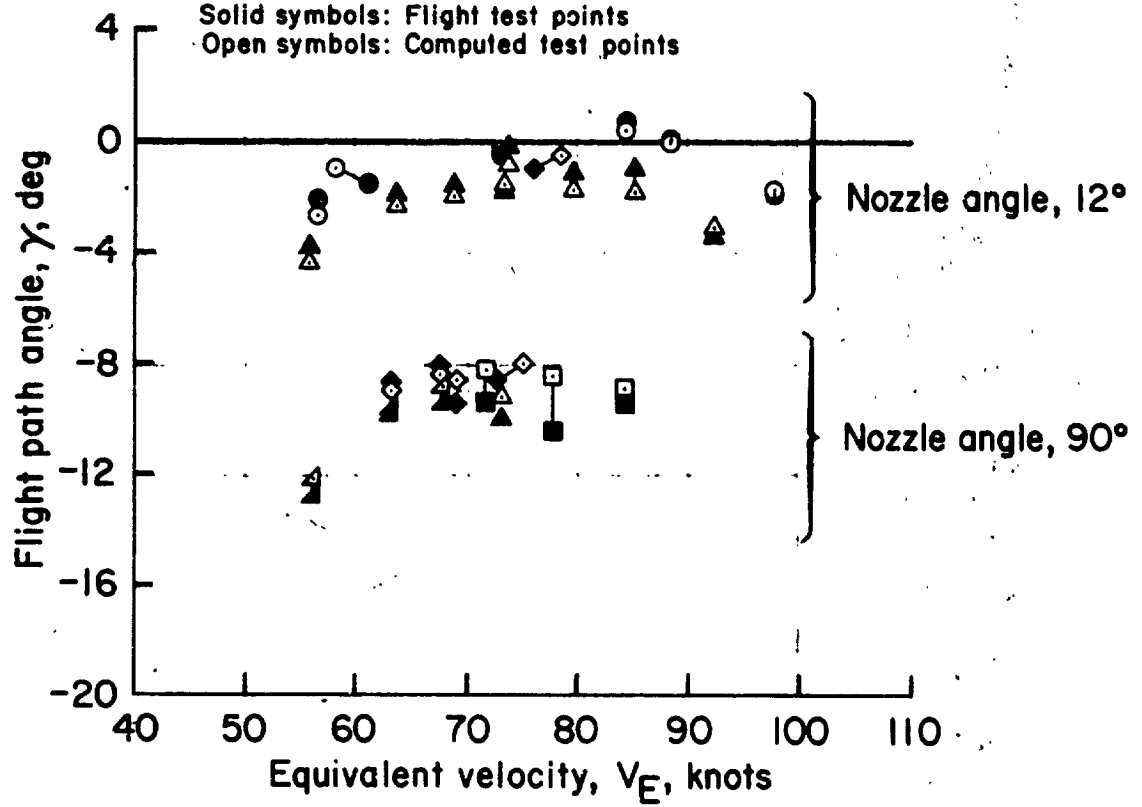

Figure 24.- Comparison of measured and computed flight path angles. $\delta_f \approx 65°$. Various gross weights, altitudes, and engine power settings.

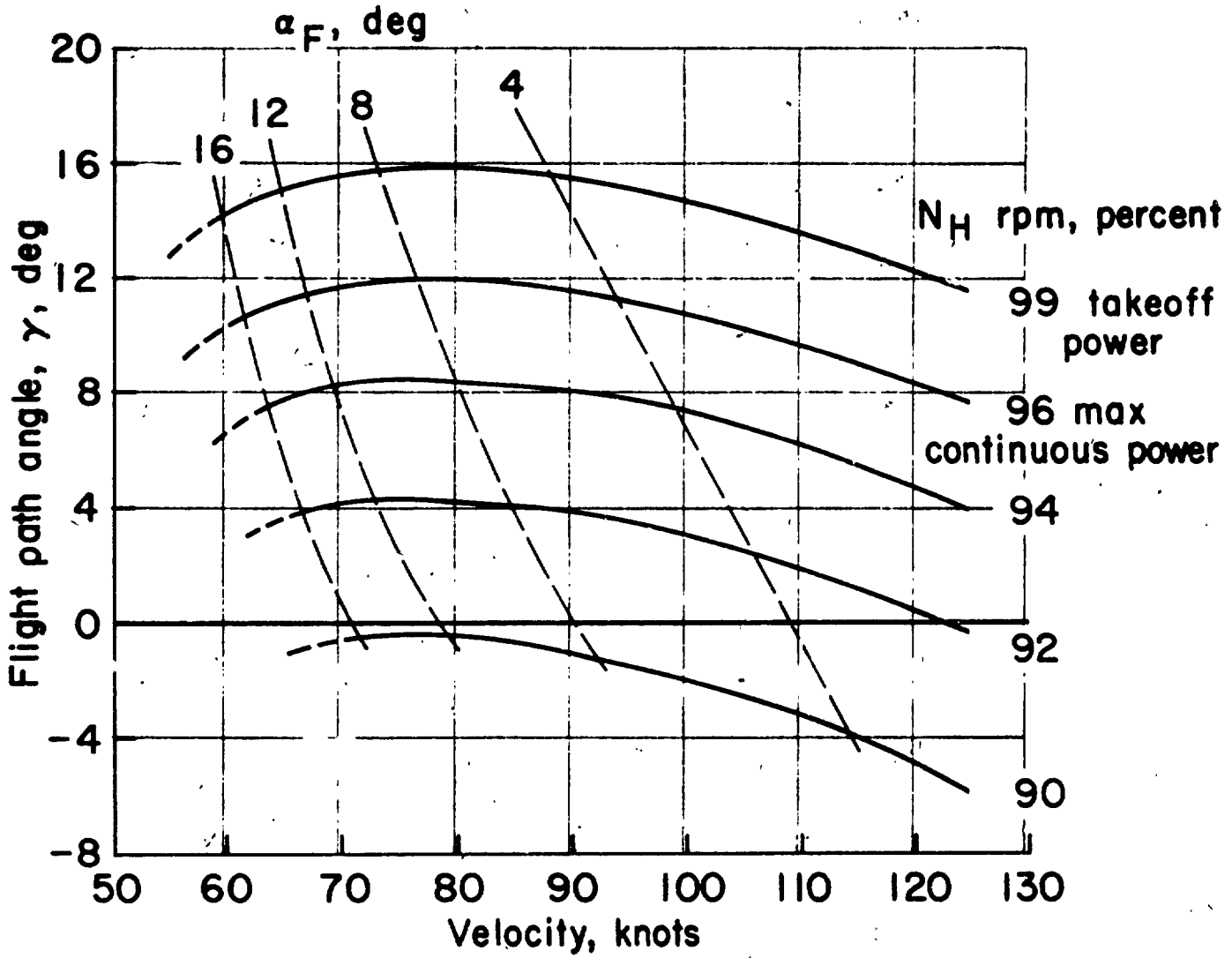

(a) Weight = 40,000 lb (18,200 kg)

Figure 25.– Effect of engine *rpm* on takeoff operational envelope. $\delta_f = 30°$. $\nu = 6°$. Sea level standard day.

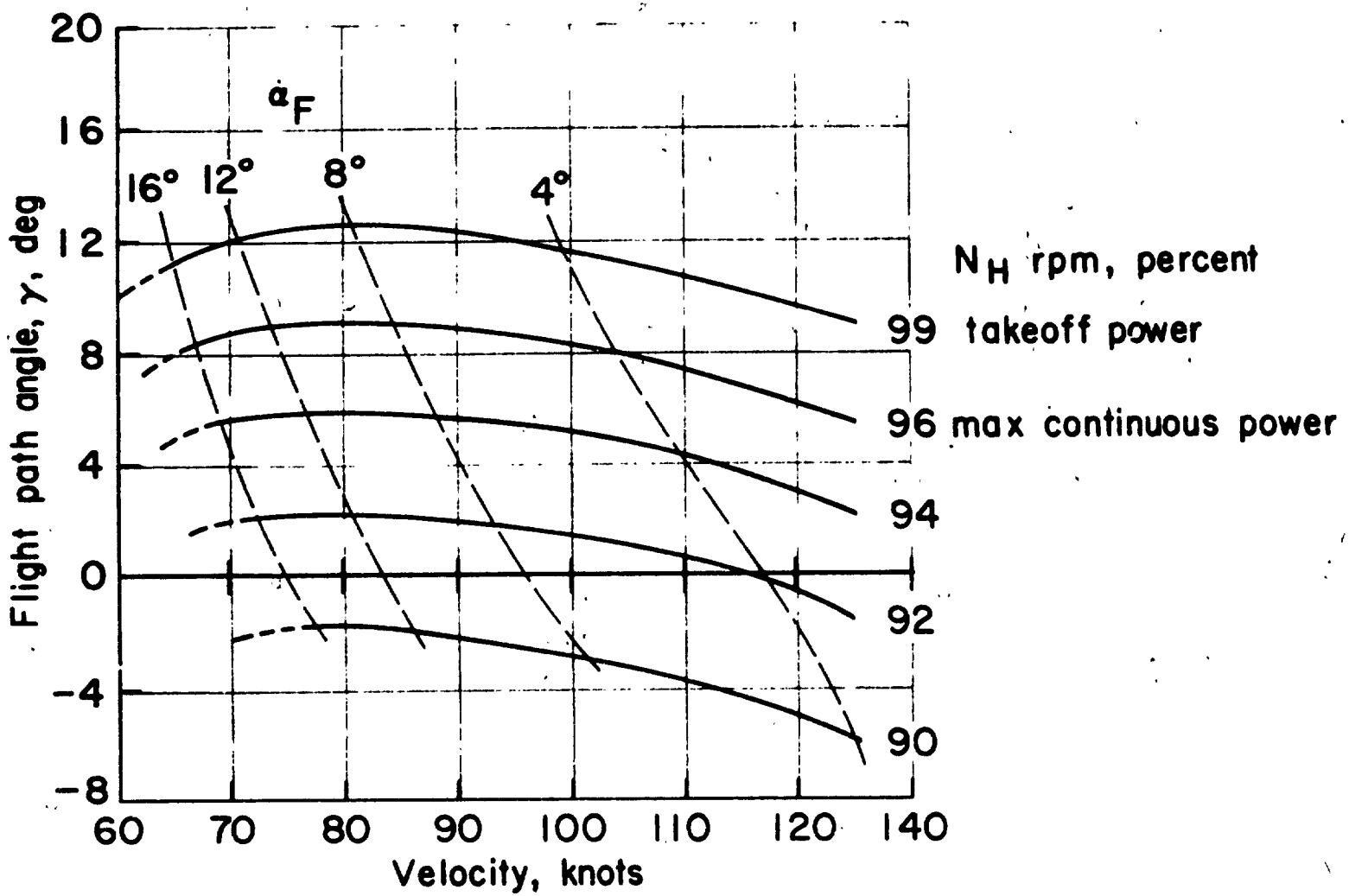

(b) Weight = 45,000 lb (20,400 kg)

Figure 25.– Concluded.

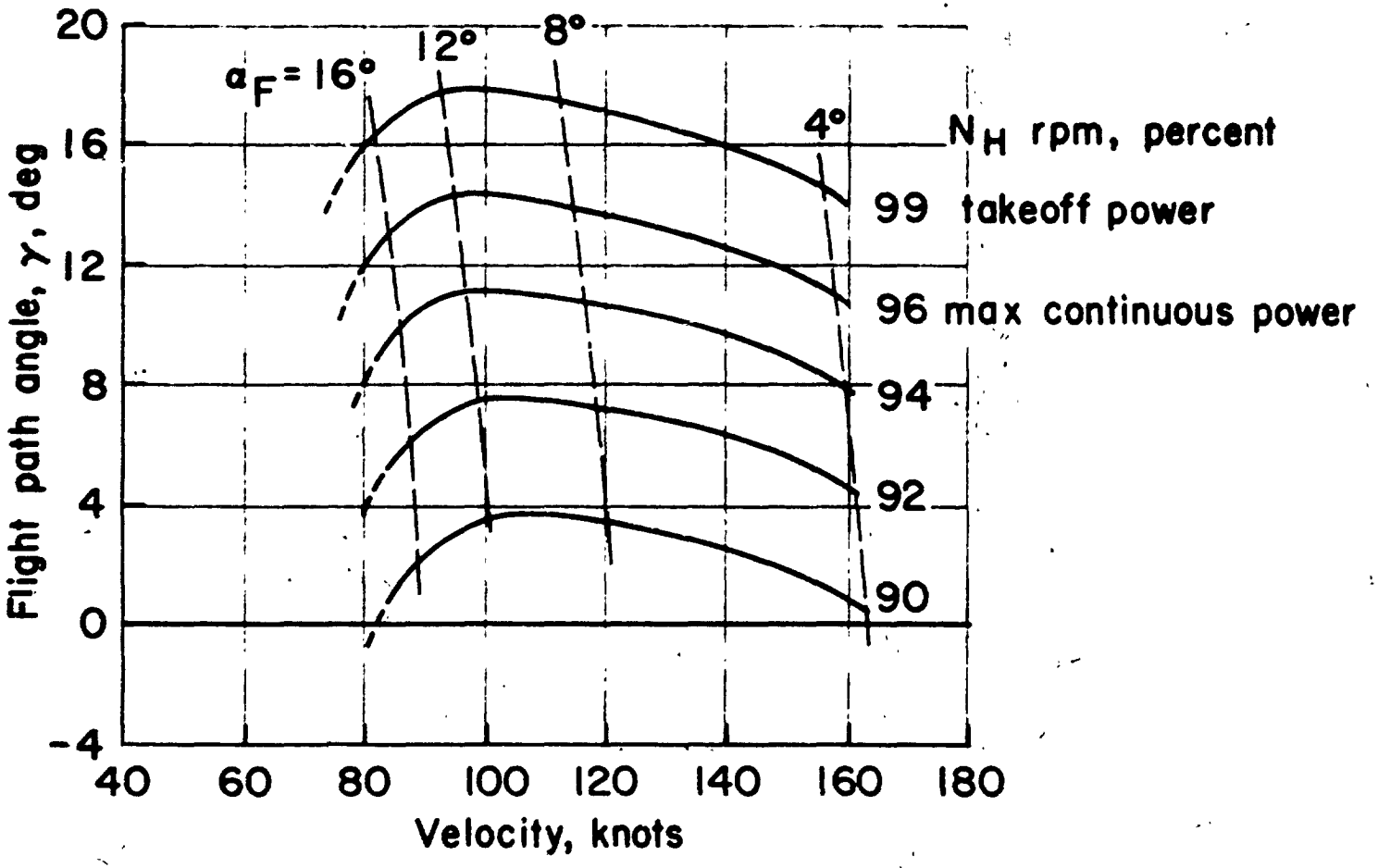

(a) Weight = 40,000 lb (18,200 kg)

Figure 26.– Effect of engine *rpm* on takeoff operational envelope. $\delta_f = 5.6°$. $\nu = 6°$. Sea level standard day.

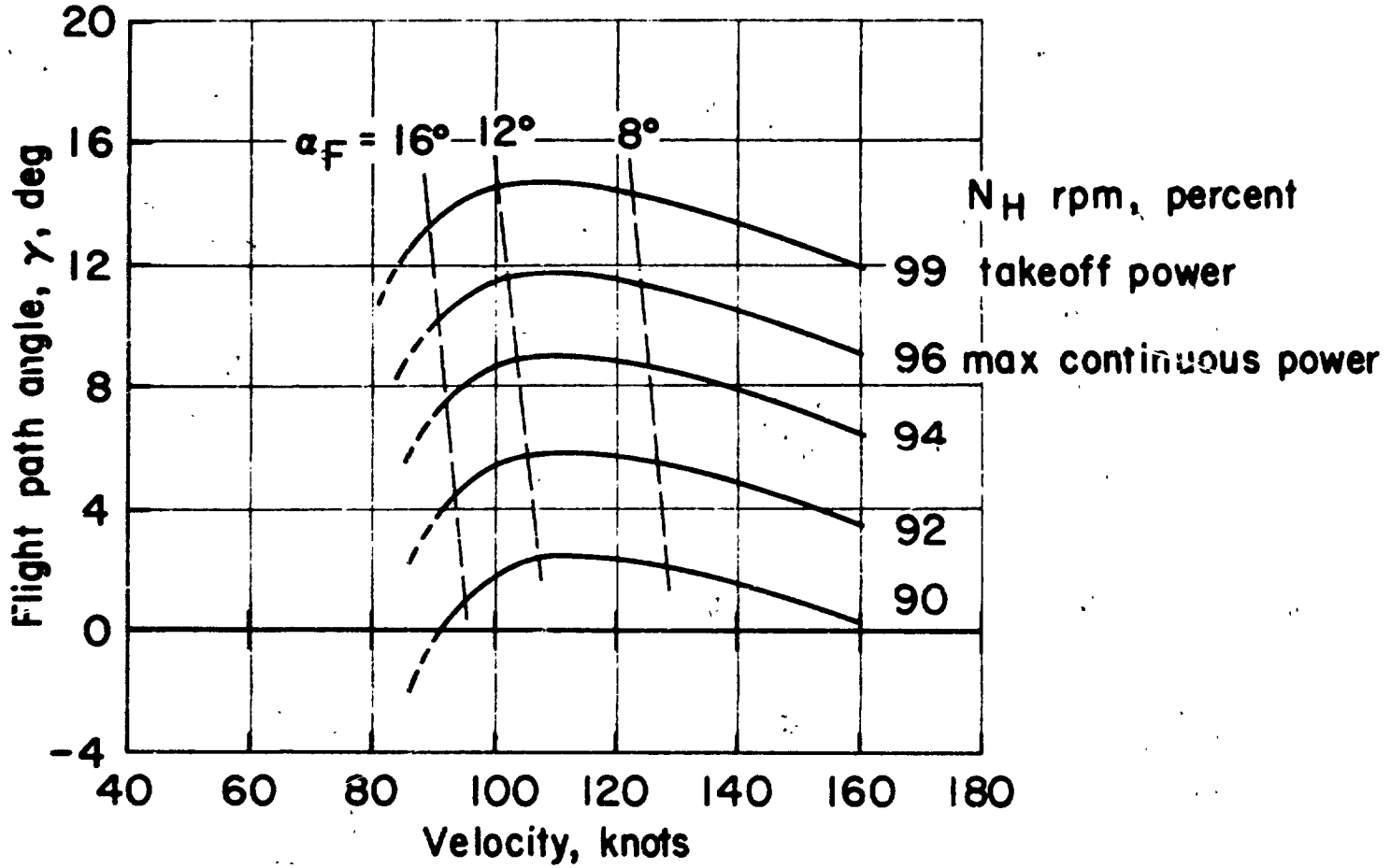

(b) Weight = 45,000 lb (20,400 kg)

Figure 26.– Concluded.

Sym	Altitude, ft	(meters)	Weight, lbs	(kilograms)
○ ●	100 – 3700	(0 – 100)	41,300 – 45,300	(18,700 – 20,600)
△ ▲	200 – 800	(100 – 200)	41,800 – 41,900	(18,900 – 19,000)
□ ■	300 – 700	(100 – 200)	39,200 – 44,500	(17,800 – 20,200)
◿ ◢	2700 – 5100	(800 – 1600)	44,200 – 45,500	(20,100 – 20,700)
◇ ◆	5500 – 8700	(1700 – 2600)	39,800 – 43,700	(18,000 – 19,800)

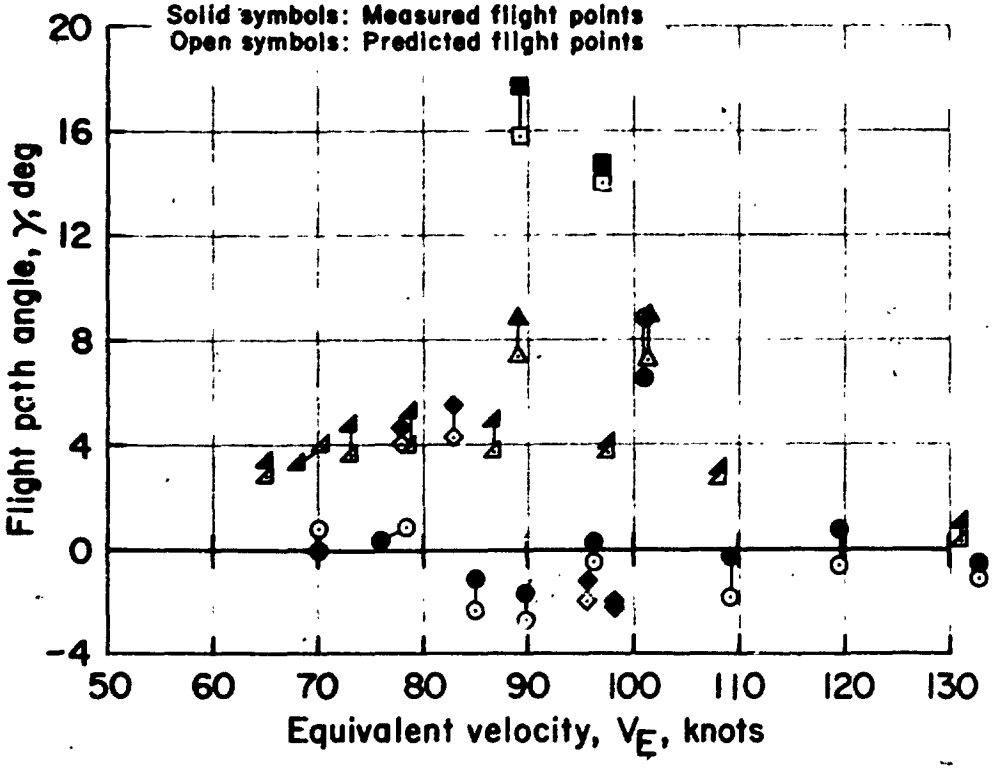

(a) $\delta_f \approx 30°$.

Figure 27.– Comparison of measured and computed flight path angles Various airplane weights, altitudes and engine power settings.

Sym	Altitude, ft (meters)	Weight, lbs (kilograms)
○ ●	3000 – 3500 (900 – 1100)	43,300 – 44,500 (19,600 – 20,200)
△ ▲	2500 – 9300 (800 – 2800)	41,100 – 44,900 (18,700 – 20,400)
□ ■	3000 – 3200 (900 – 1000)	37,600 – 38,400 (17,100 – 17,500)

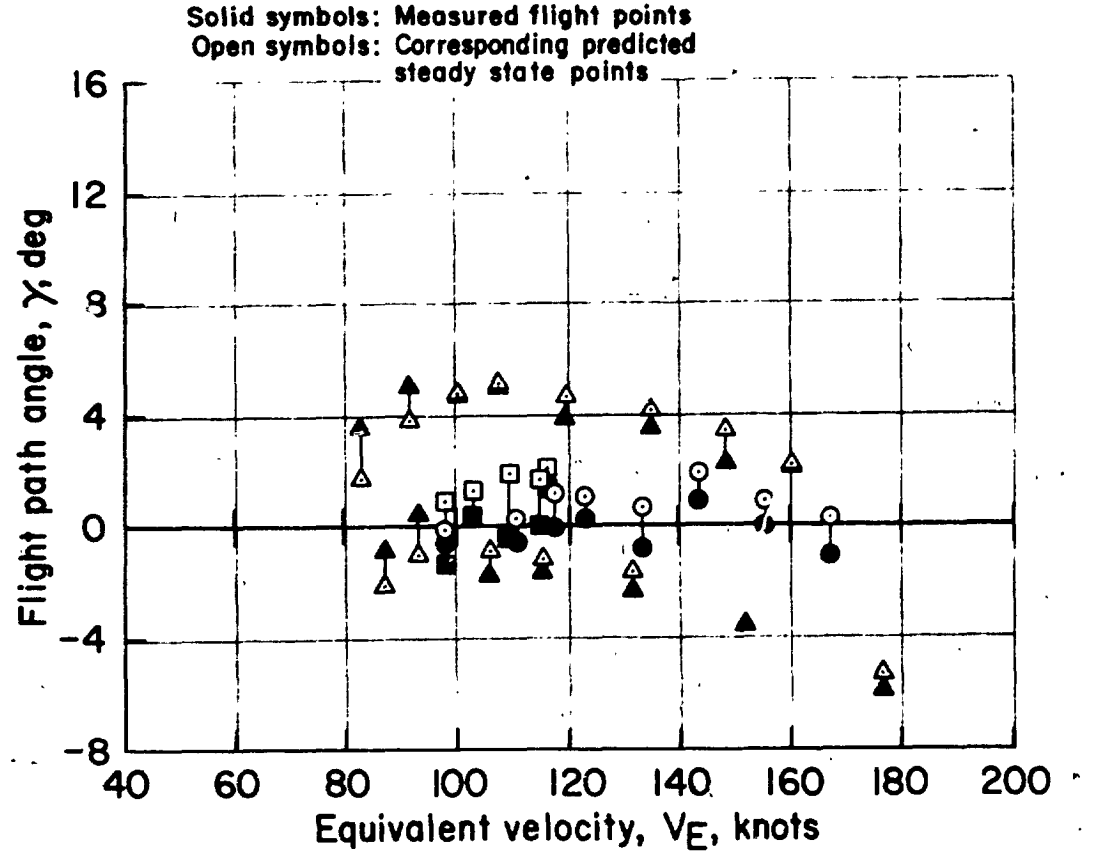

(b) $\delta_f \approx 5.6°$.

Figure 27.– Concluded.

○	$C_{L_A} = 2.3 (C_{L_T} \approx 2.95)$	Derived from analysis of
□	$C_{L_A} = 3.0 (C_{L_T} = 3.65)$	discrete test conditions

Note: Fairings based on parameter identification of entire data collected in four approaches ($C_{L_A} = 2.65$)

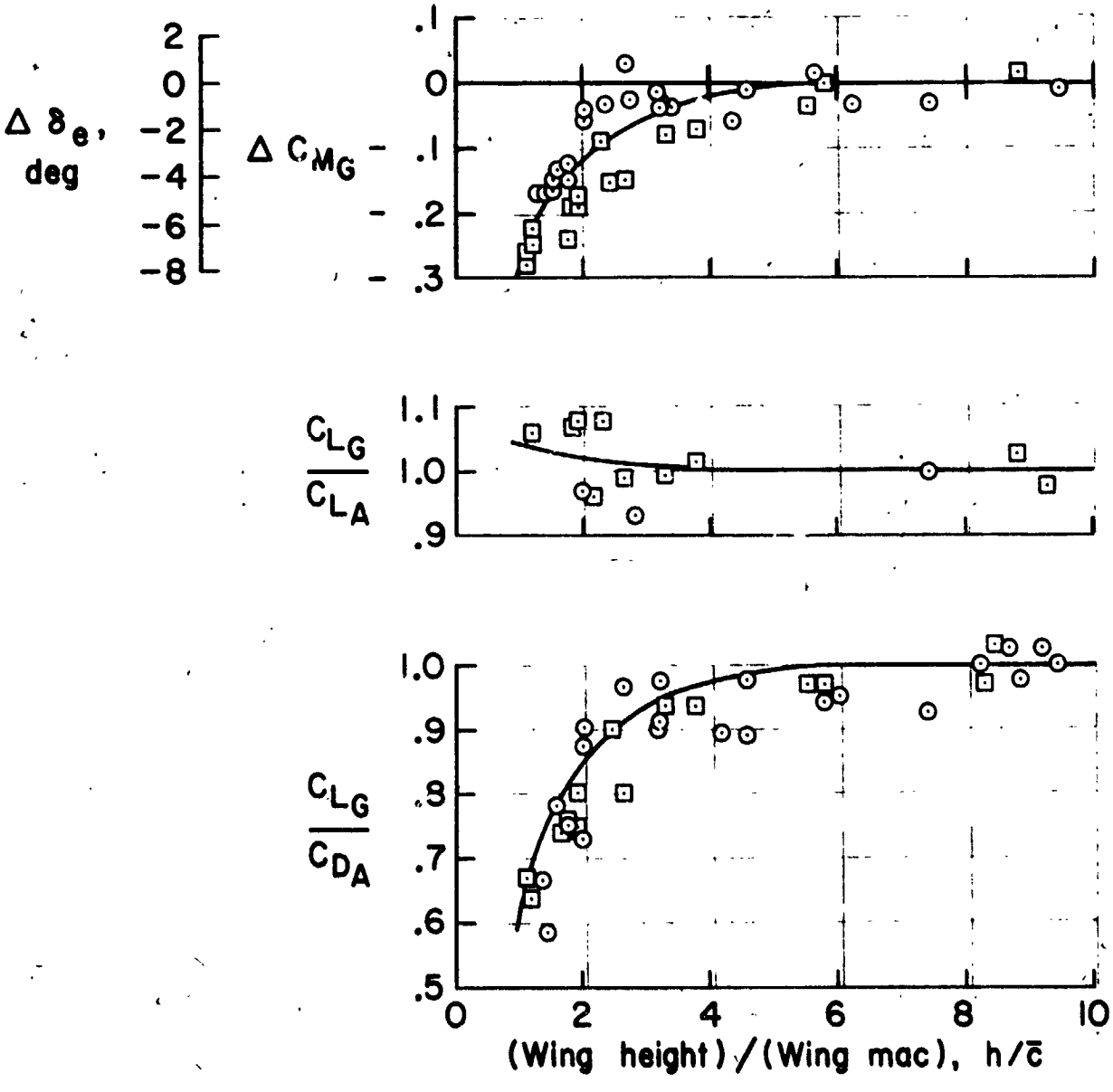

Figure 28.– Ground effect derived from flight test data. $\delta_f = 65°$. $\nu = 50°$ to $80°$. $N_H = 93$ to 96% *rpm*. $V_E = 60$ to 70 knots.

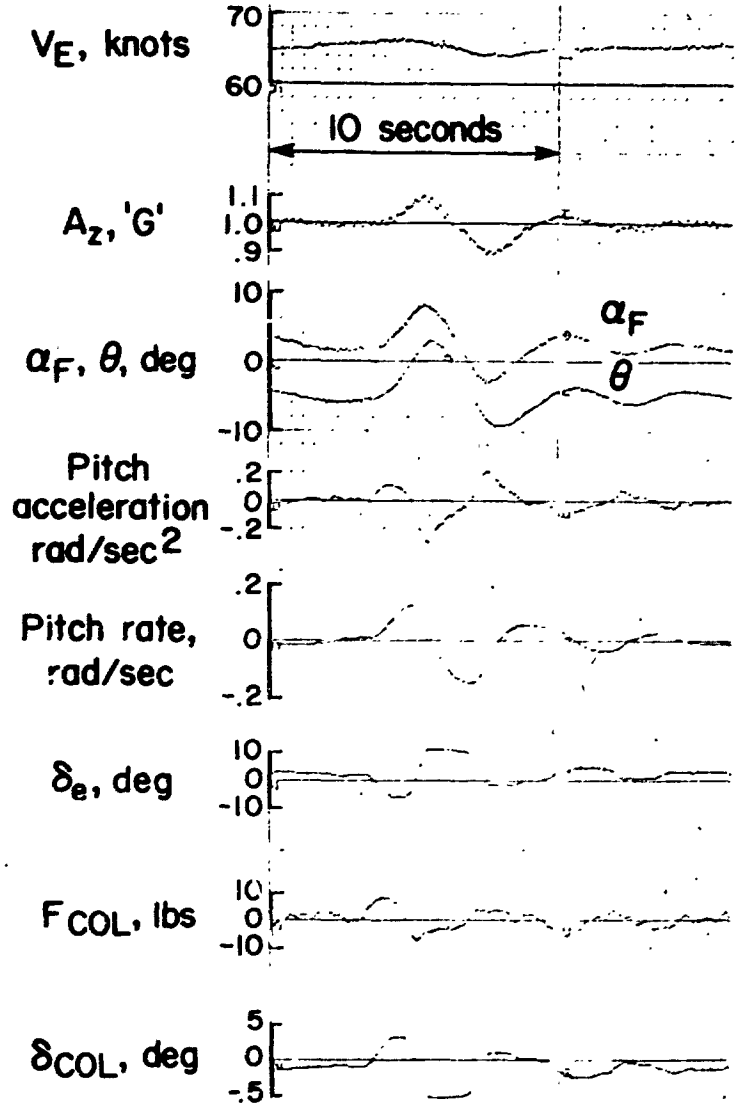

Figure 29. Elevator reversal flap 67°, nozzles 87°

Sym	δ_f, deg	ν, deg	N_H%	Weight, lbs	(kilograms)	V_E knots
● ◐ ○	67	15	94	41,300	(18,700)	See code
◧ □	67	88	95	40,700	(18,500)	
◇	33	13	95.7	42,800	(19,400)	75–82
◈	33	13	90.5	40,000	(18,200)	78
△	6	13	90	44,900	(20,400)	165
▲	6	13	88	39,600	(18,000)	137

δ_F = 67° data: Shaded, 57–59 knots; Half shaded, 60–64 knots, Unshaded, 65–69 knots

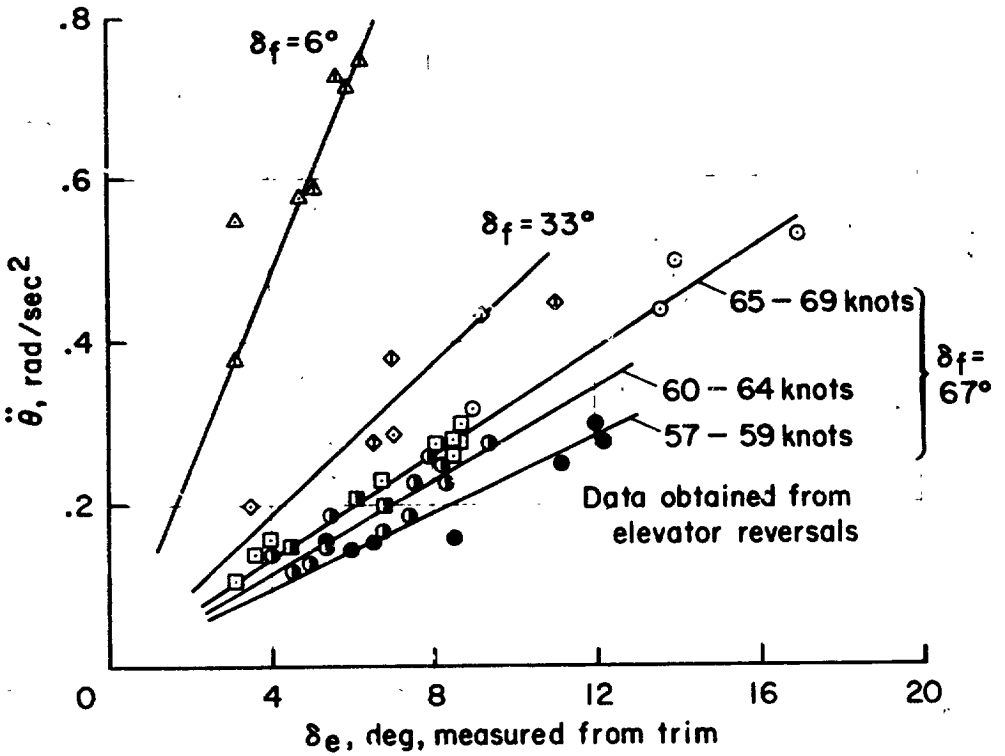

Figure 30.– Elevator effectiveness.

Sym	δ_f, deg	ν, deg	N_H%	Weight, lbs	(kilograms)	V_E knots
● ◐ ○	67	15	94	41,300	(18,700)	(See code)
■ □	67	88	95	40,700	(18,500)	
◇	33	13	95.7	42,800	(19,400)	75–82
◈	33	13	90.5	40,000	(18,200)	78
△	6	13	90	44,900	(20,400)	165
▲	6	13	88	39,600	(18,000)	137

δ_f = 67° data: Shaded, 57–59 knots; Half shaded, 60–64 knots; Unshaded, 65–69 knots

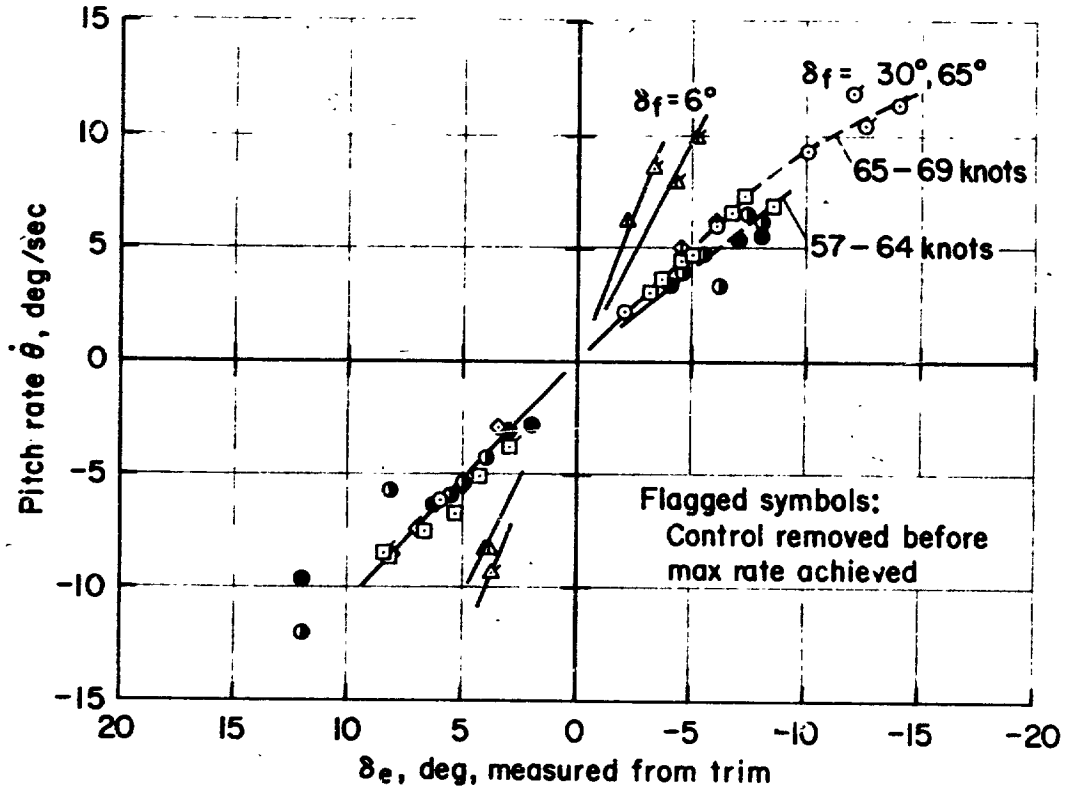

Figure 31.– Maximum pitch rate achieved in elevator reversal maneuvers.

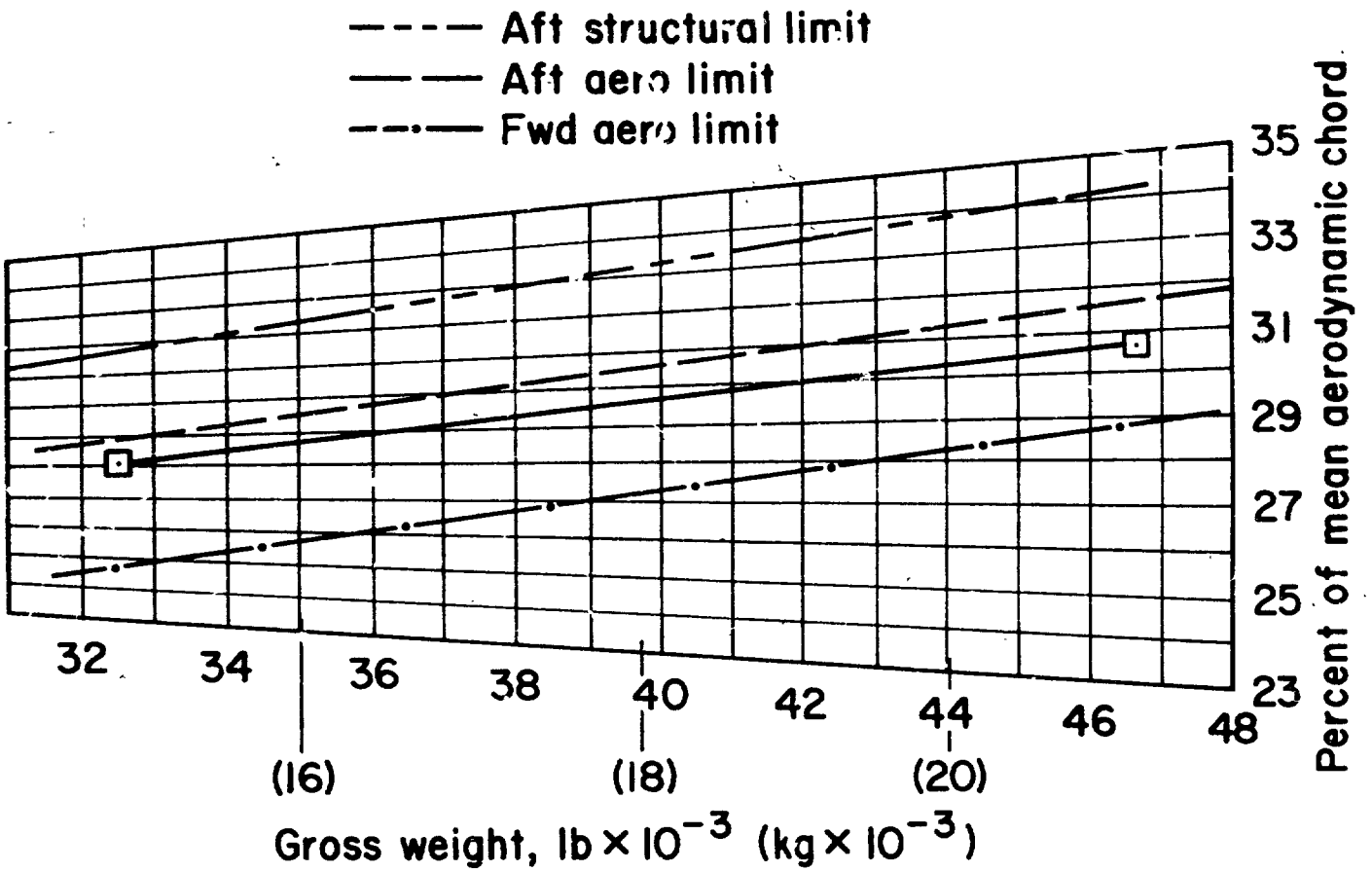

Figure 32.– Variation in center of gravity location with gross weight. Gross weight changes with fuel (JP-5) only.

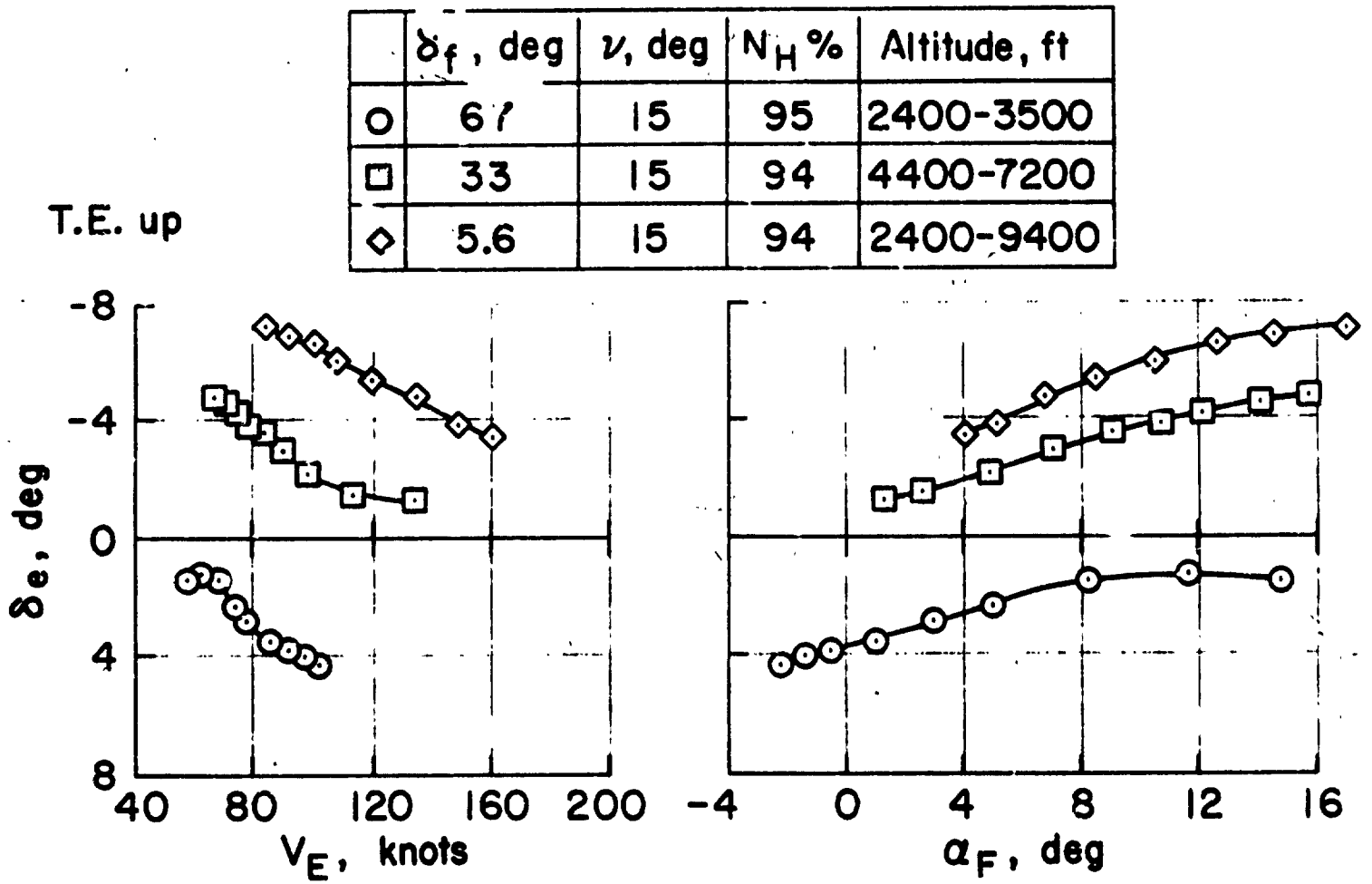

Figure 33.– Elevator-to-trim variation with flap position.

	δ_f, deg	ν, deg	N_H %	Altitude, ft
○	67	15	95	2400-3500
□	67	35	95	2600-3700
◇	67	88	95	2100-3500

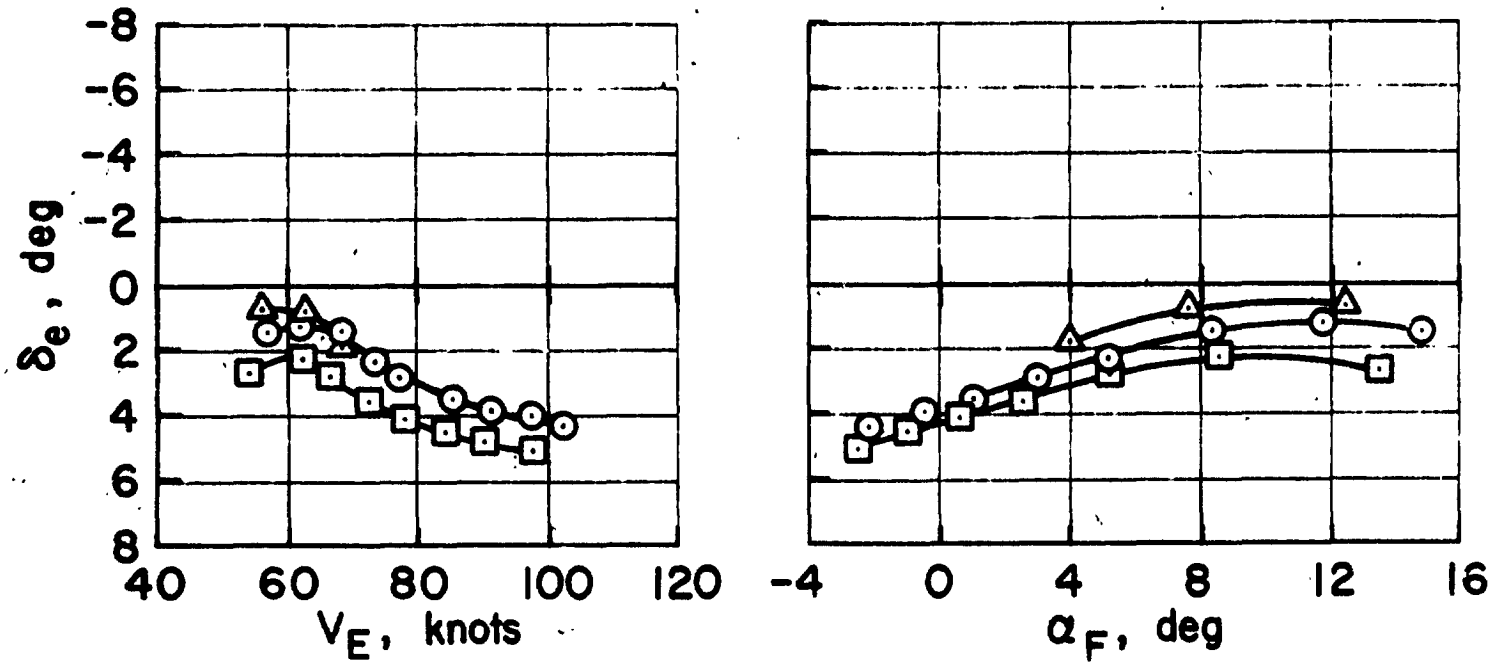

Figure 34.– Elevator-to-trim variation with nozzle position, flaps 65°.

Sym	δ_f, deg	ν, deg	N_H %	Altitude, ft
○	67	7	80	4600-6700
□	67	15	90	2100-3500
◇	67	10	93	3300-5200
△	67	15	95	2400-3500

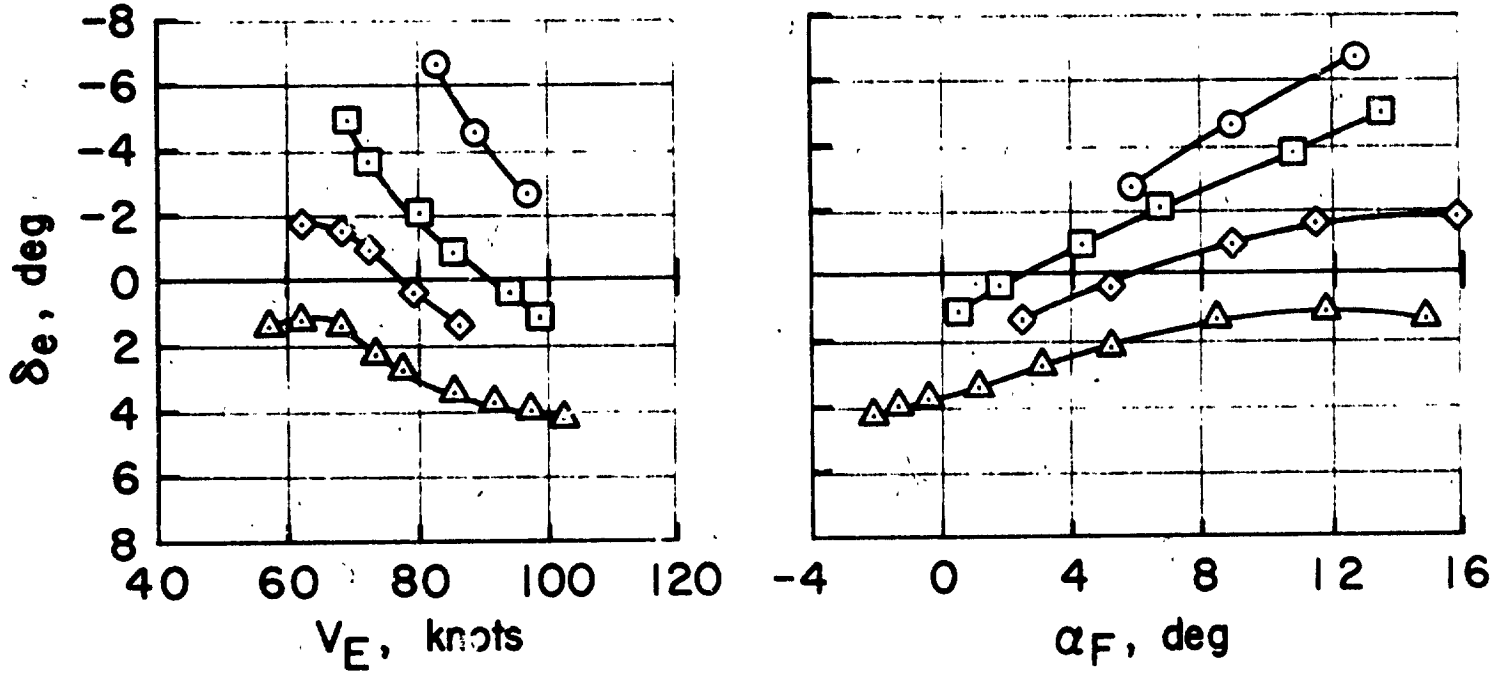

Figure 35.– Elevator-to-trim variation with power setting, flaps 65°

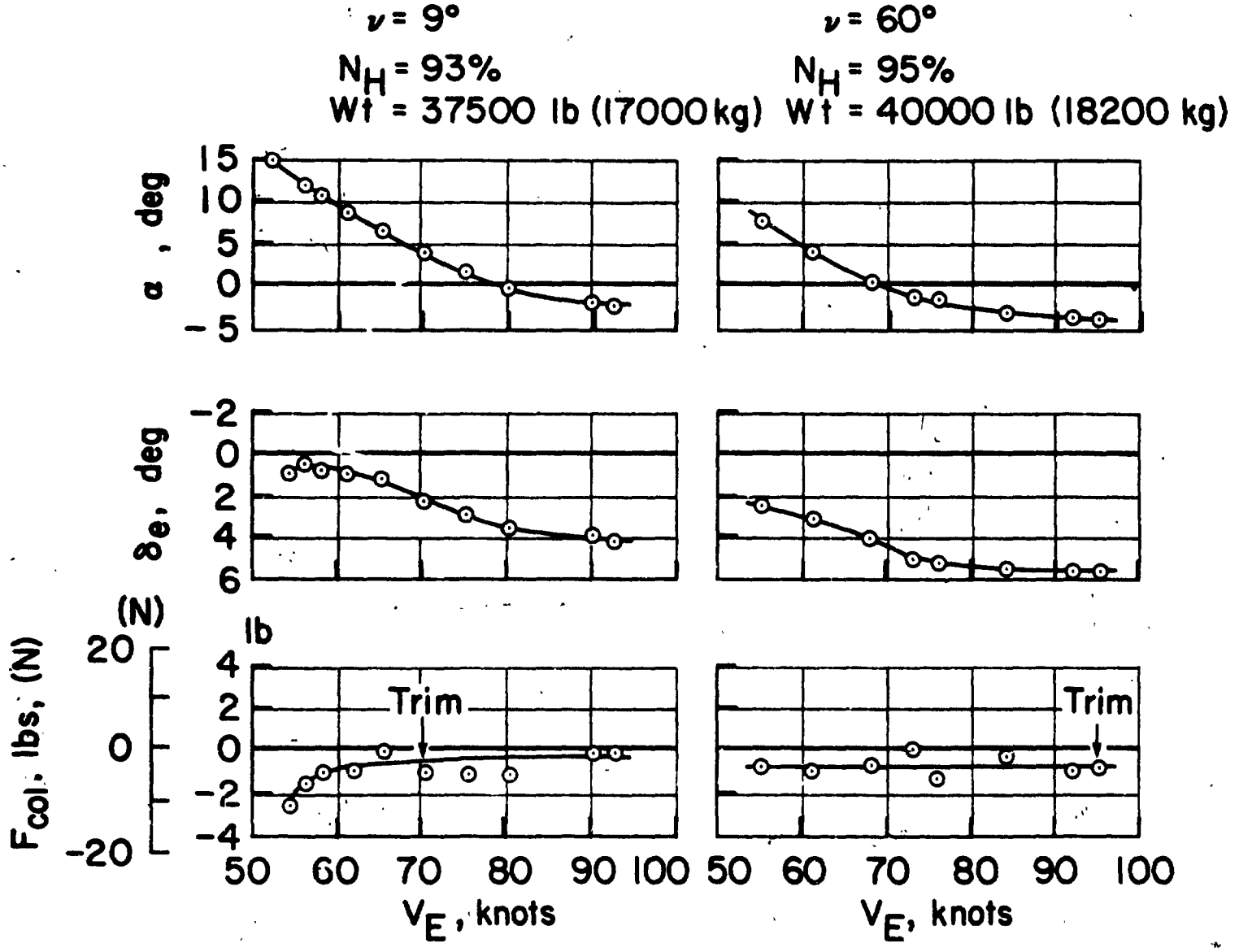

Figure 36.– Longitudinal trim, 67° flaps.

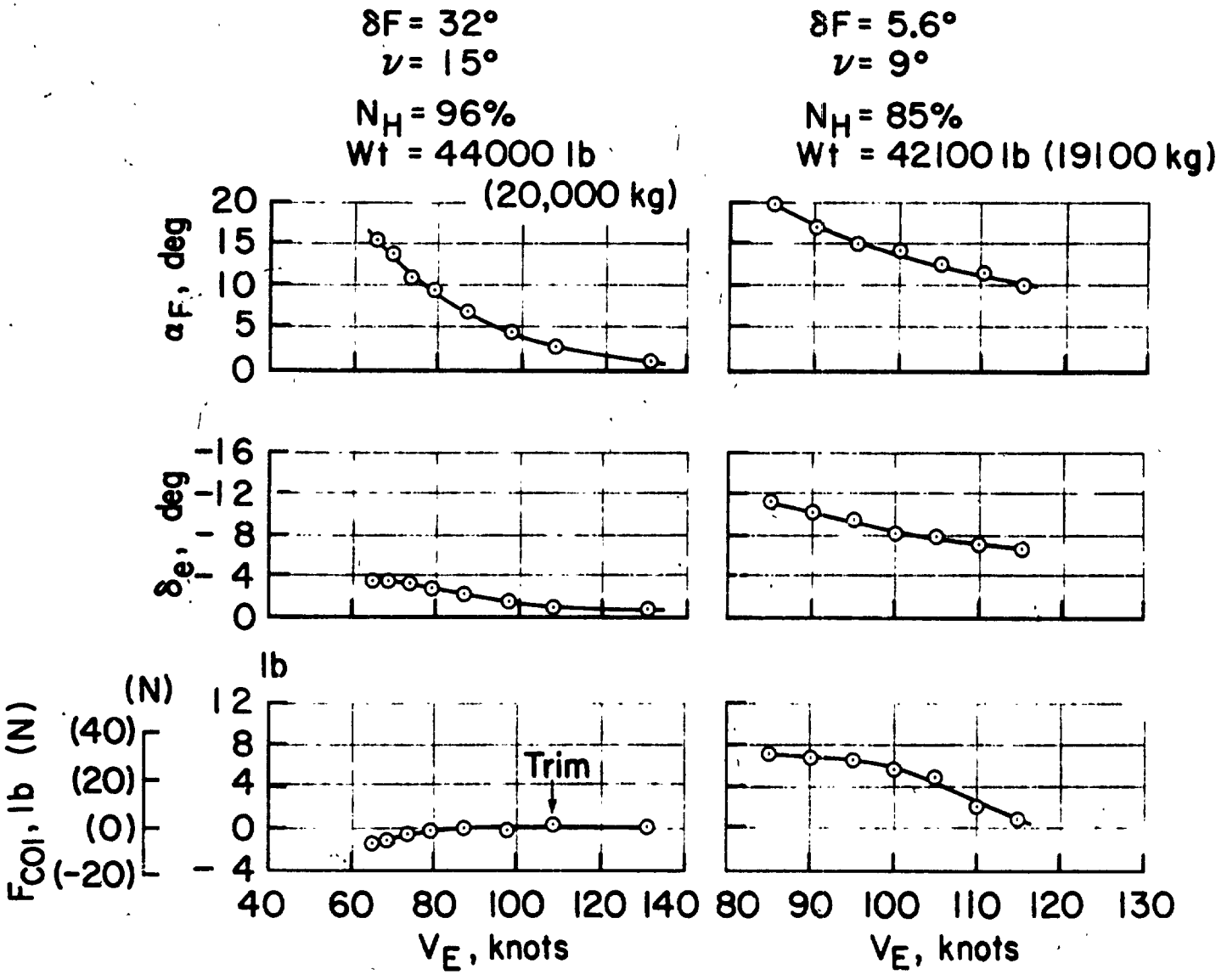

Figure 37.– Longitudinal trim, flaps 32°, 5.6°.

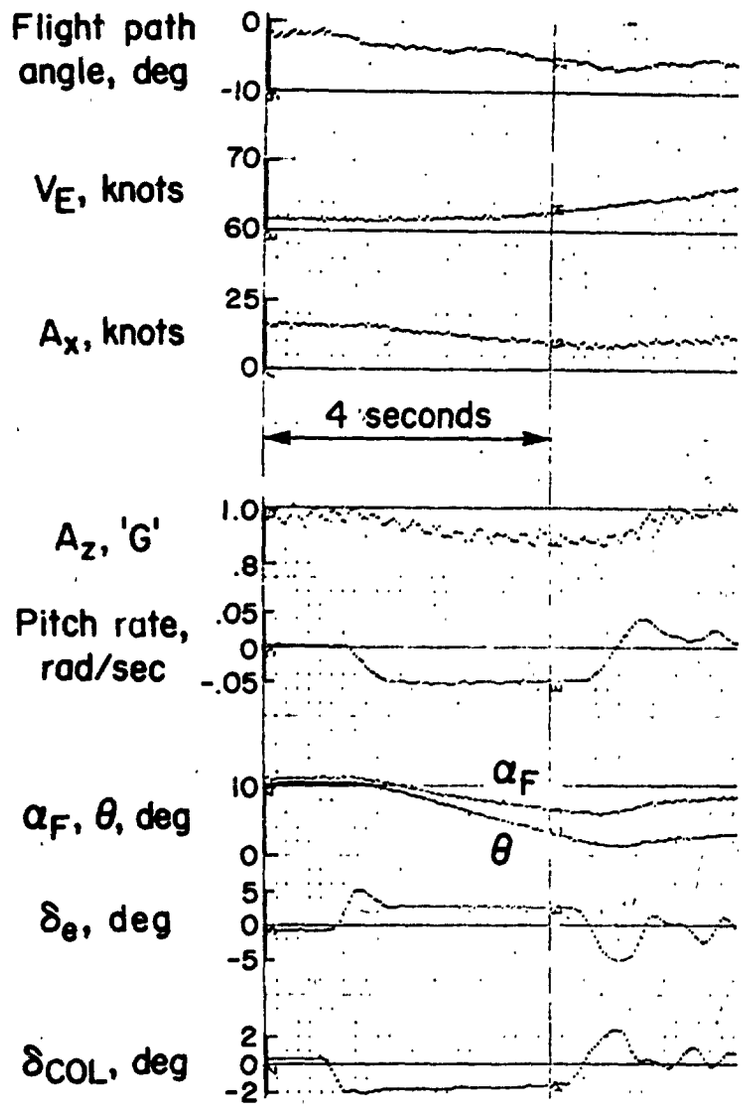

Figure 38.– Elevator step – flaps 68°, nozzles 11°.

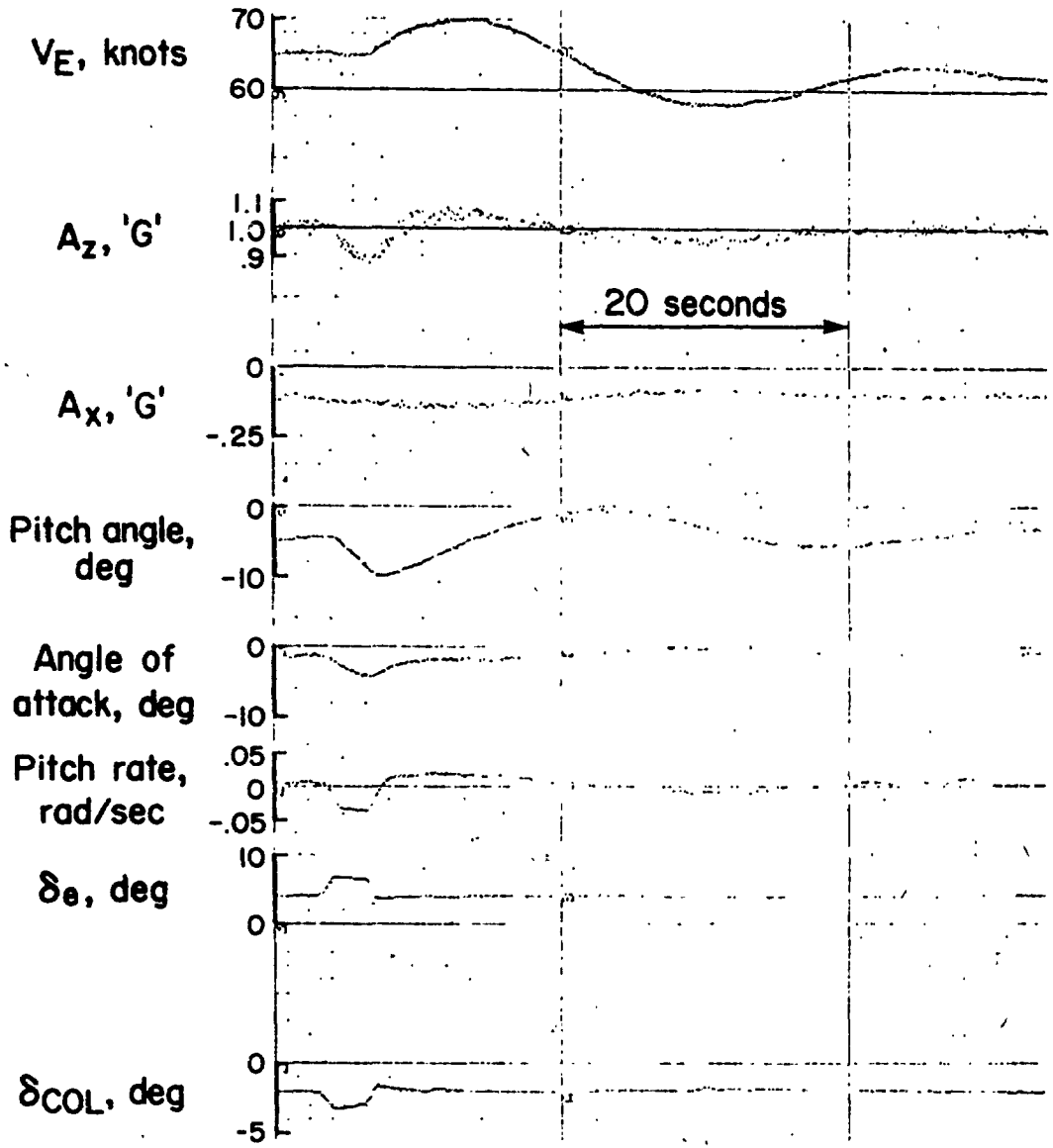

Figure 39.– Elevator pulse – flaps 67°, nozzles 77°.

Sym	δ_f, deg	Weight, lbs	(kilograms)	C.G. % Mac	Test
○	67	43,800	(19,900)	30.3	Wind-up
□	67	var	var	——	$\Delta\theta$ step
△	67	39,000	(17,700)	29.5	$\Delta\theta$ step
◇	32	41,000	(18,600)	29.8	Wind-up
▷	33	41,400	(18,800)	29.8	$\Delta\theta$ step

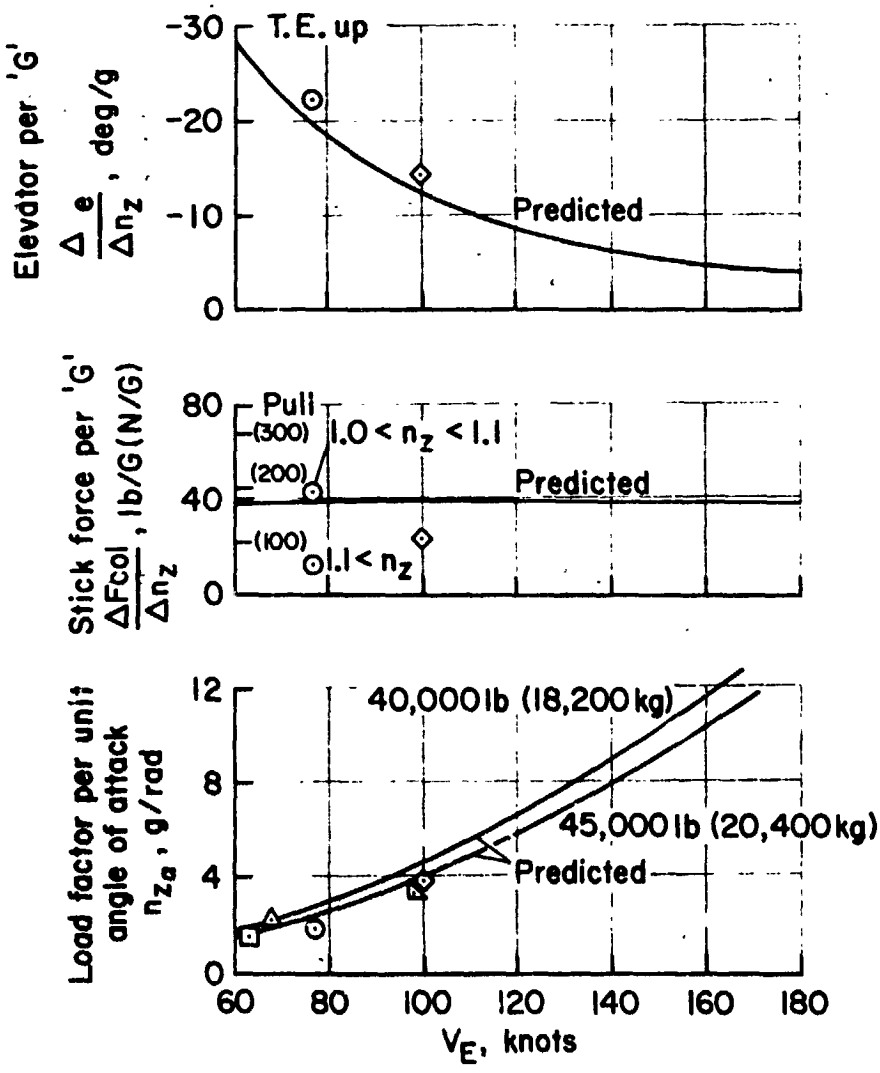

Figure 40.– Maneuvering stability summary.

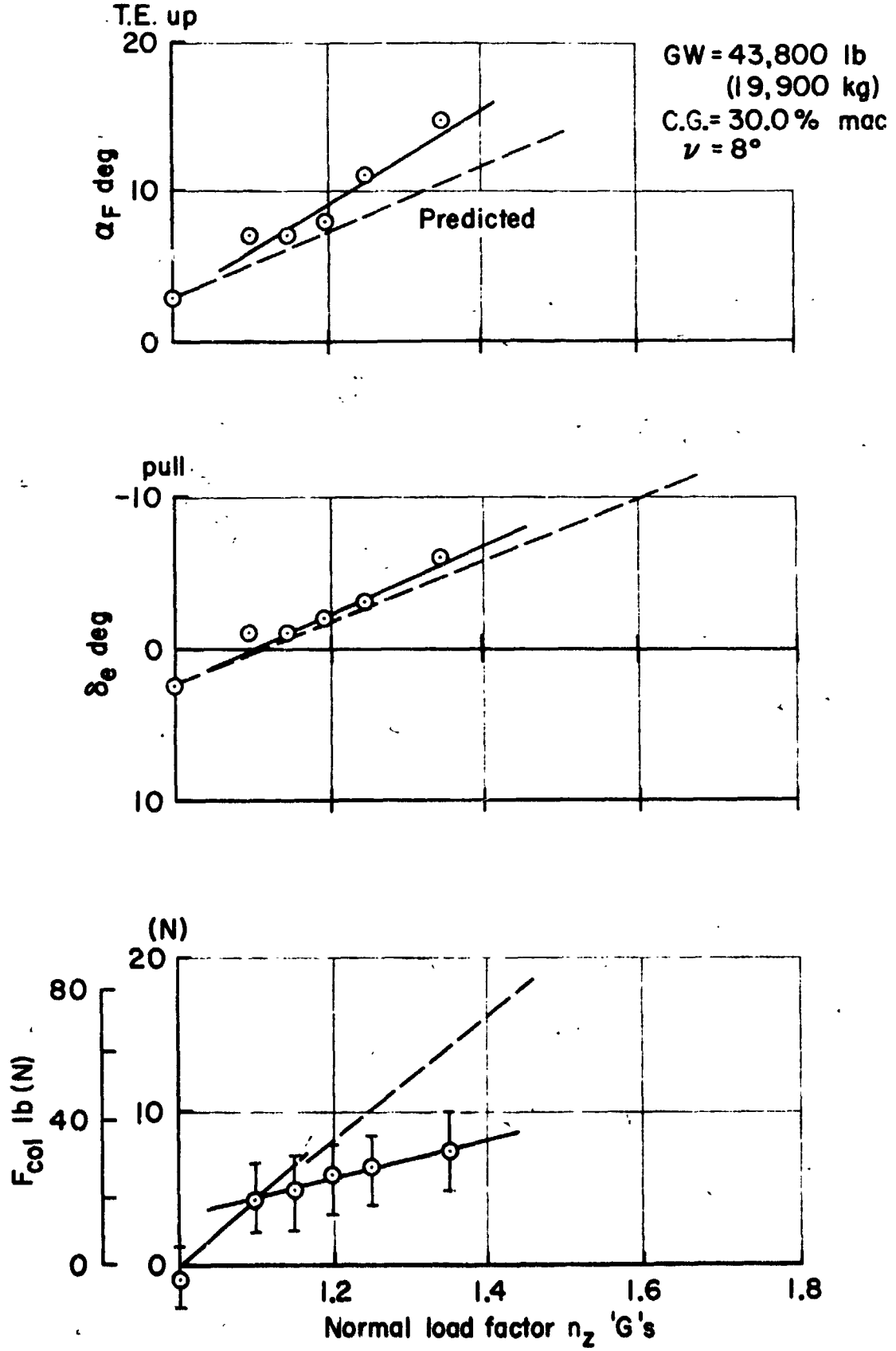

Figure 41.– Wind-up turn, flaps 67°, 77 knots.

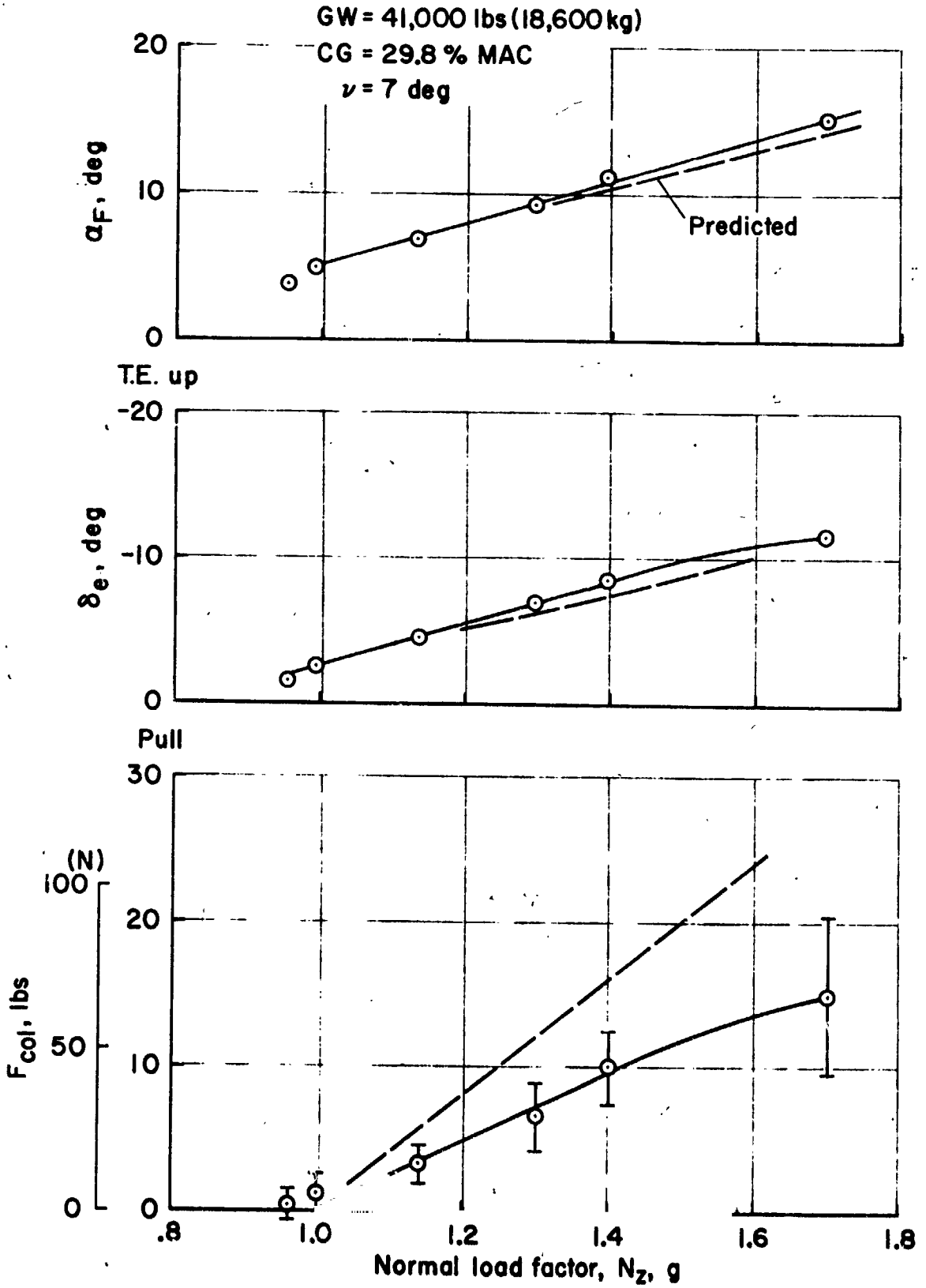

Figure 42.– Wind-up turn, flaps 32°, 100 knots.

	ν, deg	Weight, lbs	kilograms	n_{z_α}, g/rad
●	60 – 90	38,400 – 44,800	(17,000 – 20,300)	~1.55
□	60 – 90	37,000 – 45,500	(16,800 – 20,600)	~2.1
◇	7	41,400	(18,800)	~3.4

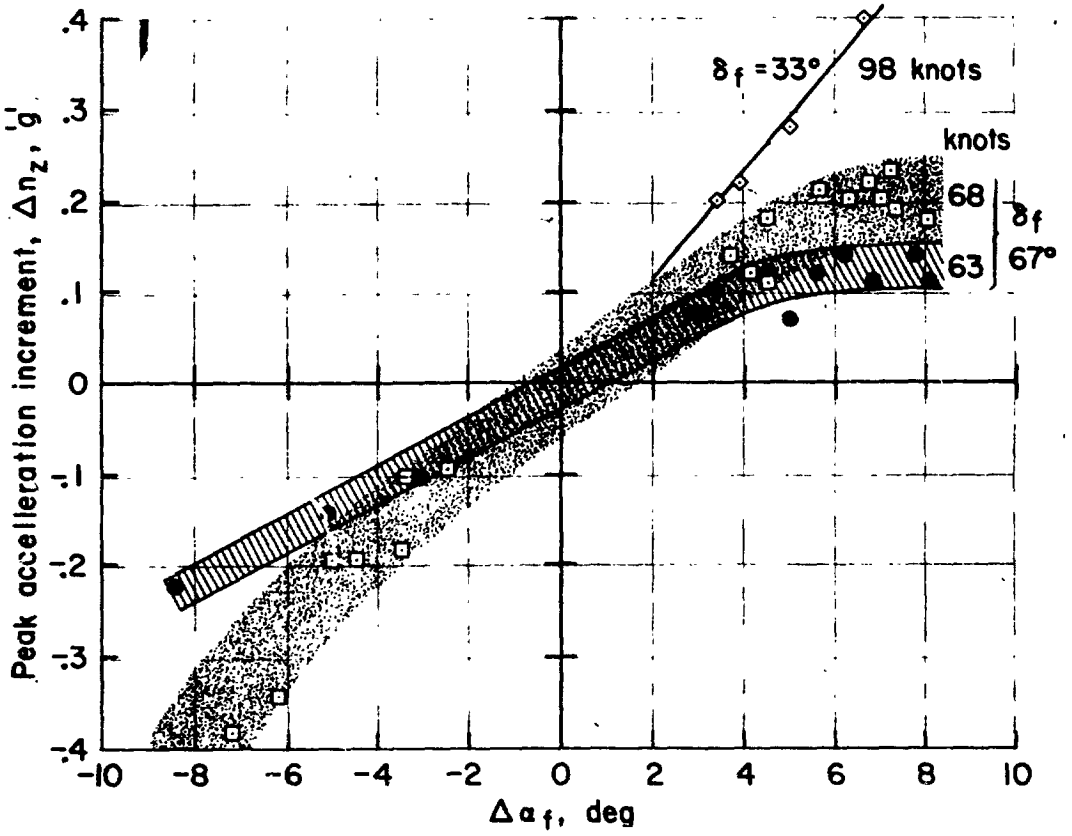

Figure 43.– Variation of vertical acceleration with changes in angle of attack.

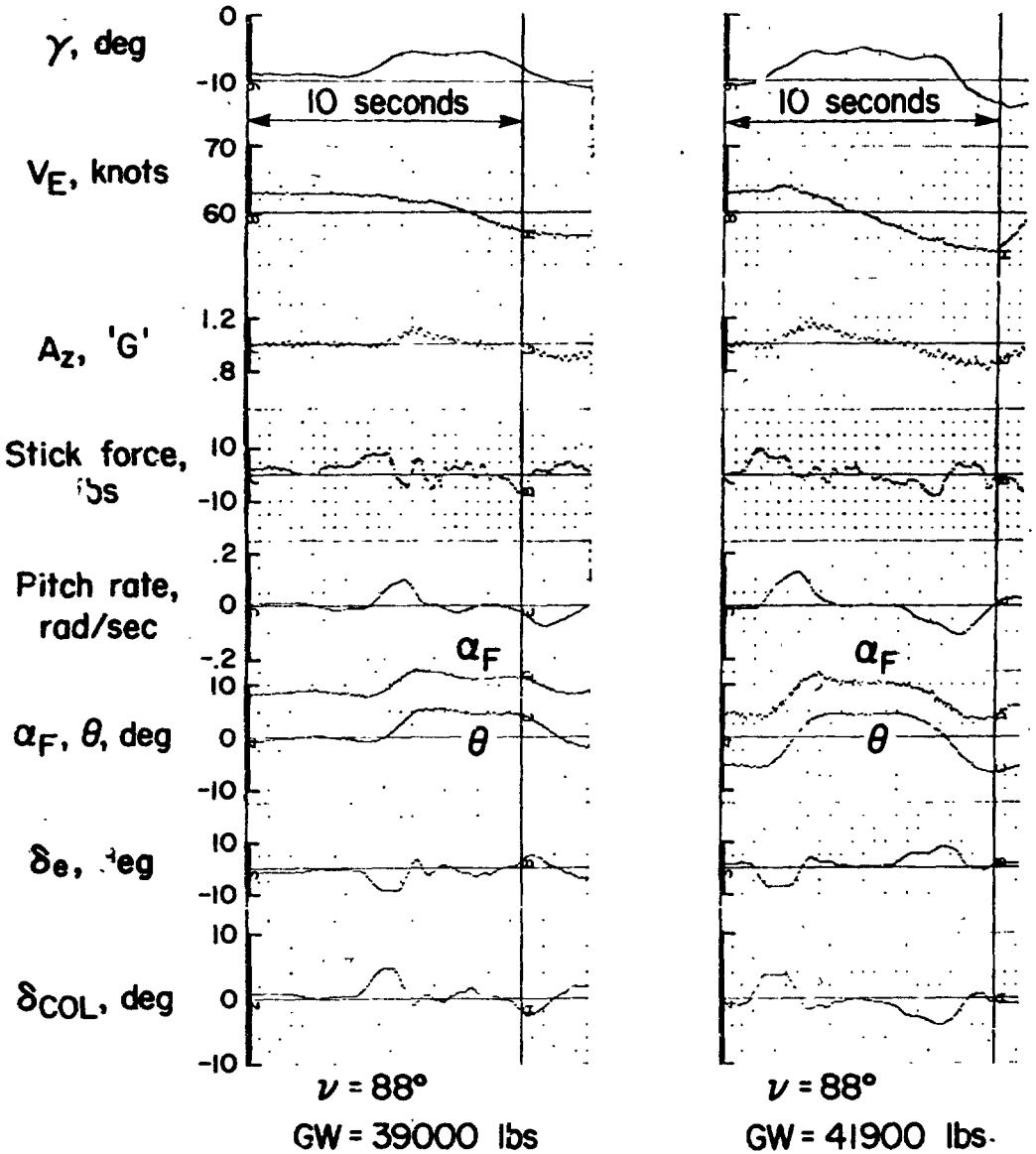

Figure 44.— Pitch attitude steps, flaps 65°.

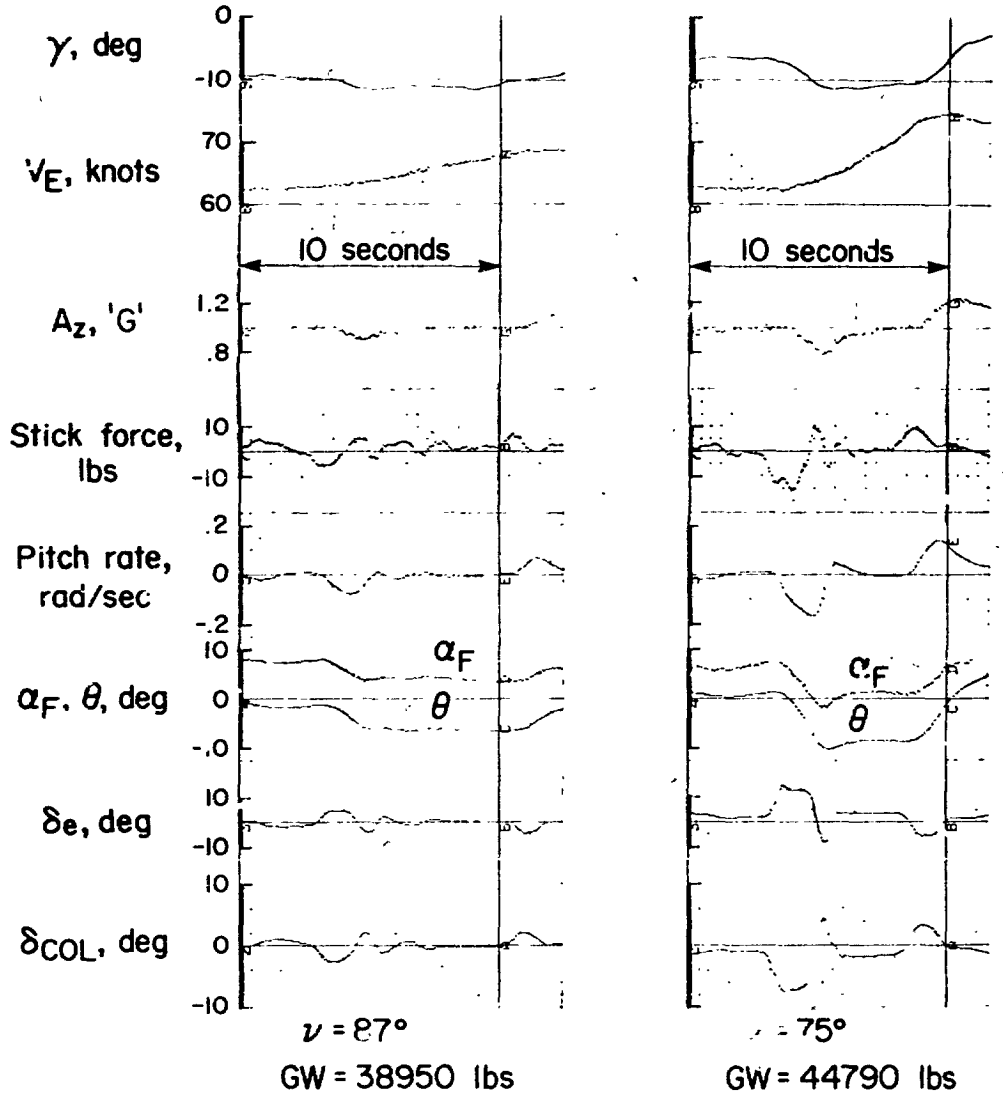

Figure 45. - Pitch attitude steps, flaps 65°.

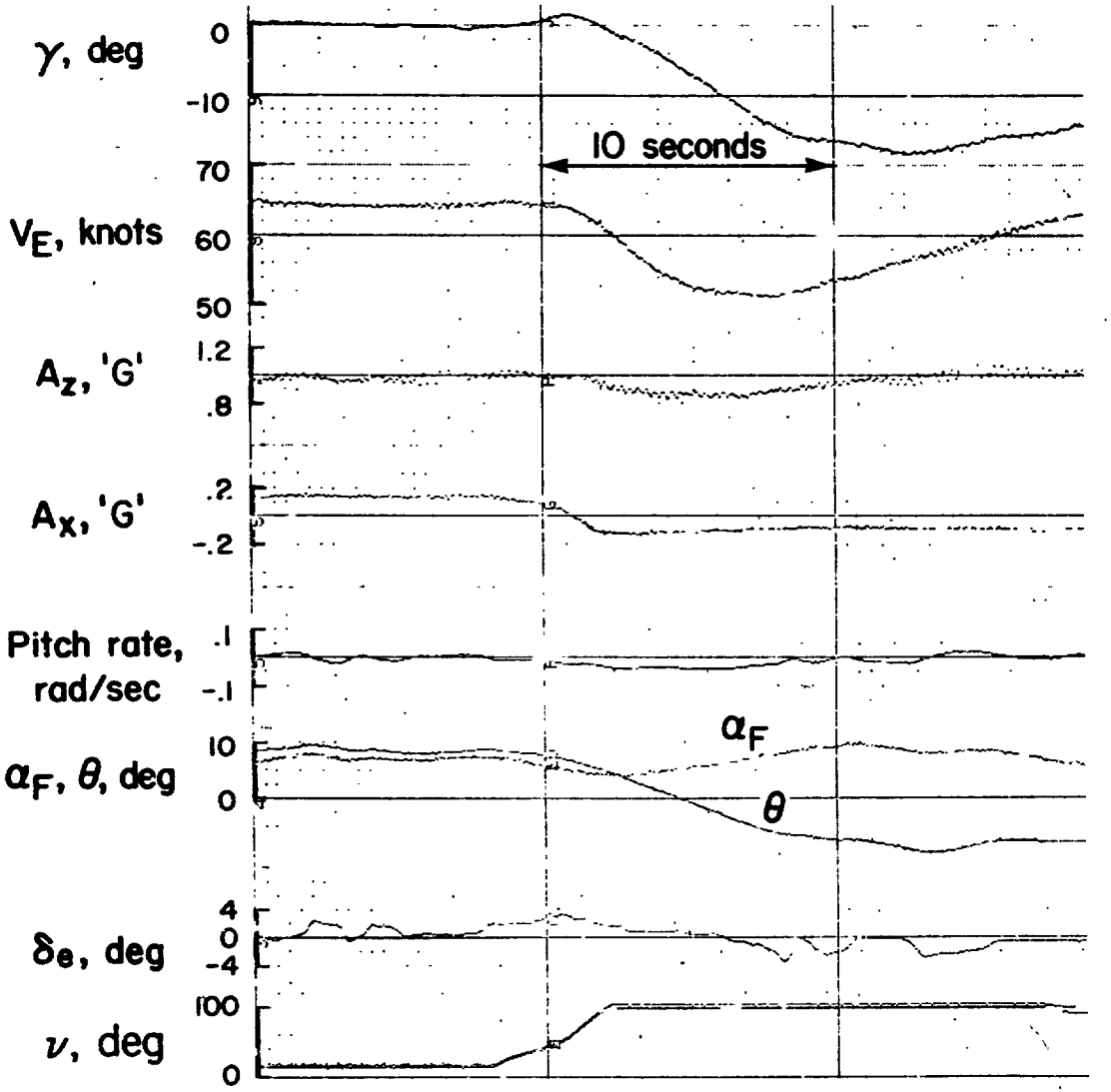

Figure 46.- Response to nozzle rotation forward, flaps 65°, 65 knots.

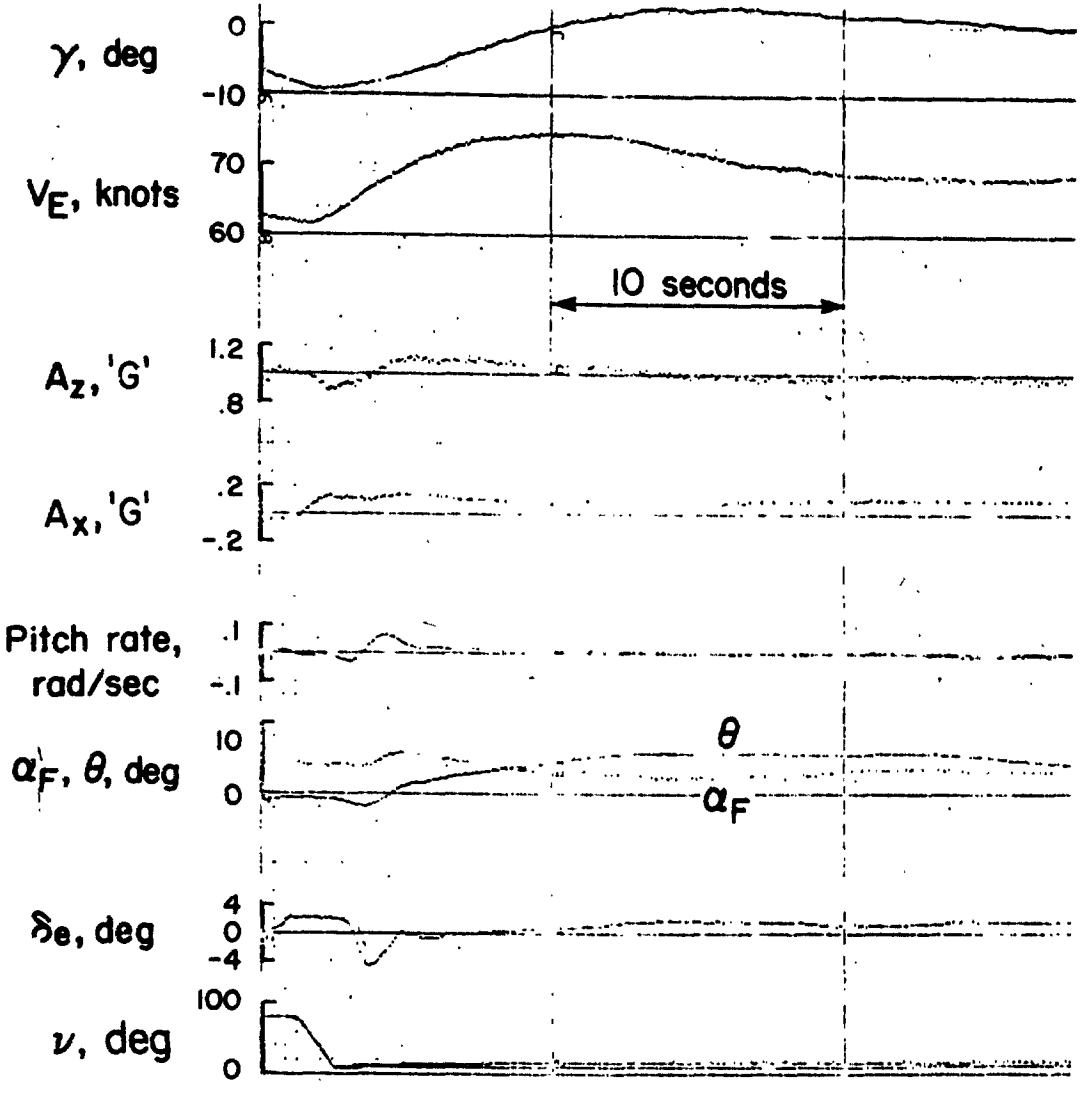

Figure 47.– Response to nozzle rotation aft, flaps 65°, 62 knots.

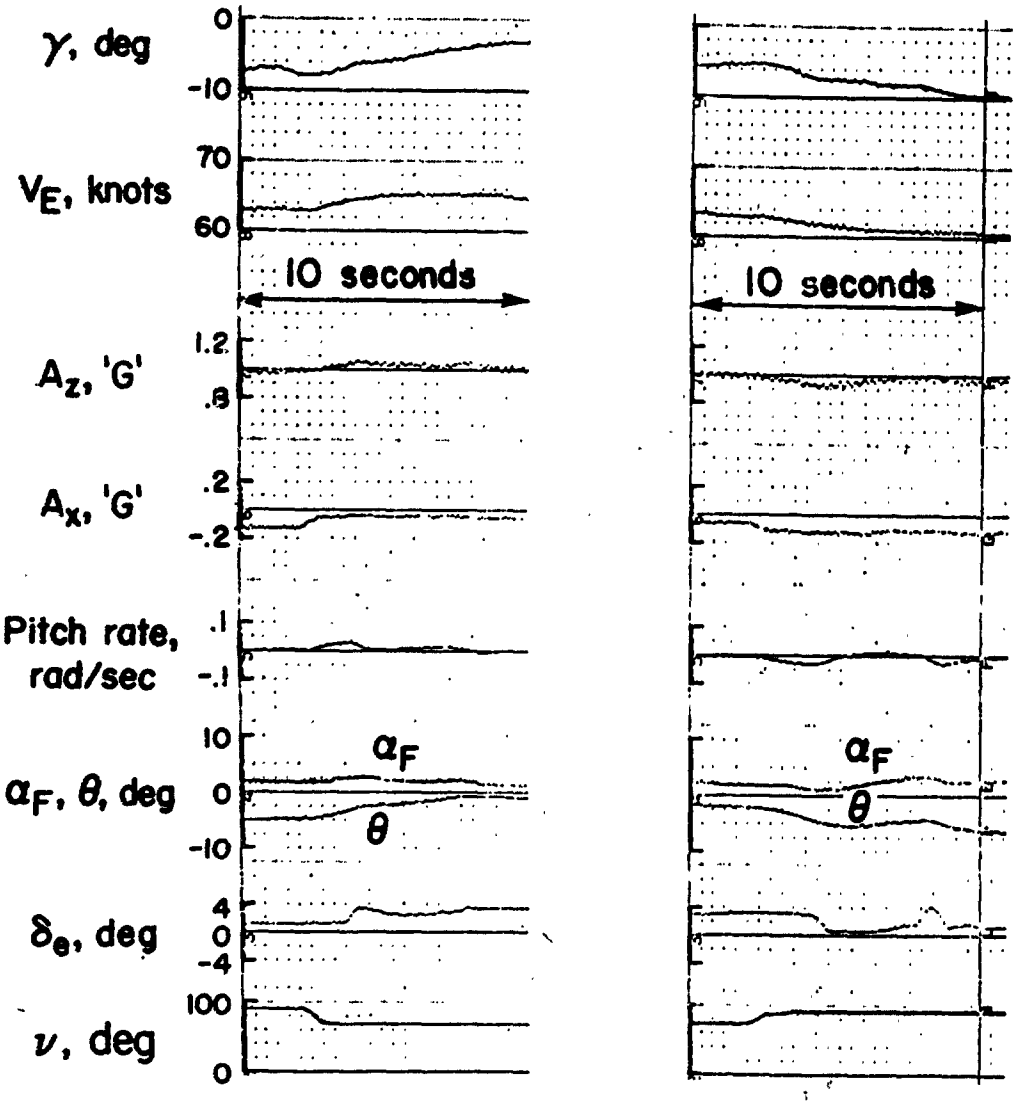

Figure 48.– Response to small nozzle steps, flaps 65°.

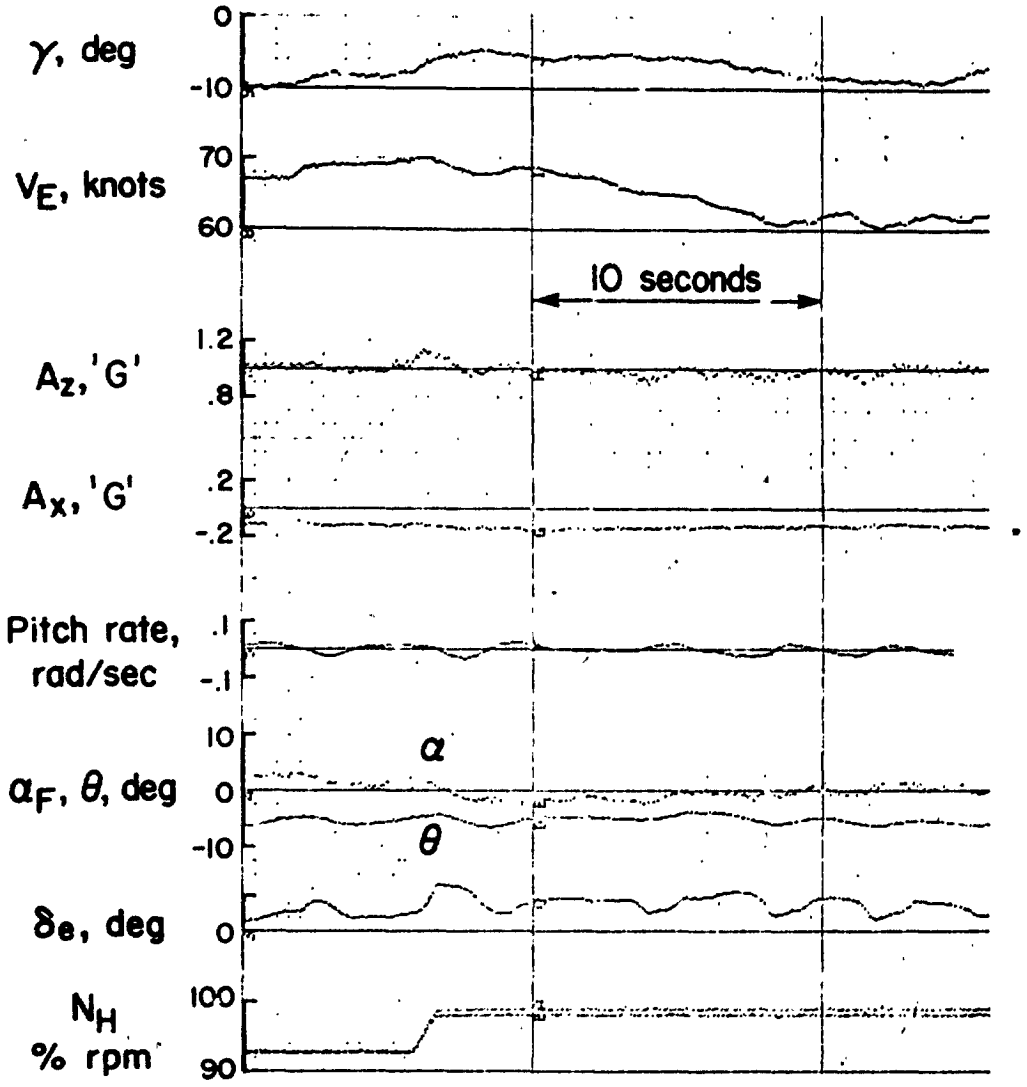

Figure 49.– Response to a throttle step increase, flaps 65°, ν = 83°.

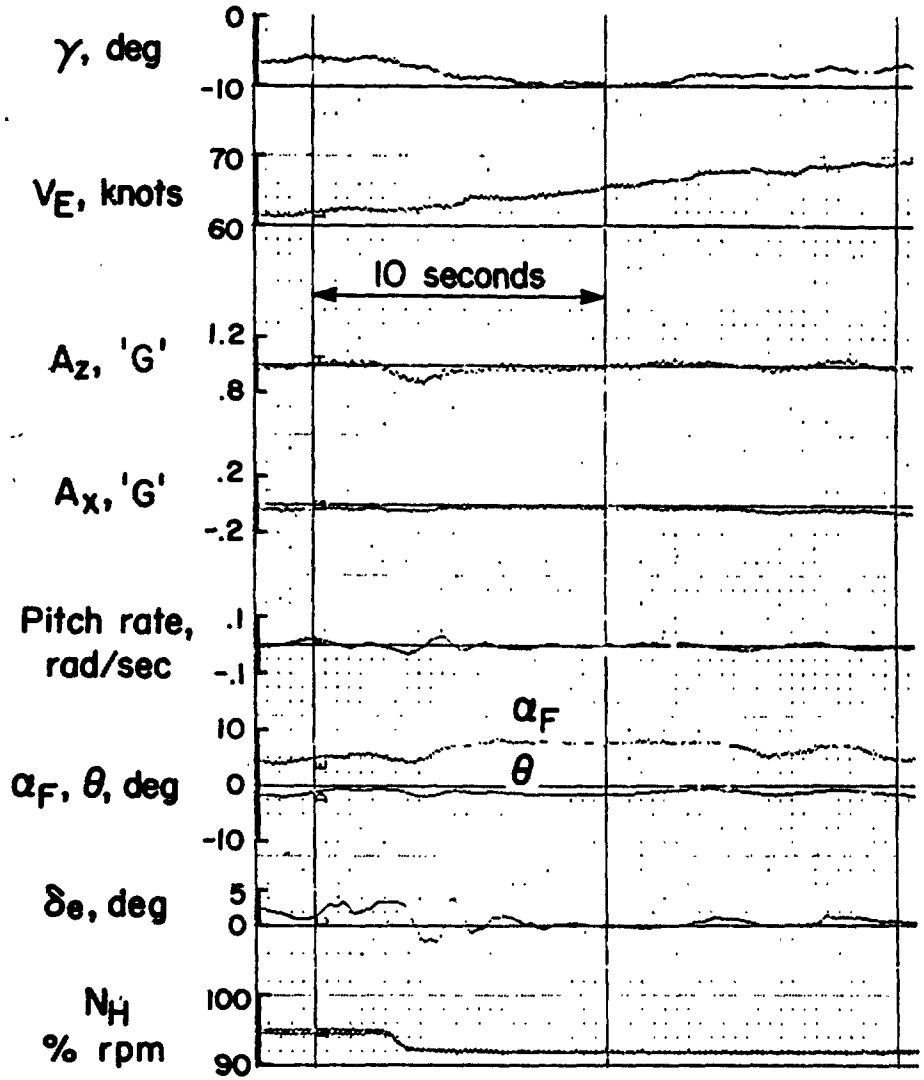

Figure 50.- Response to a throttle step decrease, flaps 65°, ν = 75°.

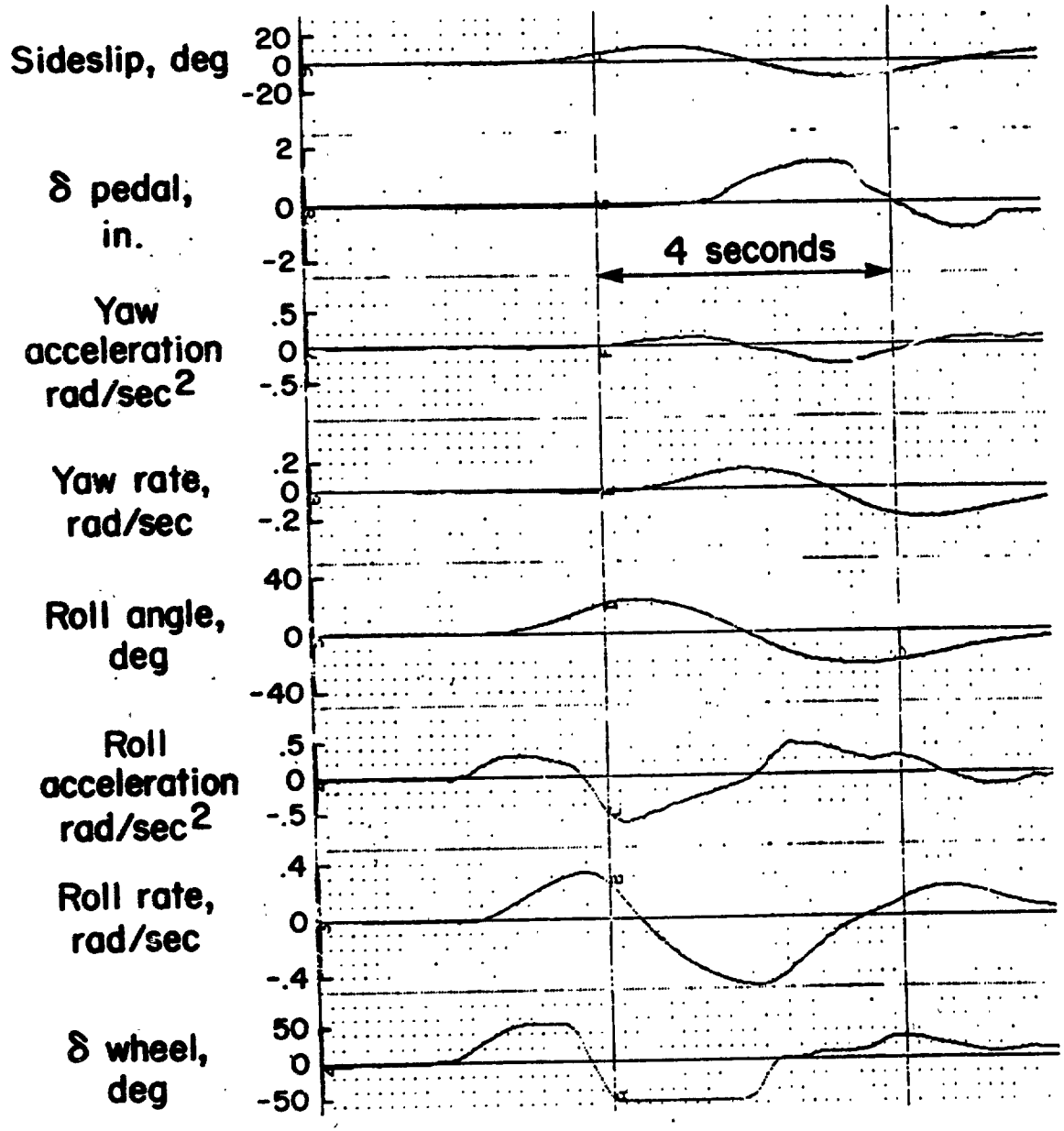

Figure 51.– Roll reversal – flaps 66°, 69 knots, *SAS* off.

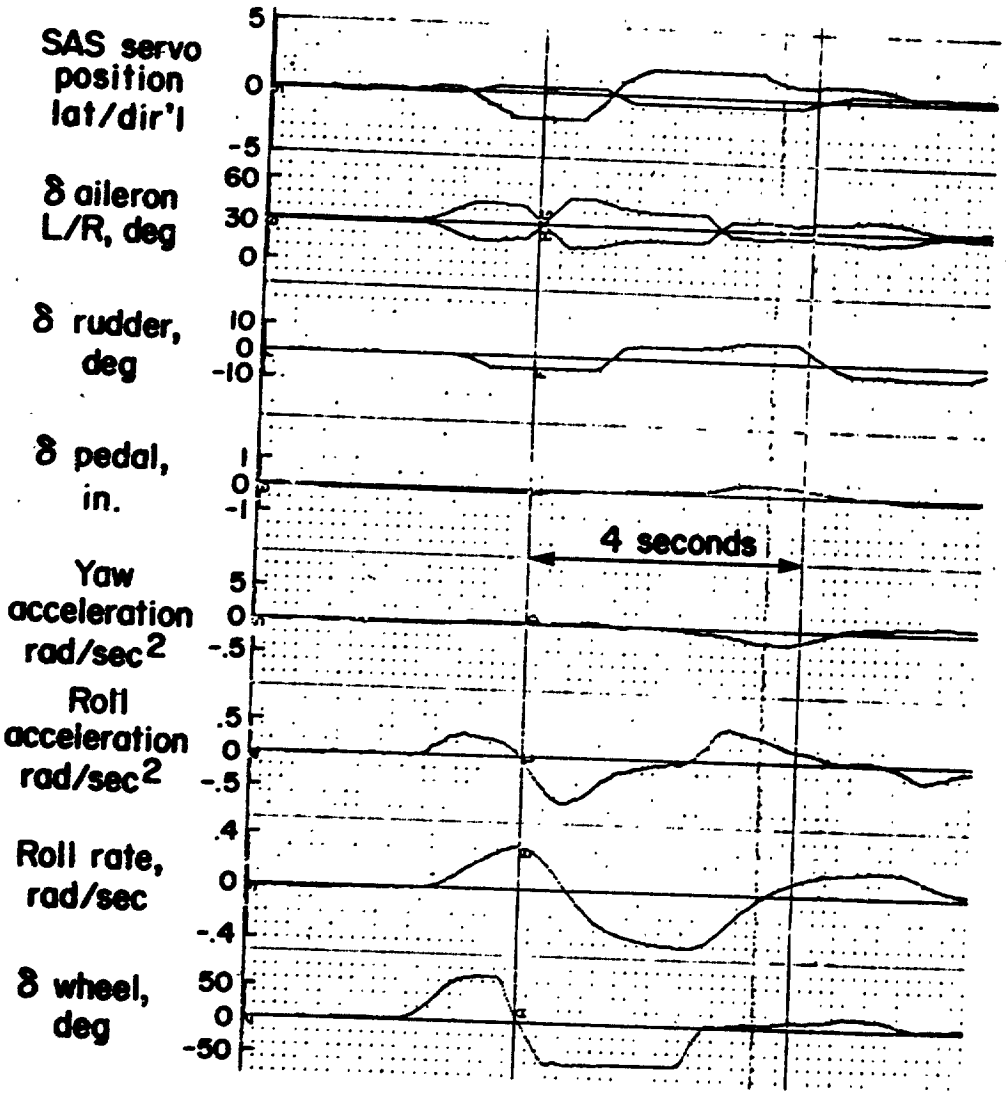

Figure 52.– Roll reversal – flaps 66°, 70 knots, *SAS* on.

	δ_f°	ν°	N_H%	Weight, lbs	(kilograms)
○	67	15	93 – 95	40,000	(18,200)
◇	67	15	94.7	45,000	(20,400)
□	33	15	92	44,800	(20,300)
△	5.6	7	92	45,000	(20,400)
▲	5.6	7	90	44,000	(20,000)
– –	65	(Predicted)		40,000	(18,200)

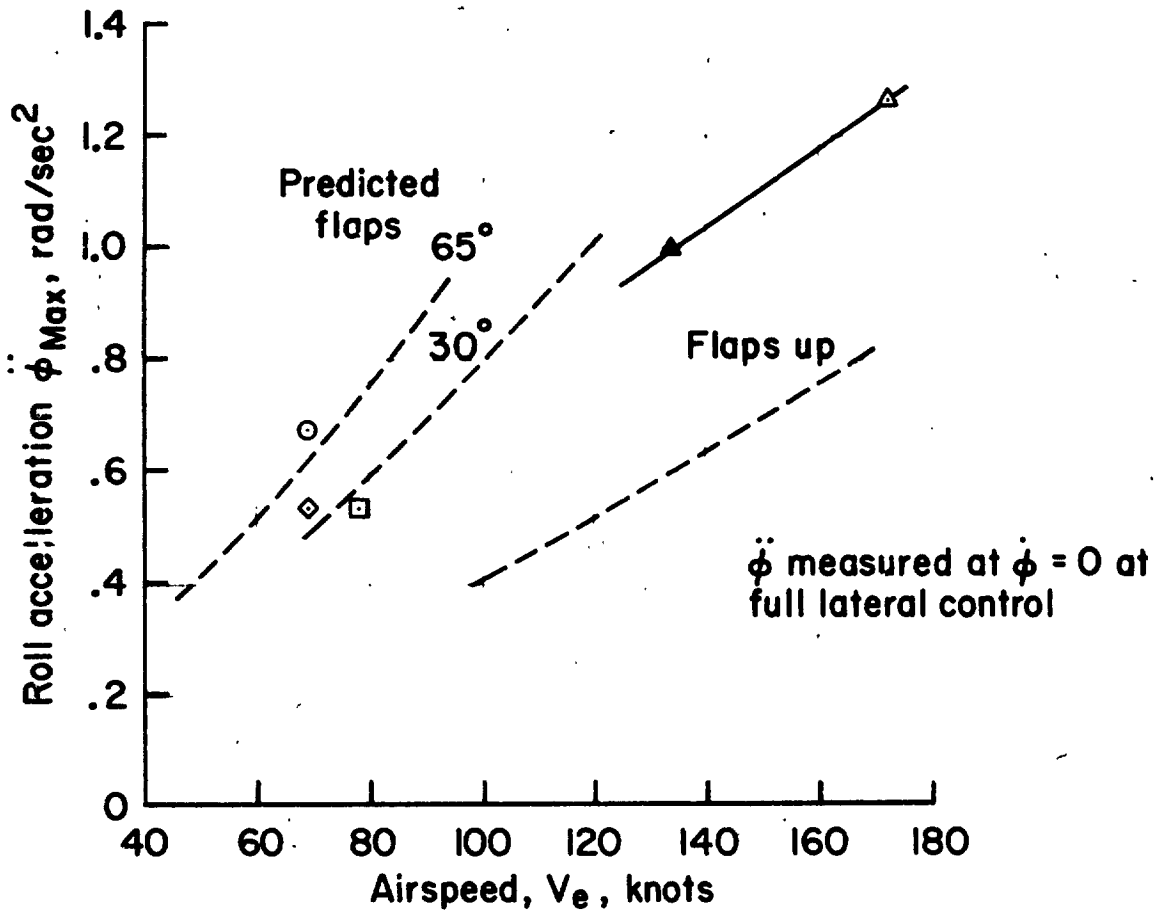

Figure 53. - Maximum roll acceleration from roll reversal maneuvers.

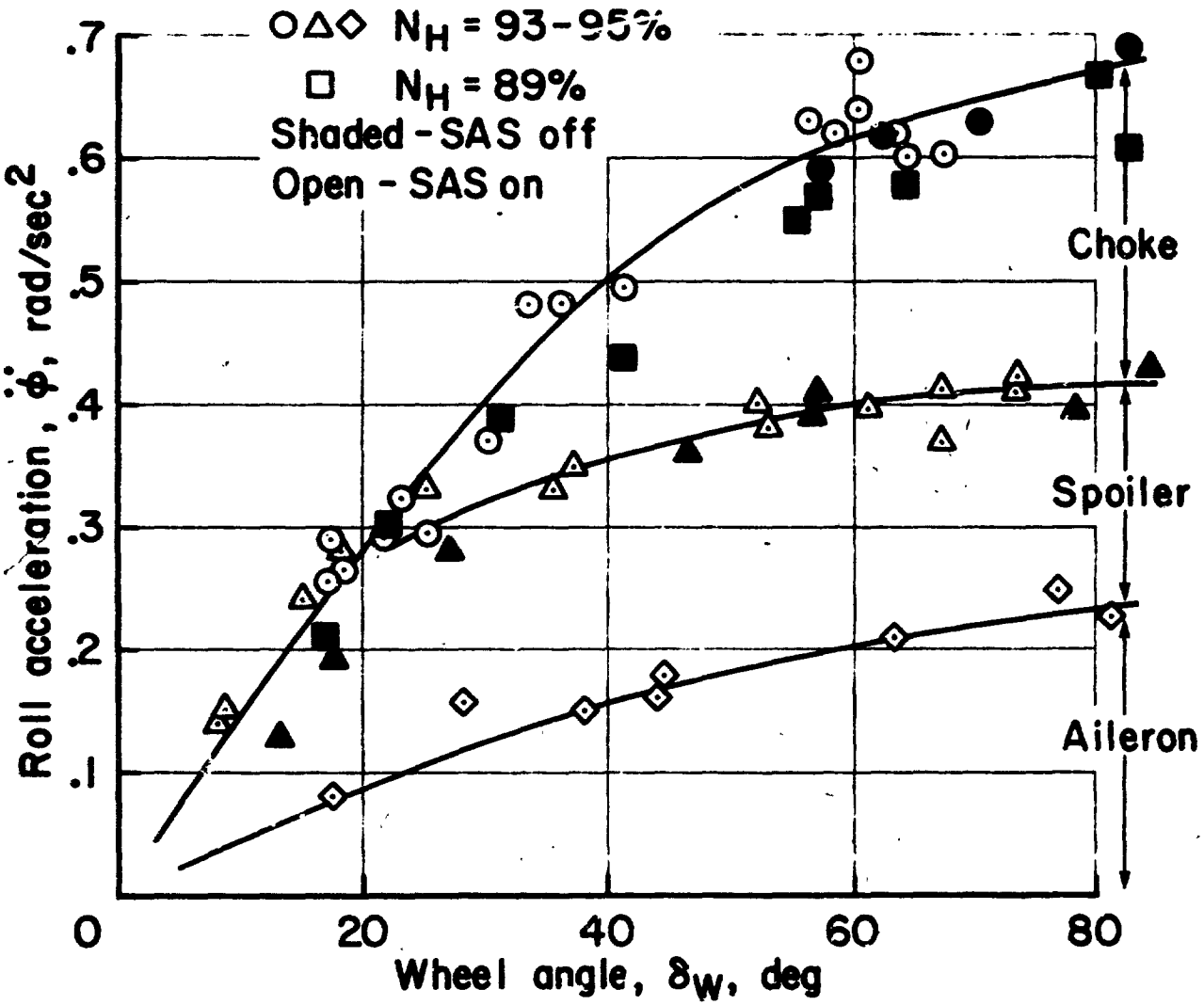

Figure 54.– Lateral control effectiveness, flaps 67°, 69 knots, $\nu = 15°$, $GW = 37{,}000$–$40{,}000$ lb.

Sym	δ_f, deg	ν, deg	N_H	V_E, knots	Weight, lbs	(kilograms)
○	67	15	94.7	70	44,800	20,300
□	66	13		68	45,300	20,600

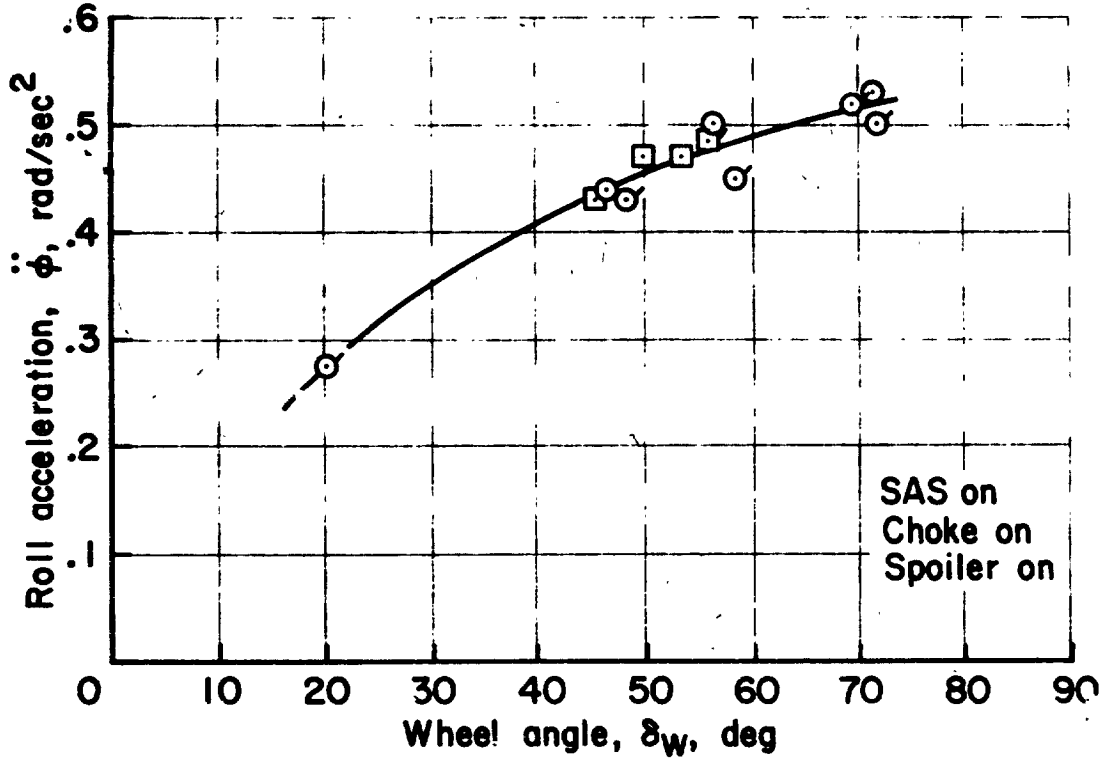

Figure 55.– Lateral control effectiveness – flaps 65°, 69 knots, 45,000 lb.

Sym	Flight	δ_f, deg	ν, deg	N_H	V_E, knots	SAS	Weight, lbs (kilograms)	
○	38	33	15	92	78	on	45,000	(20,400)
●	38	33	15	92	78	off	44,600	(20,200)
◇	55	5.6	7	92	166	——	45,000	(20,400)
△	55	5.6	7	90	134	——	44,000	(20,000)

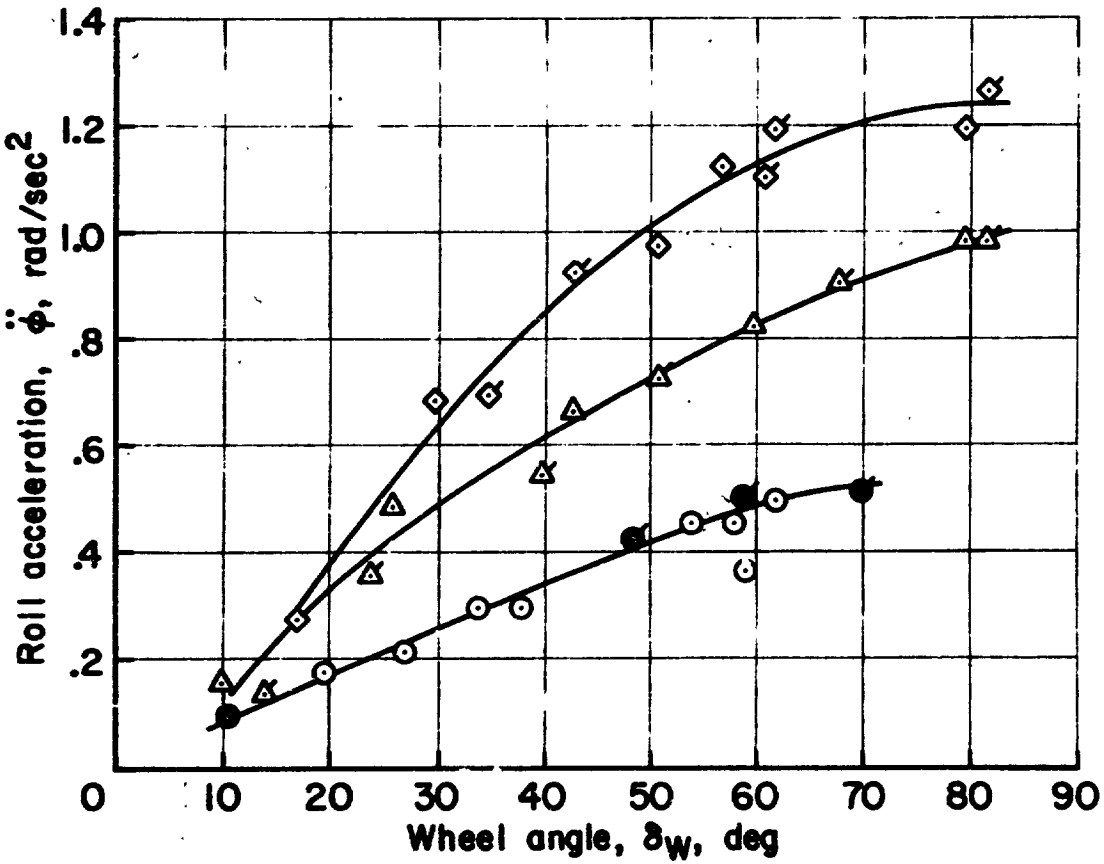

Figure 56.– Lateral control effectiveness – flaps 30° and 5.6°.

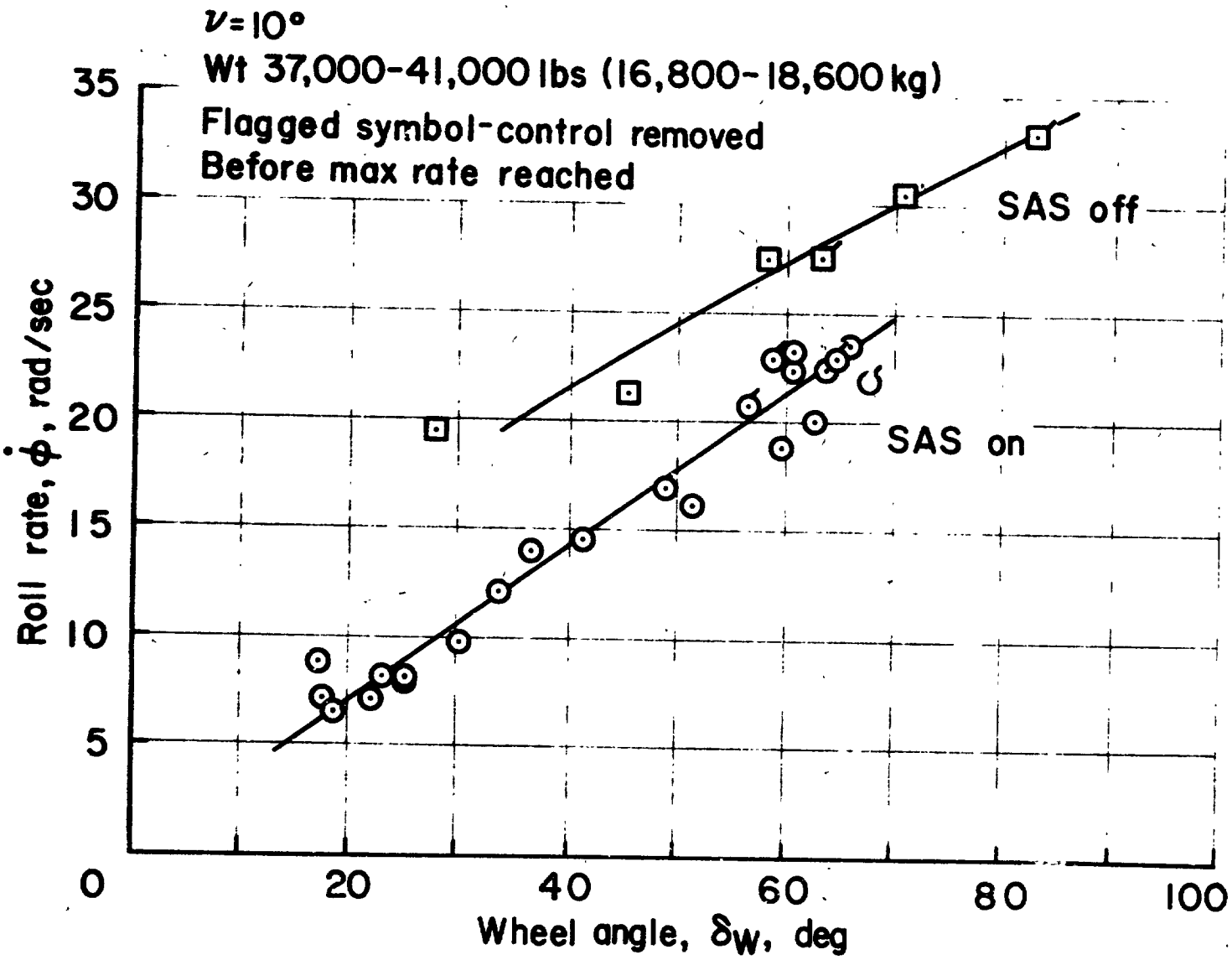

Figure 57.– Maximum roll rate from lateral control reversals, flaps 65°, 69 kn

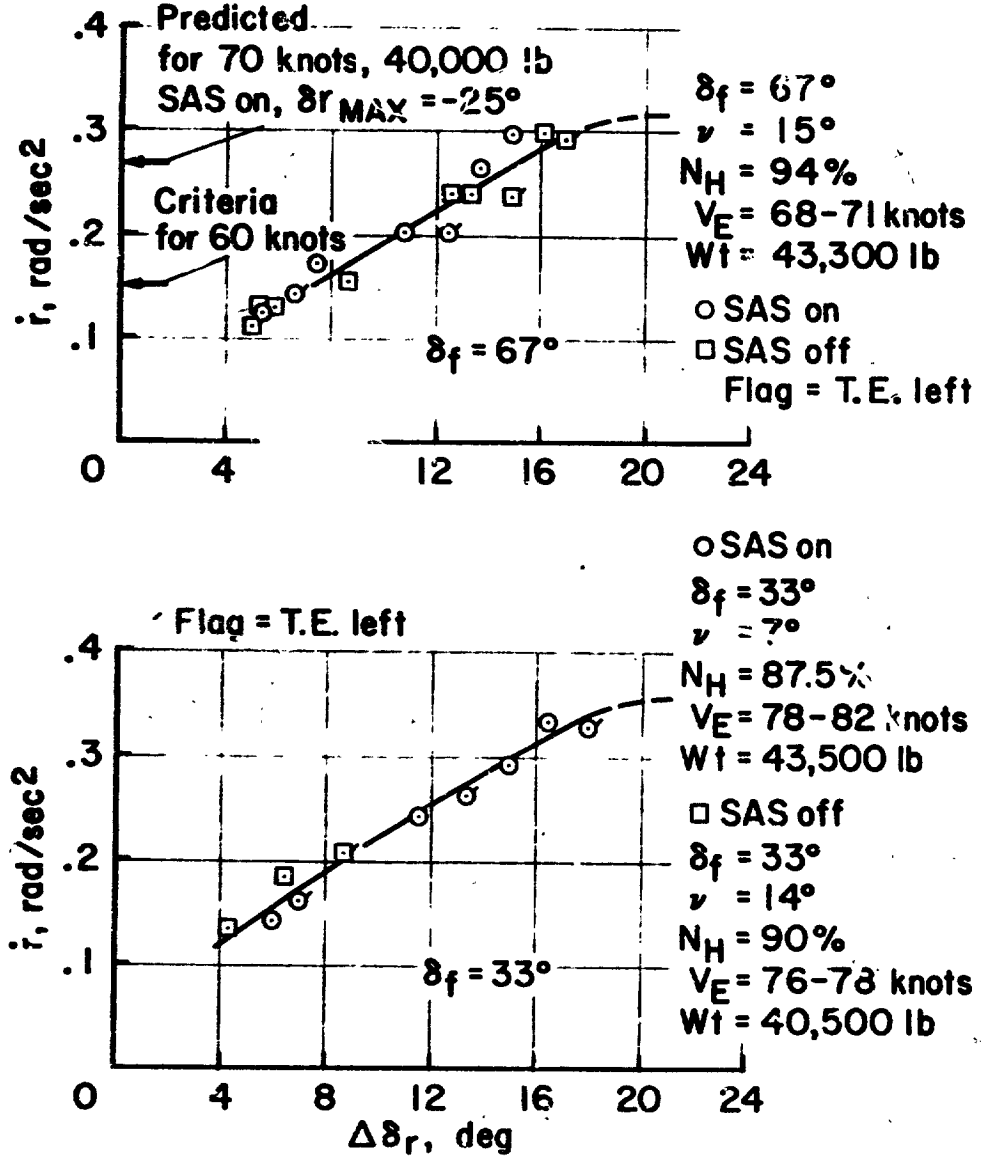

Figure 58.– Directional control effectiveness – δ_f 65° and 30°.

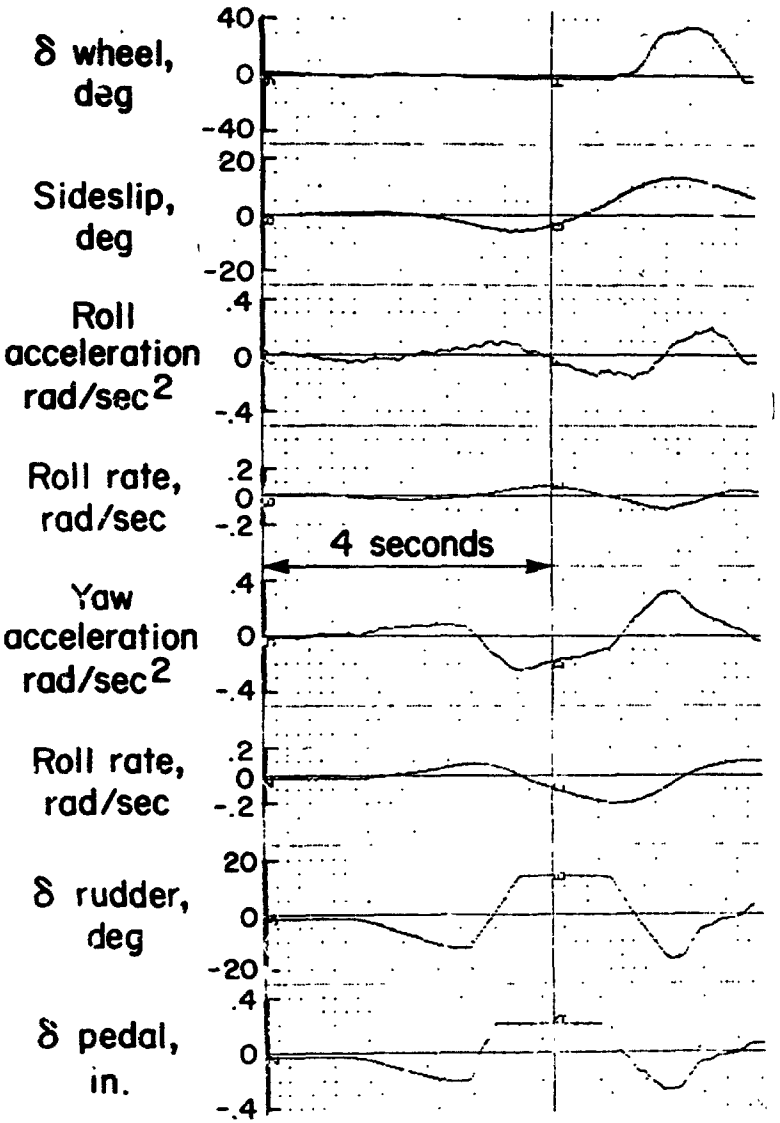

Figure 59.– Rudder reversal – flaps 67°, 68 knots, *SAS* off.

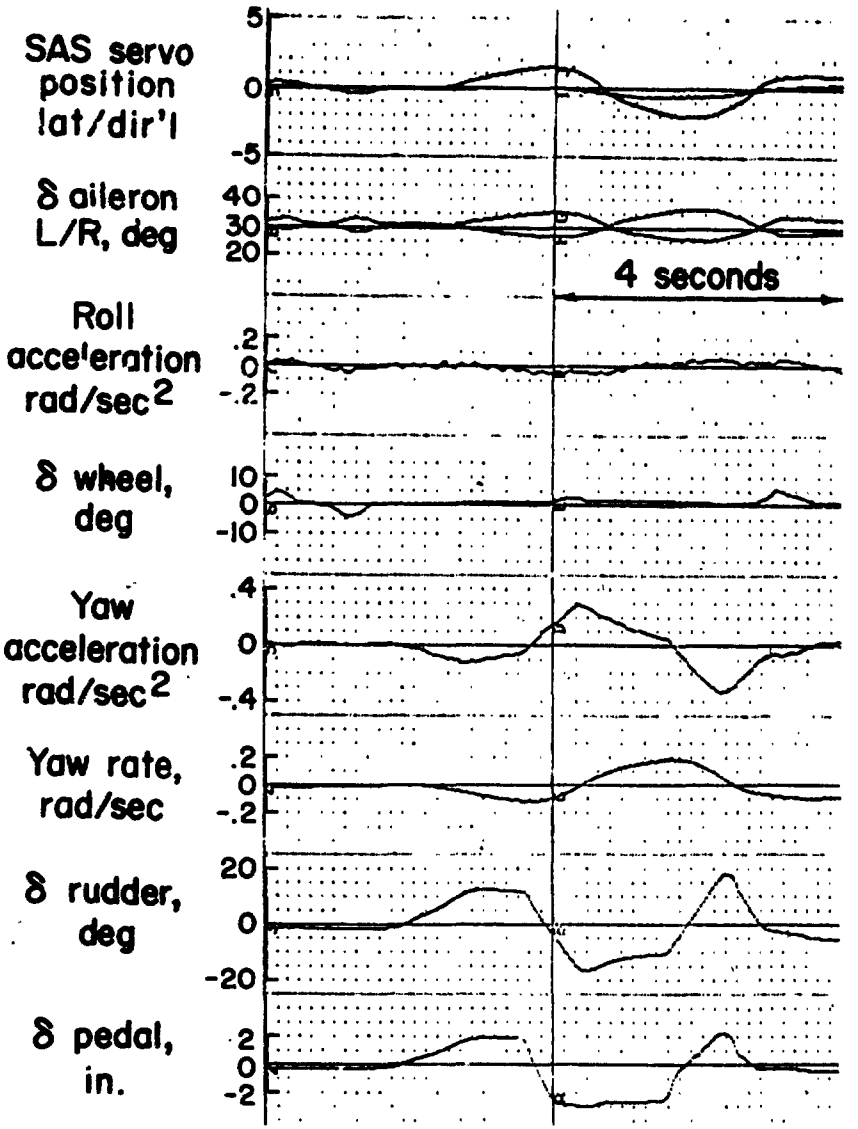

Figure 60.– Rudder reversal – flaps 67°, 70 knots, *SAS* on.

Sym	δ_f, deg	ν, deg	V_E, knots	Weight, lbs (kilograms)	
○	67	15	69	43,000	(19,500)
□	67	15	70	44,000	(20,000)
△	33	7	80	43,500	(19,800)

Flags: Control removed before max rate reached

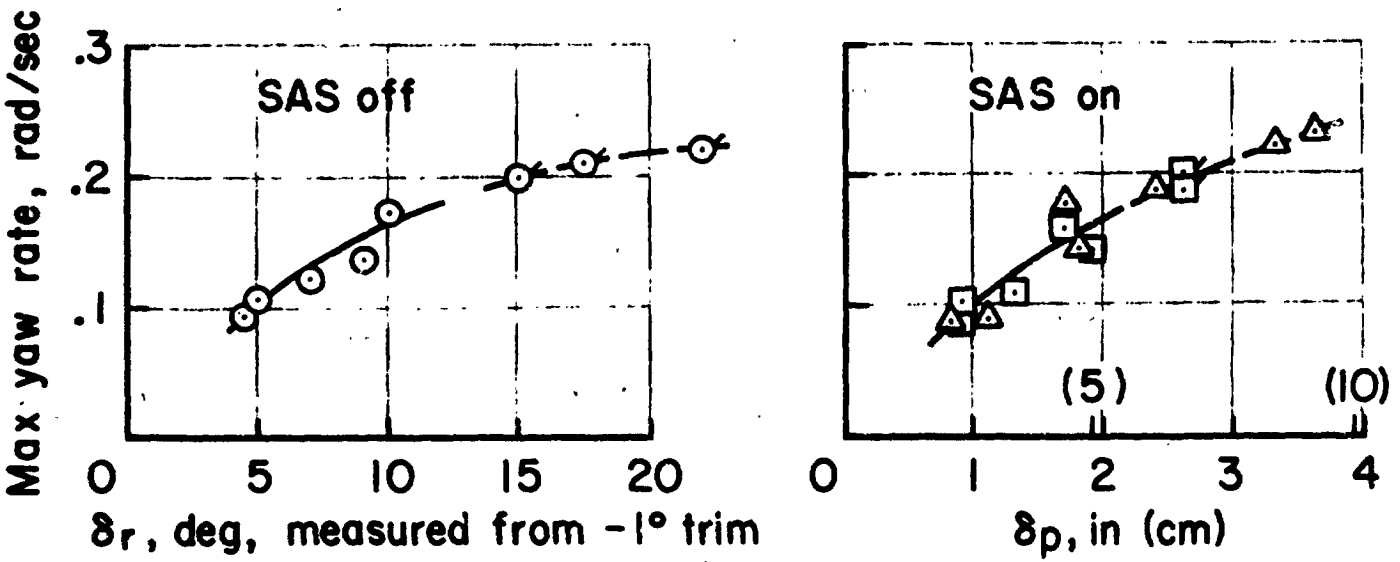

Figure 61.– Maximum yaw rate from directional control reversals.

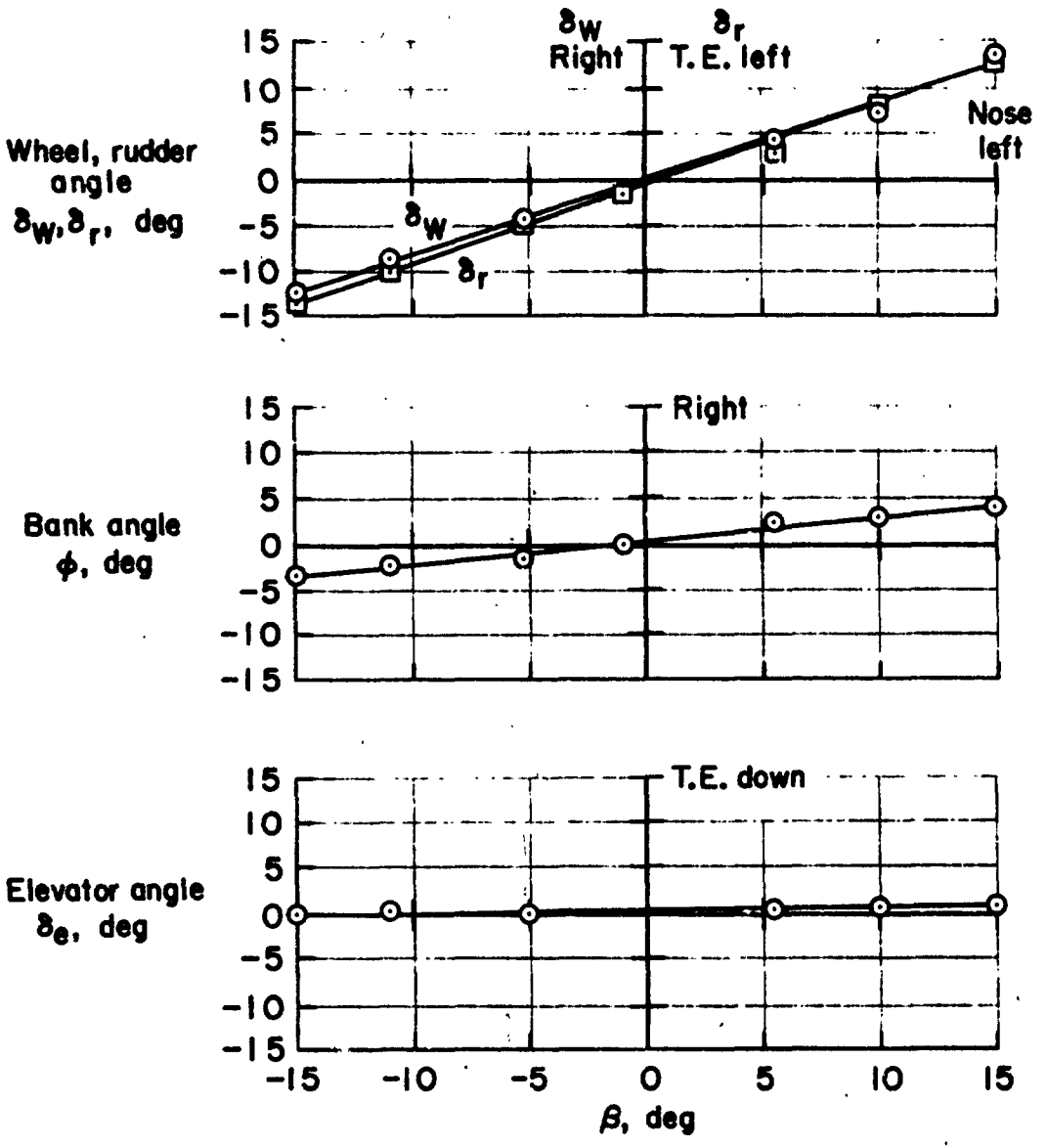

Figure 62.– Steady sideslip – $\delta_f = 65°$, $\nu = 15°$, $V = 65$ knots, $N_H = 93\%$.

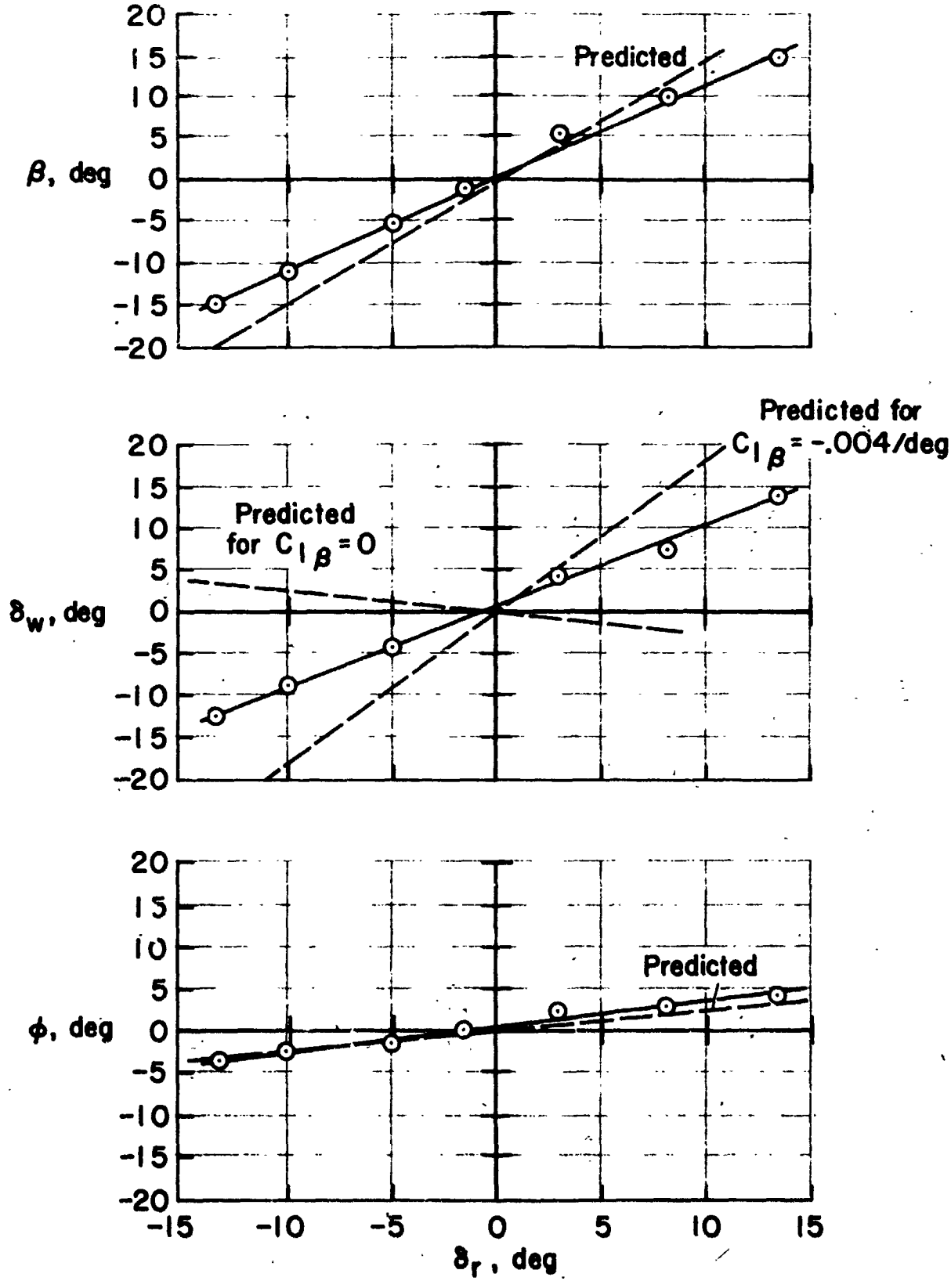

Figure 63.– Steady sideslip – $\delta_f = 65°$, $\nu = 15°$, $V_E = 65$ knots. $N_H = 93\%$, $\delta_e = 0$.

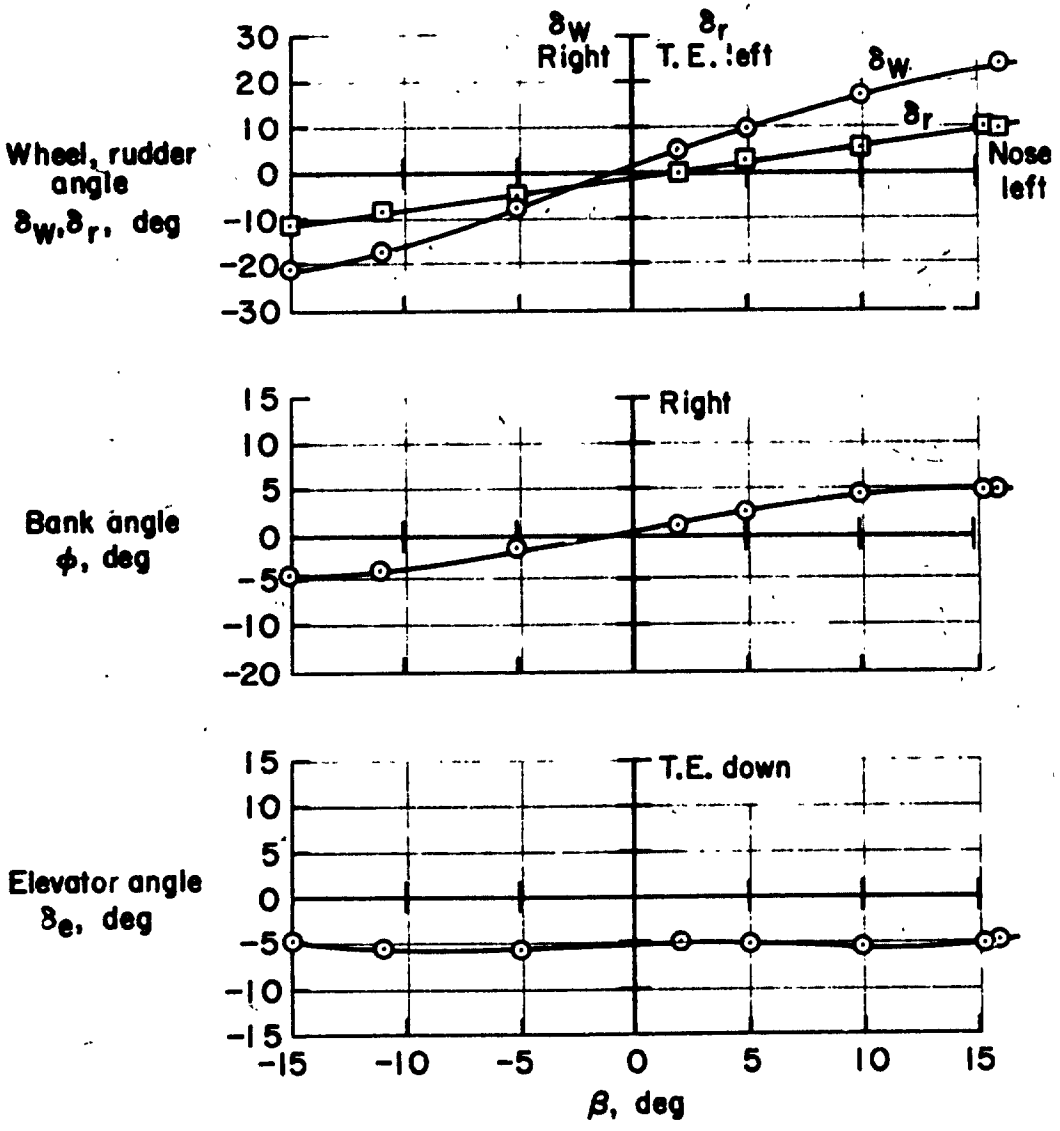

Figure 64.– Steady sideslip – $\delta_f = 30°$, $V_E = 75$ knots.

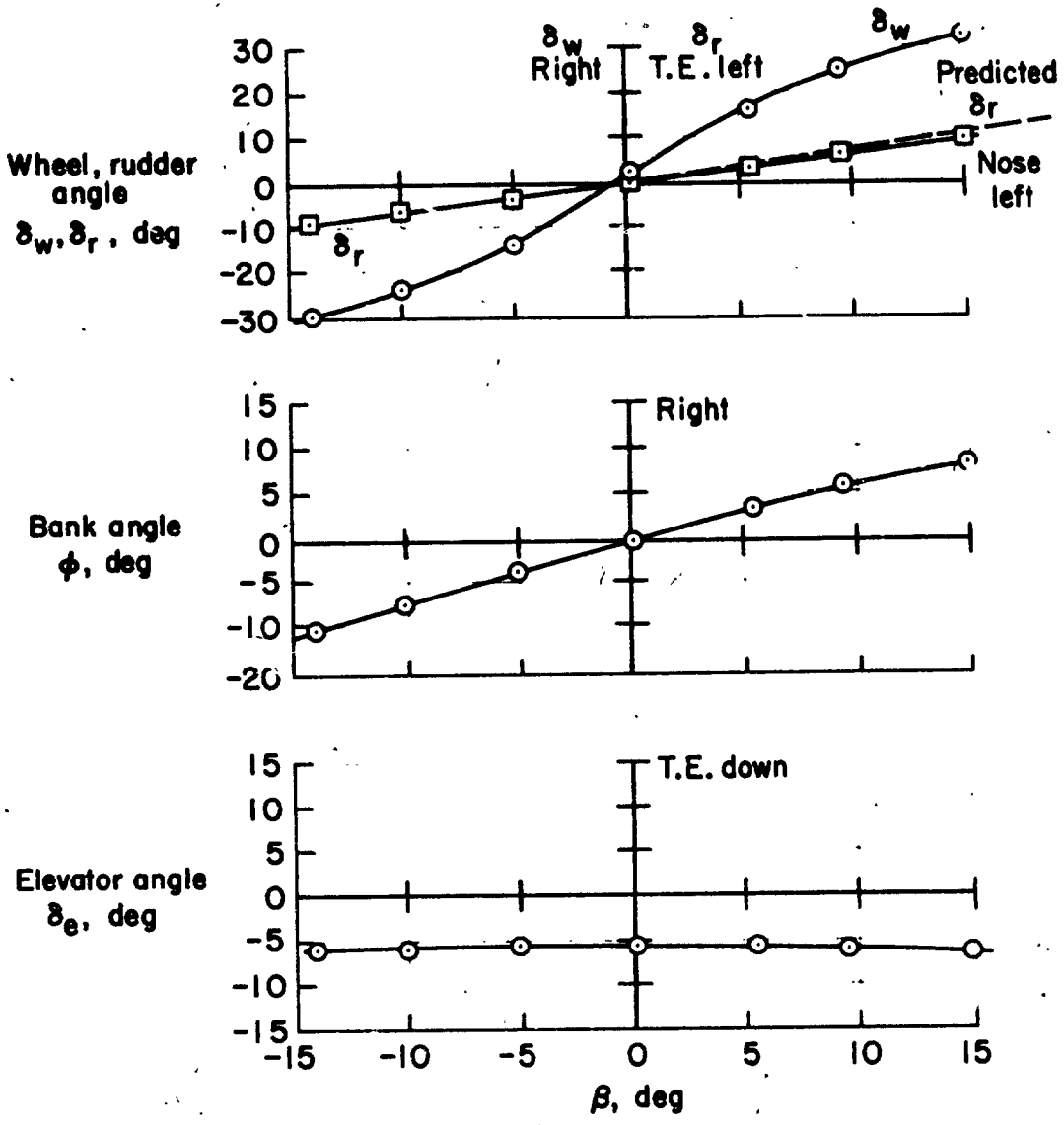

Figure 65.– Steady sideslip – $\delta_f = 5.6°$, $V_E = 120$ knots.

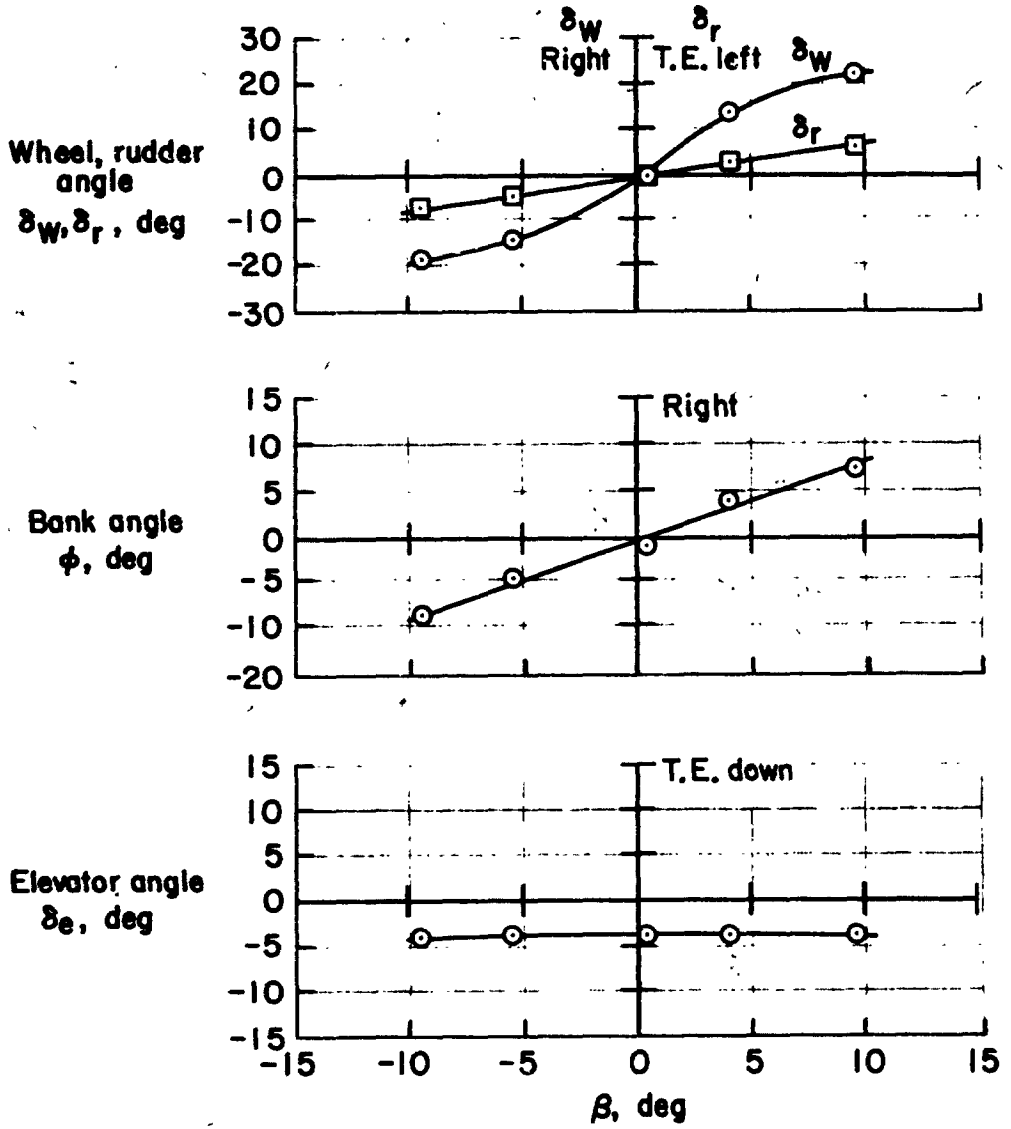

Figure 66.– Steady sideslip – $\delta_f = 5.6°$, $V_E = 150$ knots.

Sym	δ_f, deg	ν, deg	Weight, lbs	(kilograms)	SAS
○	67	10	37,000–40,000	(16,800) – (18,200)	off
●	67	17	38,600	(17,500)	on
◑	67	10	39,900	(18,100)	vss
□	67	86	40,400	(18,300)	off
⊟	67	57	41,000	(18,600)	off
◇	33	15	44,800	(20,300)	off
◈	33	9	40,000	(18,200)	off
◆	33	15	43,800	(19,900)	on
△	6	11	44,000	(20,000)	—
▲	6	11	39,700	(18,000)	—

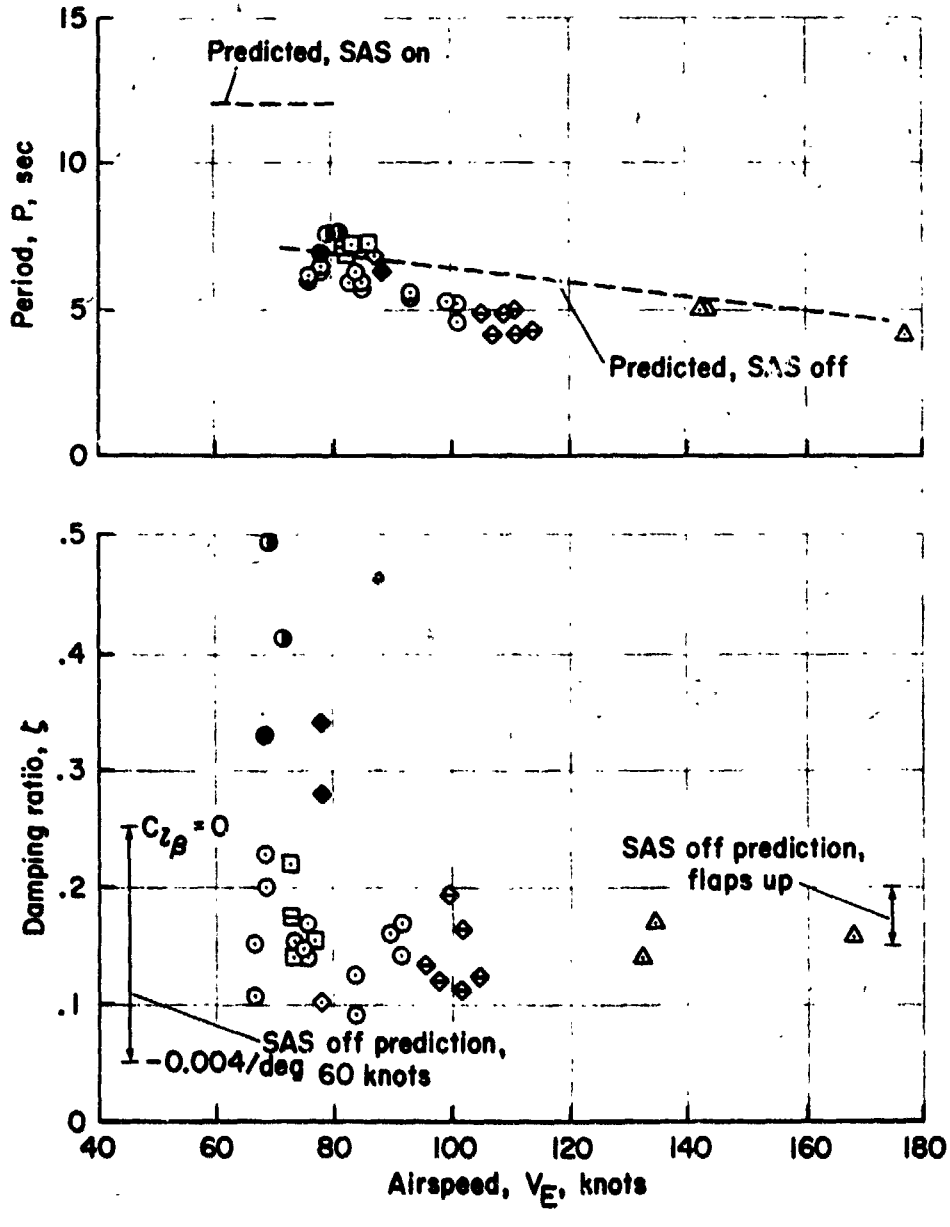

Figure 67.– Dutch roll characteristics summary.

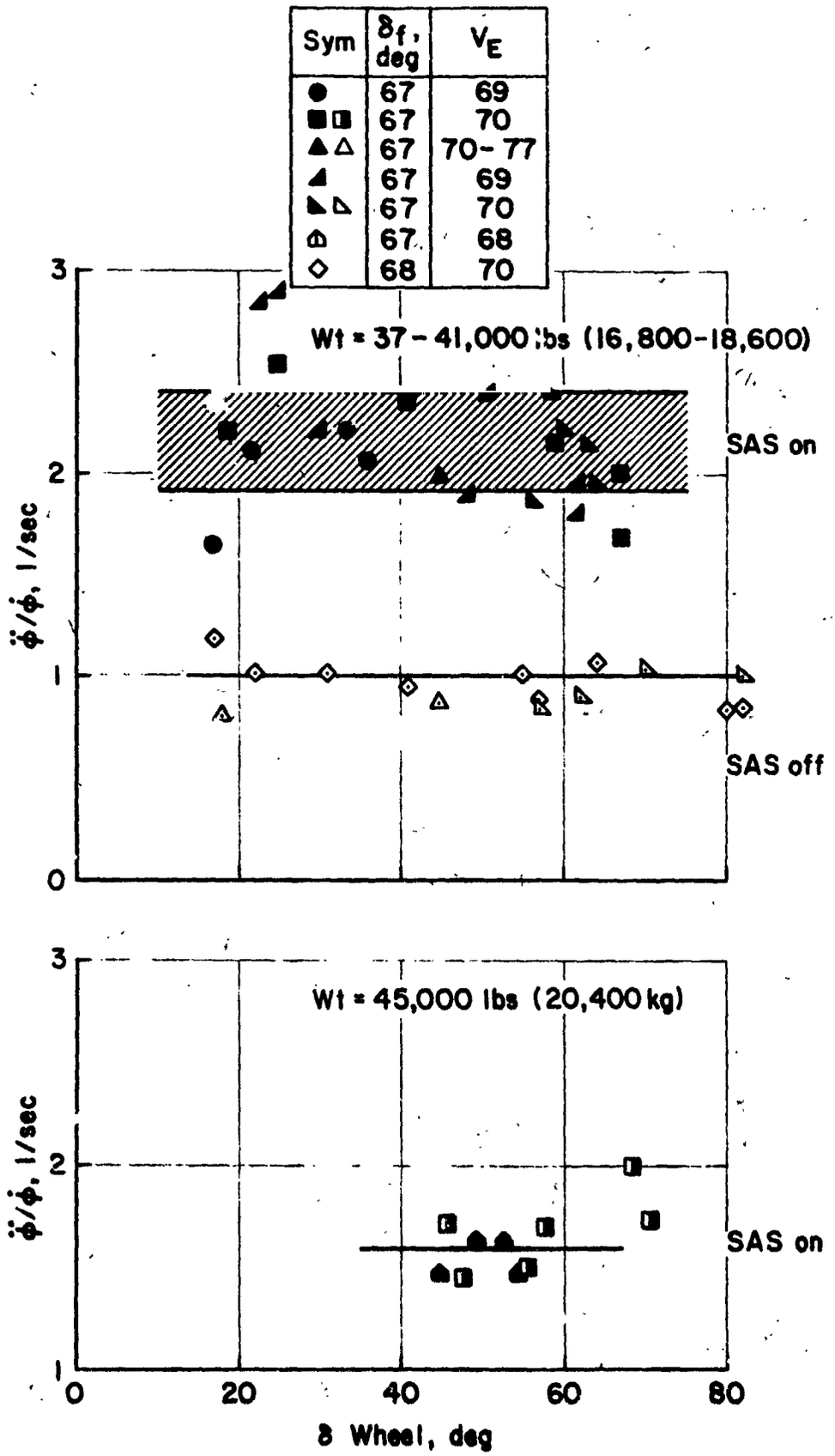

Figure 68.– Roll damping characteristics – flaps 65°.

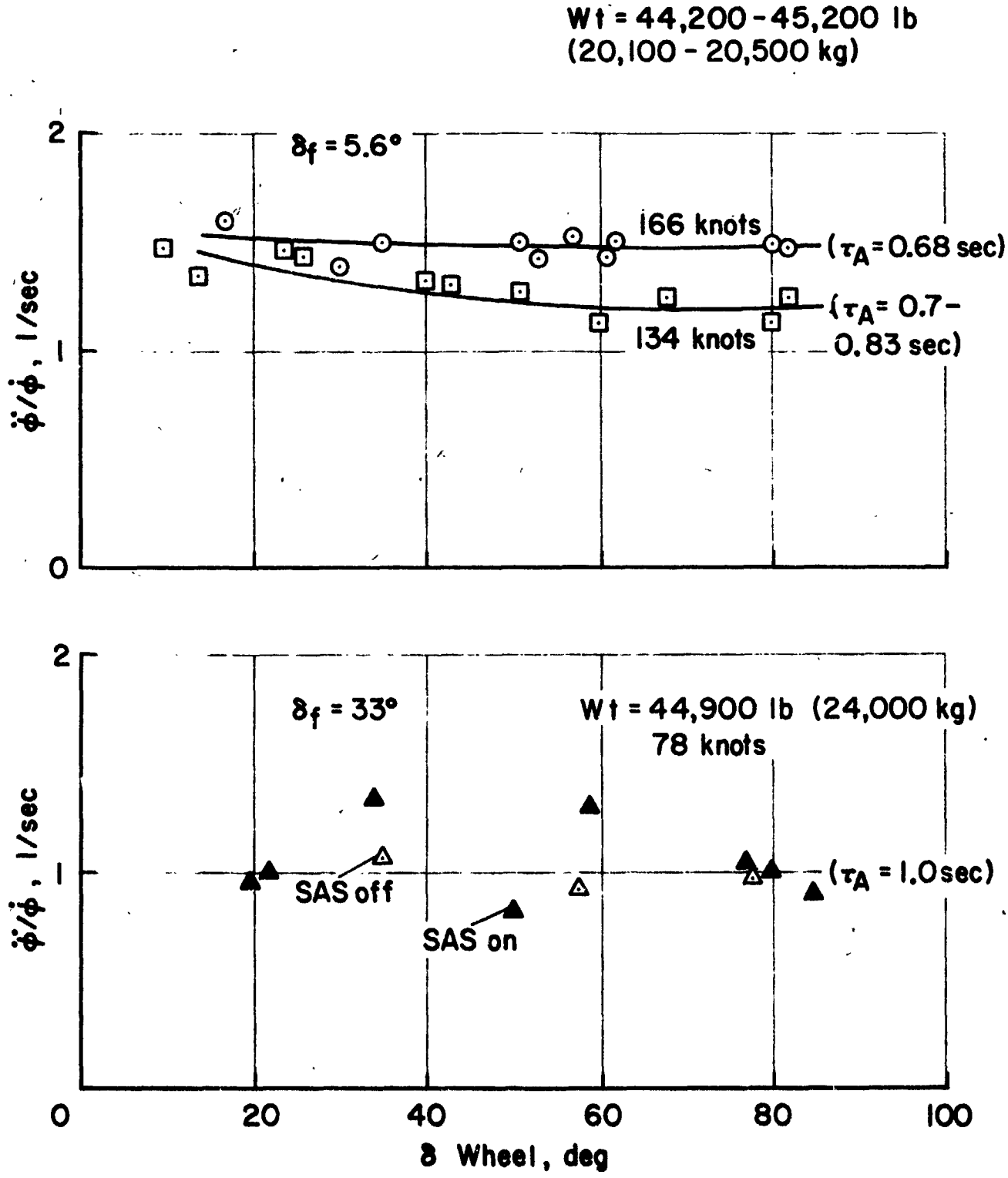

Figure 69.– Roll damping characteristics – flaps 33°, 5.6°.

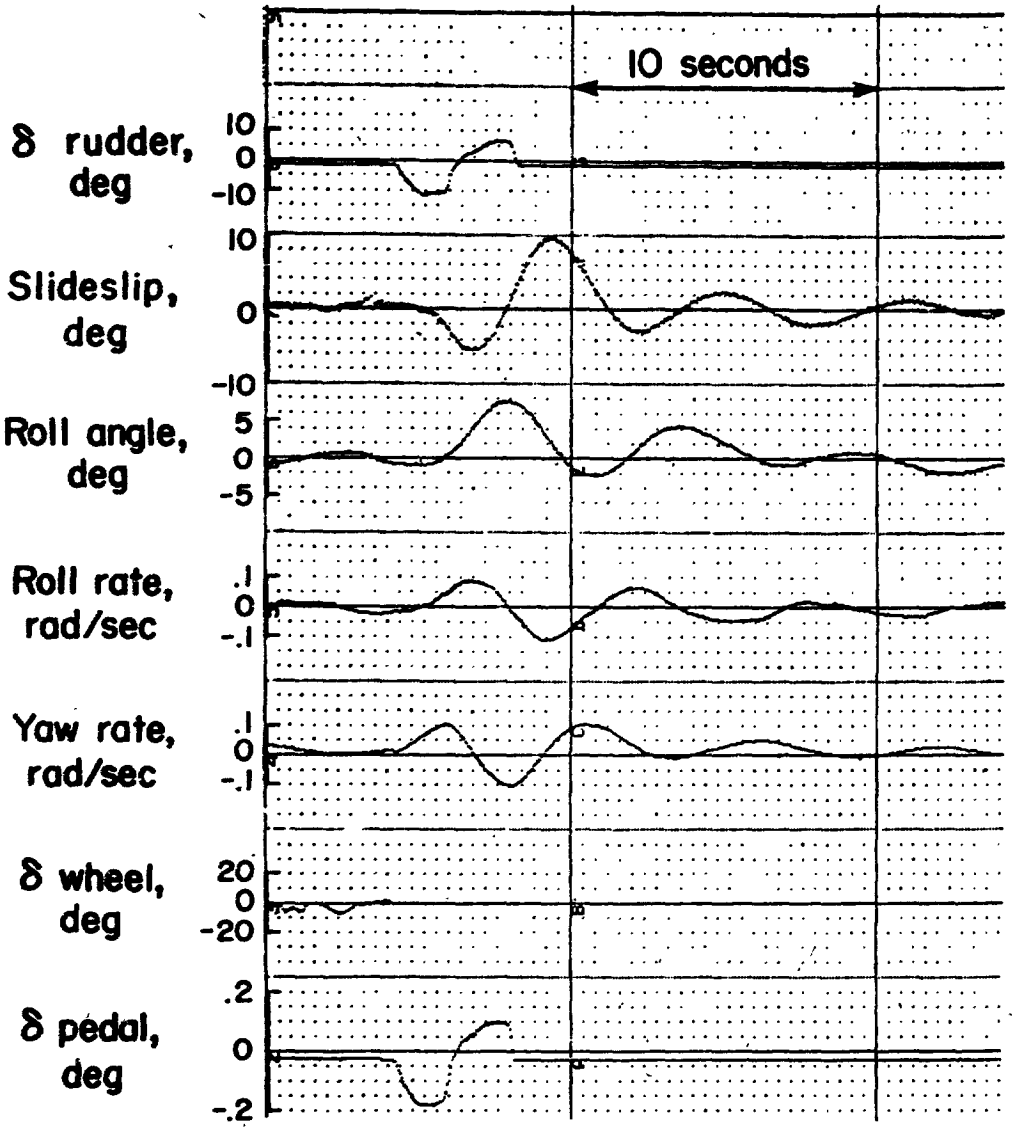

Figure 70.– Dutch roll – flaps 69°, 67 knots, *SAS* off.

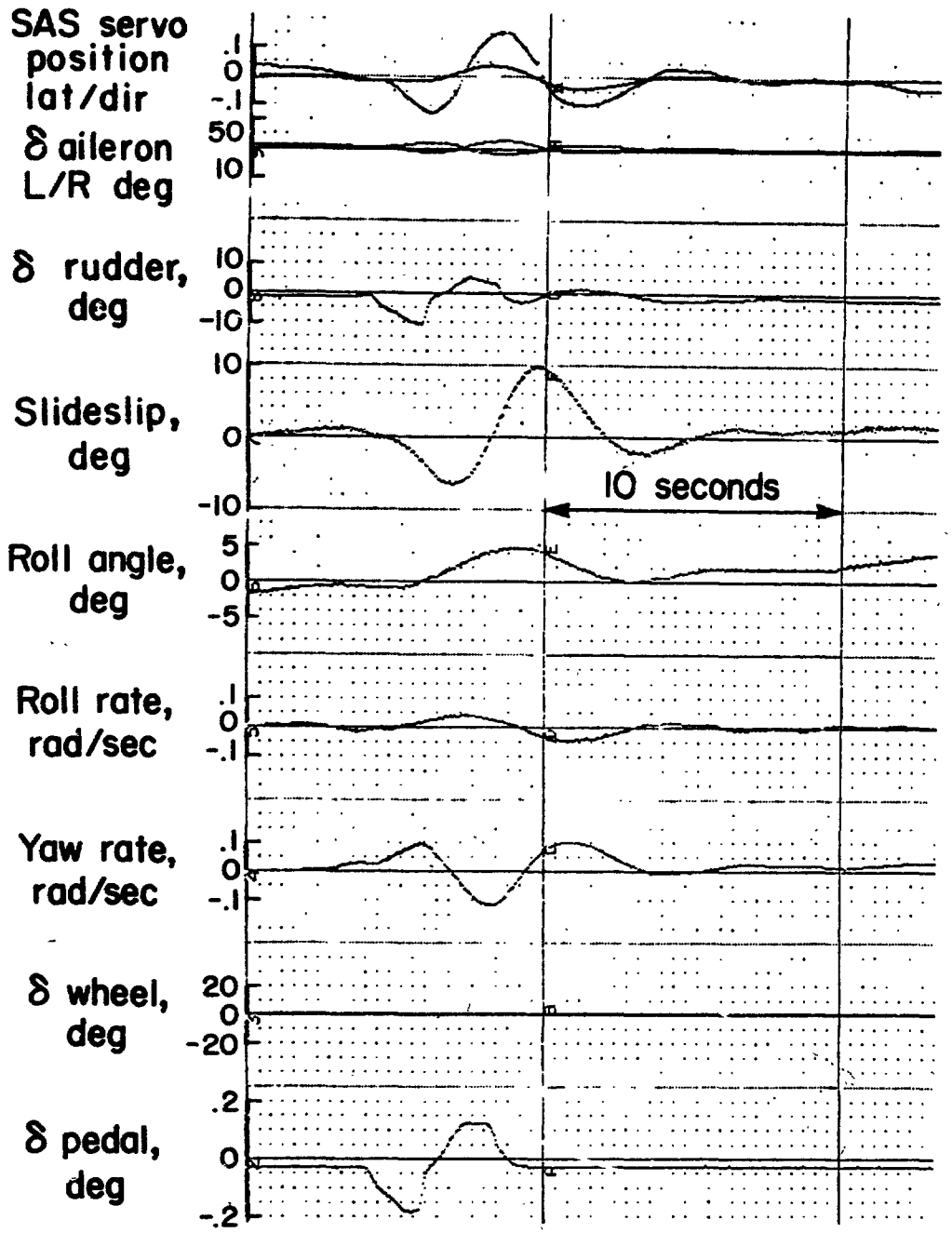

Figure 71.– Dutch roll – flaps 69°, 69 knots, *SAS* on.

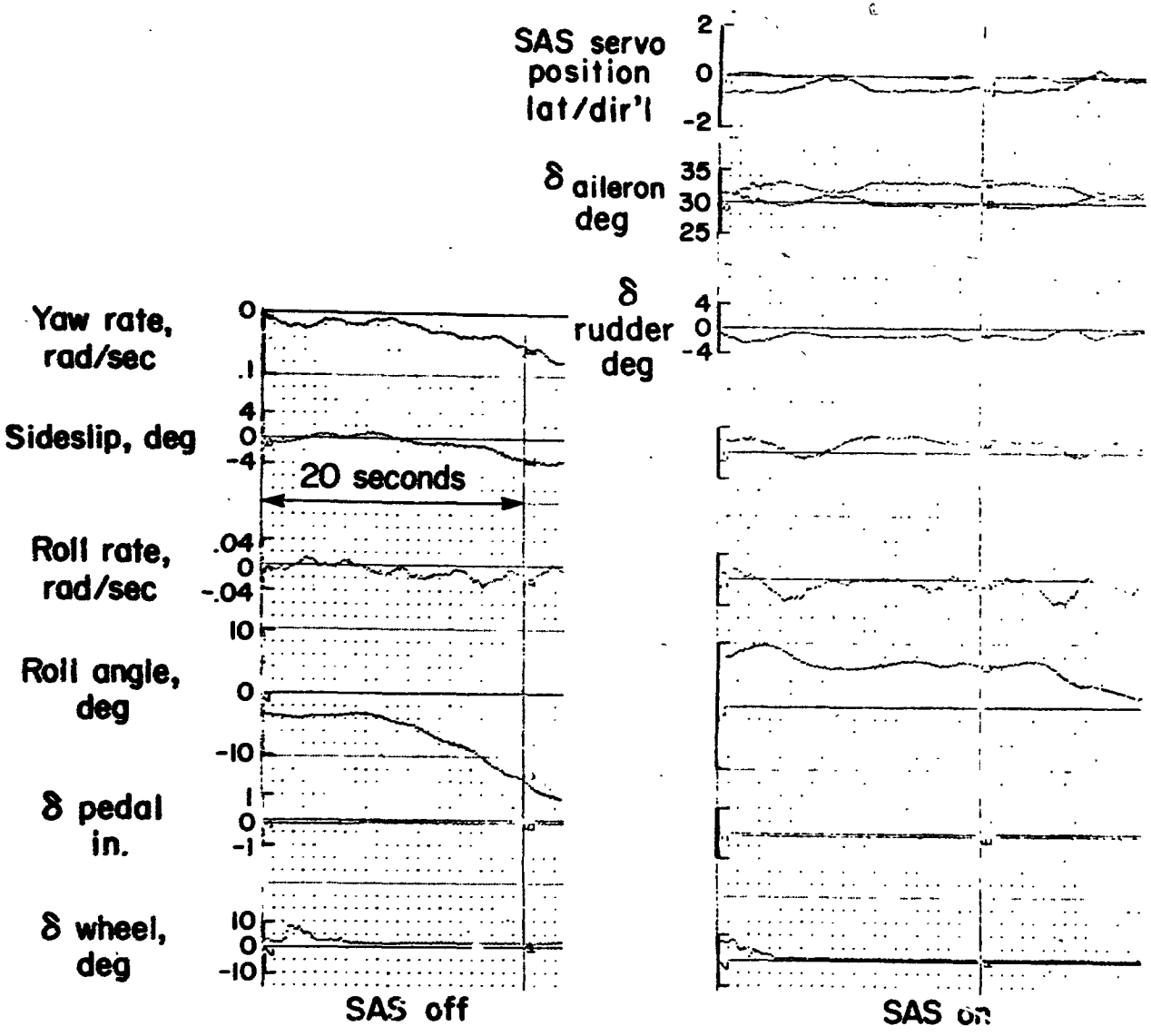

Figure 72.– Spiral mode – flaps 67°, nozzles 15°.

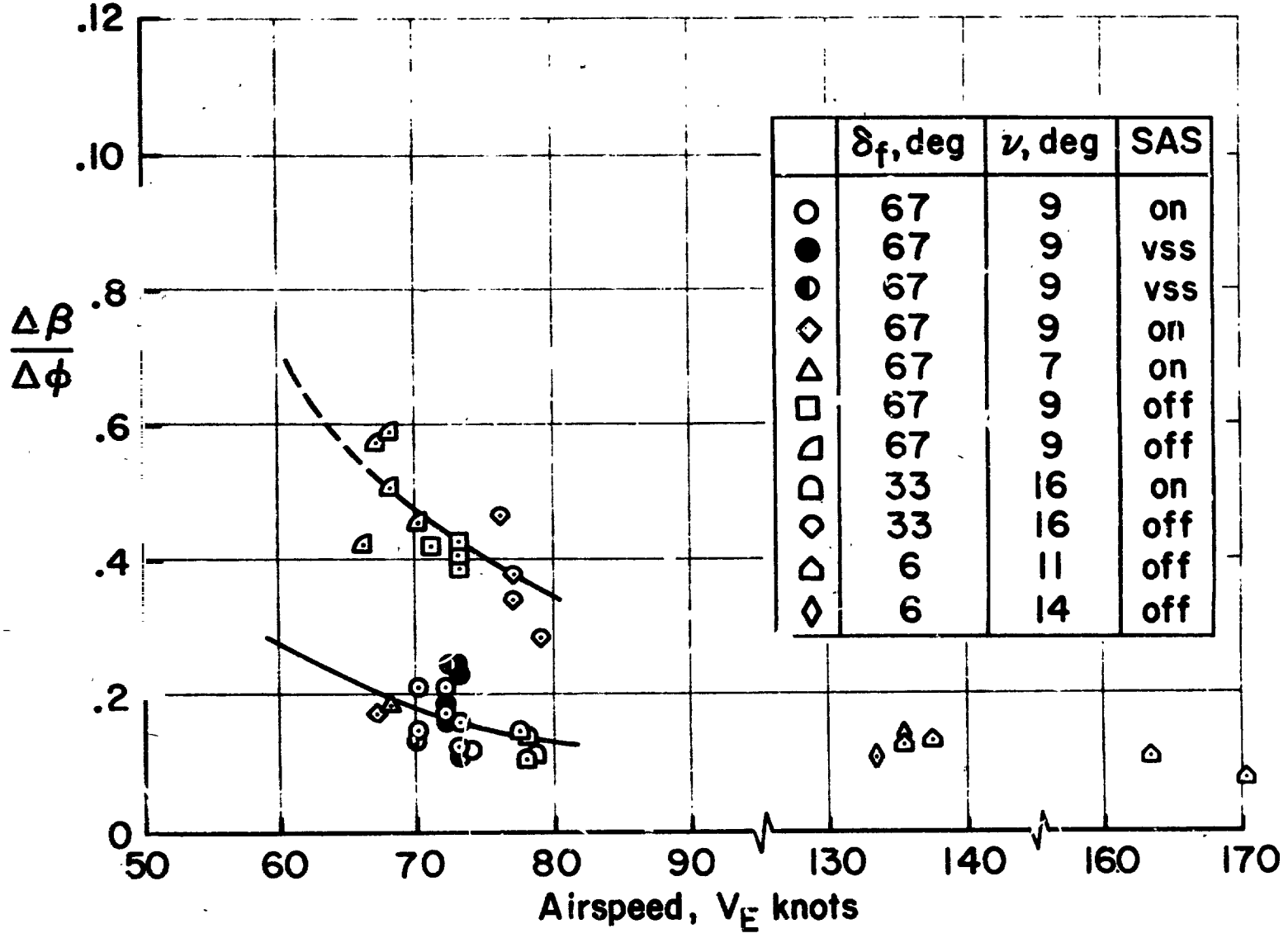

Figure 73.– Turn entry coordination data summary.

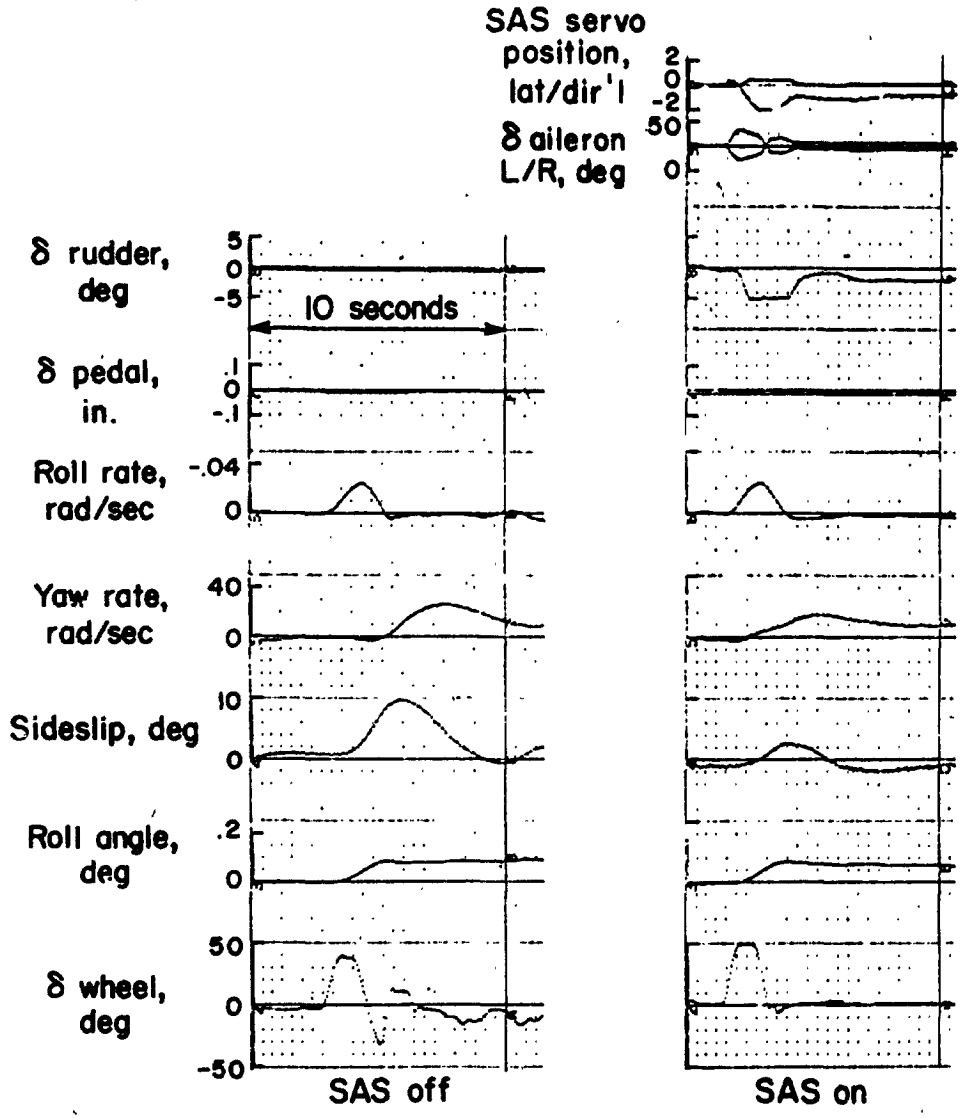

Figure 74.– Turn entry maneuvers – $\delta_f = 67°$, $V_{E_e} = 68$ knots.

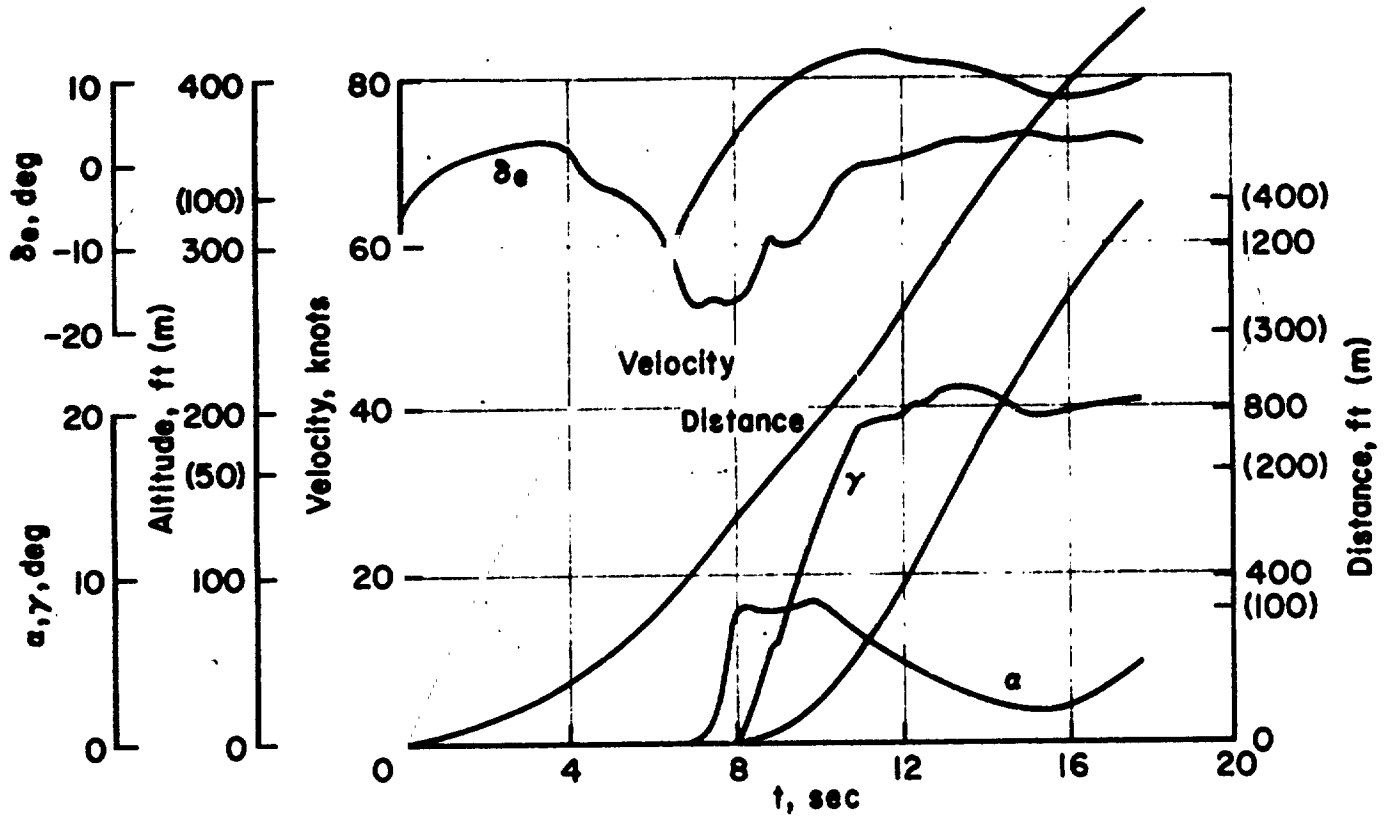

Figure 75.– Time history of takeoff, $\delta_f = 30°$, $N_H = 99\%\,rpm$, $W = 39{,}220$ lb (17,800 kg).

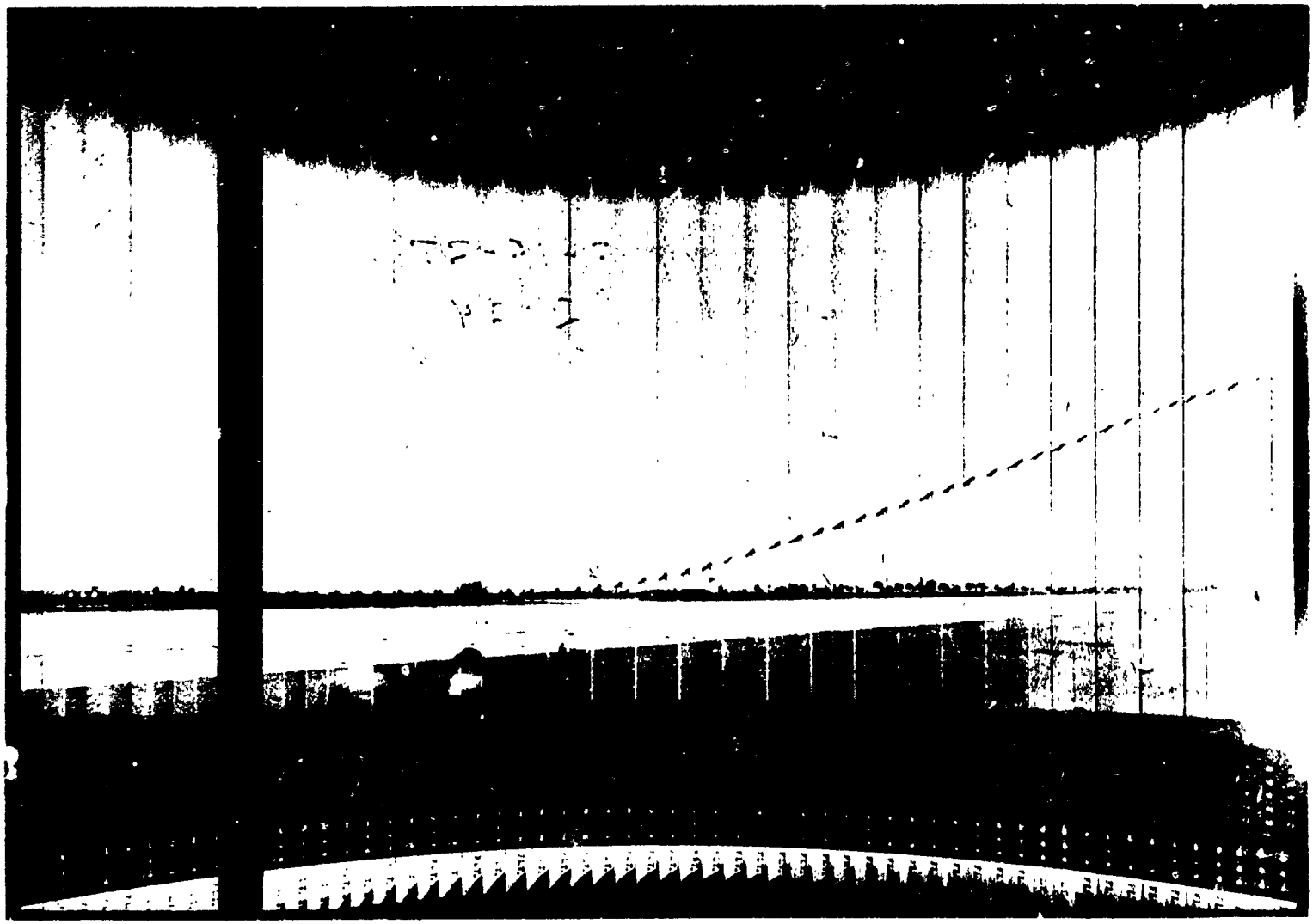

Figure 76.– Fairchild analyzer camera photograph of takeoff.

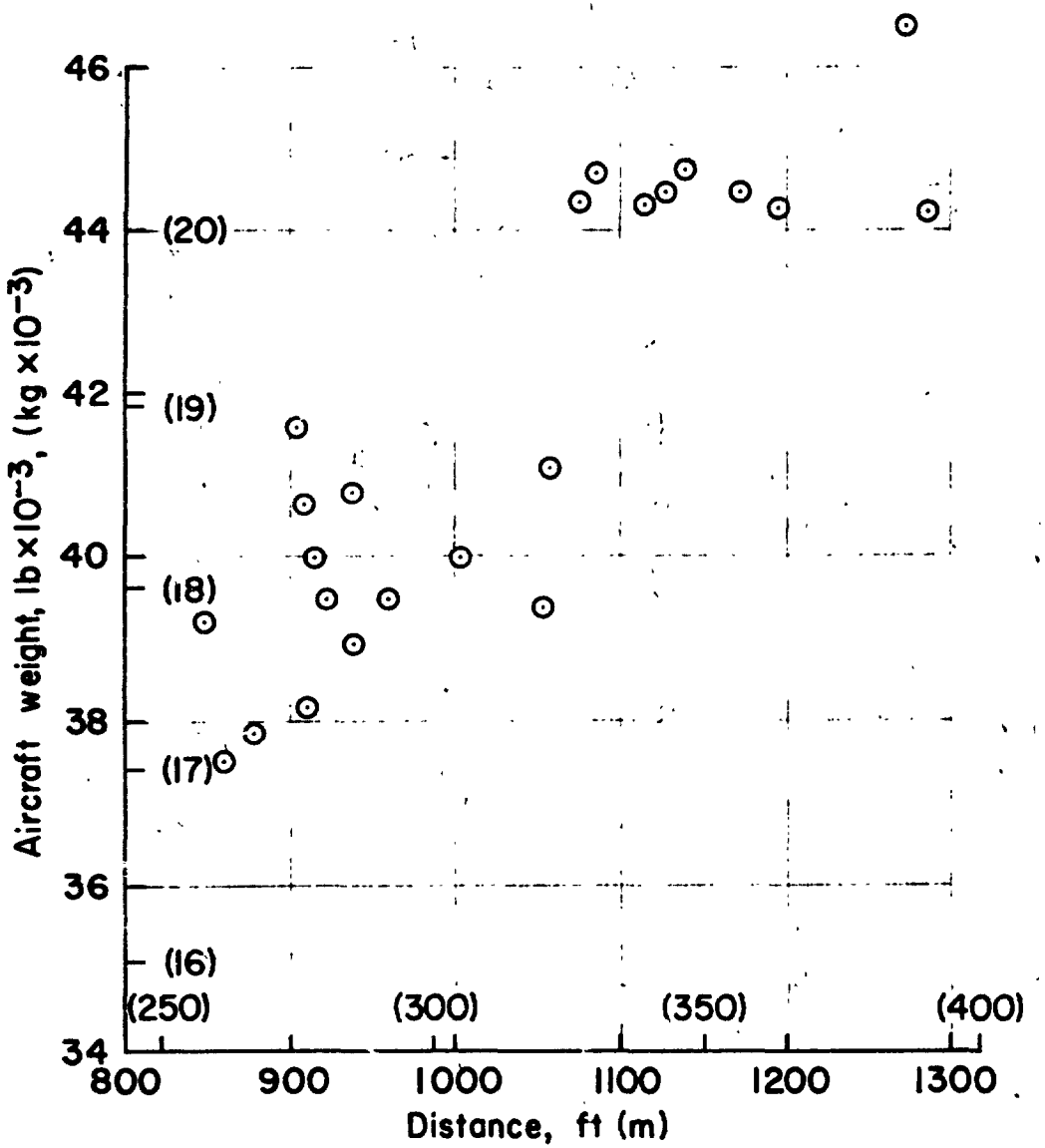

Figure 77.– Distance required to clear 35 ft on takeoff.

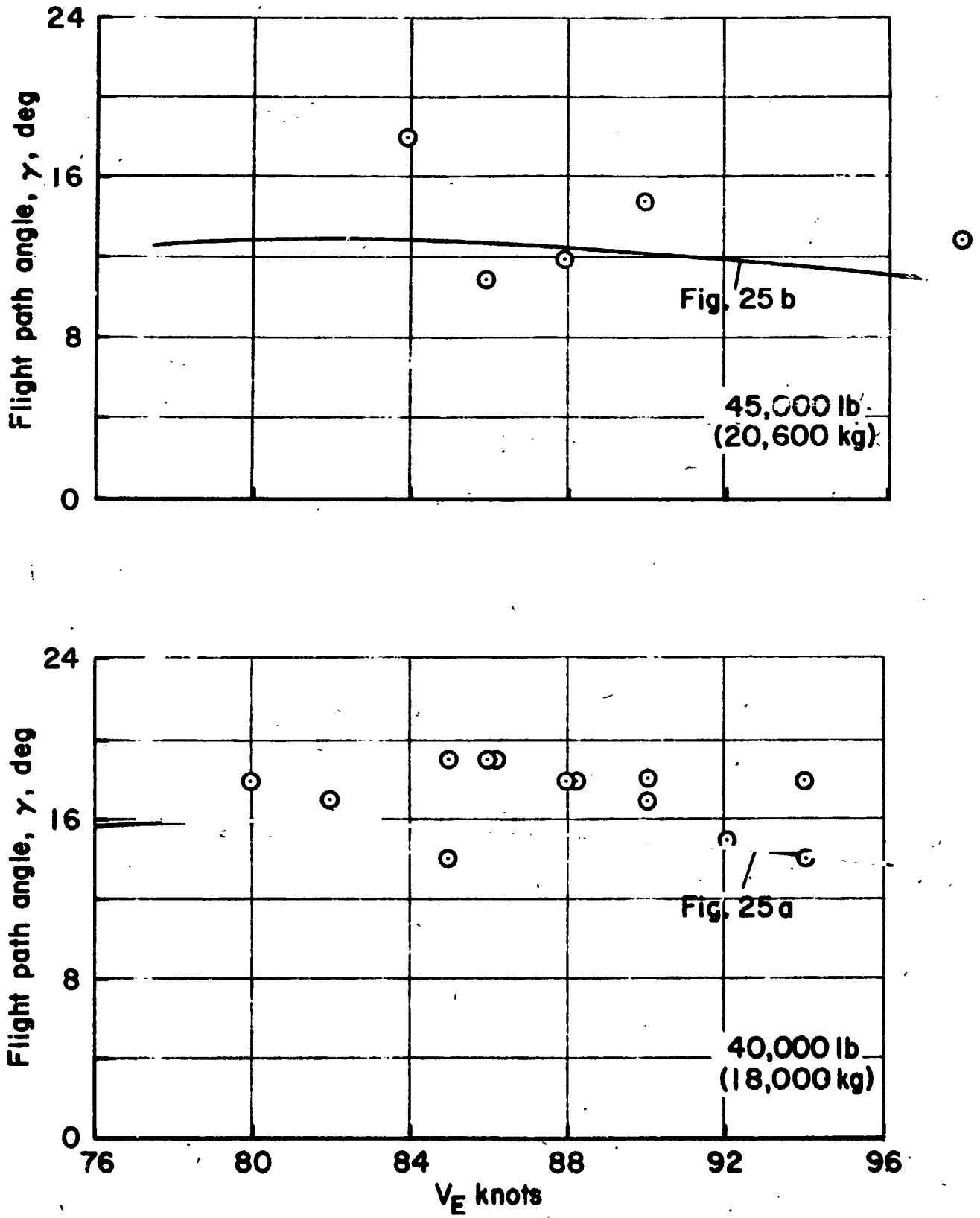

Figure 78.– Takeoff.

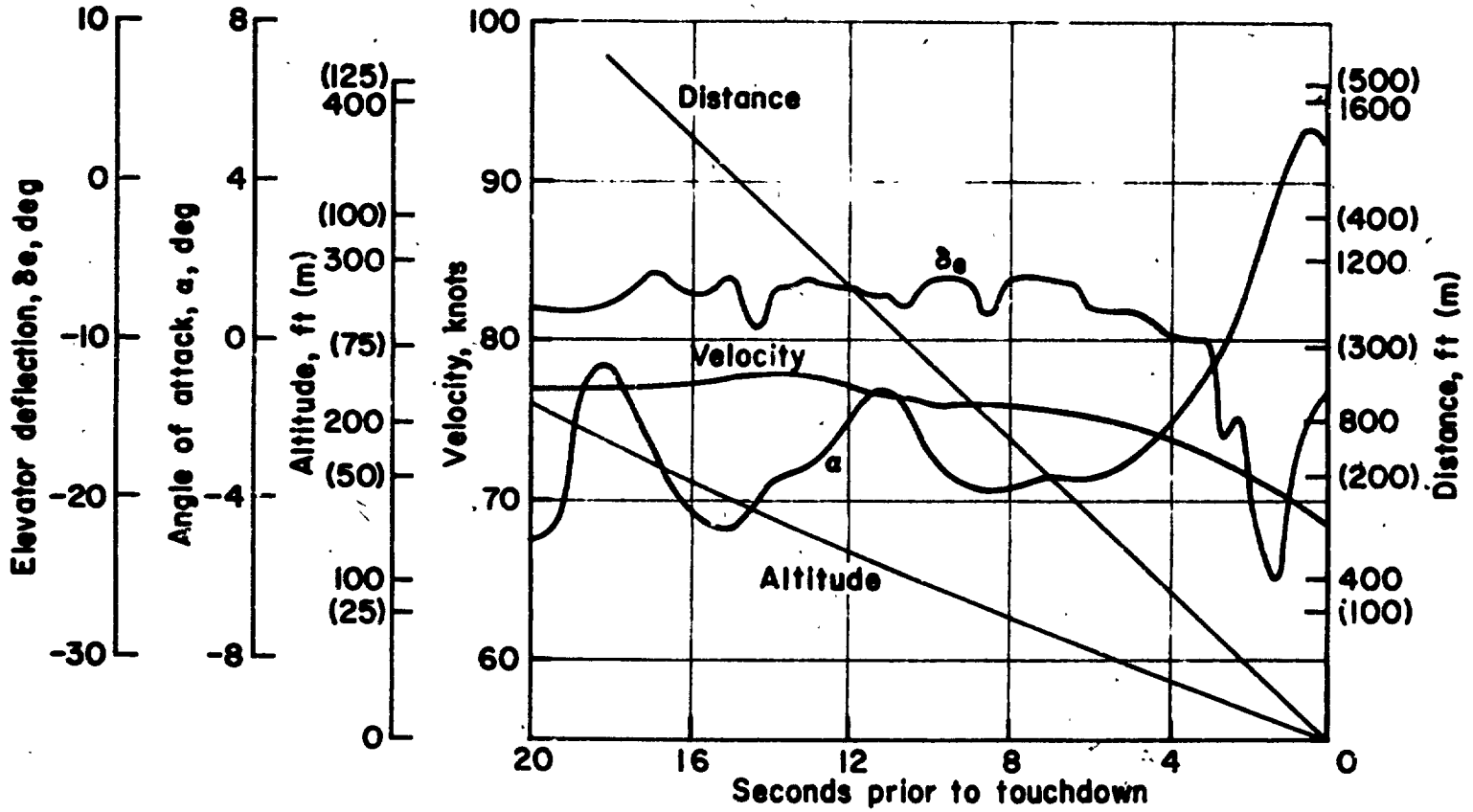

Figure 79.– Time history of −7½° flight path angle landing approach.

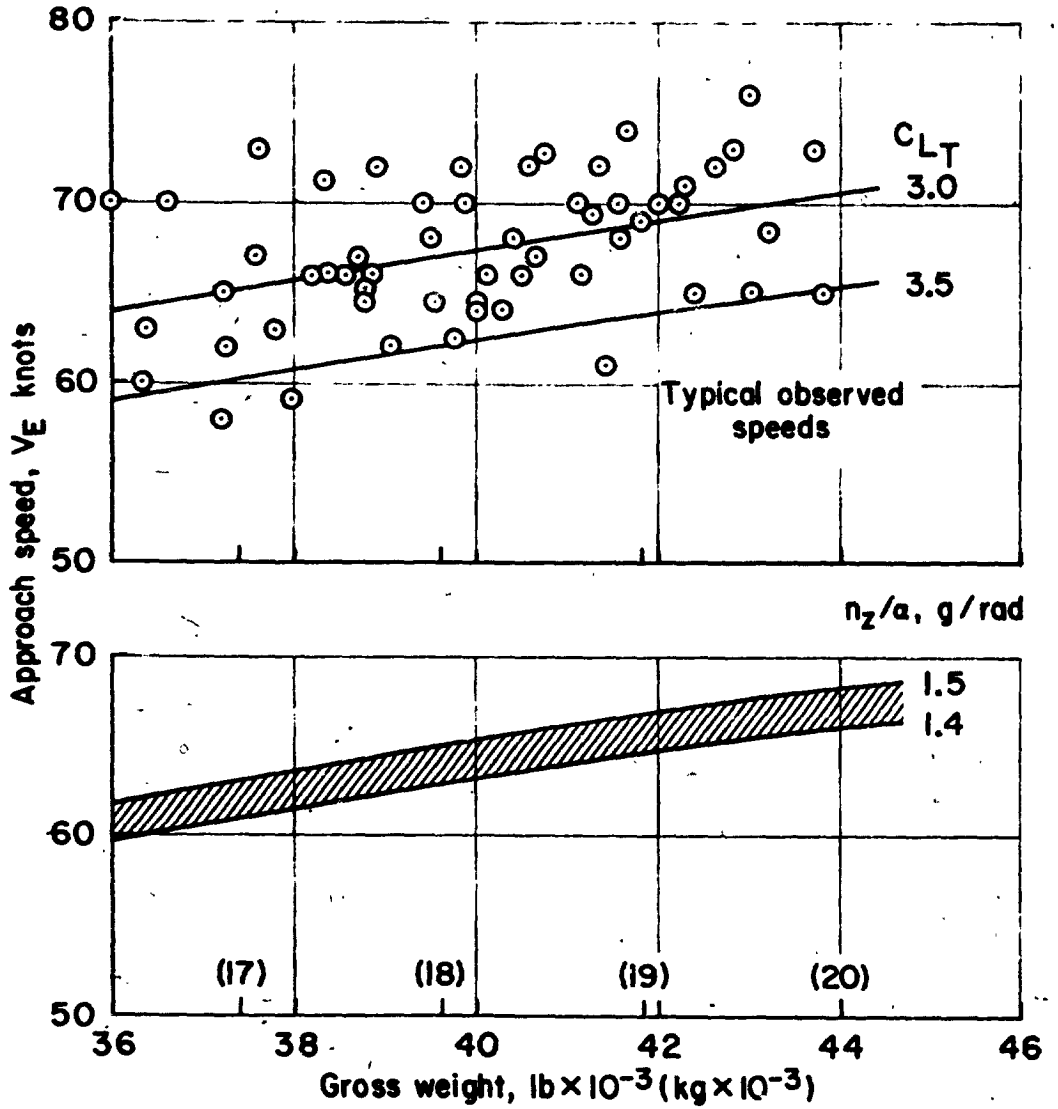

Figure 80.– STOL landing approach speeds, 65 to 70° flaps, –7.5° glideslope.

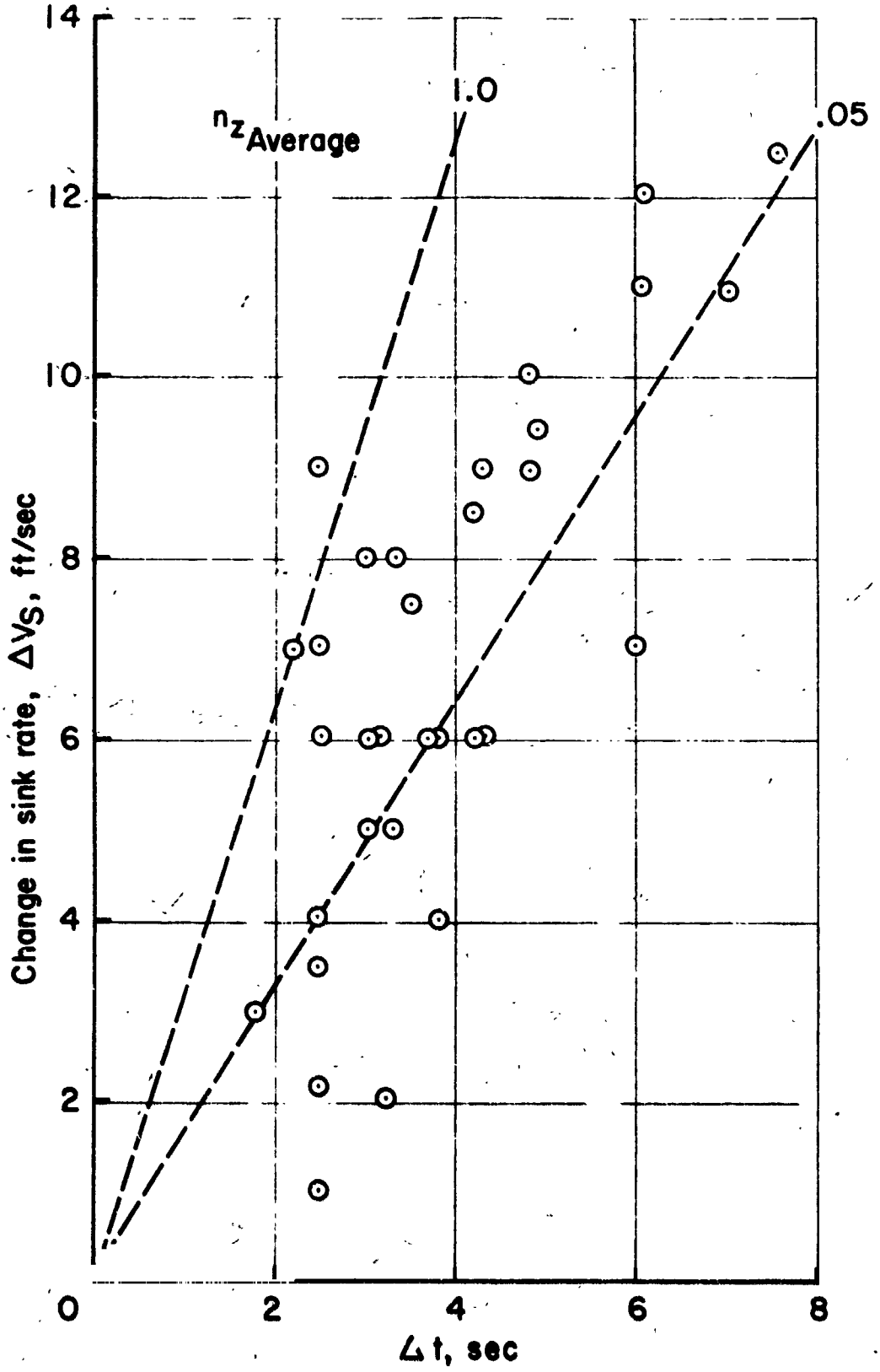

Figure 81. Change in sink rate during flare maneuver.

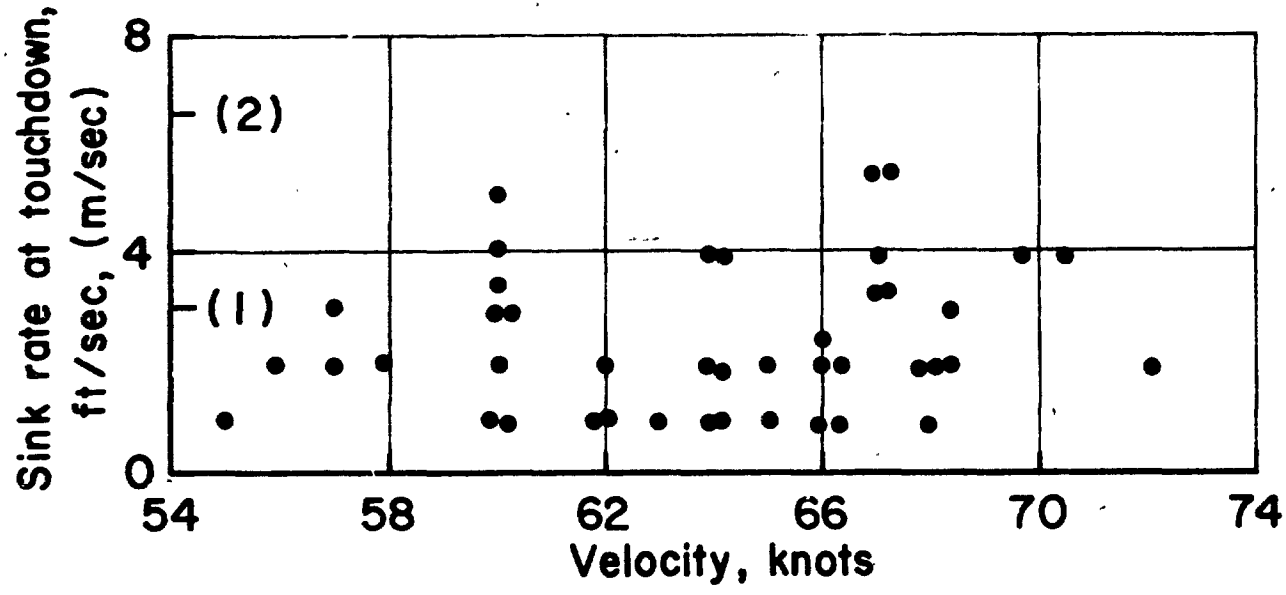

Figure 82.– Sink rate of touchdown.

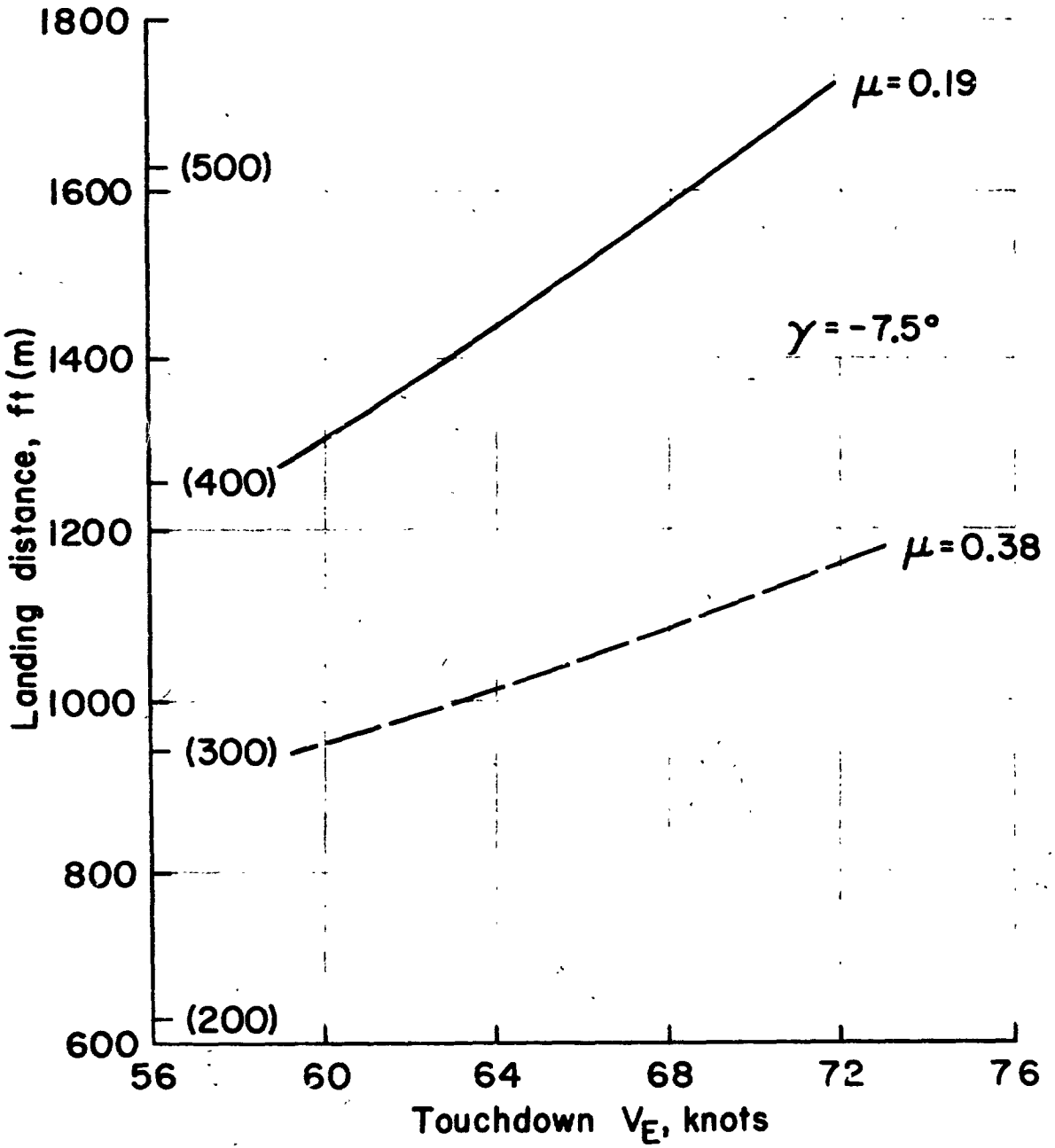

Figure 83.– Estimated ground distance to land over 35 ft obstacle.

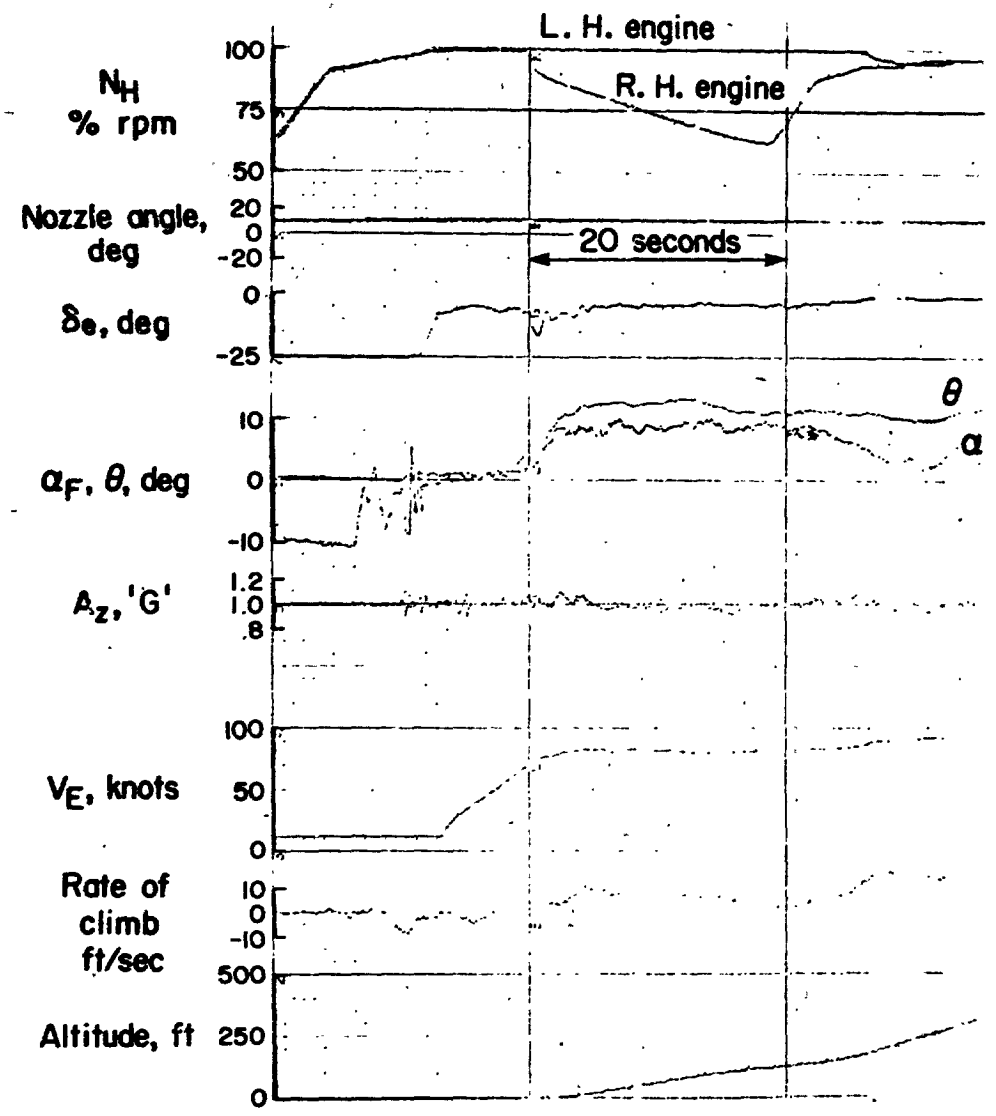

(a) Time histories of longitudinal characteristics.

Figure 84.– Simulated engine failure on takeoff, flaps 33°, 41,000 lb

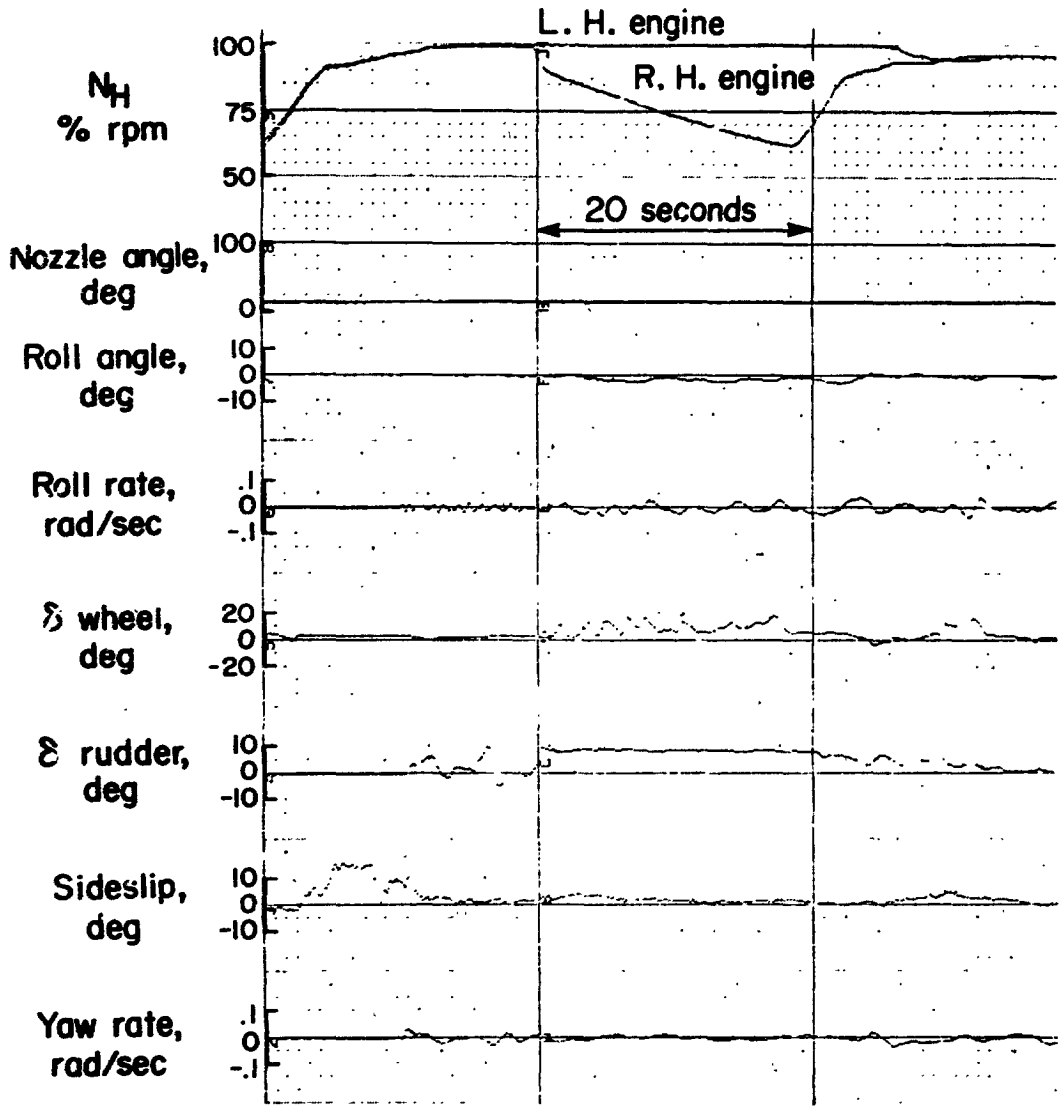

(b) Time histories of lateral-directional characteristics.

Figure 84.– Concluded.

	δ_f, deg	ν, deg	Weight, lbs	(kilograms)	Eng 1 %N_H	Eng 2 %N_H	Alt, ft	Temp, °C
○	28.6	11	45,900	(20,800)	60	99.3	500	11
□	32.0	11	44,400	(20,200)	99.5	62.0	600	14
◇	32.5	11	41,000	(18,600)	99.9	65.0	150	15
△	32.9	11	40,000	(18,200)	99.0	62.0	200	13
◿	32.7	11	38,620	(17,500)	98.8	61.8	180	14
⌂	41.3	11	37,400	(17,000)	60.0	99.3	700	14
— —	30	6	45,000	(20,400)	0	103.4	0	15

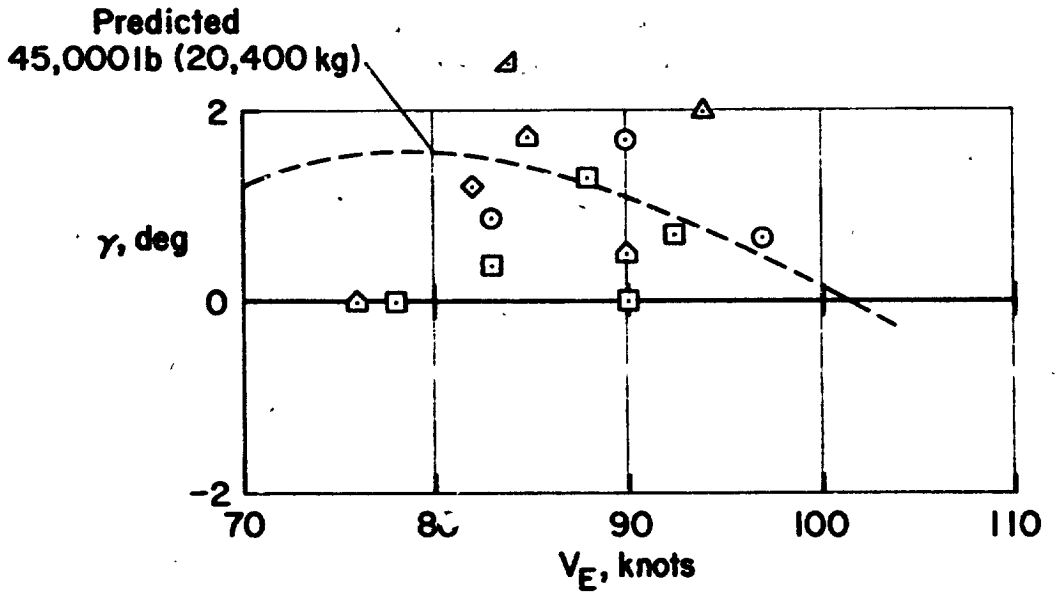

Figure 85.– Engine-out climb gradients on takeoff.

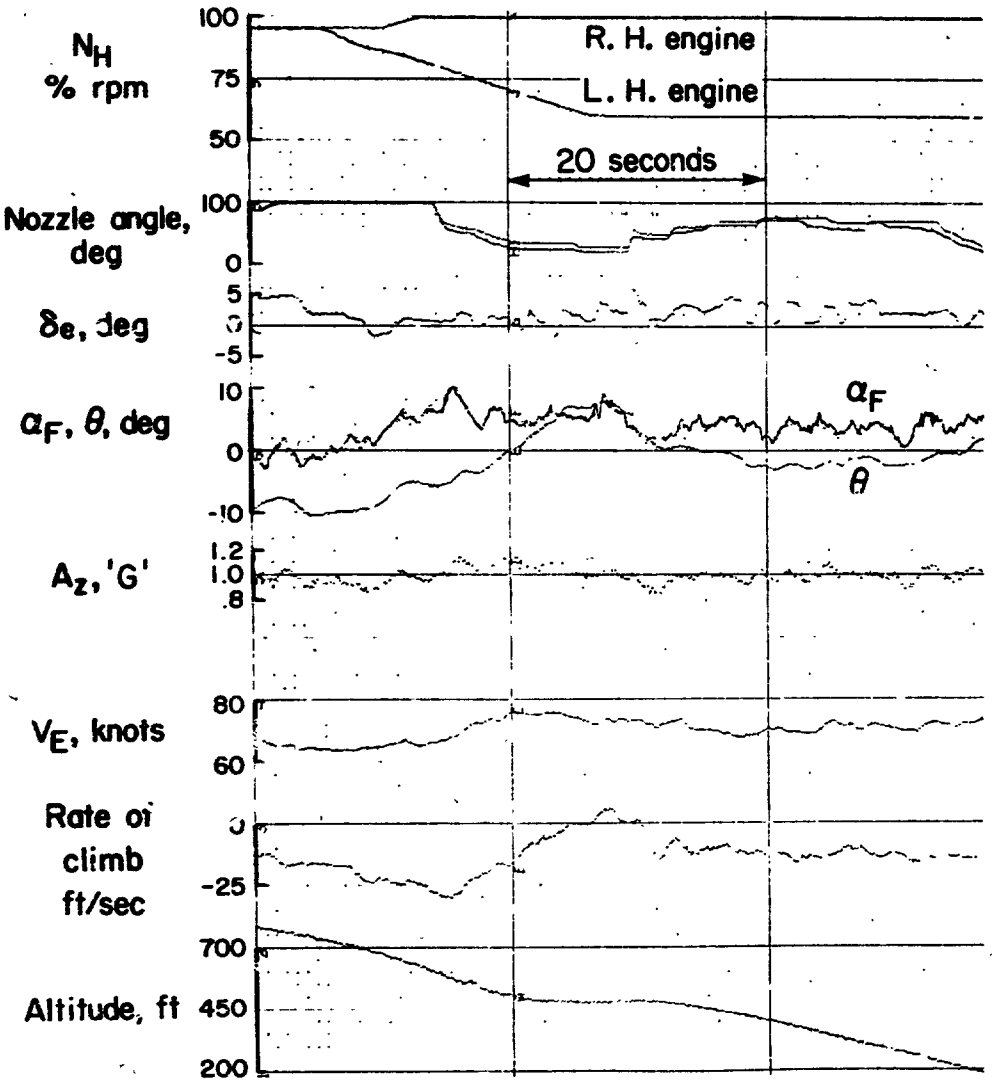

(a) Time histories of longitudinal characteristics.

Figure 86.– Simulated engine failure on approach, flaps 70°, 39,100 lb.

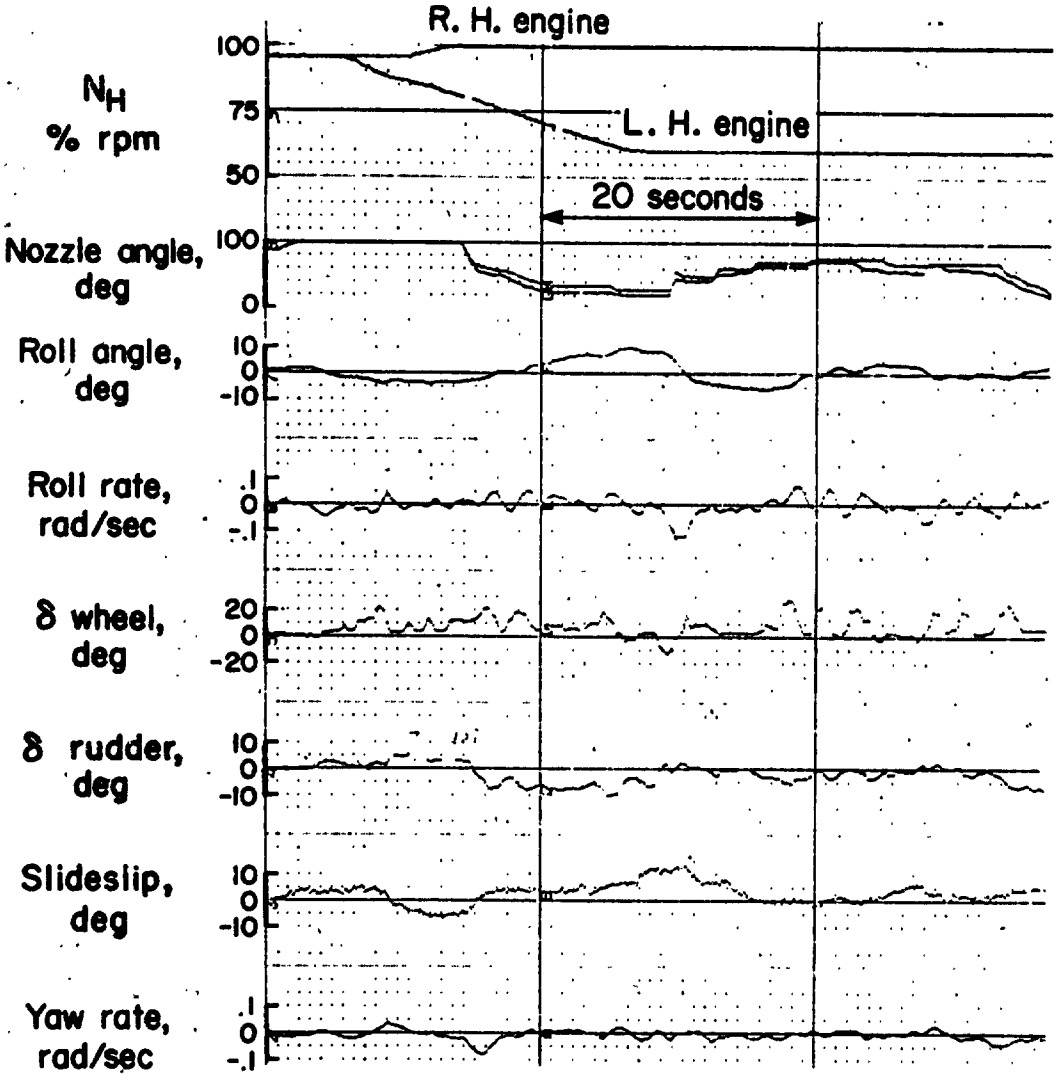

(b) Time histories of lateral-directional characteristics.

Figure 86.– Concluded.

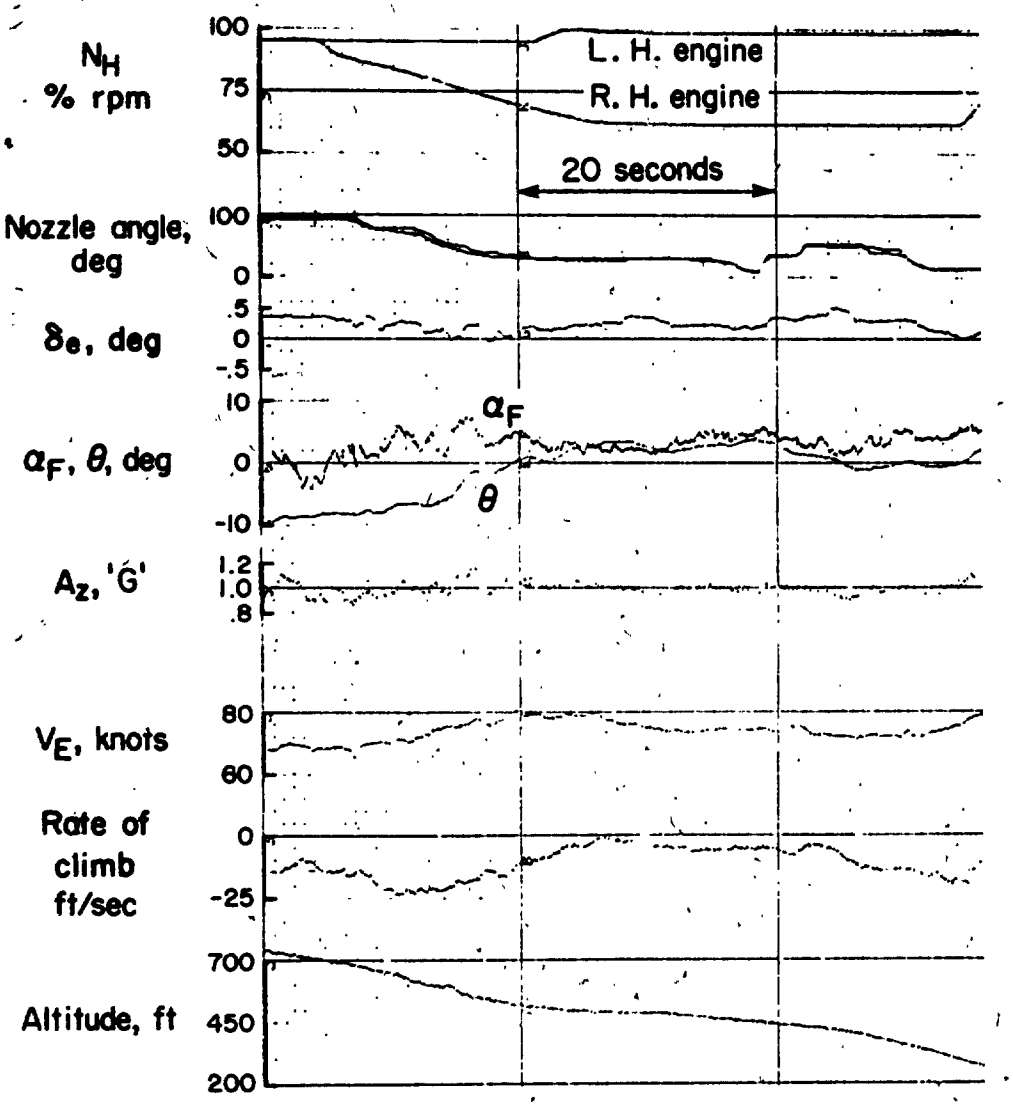

(a) Time histories of longitudinal characteristics.

Figure 87.– Simulated engine failure on approach, flaps 70°, 40,000 lb

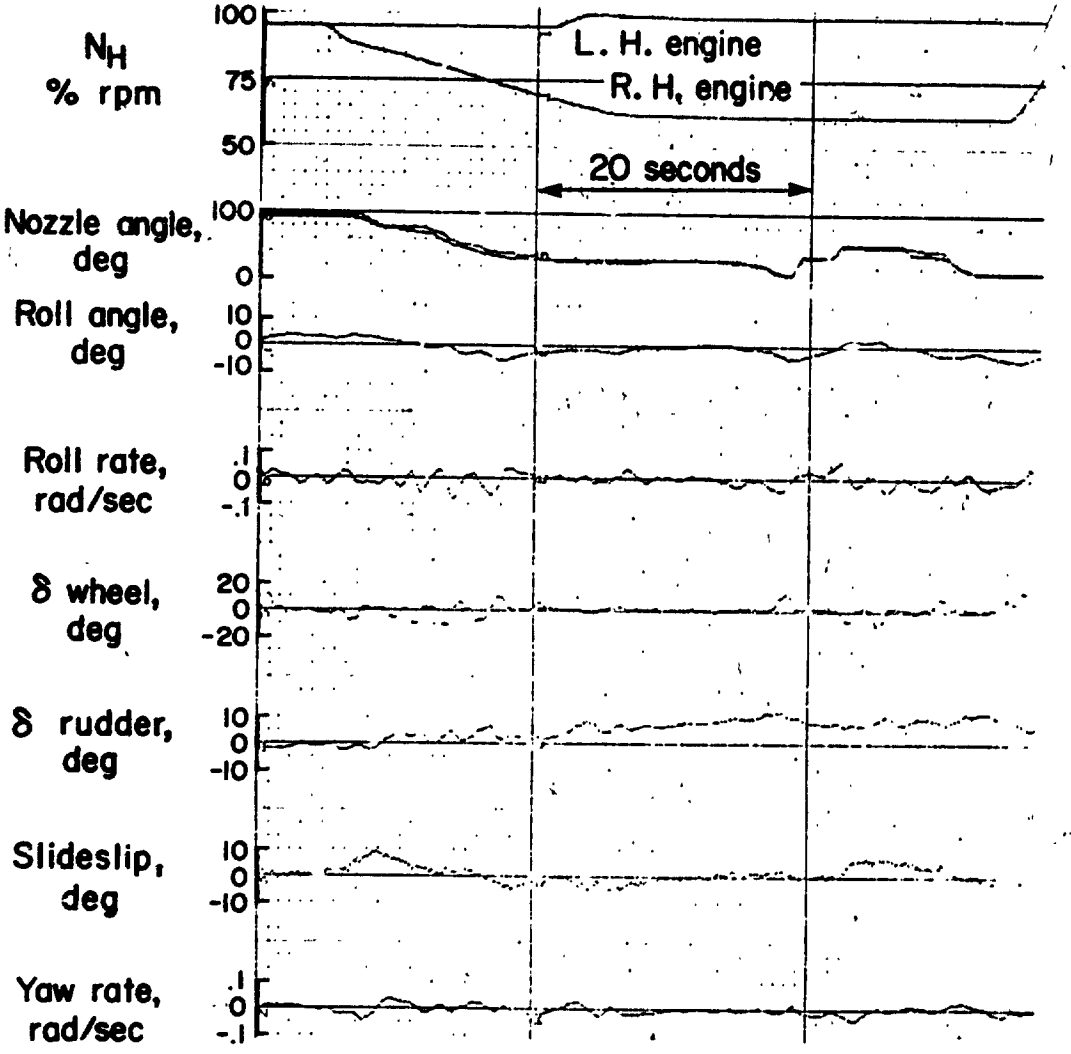

(b) Time histories of lateral-directional characteristics.

Figure 87.– Concluded.

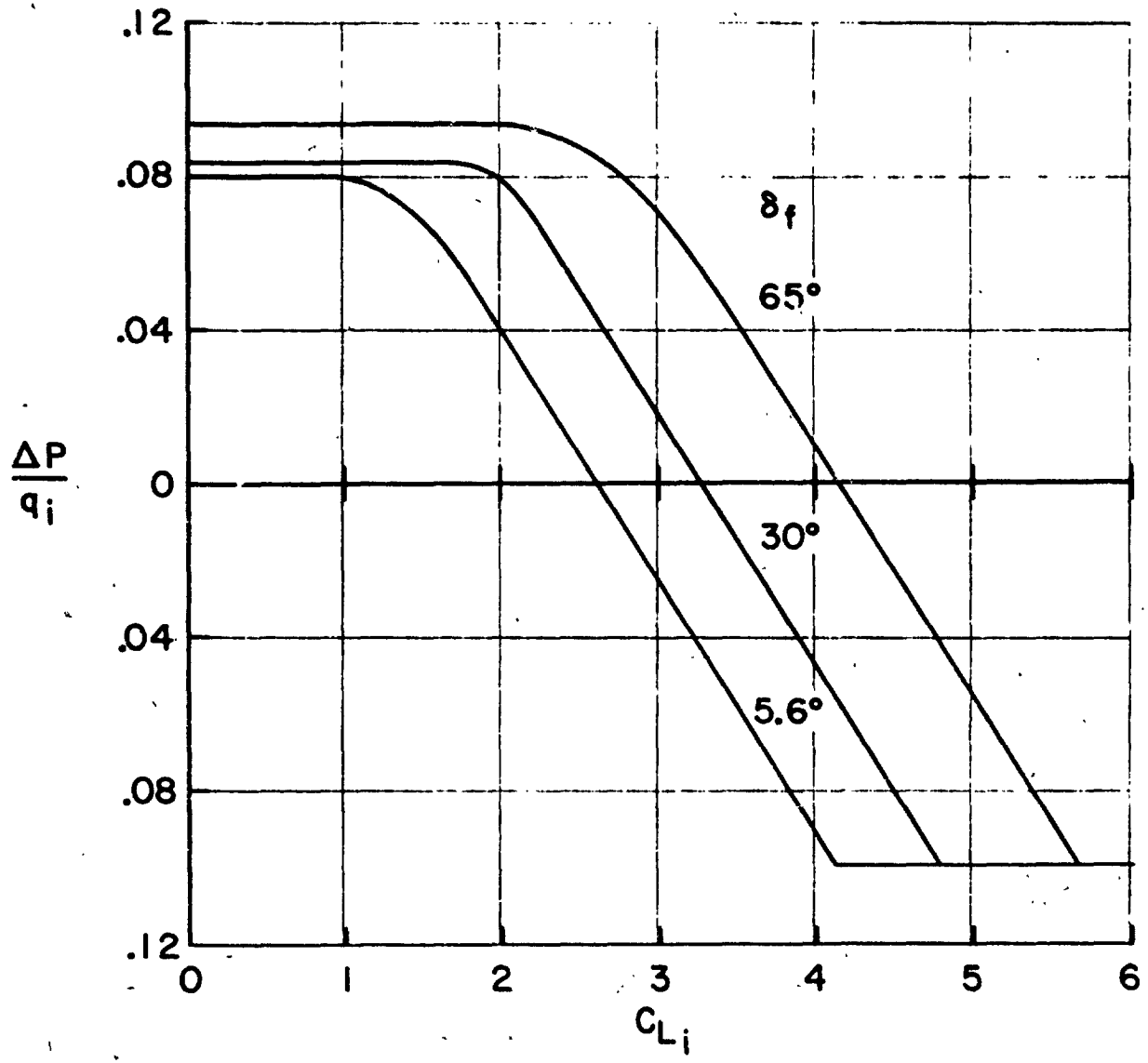

Figure 88.– Nose boom airspeed and altitude position error correction.

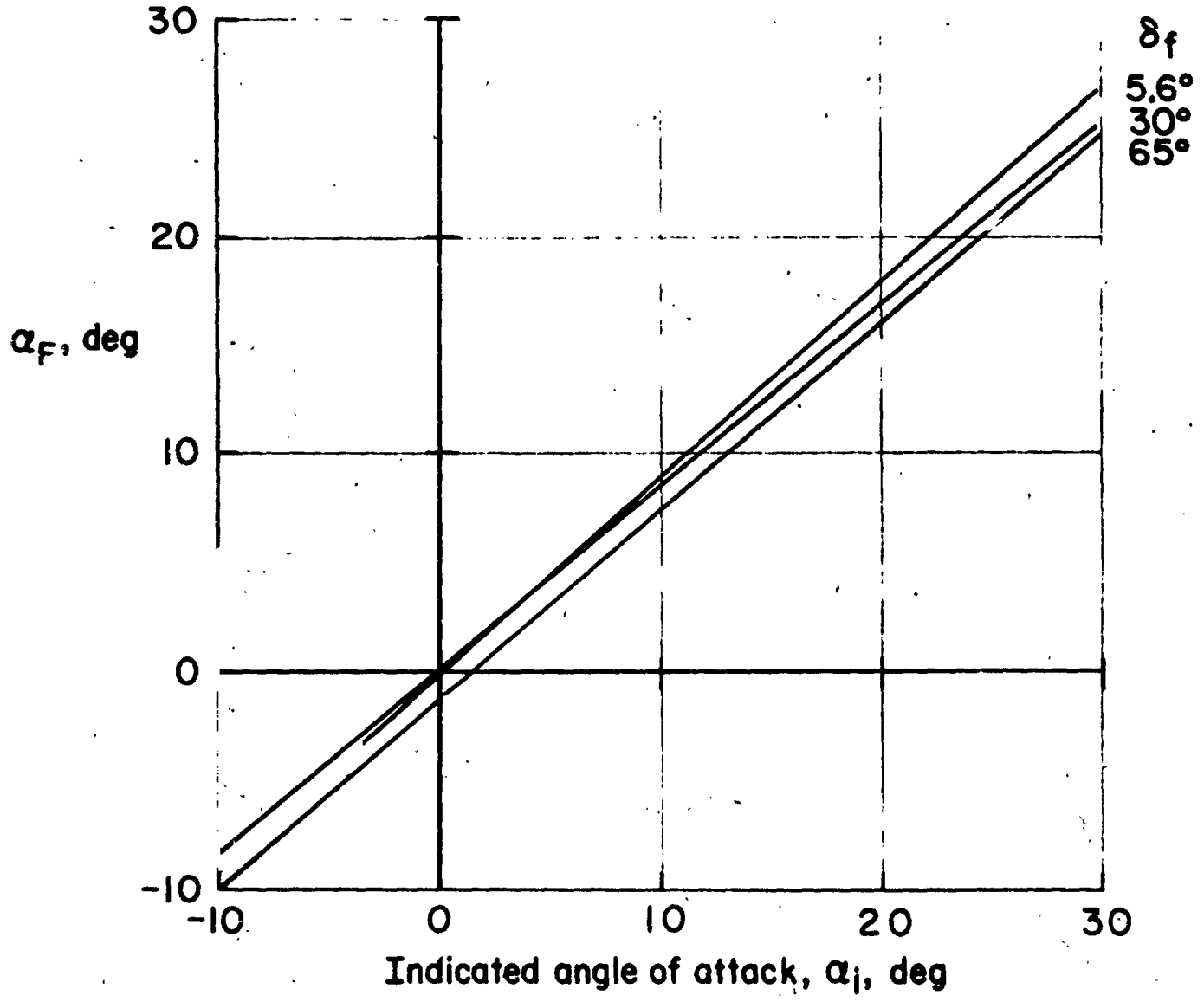

Figure 89.– Angle-of-attack position error calibration.